Étude analytique et numérique du bruit de combustion indirect généré par l'injection d'ondes entropiques dans une tuyère

Jun Zheng

université PARIS-SACLAY

CentraleSupélec

NNT : 2016SACLC070

Thèse de doctorat

de

L'Université Paris-Saclay

préparée à

CentraleSupélec

ÉCOLE DOCTORALE N°579
Sciences mécaniques et énergétiques, matériaux et géosciences

Spécialité de doctorat : Acoustique

Par

Mr Jun ZHENG

Analytical and numerical study of the indirect combustion noise generated by entropy disturbances in nozzle flows

Thèse présentée et soutenue à Châtillon, le 21 Septembre 2016

Composition du jury :

M. Christophe Bailly	Laboratoire LMFA, CNRS et ECL	Président
Mme. Aimee S. Morgans	Imperial College	Rapporteur
M. Stéphane Moreau	Université de Sherbrooke/Laboratoire LMFA, CNRS et ECL	Rapporteur
M. Eric Bouty	Safran Helicopter Engines	Examinateur
M. Sébastien Ducruix	Laboratoire EM2C, CNRS et CentraleSupélec	Directeur
M. Maxime Huet	ONERA	Co-encadrant
M. Alexis Giauque	Laboratoire LMFA, CNRS et ECL	Co-encadrant
M. Franck Cléro	ONERA	Invité

Success isn't a result of spontaneous combustion. You must set yourself into fire.

Arnold H. Glasow

To my family and Hélène.

Acknowledgements

The writer may sound cheeky by saying that the supervision of this PhD thesis was the best in comparison to other PhD students he has met, but the constant meetings, criticisms, ideas, etc., and the complete implication of the supervisors allowed the completion of the present work. Even if only one name were written in this document, the realization and the finalization of this work would have not been possible without the precious contributions of my supervisors.

The writer takes great pleasure in expressing his deep gratitude to Dr. Sébastien Ducruix for his helpful and patient discussions of the contents of this thesis, his careful reading, simulating criticism of the manuscript and his constant availability. Sébastien, your positive, kind and constant encouragements allowed me to always push forward my limit and never give up.

I am indebted to my supervisors at Onera, Maxime Huet and Franck Cléro. I know it is not an easy task to become a PhD supervisor in the middle of the process, but both of you did a very good job. Your contributions to this study were complementary and enhanced the quality and the contents of this work. Maxime, as your first PhD student, I hope this experience has given you the will to pursue and have a bunch of slaves to work for you. Good luck Ariane! Joking of course. I hope you know how lucky you are to have a very devoted supervisor! More seriously, Maxime, thank you for your time, especially during the writing of this document. Your several remarks and questions were priceless for this manuscript.

To Dr. Alexis Giauque, my sincere thanks for giving me the opportunity to tackle a subject I was not aware of. I am really grateful that you took the time for supervising my work even with your new position at ECL. Thank you for finding the time between two equations to code, to participate in the meetings, to always be available when I needed you, but also to read carefully the present document!

Also, my sincere thanks to the referees Dr. Morgans and Pr. Moreau for their careful reading and constructive criticisms of the manuscript, but also all the members of the jury for their time and above all for coming to my PhD defense as they all work far from Paris.

In a more personal way, I also need to express my deep gratitude to my family and my friends for their direct and indirect contributions (easy one).

First, I cannot thank enough my family and especially Hélène (my little 🐼) for their precious support all along this PhD thesis. Thank you for your patience and for enduring my bad mood and my complaints. I address my sincere gratitude to 🐼 for showing up in my

life and sharing the rest of it with me 😍 (you'd better!). As a compensation and the least I can do is to always be there for you!

I kiss all the current or previous PhD students that I have interacted with. My first big thumbs-up goes to Johan, Fat Jojo or 🧸 for those who understand. We have started our work at ONERA at the same time and we had a great time at work but also outside. Your joy for life or 🍺 has spread around all the PhD student when you were here! Iannis or the 🦃, after spending so much time in the same office, I can definitely state that your musical tastes are really bad and almost 💩. However, we had great time together and for that I am happy even if my I am quite sure that my productivity had suffered from it! Mathieu or aka 👆, I bow down to your incredible skill to simplify the note at the restaurant. Your awesome cooking skills permitted me to get enough energy or mainly sugar to work hard 😀! My salutation also goes to Yves or 💂 for his fun as large as his hair and for his support. I am also very happy to express my gratitude to Jean-Charles for the many rides he provided during our respective thesis at ONERA, by the way, thank you for the logistic help for the buffet 😘. Fernando, thank you for your endless conversations about paella 🍤 and which country has the best wine. My greetings also go to Paul, Paul the 🐙 or Popol (no emoji of course!) for his incredible coding and IT skills. Sofiane or Mr 😴, we drank a lot coffee together, but what should be retained are our mathematical discussions, thank you for that. Nevertheless, you should stop finding bad excuses or 🦄 courses to skip interacting with other PhD students outside ONERA 😉. Ariane, Ginny Weasley or the 🐢, now everything relies on you so good luck 🍀(joke). I hope that you will benefit from the present work and successfully pursue the study on ICN on what I did not have the time to! Tobias or Tobichou for the closest, thank you for sharing your passion about wake-boarding and kanske en dag kommer vi att tala svenska tillsammans! Robin or 🚰, thank you for showing so much love to my cat. For the new arrivals, Adil and Antoine, I unfortunately did not really had the time to know you well, especially Antoine, but I hope that both of you will enjoy your time in DAAC.

I also have to thank my other friends for their endless support. Rachele or my little Italian 🐑, you have been always available even with the distance between us, the same goes to Audrey 🇨🇦. Solène or Bibin, Kévin 🏓, Marichou, Charlottes (this is not a typo), Émilie, Axel Foley, Benoît, Derya, Benjamin, Murad, Nicola and many others for the great time we had.

I show my appreciation to the Krav Maga team (Saïd, Fred, François, Tristan, Alina, etc.,) for changing my thoughts during the training. Without you and the bruises I would never have the strength to reach my limits.

My acknowledgment also goes to all the members of the DAAC but also previous members of this department. I acknowledge Laurent L. aka the King of spoonerism for his

tricky daily jokes and Thomas alias master of darkness for knowing everything not like Jon Snow (but always check the validity of what he says). Serge, thank you for really knowing everything! Ingrid , Marc , Alain and Vincent (alias the master), your incredible musical talent have brought happiness all around the department. Cyril or Pop's, you are always cool, but also very professional at the same time and I hope you will always stay the same. I bow down to Yves D., the honorable representative of our sweet Savoyard fief (ici c'est Rebloch')! Laurent C., you have allowed me to realize many DIY projects by always providing me the tools I needed and for that I will always be grateful to you. Daniel-Ciprian, Patrick L., Eric and Fabrice, thank you for the jogging that kept me in shape or at least at the beginning of the thesis! Thank you Lydie and Ghislaine for your smiles, Sylvette or Mamie Nova for feeding me! Daniel, you will always be the King of Planteur to me . I salute Laurent S. for his discussions about culture , Frederic and Snoopy for the walks in the forest of Meudon and William for his talks about wine . I show courtesy to the rest of the DAAC (Hélène G., Marie-Line, Sandrine, Patrice M., Patrick G., Gabriel, Denis G., Jean B., Renaud, Jean V. and Stéphane) for always been kind to me.

Finally, I am very grateful to the CEDRE support team, Jérôme and Victor for the assistance on the solver, but also the CEDRE development team especially Gilles and Anthoine.

All is said, I hope I have not forgotten anyone if yes thank you! It is time for me to , I wish you all the best and follow your path like Ellen DeGeneres genuinely said: "Follow your passion, stay true to yourself, never follow someone else's path unless you're in the woods and you're lost and you see a path, then by all means you should follow that."

Jun

Contents

List of symbols and acronyms

Latin-script letters

A	Surface
A	Jacobian Matrix associated to the normal projection of the Euler hyperbolic flux on a cell face.
c	Fluid mean sound speed
C_μ	Constant of the $k-\varepsilon$ model
C_p	Heat capacity at constant pressure
C_s	Smagorinsky coefficient
C_v	Heat capacity at constant volume
E	Specific total energy
$E(\kappa)$	Energy spectrum
f	Frequency
f′	Fluctuating frequency
$K_x^{+/-}$	Wavenumber
K_s	Tangent curvature
K_τ	Normal curvature
l	Nozzle length
$\mathcal{L}$	Integral length scale
m	Mass flow rate
$\mathcal{M}$	Molar mass of the fluid
M	Mach number
p’	Fluctuating fluid pressure
P	Fluid pressure
P^+	Nondimensional amplitude of the pressure fluctuation associated with the acoustic wave propagating in the downstream direction (linear regime)
P^-	Nondimensional amplitude of the pressure fluctuation associated with the acoustic wave propagating in the upstream direction (linear regime)
P_1	Acoustic wave at the inlet flow
P_2	Acoustic wave at the outlet flow
P_3	Acoustic wave downstream of the shock
Prt	Prandtl number
q	Heat flux
$\widetilde{q}_{t_k}$	Heat flux tensor

Q	Second invariant of the gradient of u
r	Specific gas constant
r_s	Radius curvature over s
r_τ	Radius curvature over τ
R_{in}	Inlet reflecting coefficient
R_{out}	Outlet reflecting coefficient
Re	Reynolds number
$Re_{\mathcal{L}}$	Reynolds number linked to the integral length scale
$\mathcal{R}$	Molar gas constant
s	Fluid entropy
s'	Fluctuating fluid entropy
$\mathcal{S}$	Amplitude of the entropy fluctuation
S_{ij}	Symmetric part of the gradient of u
$\widetilde{S}_{ij}$	Filtered strain rate tensor
t	Time
T	Temperature
T'	Fluctuating temperature
T_t	Fluid total temperature
u	Fluid velocity
u'	Fluctuating fluid velocity
$u_{\mathcal{L}}$	Characteristic velocity of the structures at the integral length scale
u_r	Radial velocity
u_θ	Tangential velocity
u_x	Axial velocity
$\boldsymbol{U}$	Velocity vector
$\mathcal{U}^+$	Dimensionless velocity
U^+	Nondimensional amplitude of the velocity fluctuation associated with the acoustic wave propagating in the downstream direction (linear regime)
U^-	Nondimensional amplitude of the velocity fluctuation associated with the acoustic wave propagating in the upstream direction (linear regime)
x	Axial coordinate of the nozzle
y^+	Nondimensional distance to the wall
Z	Reduced impedance

Greek symbols

β^*	Constant of the Wilcox's $k-\omega$ model
Δf	Frequency step
Δ_r	Radial distance between two streamlines
Δt	Time step of the numerical simulation
ε	Dissipation rate of the energy
η	Kolmogorov scale
γ	Specific heat ratio
κ_v	Von Kármán constant
λ	Characteristic acoustic wavelength
Λ	Heat conduction coefficient
$\mu(T)$	Dynamic viscosity of the fluid
μ_t	Dynamic turbulent viscosity of the fluid
ν	Kinematic viscosity of the fluid
Ω	Nondimensional angular frequency
Ω_{ij}	Vorticity tensor
κ	Wavenumber
σ	Entropy wave
Σ_1	Outlet relaxation coefficient
Σ_5	Inlet relaxation coefficient
τ_{ij}	Viscous stress tensor
$\widetilde{\tau_{ik}}$	Turbulent Reynolds stress tensor
ρ	Density
$\rho^{'}$	Fluctuating fluid density
ξ	Height ratio of the flow

Subscripts and superscripts

$()'_a$	Acoustic part
$()'_e$	Entropic part
$()_*$	Values of the variables taken at the throat

Acronyms

CAA	Computational AeroAcoustics
CFL	Courant-Friedrichs-Lewy
CINES	Centre Informatique National de l'Enseignement Supérieur
CN	Combustion Noise
DCN	Direct Combustion Noise
DNS	Direct Numerical Simulation
EDM	Eddy dissipation model
GENCI	Grand Équipement National de Calcul Intensif
ICN	Indirect Combustion Noise
LES	Large Eddy Simulation
LHS	Left-hand side
LDDRK	Low Dissipation and Low Dispersion Runge Kutta
NPW	Number of Points per Wavelength
NGV	Nozzle guide vane
NSCBC	Navier-Stokes Characteristic Boundary Conditions
RANS	Reynolds Averaged Navier-Stokes
RHS	Right-hand side
SIBLE	Simple Integrated Boundary Layer Equations
SGS	Sub-grid scale
TDIBCs	Time-domain impedance boundary conditions

Introduction & objectives

In 1998, the X-Noise [X-Noise 1998] collaborative network project was created uniting 29 European partners over 21 countries (companies, universities and institutes) in the aeroacoustic field. This project significantly contributed to the objectives of the Advisory Council for Aeronautics Research in Europe (ACARE) to reduce the exposure of communities to aircraft noise by a factor 2 (-10 PNdB) in 2020 with respect to 2000. At the beginning of 2010, thanks to an important effort in this research topic, a drastic decrease of the noise by 5 PNdB was reached. This progress has been possible by the reduction of jet mixing noise and fan noise in modern aero engines. Yet, this reduction has also paradoxically led to an increase in the relative contribution of other noise sources. Among them, one of the most important at hearing frequencies is referred as "combustion noise" (CN).

During the 70's, two mechanisms have been identified as CN [Candel 2009]. Direct combustion noise (DCN) is generated by the unsteady heat release rate at the flame front level [Ducruix 2003]. This noise appears in unsteady combustion situations, in opened or confined configurations. This acoustic disturbance has been extensively investigated from theoretical [Bragg 1963, Strahle 1978, Hassan 1974], numerical [Richter 2005, Mühlbauer 2009] and experimental [Bake 2007, Bake 2008, Bake 2009a, Bake 2009b, Bake 2009c] points of view. In laminar configurations, the driving mechanisms are now well known but intense efforts are still carried out to investigate turbulent confined situations. Indirect combustion noise (ICN) was theoretically predicted and observed experimentally during the same period of time. This noise is induced by the acceleration of burnt gas heterogeneities in velocity (vorticity) or in temperature (entropy fluctuations) through a nozzle or a turbine. Initial measurements and theoretical works tended to show that the levels of noise due to indirect and direct mechanisms are of the same order of magnitude (see for instance the works of Candel [Candel 1972], Marble [Marble 1973], Morfey [Morfey 1973] and Leyko *et al.* [Leyko 2011]). It appears to be crucial to study those two phenomena in more details and to precisely discern their respective contribution to combustion noise.

ICN generates noise both upstream and downstream of the nozzle and the turbine. Noise radiated backward in the combustion chamber is partially reflected and can give birth to combustion instabilities. Downstream acoustic emission propagates toward the exhaust of the engine and thus contributes to the overall engine noise in the far field [Blacodon 2009]. Despite the numerous studies conducted during the last thirty years, isolating direct noise from indirect noise sources still remains a challenging issue nowadays. This is mainly due to the extreme operating conditions (high pressure and temperature

gradients), the very limited means of measurement and also to the complex physical processes (chemical reactions and variable Mach number flow). Finally, acoustic pressure and velocity amplitudes are at least two orders of magnitude lower than the aerodynamic values encountered in the systems, requiring extremely clean and sensitive computations and measurements.

Significant elements of the theory of DCN and ICN have been set by Marble & Candel [Marble 1977] for nozzle flows. They base their work on conservation principles for one-dimensional perturbations to provide the amplitude of direct and indirect noise. This approach is valid as long as the nozzle is compact with respect to the considered wavelengths. They also consider the non-compact configuration in the particular case of the supercritical nozzle without shock. More recently, Moase *et al.* [Moase 2007], Giauque *et al.* [Giauque 2012] and Duran & Moreau [Duran 2013a] extended the work of Marble & Candel [Marble 1977] to account for subcritical and supercritical shocked flows with arbitrary nozzle shapes.

Bake *et al.* [Bake 2007, Bake 2008, Bake 2009a, Bake 2009b, Bake 2009c] studied the mechanism of ICN on a dedicated test rig: the EWG (Entropy Wave Generator). The measurements collected by Bake *et al.* were studied numerically by Richter *et al.* [Richter 2007], Mülbauer *et al.* [Mühlbauer 2008, Bake 2009c] and Leyko *et al.* [Leyko 2011] amongst others for the supersonic case and the results seemed to be in a good agreement. However, regarding the subsonic case, the results are quite different between the theoretical estimation and the experimental measurements. Studies tend to show that current 1D ICN models fail to reproduce experimental results gathered by Bake *et al.* [Bake 2009c] as shown more recently by Duran *et al.* [Duran 2013b] and Giauque *et al.* [Giauque 2012]. Both of them concluded that in the EWG test rig, ICN cannot be held as the sole responsible for the measured noise level and DCN is also present.

Currently, the question of the true relative importance of the indirect mechanism as a source of CN is not settled. This might be due to a certain number of issues regarding the understanding and the modeling of entropy and vorticity disturbances in real aero engines. 1D models have been intensively used for their simplicity. All these models are based on Marble & Candel theory which neglects any radial variation of the mean flow. According to Sattelmayer [Sattelmayer 2003], the non uniform mean flow leads to residence times that vary across the cross-section. As a consequence, entropy perturbations at different radial positions have different time delays and phases when they reach the nozzle throat. This will tend to reduce their cumulative effect and consequently modify the amplitude of the generated acoustic waves. In addition, diffusion and dispersion phenomena (change in amplitudes and phases) are also important and can modify the resulting entropy noise. Many authors including Sattelmayer [Sattelmayer 2003], Eckstein *et al.* [Eckstein 2006],

Morgans *et al.* [Morgans 2013], Morgans & Li [Morgans 2015], Giusti *et al.* [Giusti 2016], Xia *et al.* [Xia 2016], Hosseinalipour *et al.* [Hosseinalipour 2017] noted the importance of entropy waves dispersion but so far it has not been considered in any analytical models of ICN in **nozzle** flows. Leyko [Leyko 2010] in his thesis and in [Leyko 2014] studied the distortion of injected planar entropy waves while Mishra & Bodony [Mishra 2013] studied the distortion of entropy spots as they approach a static turbine blade. Recently, Livebardon *et al.* [Livebardon 2016] and Bauerheim *et al.* [Bauerheim 2016] proposed a compact analytical model to take into account this distorsion to a **stator-rotor stage**. The same behavior is expected to happen in a combustion chamber as the entropy waves approach the **nozzle**. Indeed, the inhomogeneous acceleration profile present in the nozzle as one goes from the centerline to the outer wall may be responsible of a distortion.

Based on these observations, the aim of this PhD thesis is to develop a non compact two-dimensional axisymmetric semi-analytical model taking into account the distortion of the entropy waves in order to predict the ICN for nozzle flows using numerical and analytical methods.

Chapter 1 gives an overview of the different ways adopted to study ICN. With the large computing capacities improvements in the previous decades, the trend is to perform numerical simulations on increasingly complex configurations. However, those computations suffer from the lack of experimental databases since only one reference case made by Bake *et al.* [Bake 2009c] was available at the beginning of the PhD thesis.

The tools available at Office Nationale d'Étude et de Recherche en Aérospatiale (ONERA) for studying ICN are described in Chapter 2. First, 1D tools, solving Euler equations are introduced. Then, a 3D numerical solver called CEDRE solving the Navier-Stokes equations is described. The different approaches regarding the steady and unsteady computations are detailed.

The incapability of the 1D models to take into account the deformation of the entropy front by the mean flow has been pointed out previously. It is the objective of chapter 3 to develop a 2D semi-analytical model for nozzle flows that includes such a distortion of the entropy source term. In order to take this phenomenon into account, the radial evolution of the convected entropy front through the nozzle must be incorporated. To do so, the Euler equations are rewritten in 2D form for the entropic part while acoustic perturbations are considered to be 1D. The mean flow is provided by a RANS computation of the DISCERN nozzle (described in chapter 4). Through the inversion of a matrix in the frequency domain, the resulting model allows to obtain the acoustic response of the nozzle.

Navier-Stokes numerical simulations are carried out in chapter 4. A RANS computation of the nozzle is run to provide the mean flow needed for the application of the 2D model. In order to validate the results provided by the 2D semi-analytical model, LES simulations

of the nozzle are also performed on a finer hybrid mesh than the one used for the RANS computation to capture the acoustic and entropy waves as well as the turbulence generated by the flow. Planar entropy waves are forced at the entrance of the geometry and two kinds of entropy fluctuation forcings are simulated. A harmonic forcing is used in order to characterize the numerical dissipation, to quantify the thermal and viscous diffusions and also to allow a precise study of the flow and the fluctuations inside the domain. A multi-harmonic forcing then allows to compute the entropy generated noise for a large panel of frequencies with a single simulation in order to obtain the spectral response of the nozzle.

In Chapter 5, the application and validation of the 2D model is carried out. Firstly, the Thermo-Acoustic Transfer Functions (TATFs) obtained from the 2D model are compared to ONERA's 1D solver MarCan using a purely 1D flow as to assess the capability of the 2D model to retrieve 1D solutions. Secondly, the mean flow provided by the RANS computation is used as an input for the 2D model where two different cases are studied assuming: (1) fully non-reflective boundaries and (2) partially reflective boundaries. The first case allows a comparison between the TATFs from the 2D model and MarCan, while the second case reproduces the partially reflective boundaries in the LES computations. The TATFs provided by the 1D model MarCan, the 2D model and from LES computations are finally compared and the capability of the 2D model is assessed.

Chapter 1

State of the art

There are now three types of scientists: experimental, theoretical and computational.

Silvan S. Schweber

Contents

In this section an overview of the combustion noise (CN) is given. Over the last decades, it has been studied analytically, experimentally and numerically. With the drastic increase of computing resources, the trend is to perform more and more numerical simulations. However, this approach still remains costly from an industrial point of view. More specifically, the lack of available experimental databases on ICN (one experimental test bench [Bake 2009c] *at Deutsches Zentrum für Luft- und Raumfahrt (DLR)) has lead to the European project RECORD (Research on Core Noise Reduction, FP7 Jan 2013-Dec 2015) aiming at understanding the mechanisms of generation and transmission of combustion noise, providing a new database and developing reduction methods. Meanwhile, another approach is to study ICN analytically with one-dimensional models as this approach is fast and responsive to the problem. However, the strong hypotheses made on the flow and on the geometry tend to give a global estimation of the noise and might suffer in terms of accuracy urging the development of new 2D models.*

Over the past 20 years, substantial progress has been made in order to reduce aircraft noise. Improvements related to the airframe and jet exhausts have been particularly significant. The noise produced by the engine is experiencing a growing interest, particularly the combustion noise, also named core noise. During the 70's, Strahle [Strahle 1971, Strahle 1973, Strahle 1978] has identified two main different sources of combustion noise. The direct combustion noise (DCN) is related to the unsteady heat release fluctuation in the combustion chamber. The indirect combustion noise (ICN) is related to the acceleration in a nozzle or a turbine row of temperature or vorticity inhomogeneities created by the flame, see Fig. 1.1. It was also shown during the last decades that combustion instabilities are the major source of acoustic disturbances in a combustion chamber. Since the aim of this PhD thesis is to study ICN in nozzle flows, the DCN and the ICN generated through a turbine row are not described. The reader is invited to read the work of [Cumpsty 1977, Kaji 1970a, Kaji 1970b, Muir 1977a, Muir 1977b, Pickett 1975] for details regarding ICN in turbines stages.

In 1970, Giammar & Putnam [Giammar 1970] gave a summary regarding CN. According to their experiment, CN fills the lower part of the audible frequency spectrum ($\leq$ 1500 Hz). In its appropriate frequency range, CN can overwhelm jet noise. Safran Aricraft Engines estimates for a turbojet engine that the typical contribution of CN at approach phase is relatively important to the total engine noise, see Fig. 1.2. More especially in the scope between 350 to 1000 Hz, its contribution can even be the major source of the engine total noise. This point occurs mainly at landing or take-off phases while the engine is not at its optimum operating point. As the frequency range of CN is low (large wavelength), it is extremely difficult to silence this noise disturbance by using conventional absorbers. In

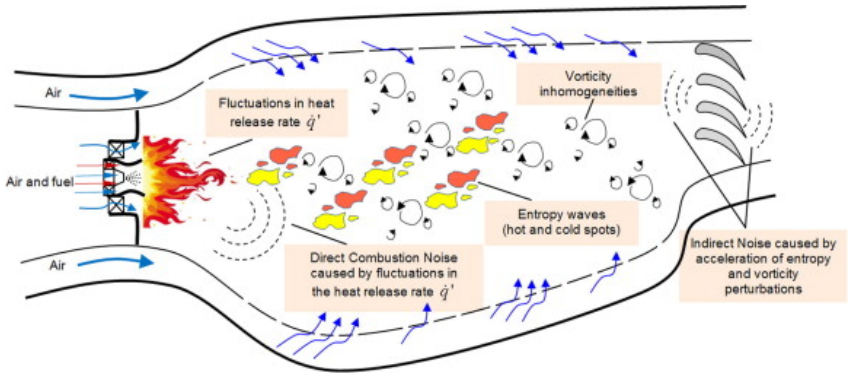

Figure 1.1: Direct and indirect noise in a combustion chamber extracted from Dowling & Mahmoudi [Dowling 2014].

this way, the challenge regarding CN is to develop new theoretical models, build test facilities and obtain a better understanding regarding the turbulence inside the combustion chamber.

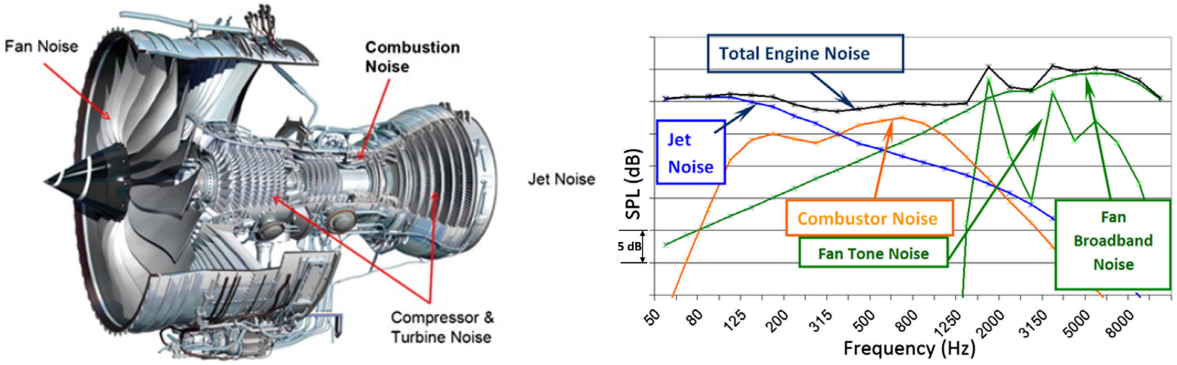

Figure 1.2: Summary of engine noise sources of a Rolls-Royce Trent 1000 (*left*). Typical contribution of noise sources on a turbojet engine at approach phase from Safran Aircraft Engines (*right*).

Acoustic disturbances involve velocity, pressure, density and temperature fluctuations. Chu & Kovásnay [Chu 1958] analyzed the interaction of acoustic, entropy and vorticity waves in the 1D case by solving the full Navier-Stokes equations. Acoustic disturbances are isentropic and irrotational, entropic disturbances are incompressible and irrotational and vortical disturbances are incompressible and isentropic. The acoustic disturbances propagate at the speed of sound with neither vortical nor entropy fluctuations while the entropy and vorticity disturbances are only convected with the mean flow. ICN is related to the acceleration in a nozzle or a turbine stage of entropy or vorticity inhomogeneities. The density of the perturbation being different from that of the steady flow, its acceleration caused by the mean pressure gradient differs from that of the unperturbed fluid. This leads

to a local disequilibrium that is compensated by the generation of acoustic wavefronts that correspond to ICN. Different methods for generating and modeling this noise are presented in the following sections.

1.1 Analytical methods

Tsien [Tsien 1952] studies analytically the propagation of acoustic waves in a supercritical rocket nozzle for the determination of nozzle-end acoustic impedance. The flow is supposed to be isothermal (non isentropic), non-reacting, and inviscid for perfect gas. By assuming a linear velocity distribution (Tsien's assumption) inside the nozzle, he calculates the transfer function of the nozzle with an unsteady one-dimensional flow. His results stand for low frequencies and he gives also the asymptotic response to very high frequencies. He introduces a characteristic non-dimensional frequency (Ω reduced frequency) as the angular frequency ω divided by the velocity gradient along the nozzle that allows the correlation between rocket nozzles of different sizes. To end, he underlines the fact that for high frequencies (for very long nozzle), the wavelengths might be small in comparison with the nozzle length and the one-dimensional flow assumption might introduce appreciable error.

One year after, Crocco [Crocco 1953], studying also the rocket instability problem, extends the model of Tsien to the non-isothermal case in the intermediate range of frequencies for a supersonic nozzle. Rather than using the transfer function, linking the fractional variation of mass flow to the fractional variation of pressure introduced by Tsien, Crocco introduces the notion of impedance at the inlet and outlet boundaries. Again a linear velocity distribution in the subsonic portion of the nozzle is assumed allowing some analytical simplifications. Using the critical sound speed reached at the throat and applying again non-dimensional variables (reduced angular frequency), he solves the continuity, momentum and energy equations (the conservation of entropy). Looking for solutions in a harmonic form, he expresses pressure and velocity perturbations as a combination of hypergeometric functions and uses a particular relation proposed by Snow [Snow 1952] to compute the acoustic transfer functions of the rocket nozzle.

20 years later, Candel [Candel 1972] in his PhD thesis employs the model of Tsien to study for the first time the passage of entropy spot regions of non-uniform temperature through a choked nozzle. In 1973, Marble [Marble 1973] considers the problem of noise production for low frequencies. He concludes that noise production by entropy fluctuations can be important. He also states that in many technological situations the nozzle can be considered as compact (the nozzle length is small compared to the interested wavelengths). Marble obtains the compact solutions for both choked and subcritical nozzles. Marble & Candel [Marble 1977] merge their stand-alone works to provide the reference article that

will be used over the next 30 years on CN generated by the passage in a nozzle of an acoustic or an entropy wave. The next section describes this reference article in details.

1.1.1 One-dimensional compact case of Marble & Candel

1.1.1.1 General equations

Basically, all acoustic analogies are derived from four governing equations:

- the continuity equation
- the momentum equation
- the energy equation
- the state equation

For the one-dimensional case, Marble & Candel [Marble 1977] make some hypotheses on the flow, which is supposed to be:

- One-dimensional (axial flow)
- With no viscous effects (Euler equation)
- Composed of a thermodynamically perfect gas (constant γ)
- Giving rise to equations that can be linearized (small fluctuations)
- In a nozzle that can be considered compact compared to all wavelengths[1]

In the compact case, the nozzle can be seen as a discontinuity and matching conditions can be written between the region upstream of the nozzle (noted with the subscript '1' in Fig. 1.3) and the region downstream of the nozzle (noted '2') for the conservation variables mass flow rate, total temperature and entropy (if no shock is present in the diverging part).

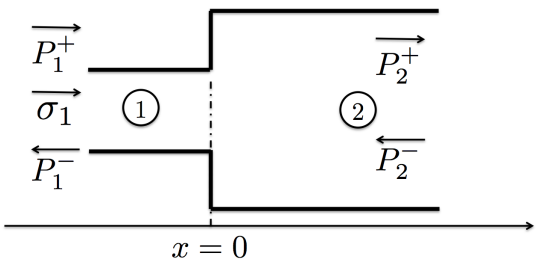

Figure 1.3: Compact nozzle with subscripts.

[1]The compact nozzle assumption states that the wavelengths of the acoustic and entropy perturbations are large compared to the axial length of the nozzle. This is only valid for low-frequency perturbations and means that acoustic and entropy waves propagate quasi-steadily through the nozzle.

$$\left(\frac{m'}{m}\right)_1 = \left(\frac{m'}{m}\right)_2 \tag{1.1}$$

$$\left(\frac{T_t'}{T_t}\right)_1 = \left(\frac{T_t'}{T_t}\right)_2 \tag{1.2}$$

$$\left(\frac{s'}{C_p}\right)_1 = \left(\frac{s'}{C_p}\right)_2 \tag{1.3}$$

In the linear regime, the previous perturbed quantities write, as a function of the dimensionless primitive variables:

$$\frac{m'}{m} = \frac{1}{M}\frac{u'}{\overline{c}} + \frac{\rho'}{\overline{\rho}} \tag{1.4}$$

$$\frac{T_t'}{T_t} = \frac{1}{1+\frac{1}{2}(\gamma-1)M^2}\left[\gamma\left(\frac{p'}{\overline{\gamma p}}\right) - \frac{\rho'}{\overline{\rho}} + (\gamma-1)M\frac{u'}{c}\right] \tag{1.5}$$

$$\frac{s'}{C_p} = \frac{p'}{\overline{\gamma p}} - \frac{\rho'}{\overline{\rho}} \tag{1.6}$$

Using Eq. 1.6, it is possible to replace the expression of $\frac{\rho'}{\overline{\rho}}$ in Eqs. 1.4-1.5. The pressure and velocity fluctuations satisfy the general acoustic wave equations and are written as follows assuming harmonic solutions, where plus or minus stand respectively for a wave propagating in the same direction as the flow and in the opposite direction:

$$\frac{p'}{\gamma p} = P^+ \exp\left[i\omega\left(t - \frac{x}{u+c}\right)\right] + P^- \exp\left[i\omega\left(t - \frac{x}{u-c}\right)\right] \tag{1.7}$$

$$\frac{u'}{c} = U^+ \exp\left[i\omega\left(t - \frac{x}{u+c}\right)\right] + U^- \exp\left[i\omega\left(t - \frac{x}{u-c}\right)\right] \tag{1.8}$$

The amplitudes of the pressure and velocity fluctuations are linked: $U^+ = P^+$ and $U^- = -P^-$, so that one can rewrite:

$$\frac{u'}{c} = P^+ \exp\left[i\omega\left(t - \frac{x}{u+c}\right)\right] - P^- \exp\left[i\omega\left(t - \frac{x}{u-c}\right)\right] \tag{1.9}$$

In the compact case, the location of the discontinuity occurs at $x = 0$ (see Fig. 1.3) and the general acoustics wave equations as well as the entropy equation can be simplified and easily evaluated as:

$$\frac{p'}{\gamma p} = P^+ \exp(i\omega t) + P^- \exp(i\omega t) \tag{1.10}$$

$$\frac{u'}{c} = P^+ \exp(i\omega t) - P^- \exp(i\omega t) \tag{1.11}$$

$$\frac{s'}{C_p} = \sigma \exp(i\omega t) \tag{1.12}$$

Eqs. 1.4-1.5 finally becomes:

$$\frac{m'}{m} = \frac{1}{M}\frac{u'}{\overline{c}} + \frac{p'}{\overline{\gamma p}} - \frac{s'}{C_p} \tag{1.13}$$

$$\frac{T_t'}{T_t} = \frac{1}{1+\frac{1}{2}(\gamma-1)M^2}\left[(\gamma-1)\left(\frac{p'}{\overline{\gamma p}}\right) + \frac{s'}{C_p} + (\gamma-1)M\frac{u'}{c}\right] \tag{1.14}$$

1.1.1.2 Subsonic Flow

In the subsonic case, three waves are entering the nozzle while three waves are exiting the nozzle. These three unknowns are found using the jump relations (Eq. 1.1-1.3). As the system is solved in the linear domain, the three possible forcings are considered separately for a subsonic nozzle flow:

- Acoustic forcing from the inlet
  In this case, only $P_1^+ = \varepsilon$ is imposed at the inlet. This means that there is no downstream propagating wave downstream of the nozzle $P_2^- = 0$ and no entropy forcing at the inlet $\sigma = 0$. Combining Eqs. 1.10-1.12 with Eqs. 1.13-1.14 provides a linear system of 2 equations with 2 unknowns, whose solutions are the generated acoustic waves. They write

$$P_1^- = \left(\frac{M_2 - M_1}{1 - M_1}\right)\left(\frac{1+M_1}{M_2+M_1}\right)\left[\frac{1-\frac{1}{2}(\gamma-1)M_1M_2}{1+\frac{1}{2}(\gamma-1)M_1M_2}\right]\varepsilon \tag{1.15}$$

$$P_2^+ = \left(\frac{2M_2}{1+M_2}\right)\left(\frac{1+M_1}{M_2+M_1}\right)\left[\frac{1+\frac{1}{2}(\gamma-1)M_2^2}{1+\frac{1}{2}(\gamma-1)M_1M_2}\right]\varepsilon \tag{1.16}$$

- Acoustic forcing from the outlet
  In this case, only $P_2^- = \varepsilon$ is imposed at the outlet. Since neither acoustic wave nor entropy forcing are imposed at the inlet $P_1^+ = \sigma = 0$. The resolution process is similar to that of the acoustic forcing at the inlet and the generated waves finally write

$$P_1^- = \left(\frac{2M_1}{M_1+M_2}\right)\left(\frac{1-M_2}{1-M_1}\right)\left[\frac{1+\frac{1}{2}(\gamma-1)M_1^2}{1+\frac{1}{2}(\gamma-1)M_1M_2}\right]\varepsilon \tag{1.17}$$

$$P_2^+ = -\left(\frac{M_2 - M_1}{1+M_2}\right)\left(\frac{1-M_2}{M_2+M_1}\right)\left[\frac{1-\frac{1}{2}(\gamma-1)M_1M_2}{1+\frac{1}{2}(\gamma-1)M_1M_2}\right]\varepsilon \tag{1.18}$$

- Entropy forcing
  Here only the entropy forcing is imposed at the inlet $\sigma \neq 0$ and no acoustic waves are imposed at the boundaries: $P_1^+ = P_2^- = 0$. The generated acoustic waves write in this

case

$$P_1^- = -\left(\frac{M_2 - M_1}{1 - M_1}\right)\left[\frac{\frac{1}{2}M_1\sigma}{1 + \frac{1}{2}(\gamma-1)M_1M_2}\right] \tag{1.19}$$

$$P_2^+ = \left(\frac{M_2 - M_1}{1 + M_2}\right)\left[\frac{\frac{1}{2}M_2\sigma}{1 + \frac{1}{2}(\gamma-1)M_1M_2}\right] \tag{1.20}$$

1.1.1.3 Supersonic Flow

Two cases have to be considered here, because the solutions are different whether there is a shock in the diffuser or not.

For the compact supercritical nozzle with no shock, the wave P_2^- propagates in the downstream direction and cannot be imposed (see Fig. 1.6). Two incoming waves have to be imposed but four waves are generated, thus requiring 4 relations. As a consequence, an additional equation is needed and is based on the choked flow condition imposed at the throat (the Mach number fluctuation is zero at the throat). The fractional mass flow variation can hence be deduced since it is directly proportional to the stagnation pressure and inversely proportional to the square root of the stagnation temperature.

$$\frac{m'}{m} = \frac{1}{1 + \frac{1}{2}(\gamma-1)M^2}\left[\frac{\gamma}{2}(1-M^2)\frac{p'}{\gamma p} + \frac{\gamma+1}{2}M\frac{u'}{c} + \frac{1}{2}(1+\gamma M^2)(\frac{p'}{\gamma p} - \frac{s'}{C_p})\right] \tag{1.21}$$

Combining Eqs. 1.21 and 1.4, it finally comes the relation below that holds in the regions upstream and downstream of the nozzle

$$\frac{u'}{c} - \frac{\gamma}{2}M\left(\frac{p'}{\gamma p}\right) + \frac{1}{2}M(\frac{p'}{\gamma p} - \frac{s'}{C_p}) = 0 \tag{1.22}$$

- Acoustic forcing from the inlet
  Using $P_1^+ = \varepsilon$, $\sigma = 0$ and combining Eqs. 1.10-1.12 with Eqs. 1.13-1.14 and Eq. 1.22 provides a linear system of 4 equations with 4 unknowns, whose solutions are the generated acoustic waves. They write

$$P_1^- = \left[\frac{\left(1 - \frac{1}{2}(\gamma-1)M_1\right)}{\left(1 + \frac{1}{2}(\gamma-1)M_1\right)}\right]\varepsilon \tag{1.23}$$

$$P_2^+ = \left[\frac{1 + \frac{1}{2}(\gamma-1)M_2}{1 + \frac{1}{2}(\gamma-1)M_1}\right]\varepsilon \tag{1.24}$$

$$P_2^- = \left[\frac{1 - \frac{1}{2}(\gamma-1)M_2}{1 + \frac{1}{2}(\gamma-1)M_1}\right]\varepsilon \tag{1.25}$$

- Entropy forcing

Considering now $P_1^+ = 0$ and $\sigma \neq 0$, the resolution of the system leads to:

$$P_1^- = \left[\frac{-M_1}{\left(1+\frac{1}{2}(\gamma-1)M_1\right)}\right]\frac{\sigma}{2} \tag{1.26}$$

$$P_2^+ = \left[\frac{\frac{1}{2}(M_2-M_1)}{1+\frac{1}{2}(\gamma-1)M_1}\right]\frac{\sigma}{2} \tag{1.27}$$

$$P_2^- = \left[\frac{-\frac{1}{2}(M_2+M_1)}{1+\frac{1}{2}(\gamma-1)M_1}\right]\frac{\sigma}{2} \tag{1.28}$$

For the compact shocked supercritical nozzle, Marble & Candel focus on a case where the shock is oscillating downstream of the outlet with the velocity u_s' (see Fig. 1.4 where the subscript 3 stands for the state after the shock). This is not a common situation as the shock is generally located inside the diffuser. This more general case is investigated by Moase *et al.* [Moase 2007]. The geometry of the nozzle is shown in Fig. 1.5.

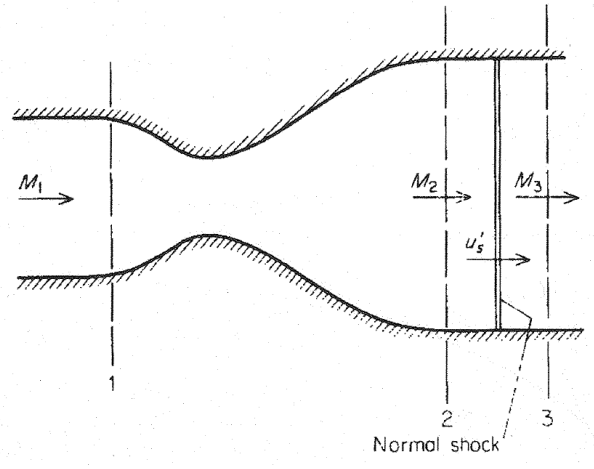

Figure 1.4: Compact supersonic nozzle with normal shock downstream.

Moase *et al.* consider the cases of choked nozzles and supersonic diffusers, however only the choked nozzle is described in this document as the flow coming out of the combustion chamber is not supersonic in our configurations of interest, as opposed for instance to scramjets. In the compact case, Eqs. 1.1-1.2 still hold. Only the entropy conservation Eq. 1.3 is not valid and must be replaced by the fluctuation of the Mach number upstream of the nozzle, imposed to be zero under the low-frequency assumption because the nozzle is choked, this states

$$\left(\frac{M'}{\overline{M}}\right)_1 = 0 \tag{1.29}$$

where $\overline{(.)}$ corresponds to the steady flow quantities. This gives three equations for three unknown outgoing waves (P_1^-, P_2^+ and σ_2). To obtain the transmission and the reflection

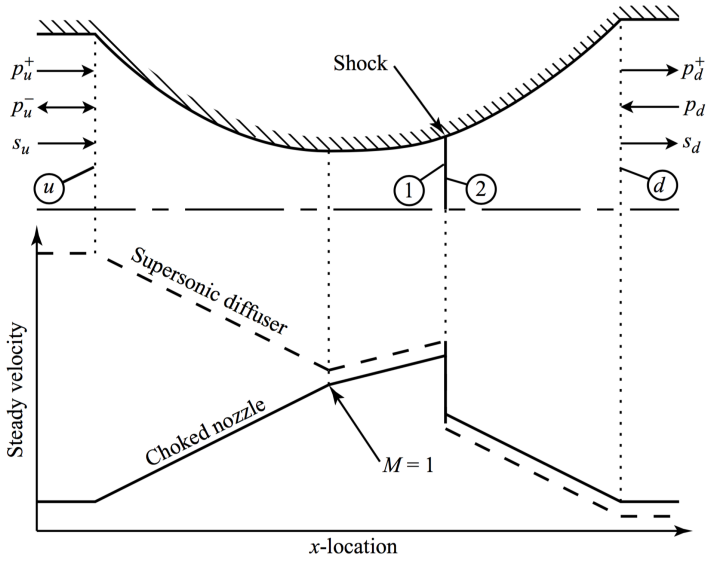

Figure 1.5: Compact supersonic nozzle with normal shock inside the diffuser extracted from Moase *et al.* [Moase 2007].

coefficients, once again only one incoming wave (P_1^+, P_2^- and σ_1) is resolved at a time. This gives the expression of the coefficients regarding the type of forcing (see Table 1.1) in the formalism of Marble & Candel (Moase *et al.* used a different expression for the acoustic invariants).

	Response to P_1^+	Response to P_2^-	Response to σ_1
P_1^-	$\frac{1-\frac{1}{2}(\gamma-1)\overline{M_1}}{1+\frac{1}{2}(\gamma-1)\overline{M_1}}$	$\frac{-\frac{1}{2}\overline{M_1}}{1+\frac{1}{2}(\gamma-1)\overline{M_1}}$	0
P_2^+	$\frac{\overline{M_2}(3\gamma-1+(\gamma-1)^2\overline{M_2}^2)}{(1+\frac{1}{2}(\gamma-1)\overline{M_1})(1+\overline{M_2}(1+(\gamma-1)\overline{M_2}))}$	$\left(\frac{1-\overline{M_2}}{1+\overline{M_2}}\right)\left(\frac{1-(\gamma-1)\overline{M_2}}{1+(\gamma-1)\overline{M_2}}\right)$	$\frac{\frac{1}{2}\overline{M_2}(1-\gamma\overline{M_1}+(\gamma-1)\overline{M_2}^2)}{(1+\overline{M_2})(1+(\gamma-1)\overline{M_2})(1+\frac{\gamma-1}{2}\overline{M_1})}$
σ_2	$\frac{2(\gamma-1)(1-\overline{M_2})(1-\frac{1}{2}(\gamma-1)\overline{M_2})}{(1+\frac{1}{2}(\gamma-1)\overline{M_1})(1+(\gamma-1)\overline{M_2})}$	$\frac{-2(\gamma-1)(1-\overline{M_2})}{1+(\gamma-1)\overline{M_2}}$	$\frac{1+\frac{\gamma-1}{2}\overline{M_2}(1+\overline{M_2})+\frac{\gamma(\gamma-1)}{2}\overline{M_1}\overline{M_2}}{(1+\frac{\gamma-1}{2}\overline{M_1})(1+(\gamma-1)\overline{M_2})}$

Table 1.1: Reflection and transmission coefficients for a compact choked nozzle with a shock in the diffuser.

So far, the compact nozzle is treated assuming a linear regime. However, under some circumstances this hypothesis might not be verified because acoustic or most likely entropy perturbations become very large in the combustion chamber, for instance in the presence of combustion instabilities (see for example Huet & Giauque [Huet 2013]). In these cases, the nonlinear effects have to be considered and their possible modeling is described in the next section.

1.1.1.4 Nonlinear approaches

Recently, Huet & Giauque [Huet 2013] extend the compact nozzle model of [Marble 1977] to the nonlinear domain in order to study the generation of sound through a subcritical or choked (with no shock) nozzle. The aim is to study the generation of sound by the passage of acoustic or entropy disturbances through a nozzle at low frequency where the wavelength of the fluctuations are comparable to the turbulent integral scale in the engine. They develop a second-order model but also a fully nonlinear model. It is found that the second-order model is really accurate for both waves on a supercritical nozzle and also accurate for a subcritical converging nozzles even for high forcing amplitude σ up to 0.5. For those configurations, the nonlinearities lead basically to the generation of additional noise at the first harmonic of the forcing frequency.

In the case of a subsonic diverging nozzle with an entropy forcing, the results of the second-order model are accurately compared to the fully nonlinear model for the acoustic wave moving downstream towards the divergent exit (P^+). Discrepancies arise when looking at the acoustic wave moving upstream of the diverging nozzle. For this configuration, the authors show that high-order nonlinearities occur (order 3 or above) in the flow and might be responsible for important modifications of the generated acoustic wave P^- especially if both inlet and outlet Mach number are highly subsonic. Consequently, the forcing amplitude σ needs to be reduced to 0.1 and even below for the nonlinearities to have a small impact on the solution. Yet in real engine where the inlet Mach number is small and the outlet one is large, the second-order model remains very accurate.

1.1.2 Non-compact case

As stated by Marble [Marble 1973], for many technological devices the compact assumption is a good approximation. However, in some particular cases, the wavelengths considered are of the same dimension or smaller than the nozzle. Therefore, intense efforts have been made over the last decade to provide solutions at arbitrary frequencies and especially at low frequencies. Marble & Candel [Marble 1977] in the last part of the article study the reflection and the transmission coefficients of a supercritical nozzle of finite length with a linear velocity profile. However, this hypothesis is too restrictive to deal with general nozzle shapes where the velocity profile can be of any kind. Moreover, for practical configurations a shock might be present in the diffuser for supercritical nozzles. The additional works performed during the last decade provide solutions for such flows and are detailed in the following. Three different types of flow are analyzed: a supersonic flow without shock, a supersonic flow with a normal shock in the diffuser.

1.1.2.1 Supersonic Flow

For a supersonic flow, theoretical works have been carried on nozzles and thin annular ducts giving the structure of this subsection.

• Nozzle

Under the 1D flow assumption, Marble & Candel write the conservation equation of mass, momentum and entropy as follows:

$$\frac{1}{\rho}\left(\frac{\partial \rho}{\partial t} + u\frac{\partial \rho}{\partial x}\right) + \frac{\partial u}{\partial x} = -u\frac{1}{A}\frac{dA}{dx} \tag{1.30}$$

$$\frac{\partial u}{\partial t} + u\frac{\partial u}{\partial x} + \frac{1}{\rho}\frac{\partial p}{\partial x} = 0 \tag{1.31}$$

$$\frac{\partial s}{\partial t} + u\frac{\partial s}{\partial x} = 0 \tag{1.32}$$

Assuming that the perturbations are small compared to the undisturbed steady flow ($z'/z \ll 1$), and expressing the terms as a sum of a fluctuating part and a mean part: $z = \overline{z}\left(1 + \frac{z'}{\overline{z}}\right)$, where z can take any flow variables (pressure, density, velocity and entropy), one can linearize Equations 1.30, 1.31 and 1.32 to obtain:

$$\left(\frac{\partial}{\partial t} + \overline{u}\frac{\partial}{\partial x}\right)\left(\frac{p'}{\overline{\gamma p}}\right) + \overline{u}\frac{\partial}{\partial x}\left(\frac{u'}{\overline{u}}\right) = 0 \tag{1.33}$$

$$\left(\frac{\partial}{\partial t} + \overline{u}\frac{\partial}{\partial x}\right)\left(\frac{u'}{\overline{u}}\right) + \frac{c^2}{\overline{u}}\frac{\partial}{\partial x}\left(\frac{p'}{\overline{\gamma p}}\right) + \left(2\frac{u'}{\overline{u}} - (\gamma - 1)\frac{p'}{\overline{\gamma p}}\right)\frac{d\overline{u}}{dx} = \frac{d\overline{u}}{dx}\frac{s'}{C_p} \tag{1.34}$$

$$\frac{s'}{C_p} = \frac{s'}{C_p}\left(t - \int^x \frac{d\xi}{du}\right) \tag{1.35}$$

They define the nozzle length as l with $0 \leqslant x \leqslant l$ and use the subscript 1 and 2 for respectively the inlet ($x < 0$) and the outlet flow ($x > l$) (see Fig. 1.6).

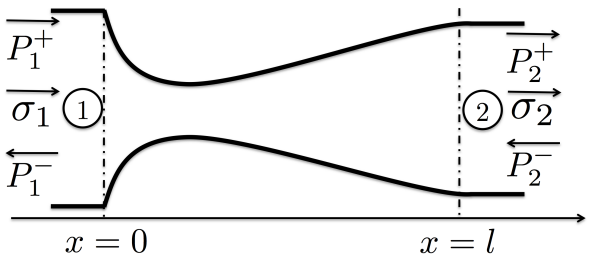

Figure 1.6: Compact supersonic nozzle with subscripts.

For the supercritical nozzle of finite length in which the undisturbed gas velocity increases linearly (Tsien's assumption) through the nozzle and in which **no shock** is present, Marble & Candel provide the response to entropy disturbances. Eqs. 1.33 and 1.34 are mod-

ified using dimensionless variables:

- $\frac{u_0(x)}{c_*} = \frac{x}{x_*}$
- $\xi = (\frac{x}{x_*})^2$
- $d\xi = \frac{2x}{x_*}dx$
- ${c_0}^2 = (\frac{\gamma+1}{2}){c_*}^2 - (\frac{\gamma-1}{2}){u_0}^2$
- $\frac{\partial u_0}{\partial x} = \frac{c_*}{x_*}$
- $\tau = \frac{c_* t}{x_*}$
- $\Omega = \frac{x_* \omega}{c_*}$

The terms with the subscript $()_*$ denote the values at the throat. Assuming harmonic solutions for the velocity, the pressure and the entropy disturbances are defined as:

$$\frac{u'}{\overline{u}} = \widehat{U}(\xi)e^{i\Omega t} \tag{1.36}$$

$$\frac{p}{\overline{\gamma p}} = \widehat{P}(\xi)e^{i\Omega t} \tag{1.37}$$

$$\frac{s'}{C_p} = \widehat{\sigma}e^{i\Omega(\tau - \log\sqrt{\frac{\xi}{\xi_1}})} \tag{1.38}$$

Eqs. 1.33 and 1.34 can be recast as follows:

$$i\Omega\widehat{P(\xi)} + 2\xi\frac{\partial}{\partial\xi}\left[\widehat{P(\xi)} + \widehat{U(\xi)}\right] = 0 \tag{1.39}$$

and

$$\left(i\Omega + 2\xi\frac{\partial}{\partial\xi}\right)\widehat{U(\xi)} + \left[(\gamma+1)\frac{1}{\xi} - (\gamma-1)\right]\xi\frac{\partial\widehat{P(\xi)}}{\partial\xi} + 2\widehat{U(\xi)} - (\gamma-1)\,\widehat{P(\xi)} = -\widehat{\sigma}\left(\frac{\xi}{\xi_1}\right)^{-\frac{i\Omega}{2}} \tag{1.40}$$

Combining the two previous equations to remove the velocity terms, it comes a hypergeometric equation (Eq. 1.41) for the pressure perturbation $\widehat{P(\xi)}$:

$$\xi(1-\xi)\frac{\partial^2\widehat{P}}{\partial\xi^2} - \left[2 + \frac{2}{\gamma+1}i\Omega\right]\xi\frac{\partial\widehat{P}}{\partial\xi} - \frac{i\Omega(2+i\Omega)}{2(\gamma+1)}\widehat{P} = -\widehat{\sigma}\frac{i\Omega}{2(\gamma+1)}\left(\frac{\xi}{\xi_1}\right)^{-\frac{i\Omega}{2}} \tag{1.41}$$

Once that $\widehat{P(\xi)}$ is obtained, the velocity perturbation $\widehat{U(\xi)}$ can be deduced from another combination of Eqs. 1.39-1.40:

$$(2+i\Omega)\widehat{U} = -(\gamma+1)(1-\xi)\frac{\partial\widehat{P}}{\partial\xi} + (\gamma-1+i\Omega)\widehat{P} + \widehat{\sigma}\left(\frac{\xi}{\xi_1}\right)^{-\frac{i\Omega}{2}} \tag{1.42}$$

The solving process of this hypergeometric equation is the same as done by Tsien [Tsien 1952] and Crocco [Crocco 1953]. The expression of the reflected and transmitted

wave strengths are expressed as:

$$P_1^- = \frac{1}{2}[\widehat{P(\xi_1)} - M_1\widehat{U(\xi_1)}] \tag{1.43}$$

$$P_2^+ = \frac{1}{2}[\widehat{P(\xi_2)} + M_2\widehat{U(\xi_2)}] \tag{1.44}$$

$$P_2^- = \frac{1}{2}[\widehat{P(\xi_2)} - M_2\widehat{U(\xi_2)}] \tag{1.45}$$

Stow *et al.* [Stow 2002] study the **reflected** acoustic waves in a choked annular duct (described later). Goh & Morgans [Goh 2011] complete the work of Stow *et al.* [Stow 2002] to compute the phase and the magnitude of the **transmitted** acoustic waves inside nozzles by removing the circumferential modes. Their expression of the *effective length* is dependent on the input perturbation type (acoustic or entropic) and improves the compact prediction with a phase correction accurate to first order in frequency.

For the supercritical nozzle with no shock, the analytical prediction for the magnitude of the transmitted noise does not vary with non-dimensional angular frequency Ω. For an acoustic disturbance at the inlet, analytical and numerical results (quasi-one-dimensional) are in good agreement both for the amplitude and the phase for P_2^+. However for P_2^-, the results are satisfactory for the phase but not really accurate for the amplitude. The magnitude discrepancies are higher between the analytical solution and the numerical computation for the case of the injection of entropy disturbance while the phase is in good agreement. This is due to the fact that entropy waves are convected with the mean flow and then their wavelengths are shorter than those of the acoustic waves. As a consequence, the small frequency hypothesis is more rapidly invalid than for the acoustic case.

For the supercritical nozzle with a shock inside or outside the diverging part, Goh & Morgans consider that fluctuations (pressure and velocity) upstream of the moving shock are not negligible (this approach was first used by Moase *et al.* [Moase 2007]). Using the linearized Rankine-Hugoniot methodology, they avoid the difficult numerical evaluation of the hypergeometric functions, the matching conditions necessary to solve them and remove the hypothesis of piecewise linear velocity profile proposed by Moase *et al.* However, they have to assume that the axial position of the abrupt change in the area of the equivalent diffuser occurs at the average of the Mach number after the shock and the Mach number downstream of the nozzle. This time the acoustic and entropy responses after a shock vary with frequency. It gives a good prediction both in magnitude and phase, but this approach is limited to nozzle with a shock and low frequencies only.

Moase *et al.* [Moase 2007] extend the non-compact analysis of Marble & Candel to a choked nozzle with a shock wave using a different method than Goh & Morgans. They use a piecewise linear velocity profile assumption. Pressure and velocity perturbations are

described in each element by the solution of the hypergeometric equation given by Marble & Candel [Marble 1977] and the fluctuations are linked between successive elements by continuity relations. Jump relations through the shock are derived from the dynamic shock relations of Rankine & Hugoniot. This leads to a linear system that is solved to reconstruct the acoustic waves generated inside the nozzle. It is a model that predicts the one-dimensional frequency response of choked nozzles and supersonic diffusers containing shocks under both incident pressure and entropy waves. This model works for any nozzle geometry as long as the steady velocity distribution can be approximated as piecewise linear. Also the nonlinear response, plus conditions for unchoking, unstart and over-choking of compact choked nozzles and compact supersonic diffusers are provided in their paper thanks to computations using a quasi-1D numerical solver.

Moase *et al.* give the transmission response of disturbances with no restriction on the frequency. They conclude that a large part of the nonlinearity in amplitude or as a function of the frequency appears when the nozzle acts as an inlet (excitation coming from downstream) rather than when the nozzle acts as an outlet (excitation coming from upstream). The nonlinearity increases as the upstream and downstream Mach numbers are increased.

Another approach is adopted by Duran & Moreau [Duran 2013a] using the flow invariant and the Magnus expansion [Magnus 1954]. They extend the compact nozzle solution of Marble & Candel [Marble 1977] for both subsonic and choked flows with or without shock waves. Their method differs from the method adopted by Stow *et al.* [Stow 2002] and Goh & Morgans [Goh 2011]. The quasi-one dimensional linearized Euler equations are written as a function of dimensionless mass, total temperature and entropy fluctuations (Eqs. 1.4-1.6). A first-order linear system of differential equations is obtained and solved using the Magnus expansion [Magnus 1954]. For each type of flow, different boundary conditions are applied and for the choked case with a shock located in the diverging part, the nozzle has to be divided into two regions, the shock representing the interface of the two zones (for this case the linearized Rankine-Hugoniot shock relations used also by Stow *et al.* and Goh & Morgans are applied). Good results between the invariant method and the hypergeometric equations (choked nozzle without shock) are found. Regarding a subsonic nozzle, the results obtained with this method are described in the next subsection.

• Annular duct

An asymptotic approach is done by Stow *et al.* [Stow 2002] to study the **reflected** acoustic waves in a choked annular duct with a contraction with the **presence of a shock** inside the diverging part of the duct. The configurations considered correspond either to a forcing from acoustic, vorticity or entropy disturbances traveling downstream towards the nozzle contraction (choked outlet configuration, see Fig. 1.7) or to an acoustic wave propagating upstream and reflected at the shock location (choked inlet, see Fig. 1.8).

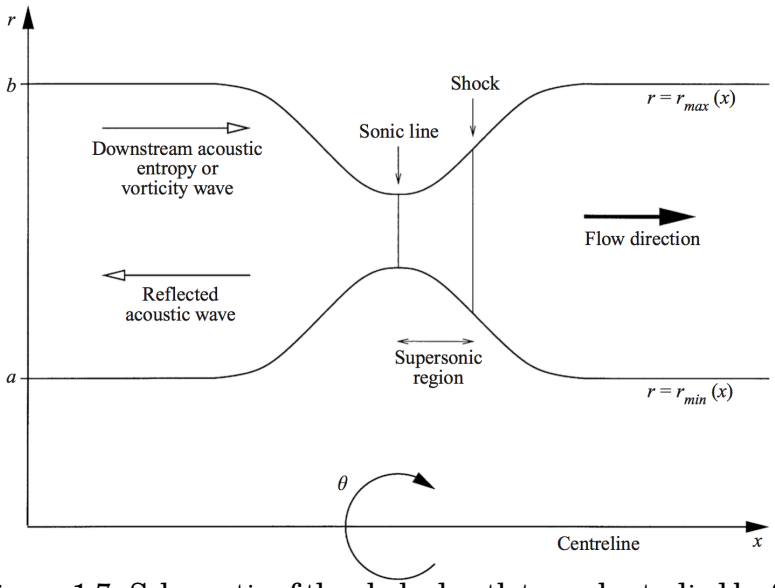

Figure 1.7: Schematic of the choked outlet nozzle studied by Stow *et al.* [Stow 2002].

Their objectives are to find boundary conditions that apply to flow perturbations at the choked inlet/outlet for a thin annular geometry. A linear disturbance in a straight annular duct can be decomposed as a sum of acoustic, entropy and vorticity waves. While acoustic waves travel at the speed of sound, entropy and vorticity disturbances convect with the mean flow. The set of equations is formulated as boundary conditions that can be applied at the inlet/outlet.

For the *choked outlet nozzle* case, an asymptotic analysis for low frequency is carried out. They use non-dimensional angular frequency Ω (disturbances have complex angular frequency ω), dimensionless speed using the value at the throat, adiabatic nozzle (entropy is simply convected) and assume that there is no viscosity and heat conduction. An asymptotic expansion of the linearized Euler equations for small Ω is used. The Mach number is purely a function of the cross-sectional area (provided the nozzle stays choked). To first order, the boundary condition for linear perturbations is found to agree well with the Marble & Candel form for one-dimensional waves. Extending the boundary conditions to second order in compactness ratio (the product of wavenumber and nozzle length), the solution is found to depend on the mean flow. This correction might be expressed as an *effective length* and is simply the mean velocity at the inlet multiplied by the convection time to the throat. The results are expressed in the form of a reflection coefficient and an *effective length* for the nozzle in terms of the mean flow.

For the *choked inlet nozzle* case, the objectives are to calculate the downstream traveling acoustic, entropy and vorticity wave produced by an incident upstream propagating acoustic wave. They find that a weak shock assumption followed by a smooth area increase

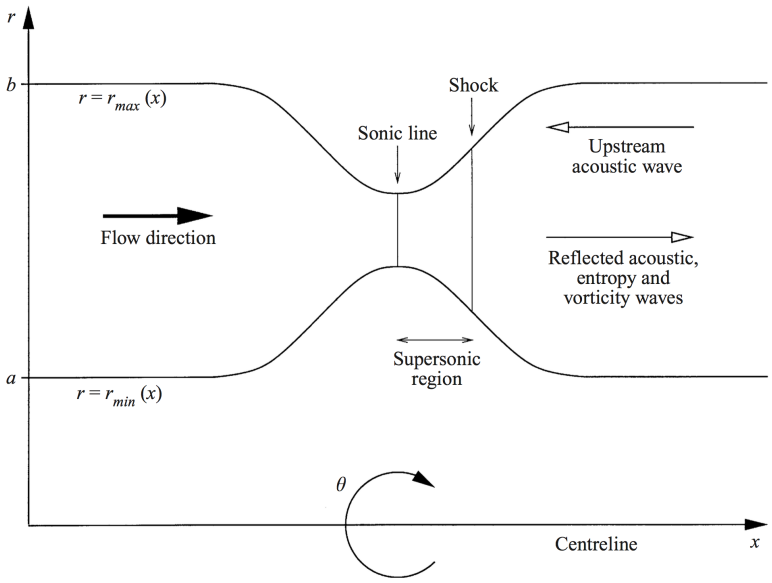

Figure 1.8: Schematic of the choked inlet nozzle studied by Stow *et al.* [Stow 2002].

commonly used is incorrect and they propose a new boundary condition by considering the interaction between the shock position and the perturbed flow. They apply the linearized Rankine-Hugoniot shock relations previously used by Culick & Rogers [Culick 1983] and Kuo & Dowling [Kuo 1996]. The linearized interaction between the flow perturbations and the moving shock inside the diverging part of the nozzle is neglected. The fluctuations upstream of the shock are also neglected.

The results for the amplitude for the choked outlet or inlet are accurate for an arbitrary low forcing frequency. Good agreement with numerical computations is found up to a non-dimensional frequency ($\Omega/2\pi$) of 0.3 for acoustic waves and 0.15 for convected waves (both entropy and vorticity), above those limits analytical and numerical results differ. For the phase of the reflection coefficient, the results for arbitrary non-dimensional frequency are improved compared to the compact solutions of Marble & Candel. The relevant conclusion of their study is that the boundary condition of Marble & Candel is applicable even for circumferential waves.

The analytical model developed by Duran & Moreau [Duran 2013a] presented before is extended by Duran & Morgans [Duran 2015] for annular duct. This analytical model allows to consider circumferential waves for both subsonic and choked flows[2]. It can accurately predict the transfer functions for acoustic, entropy and vorticity waves for any circumferential mode with comparison to numerical simulations. However, the entropy

[2]One should also note the contribution of Dowling & Mahmoudi [Dowling 2014] for circumferential modes in annular duct in the **compact case** and for **very low mach numbers** where algebraic exact solutions are developed for acoustic, entropy and vorticity waves. The very low Mach number approximation is verified numerically using the linearized Euler equations.

waves distortion is not taken into account in the model.

1.1.2.2 Subsonic Flow

Bohn [Bohn 1976, Bohn 1977] study the one-dimensional response of a subsonic nozzle flow to small pressure and entropy disturbance. The aim is to extend the work of Marble & Candel to flow fields which are entirely subsonic. The response is decomposed in terms of transmitted and reflected acoustic waves for a subcritical nozzle flow. Solutions for high-frequency disturbances are nondimensionalized with respect to the compact solution. This normalization allows to conclude that the ATFs created by two independent acoustic disturbances (a downstream-propagating acoustic wave impinging upon the nozzle inlet and an upstream-propagating wave impinging upon the nozzle exit) can be expressed as a single function of frequency. However, for an entropy wave convected though the nozzle, the TATFs depend also of the Mach numbers at the inlet and the outlet. For the very high frequencies, an asymptotic solution is found by assuming a mean linear velocity profile. He uses the model of Tsien [Tsien 1952] to solve the hypergeometric equation Eq. 1.41. He assumes that the inhomogeneous solution of Eq. 1.41 has a particular form with an expansion in the inverse power of $i\Omega$. For the homogeneous solution, he also assumes a specific expansion of the form of the solution. He then obtains a solution for the pressure fluctuation as a sum of two independent solutions where the two coefficients preceding each expanded term are imposed by the boundary conditions. His analytical model for all the frequencies is only validated with numerical solutions obtained by using a fourth-order Runge-Kutta method with automatic error control for the integration process (Eqs. 2.6-2.8 of his PhD thesis) as it is the first analytical model for non compact subsonic flows.

Bloy [Bloy 1979] uses the method of characteristics in an unsteady one-dimensional flow to calculate the pressure disturbances generated by the convection of a temperature fluctuations (low frequency and large amplitude) through a high subsonic nozzle. His simple flow model gives a good agreement with the prediction of the mean pressure disturbances with numerical solutions. He shows that the pressure disturbances generated are proportional to the fractional density change (due to the temperature disturbance time) times l/λ, where l and λ are respectively the lengths of the temperature disturbance and the pressure wave. He also studies the effect of the contraction shape (conical, bellmouth or smooth) on the pressure fluctuations, and concludes that the bellmouth shape is the one generating smallest peak disturbances.

Recently, Giauque *et al.* [Giauque 2012] revisit the model of Moase and apply it to subcritical nozzles with complex geometries. The nonhomogeneous hypergeometric equation Eq. 1.41 is solved in a different way than Marble & Candel by considering a different form for the two homogeneous solutions. The particular solution of Eq. 1.41 is found to be a linear

combination of the two homogeneous solutions multiplied by two coefficients. The coefficients for this combination are obtained using the known acoustic impedance coefficients upstream and downstream. The piecewise linear velocity approach consists in dividing the nozzle into an arbitrary number of elements n, where in each element the velocity profile is supposed to be linear. The homogeneous solutions and the particular solution are evaluated for each element. Each element is linked to its neighbors with the condition that the dimensionless pressure and velocity are continuous. The system is solved in a matrix form. Good agreement is found between this analytical model and the results from a quasi-one-dimensional numerical solver SUNDAY and a 3D Navier-Stokes flow solver CEDRE (both developed at ONERA) for different nozzle cases. SUNDAY and CEDRE are described in details in Chapter 2. The authors show that acceleration discontinuities at the boundaries between adjacent elements do not influence the actual acoustic transfer functions. The issue of nozzle compactness is also addressed. In the subcritical domain, spectral results are nondimensionalized using the flow-through-time of the entire nozzle. Transfer functions of nozzles of different lengths are successfully compared and a compactness criterion can be expressed as $\omega * \int_0^L \frac{d\zeta}{u(\zeta)} < 1$ with L the axial length of the nozzle.

As mentioned in the previous subsection, the method developed by Duran & Moreau [Duran 2013a] is also valid for subsonic flows. In the section 6.1 of their article, they compare their model with the piecewise linear velocity profile approach proposed by Giauque *et al.* [Giauque 2012] and show that the results were in perfect agreement.

All the one-dimensional method developed over the last decades might be seen as a good way to study CN, however because of their 1D nature, these models cannot take into account a critical feature of the flow in a confined environment, namely the presence of boundary layers at the walls. In addition, the effect of viscosity on the flow is not taken into account in those models. Viscous effects are expected to damp entropy fluctuations that travel at the mean convective velocity in the nozzle. This last point is important because this expectation is responsible for the fact that a significant part of the research community is still convinced that ICN can be neglected in realistic engines as entropy waves do not get to interact with the nozzle before as they are dissipated.

1.1.3 Two-dimensional approaches

In the literature, one can find two semi-analytical attempts to take into account some of the additional effects introduced by considering 2D or 3D flows in nozzles. Crocco & Sirignano [Crocco 1967] focus on the behavior of a supercritical nozzle submitted to a 3D oscillating inlet boundary condition. This boundary condition is expressed by a relation between the various perturbations (velocities, pressure, entropy) and results in the "admittance condition". Assuming a small amplitude of the perturbations, the continuity, momentum

and entropy equations are linearized. The increase in complexity induced by additional degrees of freedom related to the transverse perturbations is overcome by assuming that the unperturbed flow in the nozzle is **one-dimensional** or irrotational, isoenergetic and isentropic. Hence, the system of partial differential equations becomes a system of ordinary differential equations. Indeed, on the one hand, the variables describing the transverse dependencies of the flow properties are governed by Bessel's differential equations. On the other hand, the axial dependencies are governed by differential equations that must be solved numerically. The nozzle admittance coefficients are related to the axial dependencies of the flow properties. In this study, a reduction of the order of the differential equations for a easier calculation of the admittance coefficients is undertaken. These coefficients at the nozzle entrance are obtained for a conical nozzle (see Fig. 1.9), called "reference nozzle". From this "reference case", the application of the method to a whole family of nozzles obtained by linear deformation of the axial scale is possible.

It can be seen that the assumption made on the unperturbed flow to be one-dimensional is a strong assumption. This means that the steady-state velocity field and density are uniform on each surface (x=constant) which is not true in real engines due to the presence of boundary layers. In addition, the tables provided by the authors cannot be immediately applied to arbitrary nozzle shape as it needs to have a conical nozzle shape (see Fig. 1.9).

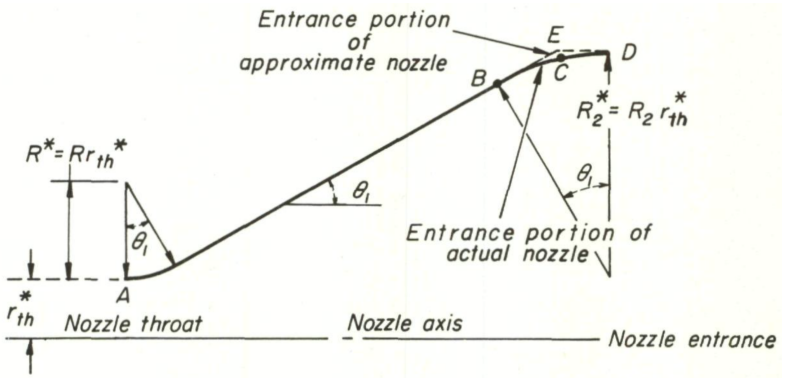

Figure 1.9: Nozzle geometry and comparison of entrance portions of approximate and actual nozzle contours from Crocco & Sirignano [Crocco 1967].

Bohn during his PhD thesis [Bohn 1976] focuses on an analytical evaluation of the transmission and reflection coefficients to calculate the full two-dimensional solution with a variation of the flow variables across the duct. The area of the duct is considered to be small. Bohn focuses exclusively on the second-order solutions that result from the interaction of two-dimensional entropy wave and the small area variation. The equations of motion written in a two-dimensional form are expanded to the second order, where the zero-order solution corresponds to the constant-area channel flow and the first-order solution has two

parts: (1) a steady part that corresponds to the disturbance to the steady channel flow imposed by the area contraction and (2) a non-steady portion of the first-order solution that corresponds to the periodic disturbances due to the entropy wave. The final solution is a sum of the two solutions and is expressed in terms of complex amplitudes of propagating duct modes (waves propagating far upstream and far downstream of the contraction). It is shown that for low-frequency entropy disturbances, the duct responds with only planar waves propagating far away. The duct response for higher-frequencies drops rapidly. Finally, it is stated that for a symmetric entropy wave no asymmetric acoustic modes are present. In the contrary, if the entropy fluctuation is asymmetric, no symmetrical modes can exit the nozzle. Even if this approach is interesting, it cannot be applied directly to arbitrary nozzles shapes. The main hypothesis used in this method is related to the notion of "small deflection", i.e that the area variation is small. In addition, the deflection (or area variation) expressed as a function of the axial coordinate needs to have continuous first, second, and third derivatives for a rapid convergence.

1.2 Experimental method

1.2.1 Previous test rig

Bohn [Bohn 1976] in his PhD thesis studies experimentally the response of subsonic nozzles to impinging one-dimensional pressure and entropy waves. The flow composed of nitrogen is perturbed with an electrical heating system. The heater generates a periodic fluctuation in total temperature. It is composed of three identical independent heaters illustrated in Fig. 1.10 and generates an entropy and a pressure waves that propagate into the nozzle. In the chapter 5 of his thesis, as in a turbojet engine entropy disturbances do not appear as one-dimensional necessarily, he studies the response of nozzles to two-dimensional entropy fluctuations both in a subsonic and a supersonic regime. In these cases, only the top and the bottom heaters are activated with a phase shift of 180°. This leads to a varying heat addition across the duct cross section. In this experiment, he supposes that the pressure disturbances created by the pulse to be small which is true as the amplitude of the temperature fluctuation was around 1 K only. In addition, at that time he encounters technical difficulties to store enough data samples and to post-process the acquired data in the time domain. His main conclusion regarding the two-dimensional effect of entropy spot is that for a sufficiently low frequency disturbance, the two-dimensionality of the entropy spot might be neglected and the resultant pressure field will scale with the cross-sectional area occupied by the spot.

During the same period of time, Muthukrishnan [Muthukrishnan 1977] studies experimentally the separation of direct noise sources and entropy noise on a Boeing 502-7D gas

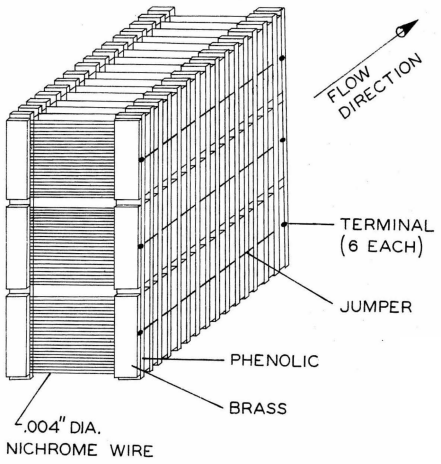

Figure 1.10: Schematic view of the pulse heater used by Bohn [Bohn 1976].

turbine unit by varying the airflow rates and for a wide range of Mach numbers (from 0.05 to 1). The rms temperature fluctuations at the burner exit plane varies from 9 to 14 % of the mean exit temperature. Muthukrishnan concludes that at low exit Mach numbers DCN is the dominant contributor to the exterior radiated noise, whereas at high exit Mach numbers, entropy noise overtakes and dominates DCN. He finishes by concluding that a third type of propagational noise source apart from DCN or entropy noise can be responsible for the partial coherence results observed and links it for the first time to the **vorticity**-nozzle interaction noise.

1.2.2 The EWG of Entropy Wave Generator

The renew in interest regarding test benches dedicated specifically to the study of entropy noise has occurred during the last 10 years. Indeed, substantial efforts were made to reveal the role of entropy waves and entropy noise in the onset of thermoacoustic instabilities. At that period of time, the Deutsches Zentrum für Luft- und Raumfahrt (DLR) built the EWG (Entropy Wave Generator), a test bench dedicated especially to study the indirect combustion noise due to entropy waves[3]. Bake *et al.* [Bake 2007, Bake 2008, Bake 2009a, Bake 2009b, Bake 2009c] study in particular two cases, a supersonic case with a normal shock in the divergent part of the nozzle denoted as "case 1" and a subsonic denoted as "case 2".

The EWG, shown in Fig. 1.11 and 1.12, is a nonreactive test rig. The flow supplied in this experimental test rig is provided by a compressed air system. This flow is calmed in a

[3] a VWG (Vorticity Wave Generator) has also been built at DLR a few years later, but as this PhD thesis is mainly focussed on studying the ICN generated by entropy waves, the details regarding the ICN generated by vortices will not be further described.

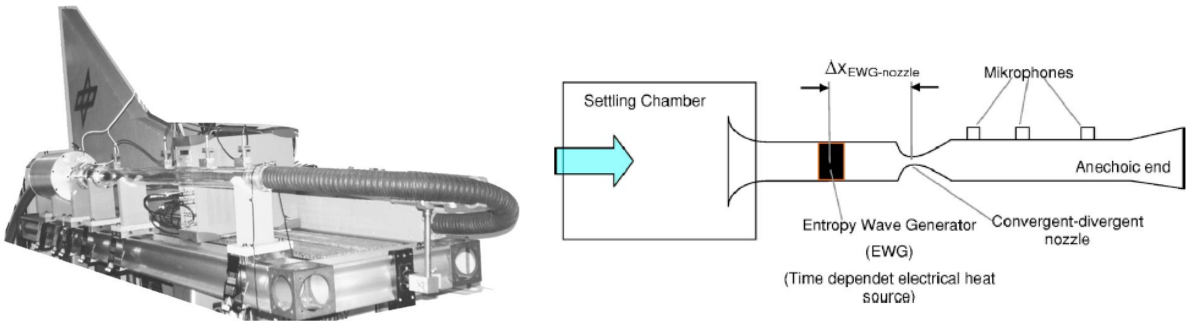

Figure 1.11: Photo (*left*) and sketch (*right*) of the Entropy Wave Generator from Bake *et al.* [Bake 2009c].

settling chamber with a honeycomb flow straightener before it enters the tube section via a bellmouth intake to keep thin boundary layers and a uniform flow. The heating system is composed of six ring sections; each ring is composed of ten platinum wires and is used to generate non-isentropic perturbations in a spatially varying flow field. The specifications and the cases studied in details by Bake *et al.* are shown in the Tables 1.2 and 1.3. They consider flow conditions from the low subsonic to the choked transonic regimes. In addition, the outlet termination of the experimental set up is not perfectly anechoic and the outlet impedance has been measured. Unfortunately regarding the inlet impedance, it has never been measured and might be lacking for the numerical computations (see Section 1.3).

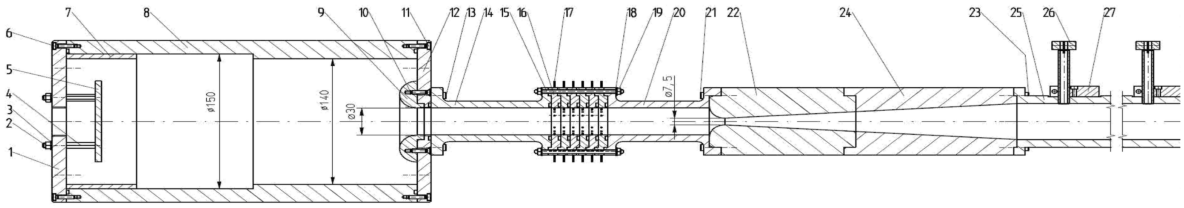

Figure 1.12: Schematic view of the EWG test rig.

The entropy disturbance in their experiments is chosen to be small enough to ensure the hypothesis of linear perturbations. As a consequence, the amplitude of the generated ICN is assumed to increase linearly with the amplitude of the temperature forcing. The amplitude of the generated sound pressure pulse as a function of the temperature for two different Mach numbers is represented in Fig. 1.13 (*left*) and agrees with the hypothesis of linear perturbations. In Fig. 1.13 (*right*), the amplitude of the generated sound pressure pulse as a function of the nozzle Mach number for two different amplitudes of the temperature fluctuations (7.5 K or 9 K) is plotted. A strong increase of the generated entropy noise is seen up to $M_a = 0.7$ after that a decrease occurs. This behavior was not understood by the authors at first [Bake 2008] and several numerical simulations of the EWG (see Section 1.3) were performed by the combustion community to understand this phenomenon. With the

Parameter	**Case 1**	**Case 2**
Mass flow rate ($\mathrm{kg.h^{-1}}$)	42	37
Mean flow velocity upstream of the nozzle ($\mathrm{m.s^{-1}}$)	12.18	11.39
Nozzle Mach number	1.0	0.7
Inlet Mach number	0.037	0.033
Outlet Mach number	0.023	0.01861
Shock Mach number	1.340	-
Plenum temperature (K)	298	296
Plenum pressure (Pa)	111700	105640
Outlet pressure (Pa)	100800	101300
Pulse duration (s)	0.100	0.100
Heating power added electrically (W)	143.7	192.7
Temperature increase ΔT (K)	9.1 at x=34mm	13.4 at x=47.5mm
Heating power measured based on ΔT (W)	106.8	138.2
Heating wired rings used (positioned from 1 to 6, where 6 is the closest ring to the nozzle and $x_6 = 0$)	3 to 6 simultaneously	1 to 6 with delay

Table 1.2: Physical parameters used in the EWG [Bake 2009c].

Convergent length	Divergent length	Inlet diameter	Outlet diameter	Throat diameter
13mm	250mm	30mm	40mm	7.5mm

Table 1.3: Geometrical parameters used in the EWG [Bake 2009c].

help of a numerical simulation provided by Mühlbauer *et al.* [Mühlbauer 2009], according to the authors the decrease of the generated noise with increasing Mach number is due to the impedance at the outlet nozzle [Bake 2009c]. Indeed, the effect of the impedance coefficients (both at the inlet and the outlet) is really important to compute numerically the correct response of the nozzle.

Bake *et al.* [Bake 2007] also compare the measurements provided by a generic combustor rig and the EWG. The main difference between the two test benches is the capability of EWG to measure only ICN, whereas the generic combustion chamber cannot separate the contributions of both direct and indirect noise. Entropy spots convected through the nozzle generate large quantities of noise in the EWG as well as in the generic combustion chamber test rig. Inside the combustion test rig, the Mach number reached only $M_a = 0.5$ but in most of the cases the combustor outlet in a real engine is choked, thus ICN is then expected to be higher.

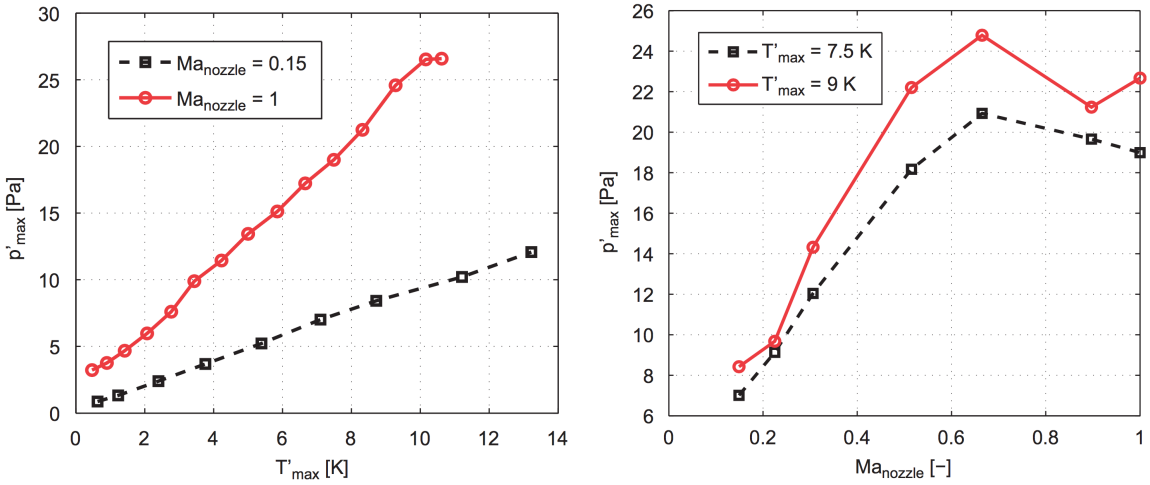

Figure 1.13: Amplitude of the generated sound pressure pulse as a function: of the amplitude of the temperature fluctuation for two different nozzle Mach numbers (*left*) and of the Mach number at the nozzle for two different amplitudes of the temperature fluctuation (*right*) from Bake *et al.* [Bake 2009c].

The reappraisal of earlier theoretical works described in the Section 1.1 on ICN is mainly due to the experiments of Bake *et al.* [Bake 2007, Bake 2008, Bake 2009a, Bake 2009b, Bake 2009c]. It has also generated many numerical studies to compare and also understand the results and conclusions made by Bake *et al.* The works aroused several questions on the EWG experiment leading to the recent development of a new test ring facility: the Hot-Acoustic Test ring (HAT).

1.2.3 The Hot-Acoustic Test ring (HAT)

Recently, the Hot-Acoustic Test ring (HAT) has been build at DLR in the RECORD project to investigate the sound propagation through a nozzle and the sound generation when cold air spots (at ambient temperature 288 K) are injected into a hot mean flow (temperature range of 288 to 823 K). Experimental results are detailed in Knobloch *et al.* [Knobloch 2015a, Knobloch 2015b]. A view of the experimental set up is visible in Fig. 1.14.

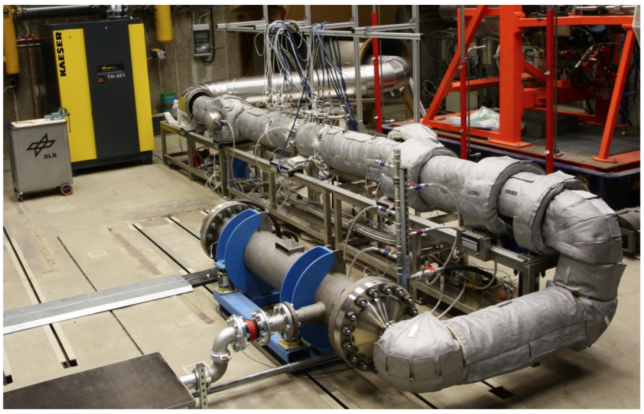

Figure 1.14: Photo of the Hot-Acoutic Test rig from Knobloch *et al.* [Knobloch 2015a].

It is composed of two symmetric measurement sections with the nozzle module between (see Fig. 1.16) and with partially anechoic terminations at both extremities of the set up. The measurement sections have an inner diameter of 70 mm and the total length of the configuration is 5.4 m. A schematic view of the HAT is represented in Fig. 1.15.

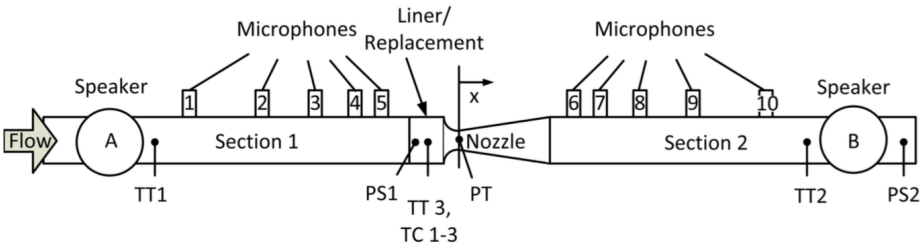

Figure 1.15: Sketch of the HAT with the position of instrumentation from Knobloch *et al.* [Knobloch 2015a]; where P_{thr}: pressure at the nozzle throat, PS 1/2: static pressure, TT: total temperature and TC: fast thermocouple probes.

The acoustic test signal is generated by loudspeakers denoted A and B in Fig. 1.15. Microphones are installed at ten non-equidistant axial positions. Temperature sensors in the section 1 and 2 perform the temperature measurements. The sensors are either resistive temperature detectors or shielded thermocouples with a precision of ± 1 K and an

immersion depth between 15 and 25 mm.

The nozzle module (see Fig. 1.16) is composed of three parts. Part 1 is a module with a bias flow liner (see Fig. 1.17) or, alternatively, a liner replacement module. Part 2 is simply a constant diameter additional part. Finally, part 3 is the converging-diverging nozzle derived from the geometry of a full-scale nozzle guide vane (NGV) of a high-pressure turbine stage. The nozzle Mach number is varied from subsonic to sonic conditions.

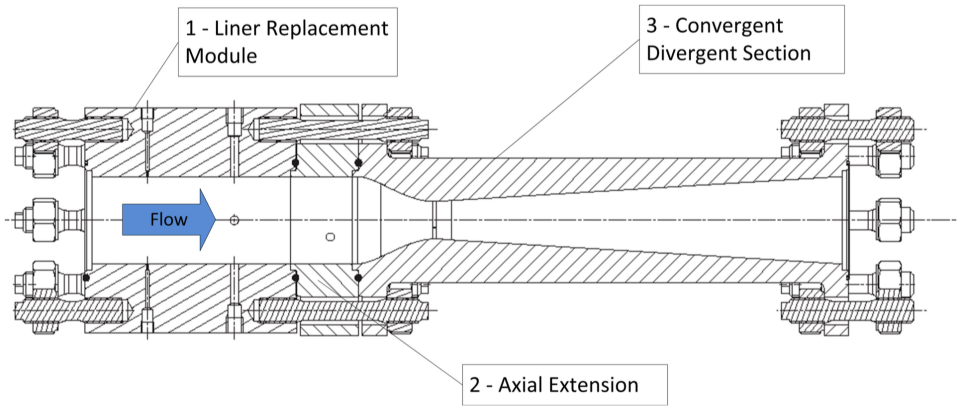

Figure 1.16: Sketch of the liner replacement section of constant diameter followed by the nozzle (converging-diverging) with a throat diameter of 30 mm and a 400 mm length from Knobloch *et al.* [Knobloch 2015a].

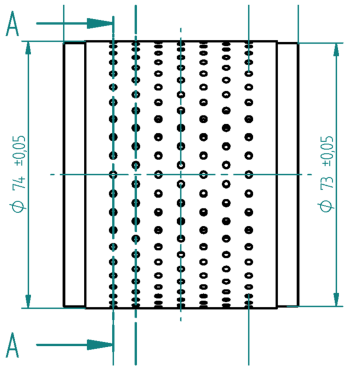

Figure 1.17: Sketch of the perforated liner used for entropy noise reduction from Knobloch *et al.* [Knobloch 2015a].

The injection of cold air is supplied by a 2 m^3 pressure reservoir at a temperature of 288 K and a pressure of 1.6 MPa and using fast switching valves. The injection is made at position 1, 2 or 3 by replacing the corresponding microphone (1, 2 or 3) radially through 6 flanges. Fig. 1.18 is a sketch of the air injection system as well as a photograph of different types of injectors.

Knobloch *et al.* in [Knobloch 2015b] perform two interesting experiments. First, the

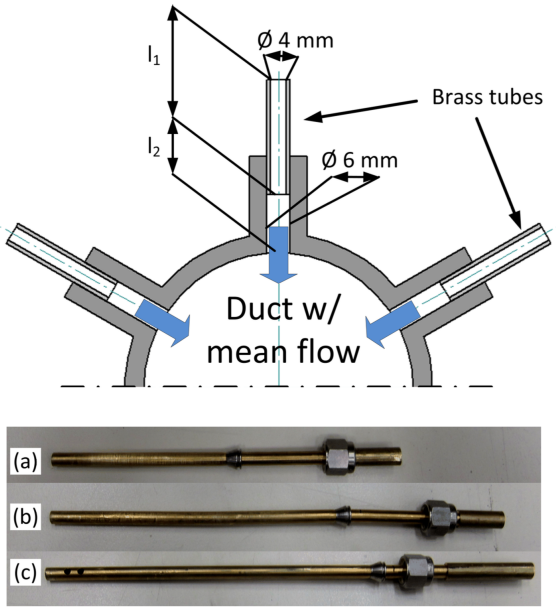

Figure 1.18: Sketch of the air injection (top) and variable injectors: (a) short mounted ($l_2 = 50$ mm), (b) flush mounted ($l_2 = 0$ mm) and (c) axial blowing ($l_2 = 20$ mm immersed in the mean flow) from Knobloch *et al.* [Knobloch 2015b].

Acoustic Transfer Functions (ATFs) are calculated by acoustic excitation using separately speaker A (upstream) and speaker B (downstream) with different nozzle Mach number (subsonic to sonic condition). This allows to obtain the reflection and transmission properties of the nozzle module (without the bias flow liner part) as a function of nozzle Mach number with a mean flow at ambient temperature (see Fig. 1.19). In the subsonic case (Mach number at 0.7), they show that using nondimensionalized frequency unit, the reflection and transmission coefficients are not influenced by the mean temperature of the flow, see Fig. 1.20. Second, cold air spots (ambient temperature) are injected into a hot mean flow going from 300 to 500 °C at sonic condition. The temperature and the position of injection of the cold spots as well as the way the cold air is injected (radial/axial blowing) are studied and the noise generation due to accelerated temperature fluctuations is assessed. The Thermo-Acoustic Transfer Functions (TATFs) are measured using pressure temporal signals upstream and downstream of the nozzle. The main conclusion of the study is that the amplitude of the noise peak depends linearly on the temperature difference between the mean flow and the injected cold air (temperature gradient). They also find that for a throat Mach number smaller than unity, no large entropy noise is observed which is in contradiction with the findings in EWG experiments explained in the previous subsection. According to the authors, in the subsonic case the amplitudes of the measured pressure signals are small and the generated ICN might be hidden in the background noise of the

configuration.

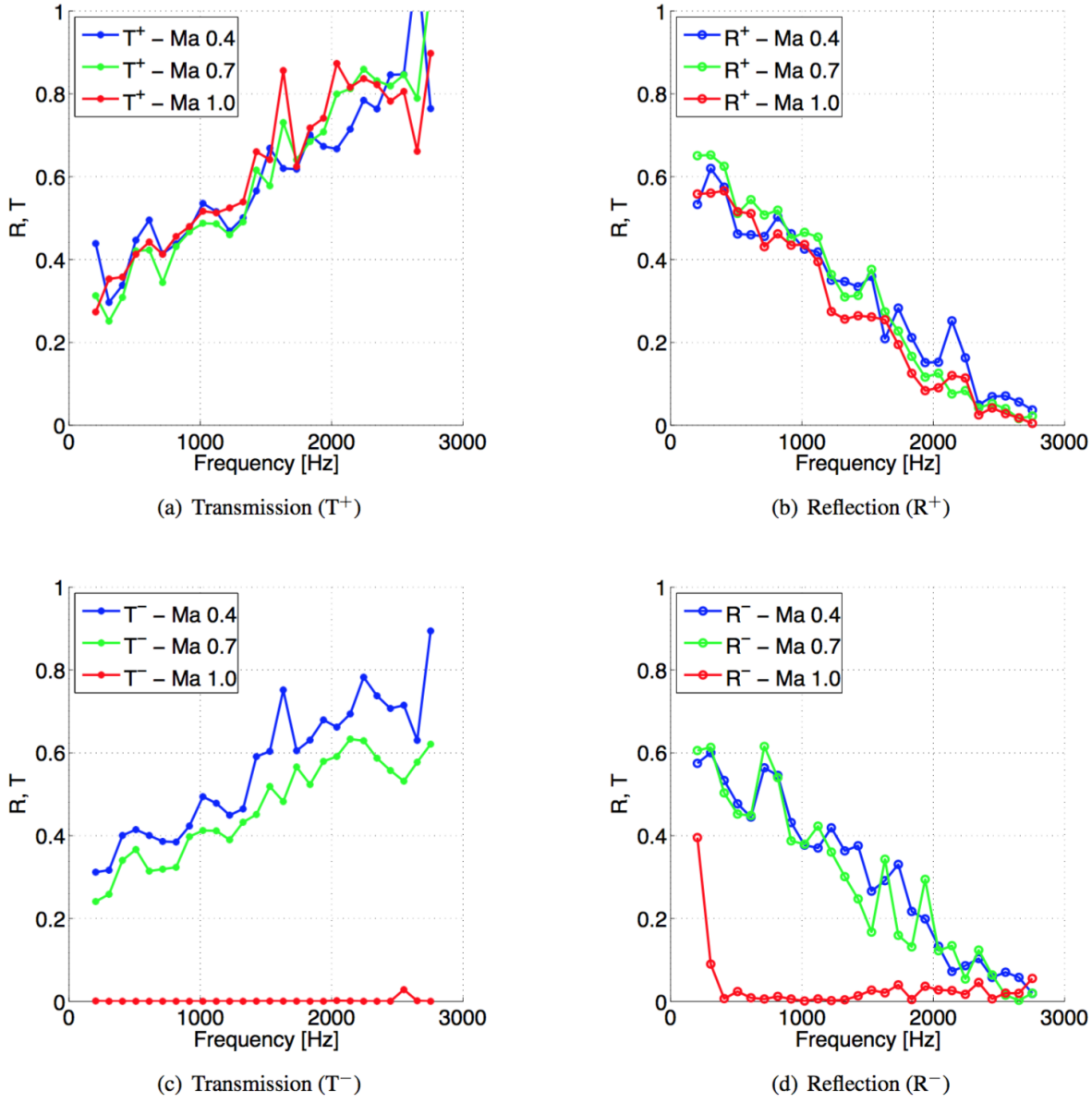

(a) Transmission (T^+)

(b) Reflection (R^+)

(c) Transmission (T^-)

(d) Reflection (R^-)

Figure 1.19: Transmission (T^+ and T^-) and reflection (R^+ and R^-) coefficients as a function of Mach number at ambient condition.

Two additional relevant findings are made by Knobloch *et al.* in [Knobloch 2015a]. Fig. 1.21 shows that a higher injected mass flow rate but with the same created temperature difference (temperature gradient) can increase the generated entropy noise up to 30%. This encourages the idea of a different shape of the cold spots in terms of spatial gradient and three-dimensional structure for the 2 considered mass flow rates. Secondly, a first attempt for entropy noise reduction by bias-flow liners is examined. The part 1 of the nozzle module is this time replaced by a perforated liner (see Fig. 1.17). The use of bias flow

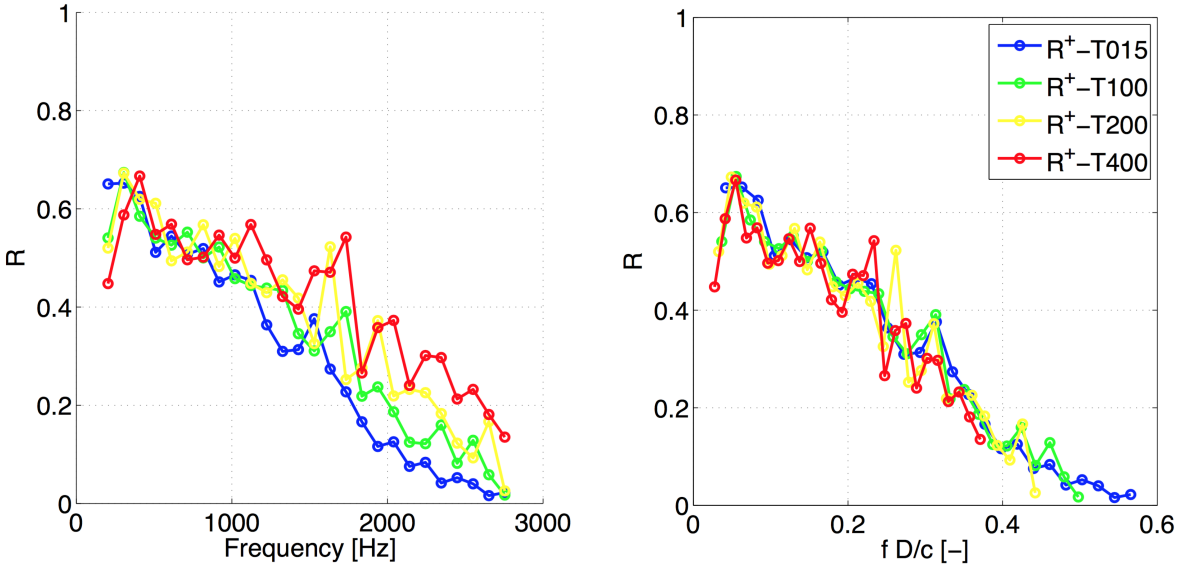

Figure 1.20: Reflection coefficient R^+ as a function of temperature for a mean flow at Mach number equals to 0.7. (*left*) SI units and (*right*) nondimensionalized frequency.

liners shows an entropy noise reduction by about 11% using low bias flow rates. A higher bias flow rate (3% pressure drop) does not remarkably improve the entropy noise reduction. This study indicates that the reduction of the generated entropy noise is caused by a rather **three-dimensional** change of the cold spot due to the bias flow. This noise reduction using bias flow is interesting but also needs to be in accordance with the engine performance associated with the injection of additional cooling air originally used in the secondary flow.

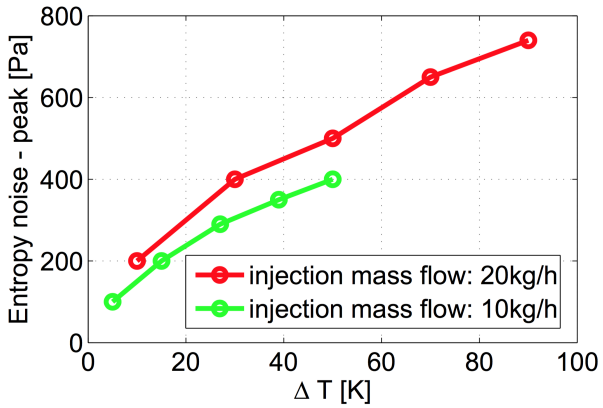

Figure 1.21: Maximum generated entropy noise amplitude recorded at microphone 7 as a function of temperature for two different mass flow rates at sonic condition from Knobloch *et al.* [Knobloch 2015a].

1.3 Numerical approaches

Following the EWG experiment, Bake *et al.* [Bake 2007,Bake 2008,Bake 2009a,Bake 2009b, Bake 2009c] study particularly two cases, a supersonic case with a normal shock in the divergent part of the nozzle denoted as "case 1" and a subsonic denoted as "case 2". The experiments generate interest in the community and multiple numerical applications arise trying to explain the experimental results. Before describing the numerical simulations performed by the community on these two cases, it is interesting to first have a look at the work done by Leyko *et al.* [Leyko 2009]. The contribution of indirect combustion noise is assessed using the one-dimensional theory of Marble & Candel [Marble 1977] combined with numerical computations. The wave propagation in this model is either determined by using the fully analytical compact method of Marble & Candel [Marble 1977] or a non-compact numerical method. Their research focuses mainly on the effect of the operating conditions on the sound production of combustion chambers situated in laboratories or enclosed in real aero-engines. The conclusion is that a low ratio of indirect to direct combustion noise is found in most laboratory combustion chambers since here the small pressure gradients yields to low acceleration speeds at the combustor exit. As a consequence, ICN is negligible in these experimental test rigs. In an opposite way, for the flow conditions inside real engines (low inlet Mach number, but high Mach number at the outlet), entropy noise is found to be much more important than DCN; for instance the indirect to direct noise ratio is found to be a factor of 10 when the nozzle inlet Mach number is fixed at 0.04 and the outlet at 0.95. This confirms the importance of ICN in real engines. Fig. 1.22 shows the ratio of indirect to direct noise plotted as a function of the Mach number at the nozzle inlet and the Mach number at the nozzle outlet.

Now that the relevance of ICN has been assessed analytically and numerically, the following sections describe the different numerical computation methods performed on cases 1 and 2.

1.3.1 Supersonic case with shock or "case 1"

Even with the computing power improvement, numerical computations remain still a bit costly regarding the physics and the accuracy aimed. The entropy noise generation in supersonic nozzles with a normal shock is first analyzed by Leyko *et al.* [Leyko 2008,Leyko 2010, Leyko 2011] yet without trying to resolve the turbulent boundary layers developing in the nozzle. A numerical and analytical approach is used to confirm the applicability of the one-dimensional theory of Marble and Candel [Marble 1977] in case of choked nozzles. Leyko *et al.* [Leyko 2011] use the AVBP code from CERFACS to compare data from the EWG test rig with their simulation (see Figure 1.23).

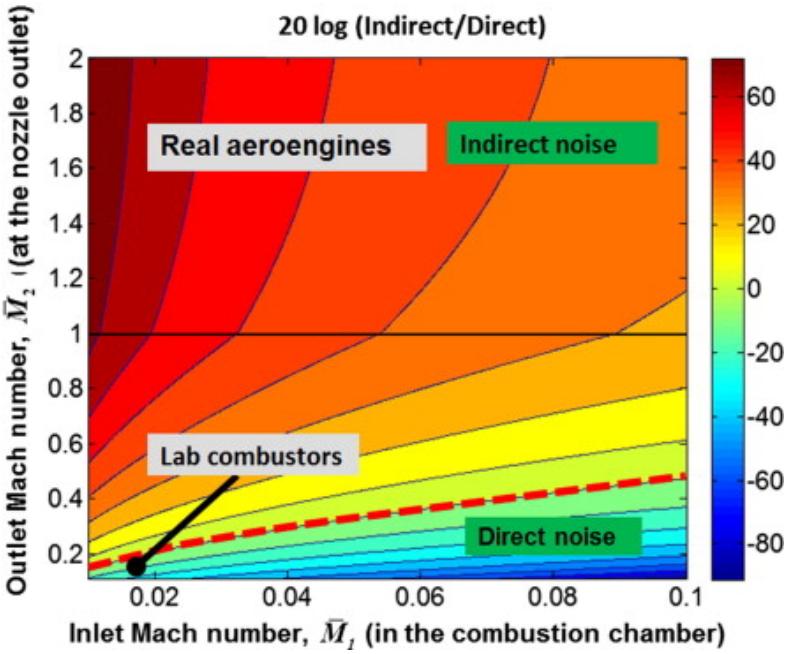

Figure 1.22: Direct/indirect combustion noise dominance extracted from Dowling & Mahmoudi [Dowling 2014] based on Leyko *et al.* [Leyko 2009].

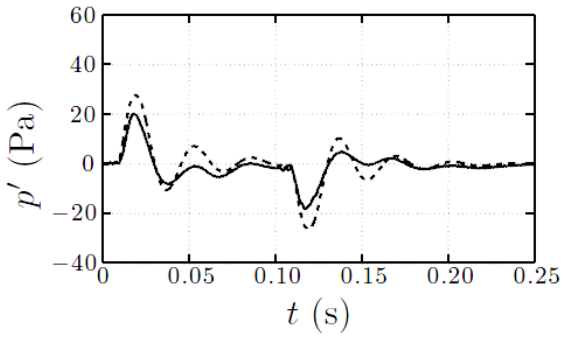

Figure 1.23: Fluctuating pressure downstream of the nozzle over time, the pressure sensor is located at 1150mm downstream of the nozzle: (–) measured pressure, (––) simulated pressure; from Leyko *et al.* [Leyko 2011].

A two-dimensional axisymmetric and a fully three-dimensional configuration with various duct lengths and boundary conditions (acoustic reflections) are studied. The disagreement between 2D computation and experimental data are not due to three-dimensional effects as using a 3D model instead of a 2D axisymmetric does not significantly affect the pressure signal (see Fig. 6 in [Leyko 2011]). Again, the discrepancies are mainly due to the boundary conditions used at the inlet and outlet. The measured pressure signals come from two main mechanisms: the conversion of entropy to acoustic due to the strong mean velocity gradient in the nozzle, but also from the acoustic reflection upstream **and** downstream of the nozzle. They also report that the linear acoustic and the compact nozzle hypothesis of [Marble 1977] is applicable on the EWG and proposed an analytical model taking into account the acoustic impedances both at the inlet and outlet.

Richter *et al.* [Richter 2007] propose an Hybrid or Zonal approach to solve the noise generated by an entropic source. Their methodology is described in [Richter 2005] and the assessment of the resolution process is performed with the help of the EWG test data. The method is a three zones approach (see Fig. 1.24) using a sound source, a propagation and a far field zone. It is cheaper than a two zones approach. For instance in a two zones approach, the sound source zone requires to be resolved using compressible Navier-Stokes equations in order to transport the acoustic modes to the interface between the sound source and the far field zone (in our case, outside the combustion chamber). In addition, high quality non reflective boundary conditions (NSCBC) [Poinsot 1992, Baum 1994, Lodato 2008, Widenhorn 2008] have to include the interfaces preventing pollution of the numerical computation due to acoustic reflections at the boundaries. On the opposite, an incompressible computation of the sound source contains the non-isentropic and the vortical part of the perturbed flow field. The method is decomposed into three steps. First accelerated entropy perturbations are obtained numerically using an incompressible 2D URANS (Unsteady Reynolds Average Navier Stokes) with a modified eddy dissipation model (EDM). Then, data are injected in a Computational Aeroacoustics (CAA) code using Neumann or Dirichlet boundary conditions. The CAA solver is based on a fourth order seven point Dispersion-Relation-Preserving (DRP) scheme of Tam *et al.* [Tam 1993] for spatial discretization and the "Low Dissipation and Low Dispersion Runge Kutta-scheme" (LDDRK-scheme) of Hu *et al.* [Hu 1996] for time integration. The propagation of the acoustic waves is solved using linear or nonlinear Euler equations. Finally, the acoustic far field is described by the Lighthill acoustic analogy ([Williams 1969] or [Piscoya 2004]). Even if the CAA requires a Courant-Friedrichs-Lewy (CFL) number $\leq$ 1, the axisymmetric assumption coupled with the highly efficient temporal scheme allowed to keep a low computational cost. The 2D mesh used consists of 78277 cells. In addition, a strong dependence of the pressure response on the upstream reflection coefficient is stated.

Indeed, the use of the implementation of the termination impedance from the experimental data is necessary since the boundary conditions in the EWG experiment are not perfectly anechoic.

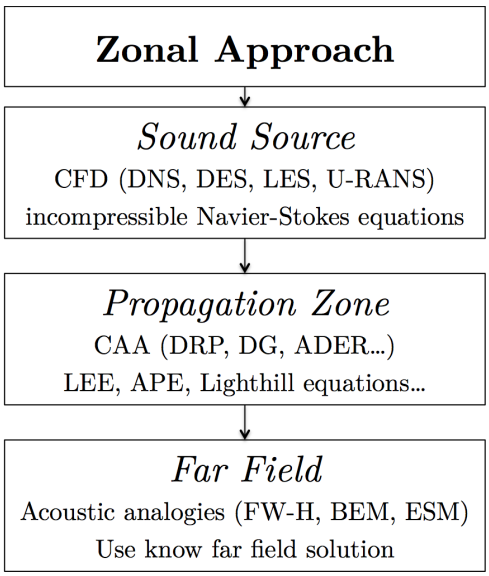

Figure 1.24: Schematic view of the three zones approach adopted by Richter *et al.* for "case 1" [Richter 2007].

Some limitations regarding this three zonal CFD-CAA approach can be stated. First, the missing influence of turbulent scales in the sound source can lead to errors at high frequency at which turbulent structures might interact with entropy fluctuations. Therefore a **three-dimensional LES** computation is a plus. Secondly, the mesh used for the numerical computation might not be sufficiently fine enough to allow the propagation and sound generation of entropy perturbation at higher frequencies. A possible solution would be to refine the mesh or to perform a LES computation used as an input. This LES computation might overcome the aforementioned limitations cited. Indeed, the possible interaction of turbulence with sources generation, dissipation and dispersion are captured by LES. In addition, the boundary layer are better resolved or modeled, this is a key to accurately predict those interferences at the source level.

Mühlbauer *et al.* [Mühlbauer 2007, Mühlbauer 2008, Mühlbauer 2009] use a three-dimensional compressible URANS approach with a $k-\varepsilon$ turbulent model to simulate the acoustic disturbance observed in the EWG test facility to determine the pressure fluctuation as well as the spectrum of entropy noise. The use of this turbulence model is justified by the fact that in preliminary numerical investigations the effect of turbulence on dissipation and dispersion of the entropy wave is very low. This three-dimensional unstructured grid is a 10° rotation of a two-dimensional segment of the EWG test rig (see Fig. 1.25 and 1.26) with periodic boundary conditions and therefore cannot be really considered as a

three-dimensional computation. 57000 nodes are considered in the final mesh.

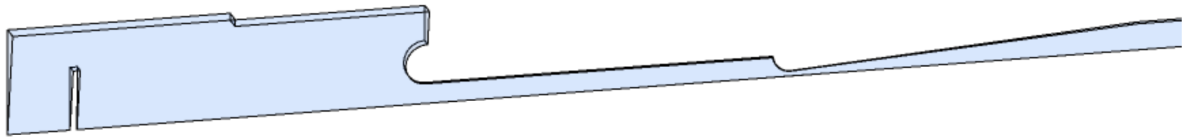

Figure 1.25: Sketch of the 3D-URANS computational domain segment [Mühlbauer 2009].

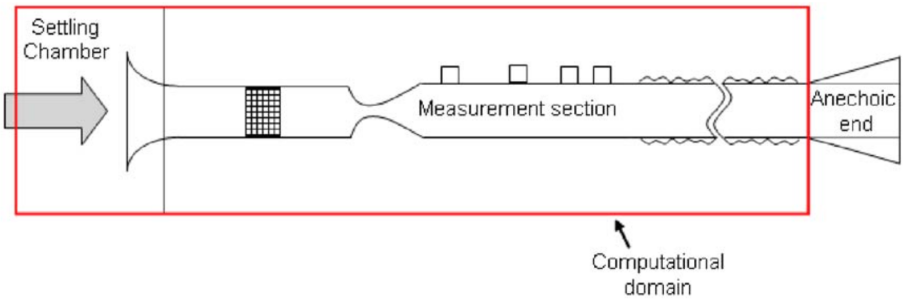

Figure 1.26: View of the 3D-URANS computational domain [Mühlbauer 2009].

Acoustics is directly resolved by the CFD solver ANSYS CFX 11 however at that time Navier-Stokes characteristics boundary conditions (NSCBC) where not really available in the solver to model partially non reflecting boundaries. The boundary conditions allows a modeling of the downstream impedance. At the inlet of the computational domain, they use a fully reflective mass flow boundary condition. They manage to give an explanation of the ICN decrease when the Mach number is higher than $M = 0.7$ by developing for the first time a numerical method for the localization of the acoustic sources of entropy noise in acceleration and deceleration regions. Mühlbauer *et al.* show that ICN sources intensity increase as the Mach number in the nozzle increases. It is concluded that the decrease of entropy noise in the case of near sonic Mach number nozzle flows is caused by the changes of the spatial structure of the entropy wave.

As one can see in Figure 1.27, the 3D-URANS numerical simulation gives almost the same results as the experimental data only when a partially reflective outlet boundary condition is used (neither the fully reflective nor the fully non reflective boundary condition managed to give the correct solutions). The minor discrepancies are due to the constant reflection coefficient with no phase shift modeling the switch between the cylinder and the square zone in this computation. A possible solution is to use instead of the NSCBC a time-domain impedance boundary conditions (TDIBCs) introduced by Widenhorn *et al.* [Widenhorn 2008] and Huber *et al.* [Huber 2008]. TDIBCs are able to consider measured reflection

coefficient and the phase shift as a function of the frequency. In addition to the previously mentioned issues occurring when using URANS simulation is the possible problem arising from coherent excitation.

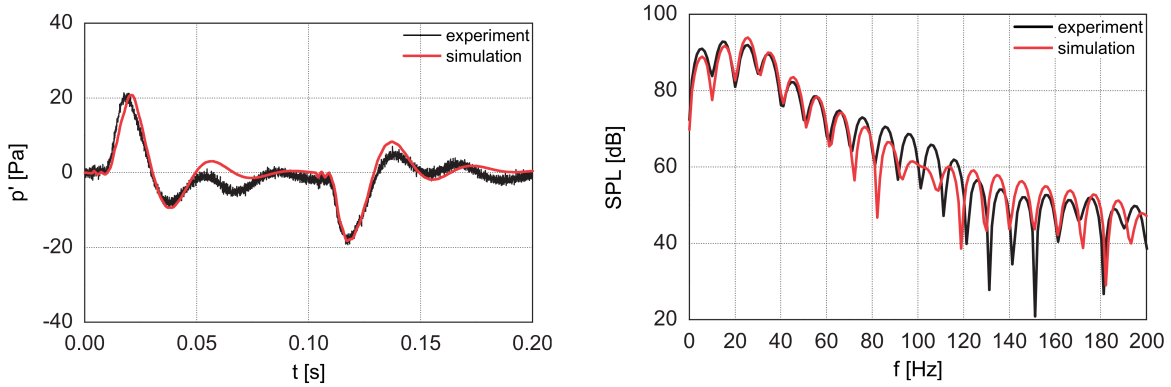

Figure 1.27: Comparison data between computed and measured values from Mühlbauer *et al.* [Mühlbauer 2009], pressure signal (*left*) and spectrum of the pressure signals (*right*) using partially reflective outlet boundary condition.

Bake *et al.* [Bake 2009c] study also the mechanisms of ICN generation with a high order CFD-CAA method. The steady base flow is provided by the 3D-URANS computation performed by [Mühlbauer 2009] described in the previous paragraph. The two-dimensional axisymmetric approach formulated by Li *et al.* [Li 2005] in the cylindrical coordinate system is applied. The boundary conditions, mean and perturbed flow fields are assumed to be constant in the azimuthal direction allowing to reduce the dimension of the problem by one. A CAA- and a reduced CAA-domain are studied, see Fig. 1.28. The spatial DRP- and time LDDRK-scheme are used.

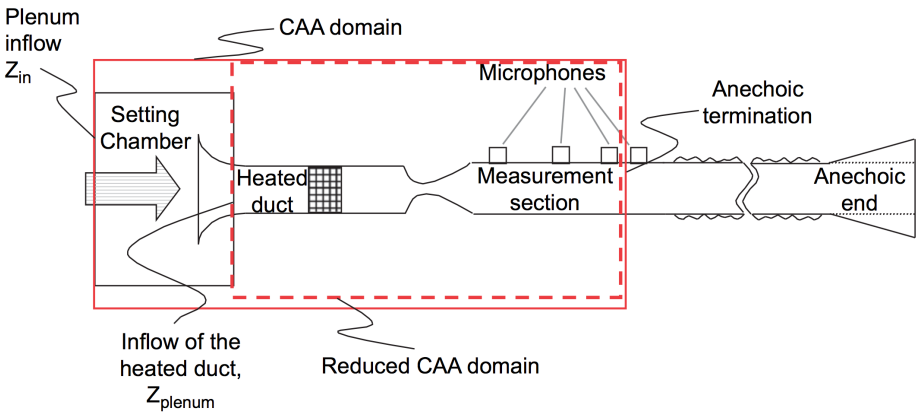

Figure 1.28: Sketch of the CAA- and the reduced CAA-domain.

The reduced CAA-domain allows the replacement of the settling chamber by a time-

domain impedance boundary conditions (TDIBCs) [Widenhorn 2008, Huber 2008]. As the plenum impedance denoted Z_{plenum} (see Fig. 1.28) was not measured and never will, it is approximated by a low frequency extended Helmholtz resonator (EHR). The results regarding a fully non reflective, a fully reflective, a partially reflective plenum and the experimental measurements of Bake *et al.* are represented in Fig. 1.29 for subsonic and supersonic flows.

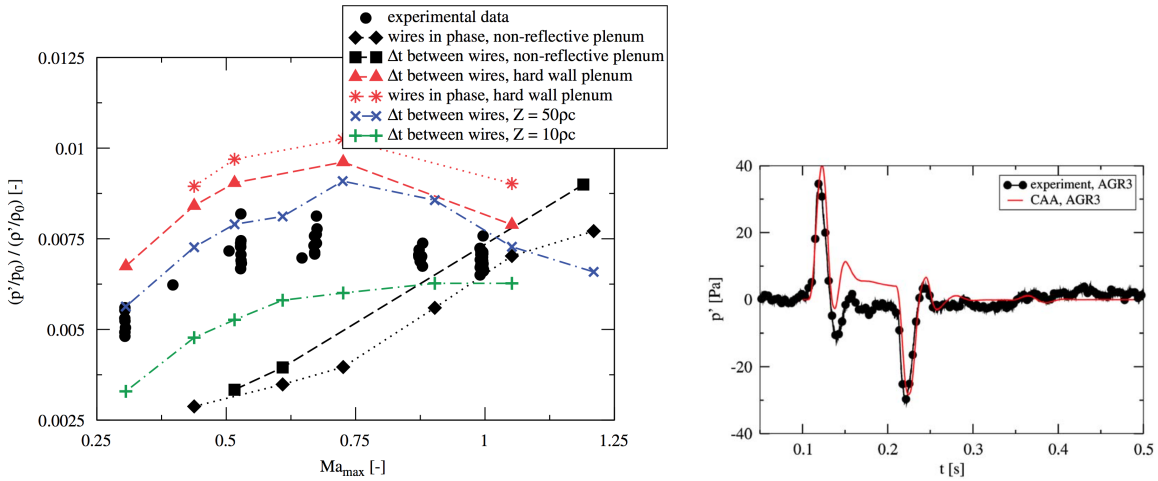

Figure 1.29: Normalized transmission coefficient of the maximum pressure fluctuations at the outlet duct and the entropy perturbation at the inlet duct (*left*). Pressure response at the exhaust duct for a Mach number $M_a = 0.73$ using the estimated plenum impedance and measured experimentally (*right*) from Bake *et al.* [Bake 2009c].

The pressure and non-isentropic density perturbation are normalized by the mean pressure in the outlet duct and the density in the heated duct respectively. The Mach number is defined by the maximum steady flow velocity divided by the local speed of sound. It can be seen that a partially reflective plenum (+ and × in the left of Fig. 1.29) gives the best fit to the trend observed experimentally regarding the transmission coefficient. On the right of Fig. 1.29, the experimental pressure response as well as the computed pressure response are shown. The computed pressure response obtained by the representation of the plenum as a low frequency Helmholtz resonator **tuned** by three parameters matches pretty well with the experimental data.

An approach different than [Mühlbauer 2009] for the acoustic sources localizations is carried. An analysis of the results based on the acoustic intensity is carried out which is in good agreement with the ones obtained by Mulhbauer *et al.* [Mühlbauer 2009]. ICN sources are found to be several orders of magnitude stronger than the DCN sources due to the heating confirming that in "case 1", ICN is the dominant source.

1.3.2 Subsonic case or "case 2"

Duran *et al.* [Duran 2011, Duran 2013b] study numerically and also analytically the EWG experiment of Bake *et al.* [Bake 2009c] in the subsonic regime. A full numerical resolution of the EWG test rig is performed using the code AVBP. A Lax-Wendroff scheme is used to solve the unsteady Euler equations. In this configuration, it was shown by Mühlbauer *et al.* [Mühlbauer 2007, Mühlbauer 2008, Mühlbauer 2009] but also Leyko *et al.* [Leyko 2011] that three-dimensional effects (impact of turbulence) are negligible. A 2D axisymmetric mesh of around 10000 nodes is then considered in the computational domain. Numerical results are supplemented by an analytical method based on the work of Marble & Candel in the low-frequency limit and a one-dimensional linearized Euler equations solver in the frequency domain.

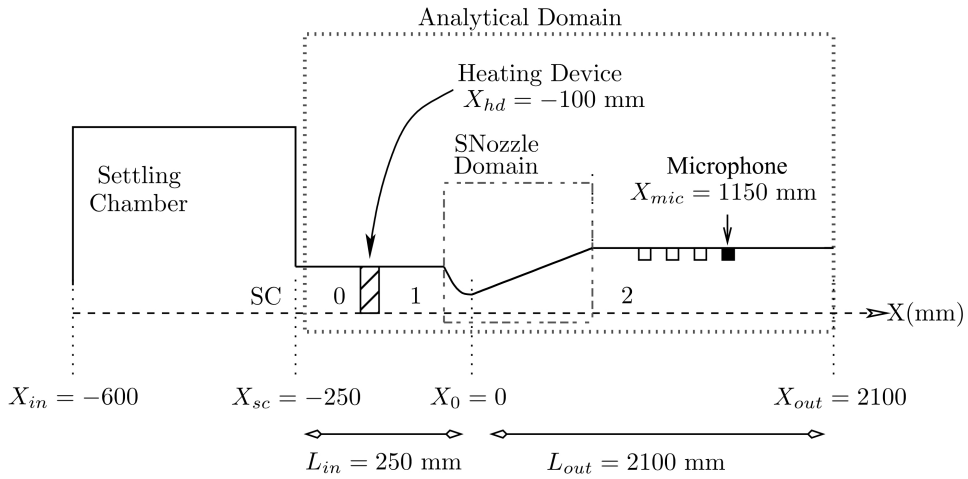

Figure 1.30: View of EWG test rig with the representation of the domains used by Duran *et al.* [Duran 2013b].

The partially reflective boundary conditions of the facility are taken into account in the simulations. The reflection coefficients are studied and show the necessity to take into account both indirect and direct combustion noise as well as partially reflecting condition at the outlet. However, as there is not a precise value of the inlet reflection coefficient some discrepancies between the results of Duran *et al.* and the measurement of Bake *et al.* can be observed. Once again this study shows the critical role of both the upstream and the downstream impedance coefficients in the determination of ICN. The influence of DCN stronger than ICN is shown by a first-order analysis of the waves generated by the heating device. It is also stated that for low Mach number flows DCN is an important contributor to the global sound emission in this test rig. This last study emphasizes the fact that for real gas turbines where the flow remains mostly subsonic, the direct noise needs also to be taken into account. Regarding the flow properties, some questionable assumptions are made. For

instance, there is no viscosity, no turbulence nor boundary layers in the computations. This might be highly restrictive since in a real aero engine, these phenomena are present.

Recently, Giauque *et al.* [Giauque 2012] apply the analytical model of Moase *et al.* [Moase 2007] to the subcritical case of the EWG. Impedance coefficients at the nozzle inlet and outlet and the experimental temperature perturbation provided by Bake *et al.* [Bake 2009c] and Leyko *et al.* [Leyko 2011] are introduced in the analytical formulation. A very good agreement is found between their results and the analytical model proposed by Howe [Howe 2010]. In the subcritical range, even if ICN is the main phenomenon responsible for the acoustic disturbance in the configuration of Bake *et al.* [Bake 2009c], the DCN has a role which cannot be neglected. The effect of the rising time of the temperature fluctuation is investigated with the result that the latter has also an influence on the amplitude of the generated entropy sound in the EWG.

This conclusion is also stated by Lourier *et al.* [Lourier 2014]. Rather than using NSCBC to model the downstream impedance used by [Mühlbauer 2009], [Leyko 2011] or [Duran 2013b], the authors propose to use instead a time-domain impedance boundary conditions (TDIBCs) [Widenhorn 2008] and [Huber 2008]. Even if Lourier *et al.* manage to obtain results in good agreement with the measurements of Bake *et al.* and the numerical computations from Duran *et al.*, no mention regarding the upstream impedance coefficient is made. In the subsonic regime, it seems that a downstream propagative acoustic wave at the inlet P_1^+ or an upstream propagative acoustic wave at the outlet P_2^- give a larger acoustic response than an entropic forcing at the inlet.

1.4 Entropy waves advection in a spatially varying mean flow

Many authors have studied the effect to the entropy wave advection in a spatially varying mean flow. Sattlemayer [Sattelmayer 2003] is the first to consider this effect in the context of combustion instabilities and to develop a model (rectangular entropy advection model). He mainly concludes that for all the frequencies, the dispersion of the entropy wave is **strong even at low frequencies**. His model is later revisited by Morgans *et al.* [Morgans 2013] who develop a model based on a gaussian profile; the comparison with numerical computations illustrates the validity of this model. Morgans *et al.* find that the dissipation of the entropy wave is negligible and the loss of entropy wave strength is caused predominantly by the mean flow shear dispersion. However this dispersion of the entropy waves is not really strong at low frequencies as stated by Sattelmayer and significant **entropy wave strength still remains** at the combustor exit. Thus, acoustic waves generated by the acceleration of low-frequency entropy waves are likely to play an important role in combustor

thermoacoustics. Similar findings are found by Giusti *et al.* [Giusti 2016], who studied experimentally and numerically the propagation of entropy waves and observed that their amplitudes decay with increasing frequency and mean residence time. The influence of entropy advection and noise generation in the frame of combustion instabilities is investigated more in details by Morgans & Li [Morgans 2015] and Xia *et al.* [Xia 2016]. The authors show that the presence of an advective shear dispersion on entropy noise has potentially a strong effect on thermoacoustic modes. This result is supported by the recent numerical results of Hosseinalipour *et al.* [Hosseinalipour 2017] who evaluated the effective modification of a combustor hydrodynamics due to the decay of the entropy wave strength.

1.5 Conclusion & limitations

Combustion noise has two origins. It can be created by the unsteady heat release fluctuation in the combustion chamber, in which case it is called DCN. It can also be related to the acceleration in a nozzle or a turbine row of temperature or vorticity inhomogeneities created by the flame; it is then called ICN. After a combustion chamber, two devices are likely to produce indirect combustion noise: the nozzle and the turbine stages. Regarding the ICN generated though the nozzle, it has been widely studied analytically, experimentally and numerically.

Analytically, the acoustic nozzle emission problem has been solved by Marble & Candel [Marble 1977] and others for several types of flows: subsonic, supersonic with or without shock. Several approaches have been studied to overcome the restrictive assumption of "the compact nozzle". So far only the quasi-one-dimensional approach is used in the design process of future engines. All the models at hand assume a uniform mean flow over the cross-sectional area and only axial perturbations. These approaches neglect any radial variation in the mean and unsteady flow field although recent numerical simulations showed the importance of the distortion of the entropy waves. Entropy waves are convected by a flow that is non-uniform in the radial direction, which leads to different resident times across the sectional area. So far no available model seems to take this phenomenon into account. Some attempts to consider the flow as two-dimensional rather than quasi-one-dimensional has been carried by Crocco and Bohn 40 years ago, but since then no progress have been made.

In the 70's, studies at California Institute of Technology (Caltech) were focused on a test rig designed to investigate ICN. However, in those experiments the amplitude of the injected temperature fluctuation was quite low (around 1 K). In 2007, a new test rig named the EWG was built at DLR generating strong interest inside the combustion community. Two reference cases, one subsonic and one supersonic with a normal shock inspired analytical

and numerical studies. However, as the operating conditions in the combustion chamber of the EWG are quite different from a real aero engine, a European project RECORD was launched in 2013 aiming at understanding the mechanisms of generation and transmission of combustion noise in a more realistic framework and also a better control of the inlet and outlet impedances.

Numerically, several approaches have been used to determine the combustion noise emitted by nozzles. The EWG experimental cases were studied using CFD-CAA, 2D/3D-URANS, 2D/3D LES approaches. However, so far an axisymmetric configuration was often considered allowing a simplification of the geometry and as a consequence a reduction of the number of cells used. In reality, the geometry of a nozzle is rarely axisymmetric. In addition, the operating conditions are far different from what is found in a real aero engine. Usually high pressure and high temperature make numerical simulations difficult to achieve.

Analytical entropy wave advection models based on numerical or experimental data have been developed to take into account the distortion of the entropy fronts. Many authors showed the importance of this phenomenon the generated entropy noise but also in the context of thermoacoustic instabilities. However, no purely analytical entropy wave convection models have been developed for nozzle flows.

Furthermore, the role played by turbulence should also be investigated as it might be important during the process of sound generation as well as during the convection of entropy waves. It is the opinion of the author that the boundary layers developing inside the nozzle should be considered as they tend to reduce the effective cross sectional area and change the location of the maximum Mach number location. Both effects are expected to modify the acoustic emission of the nozzle.

In this context, the aim of this PhD thesis is to develop a 2D semi-analytical model that will take into account these two-dimensional effects. In addition, to explore the interaction of turbulence with entropy, fully 3D LES simulations are carried out in order to compare with and validate this new model.

Chapter 2

Numerical and analytical tools

Science is not about making predictions or performing experiments. Science is about explaining.

Bill Gaede

Contents

In this section, the analytical and numerical tools available at Onera at the beginning of the thesis are described. First, one-dimensional solvers based on Euler equations are introduced. Those two solvers called SUNDAY and MarCan resolve the Euler equations in the

time and spectral domain respectively. SUNDAY and MarCan are helpful tools to understand and estimate ICN generated in a nozzle. However, they rely on strong simplifications of the physical problem (one-dimensional mean nozzle flow and perturbations, etc.). These hypotheses, by simplifying the problem at hand, also discard potential additional effects that might have a significant role in ICN. Among these phenomena are the two and three-dimensional effects on the flow disturbances due to turbulence and the presence of the end walls. To evaluate them and quantify their effects, three-dimensional numerical computations are needed. After a brief introduction to the Navier-Stokes equations and turbulence, the three-dimensional solver CEDRE is described and specific parameters (schemes, models) used for the numerical computations performed during the PhD thesis are presented.

2.1 One-dimensional tools

With the increase of computational power and the storage capabilities, it has become more and more convenient to perform numerical simulations. However, it remains still quite expensive to solve all the physics of an unsteady flow by performing Direct Numerical Simulation (DNS) and the effort has been aimed at developing and improving low-order models. One-dimensional models appear to be a good alternative in order to reduce the costs and are commonly used during the design process of future aero engines.

2.1.1 Quasi one-dimensional temporal numerical solver SUNDAY

This section describes the numerical tool SUNDAY (SimUlation of Noise in 1D flows due to fluctuAtions in entropY) designed to investigate noise emission in nozzles. It was developed at ONERA [Huet 2013]. SUNDAY solves the quasi one-dimensional nonlinear Euler equations in the time domain for the primitive variables p, u and ρ instead of the variables chosen by Marble & Candel [Marble 1977] (p,u,s). This set of equations is formally equivalent to Eqs. 1.30-1.32 where the entropy equation is replaced for numerical stability reason by Eq. 2.1 on pressure:

$$\frac{\partial p}{\partial t} + u\frac{\partial p}{\partial x} + \gamma p\frac{du}{dx} = -\gamma p u\frac{1}{A}\frac{dA}{dx} \tag{2.1}$$

The full equations are first solved to provide the undisturbed steady flow and then acoustic or entropy disturbances are injected at the inlet using nonlinear or linearized perturbation equations derived without the thermodynamically perfect gas assumption. The resolution process is performed using a finite difference method. The spatial derivatives are computed using the optimized 11-point scheme and a selective flow fields filter proposed by Bogey & Bailly [Bogey 2004]. The time integration is done with the standard explicit fourth-order Runge–Kutta algorithm [Butcher 1996]. Centered schemes are

used inside the computational domain and a switch to the upwind schemes proposed by Berland et al. [Berland 2007] is done near the boundaries. Centered and noncentered coefficients for the derivatives and the selective filtering can be found in the work of Cacqueray [Cacqueray 2010]. Finally, non-reflective boundary conditions are implemented at both extremities of the geometry using the Navier-Stokes Characteristic Boundary Conditions (NSCBC) proposed by Thompson [Thompson 1987, Thompson 1990]. Their implementation follows the form given by Poinsot & Lele [Poinsot 1992]. These conditions allow acoustic and entropy waves to leave the domain without significant reflections. In addition, these conditions are modified to enable the injection of pressure and temperature fluctuations [Kaufmann 2002]. SUNDAY has been validated for noise generation in the linear as well as in the nonlinear regimes [Giauque 2012, Huet 2013]. The resolution of the flow with injected perturbations provides the pressure and velocity fluctuations at the extremities of the converging-diverging nozzle. The stored time signals are then analyzed in the frequency domain to provide the transfer functions of the nozzle through the use of the linear Riemann invariants:

$$P^+ = \frac{1}{2}\left(\frac{p'}{\gamma P_0} + \frac{u'}{c_0}\right) \tag{2.2}$$

$$P^- = \frac{1}{2}\left(\frac{p'}{\gamma P_0} - \frac{u'}{c_0}\right) \tag{2.3}$$

2.1.2 One-dimensional analytical spectral solver MarCan

Marcan is a one-dimensional analytical spectral solver. It was developed by Giauque *et al.* [Giauque 2012] and is based on the piecewise linearity assumption of the velocity profile for a subsonic flow. It is briefly presented in §1.1.2.2. This solver is validated in [Giauque 2012] through cross validation with SUNDAY on several representative geometries of nozzles. Some additional details are however given in this paragraph, mainly to present the limitations of the method. In a given element n of the nozzle, the velocity is assumed to evolve linearly, the acceleration is thus constant and is defined as $\Lambda = \frac{\Delta U}{\Delta x} = \frac{du}{dx}$. In some cases, because of the nozzle geometry, this local acceleration can become very small leading to an issue for the analytical method. The numerical evaluation of the hypergeometric function becomes difficult and wrong. Also, regardless of the acceleration, the numerical process used to determine these hypergeometric functions does not converge if the frequency is too large. Depending on the geometry of the nozzle, the maximum frequencies that can be reached can be too low to study high frequency ICN. Finally, the results are strongly influenced by the mean velocity profile obtained using the piecewise linear decomposition and one has to ensure that the obtained profile remains sufficiently close to the initial one.

Despite their limitations, quasi one-dimensional models are helpful tools to understand

and estimate ICN generated in a nozzle. These approaches however rely on strong simplifications of the physical problem, such as one-dimensional mean nozzle flow and perturbations. Neglected effects like the distortion of entropy perturbations by the heterogeneous radial velocity profile may however modify the noise generated through the nozzle. To evaluate the contribution of such effects and the limitations of the current hypotheses, the ICN generated across a nozzle is examined later in this PhD thesis by performing three-dimensional numerical computations (chapter 3 and 4) using the numerical solver CEDRE. Before describing the solver CEDRE, a brief introduction to the Navier-Stokes equations and turbulence is given.

2.2 Equations of Fluid mechanics and theory of Turbulence

2.2.1 Introduction of the Navier-Stokes equations

The Navier-Stokes equations in a cartesian coordinate system without a heat source term write [Poinsot 2012]:

$$\begin{cases} \dfrac{\partial \rho}{\partial t} + \dfrac{\partial \rho u_k}{\partial x_k} = 0 \\ \dfrac{\partial \rho u_i}{\partial t} + \dfrac{\partial (\rho u_i u_k + \delta_{ik} P)}{\partial x_k} - \dfrac{\partial \tau_{ik}}{\partial x_k} = 0 \qquad (i = \{1,2,3\}) \\ \dfrac{\partial \rho E}{\partial t} + \dfrac{\partial \rho E u_k}{\partial x_k} + \dfrac{\partial P u_k}{\partial x_k} + \dfrac{\partial q_k}{\partial x_k} - \dfrac{\partial \tau_{kl} u_l}{\partial x_k} = 0 \end{cases} \tag{2.4}$$

where t is the time, x_i a unit of length in the i-direction, ρ the fluid density, $\mathbf{u}$ the velocity vector, P the pressure, T the temperature, E the specific total energy and q the heat flux. The Einstein summation convention is used to simplify Eq. 2.4 with i, k and l indices. The viscous stress tensor for Newtonian fluids (the relation between the viscous stress tensor and the strain rate tensor is linear) can be computed as:

$$\tau_{ij} = \mu(T)\left(\frac{\partial u_i}{\partial x_j} + \frac{\partial u_j}{\partial x_i} - \frac{2}{3}\frac{\partial u_k}{\partial x_k}\delta_{ij}\right) \tag{2.5}$$

where $\mu(T)$ is the dynamic viscosity of the fluid, linked to the kinematic viscosity by $\mu = \rho\nu$. Its variation with the temperature is expressed using the Sutherland law:

$$\mu(T) = \mu_0 \frac{T_0 + T_1}{T + T_1}\left(\frac{T}{T_0}\right)^{\frac{3}{2}} \tag{2.6}$$

where $\mu_0 = \mu(T_0) = 1.856.10^{-5}$ kg.m^{-1}.s^{-1}, $T_1 = 149.49232$ K and $T_0 = 300$ K are constants. It is also useful to introduce the rate of strain tensor S_{ij} and the vorticity tensor Ω_{ij} defined

respectively as:

$$S_{ij} = \frac{1}{2}\left(\frac{\partial u_i}{\partial x_j} + \frac{\partial u_j}{\partial x_i}\right) \tag{2.7}$$

$$\Omega_{ij} = \frac{1}{2}\left(\frac{\partial u_i}{\partial x_j} - \frac{\partial u_j}{\partial x_i}\right) \tag{2.8}$$

The heat flux follows the Fourier law:

$$q = -\Lambda \mathbf{grad}(T) \tag{2.9}$$

where Λ is the heat conduction coefficient and is computed using the Eucken's law defined by:

$$\Lambda = \mu(C_p + \frac{5}{4}\frac{\mathcal{R}}{\mathcal{M}}) \tag{2.10}$$

where NPW is the specific heat capacity at constant pressure, $\mathcal{R} = 8.314472\ \mathrm{J.mol^{-1}.K^{-1}}$ is the molar gas constant and $\mathcal{M}$ is the molar mass of the fluid.
The perfect gas law writes:

$$P = \rho\frac{\mathcal{R}}{\mathcal{M}}T \tag{2.11}$$

2.2.2 Kolmogorov theory of Turbulence

A turbulent flow is characterized by the presence of turbulent eddies of various scales. The Reynolds number defines the ratio between the inertial forces and the viscous forces. In such a flow, energy is extracted from the mean flow by the larger eddies and then cascades down to the smaller ones, where it is dissipated into heat by viscosity. The Reynolds number is expressed as:

$$Re_{\mathcal{L}} = \frac{\rho u_{\mathcal{L}} \mathcal{L}}{\mu} = \frac{u_{\mathcal{L}} \mathcal{L}}{\nu} \tag{2.12}$$

where $Re_{\mathcal{L}}$ is the Reynolds number linked to the integral length scale $\mathcal{L}$, $u_{\mathcal{L}}$ is the characteristic velocity of the structures at the integral length scale, μ is the dynamic viscosity, ν is the kinematic viscosity and ρ is the density. When $Re_{\mathcal{L}}$ is small, the flow is considered as laminar, the viscous forces are dominant and the fluid motion is rather smooth. On the other hand, when $Re_{\mathcal{L}}$ is large, the flow is considered as turbulent and vortex structures or eddies populate the flow. The relation regarding those structures has been theorized by Kolmogorov [Kolmogorov 1991]. Fig. 2.1 shows the energy spectral density $E(\kappa)$ of a typical turbulence spectrum of a homogeneous flow, as a function of the modulus of the wavenumber κ obtained by the Fourier transform of the velocity field. This number is homogeneous to the inverse of the turbulent structures scale.

The energy spectrum can be divided into three zones depending on the scale of the

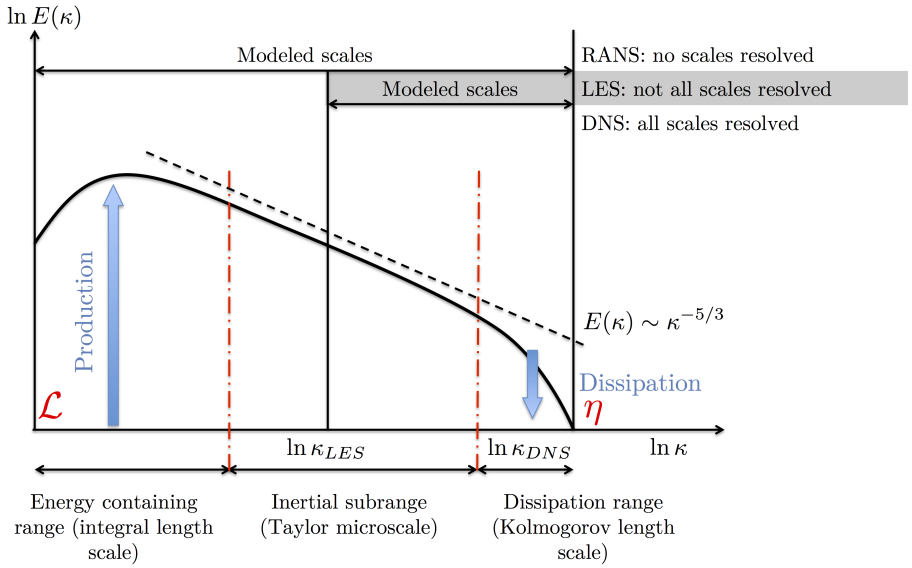

Figure 2.1: Energy spectrum of a homogeneous isotropic turbulent flow and representation of the different levels of modeling in the principal methods for simulating turbulent flows.

considered turbulent structures according to Kolmogorov:

- The Energy containing range is the zone where the kinetic turbulent energy is produced. The scale of the vortices is defined by the geometry and is associated to the integral scale $\mathcal{L}$.

- The Inertial subrange is the zone where the large eddies (smaller than the Energy-containing eddies) transfer their energy to the smallest ones without dissipation. This process is called the "energy cascade" and is self-similar, meaning that all the vortices break up in the same way, whatever their scale. This implies for a homogeneous isentropic turbulent flow, that the Energy spectrum decays as $E(\kappa) \sim \kappa^{-5/3}$.

- The Dissipation range or viscous sub-range is the zone where the smallest scales dissipate the received energy into heat. The scale of the structures is associated to the Kolmogorov scale η. For very large Reynolds numbers, the smallest scale is completely determined by the viscosity ν and the dissipation rate of the energy ε and is expressed as:

$$\eta = \left(\frac{\nu^3}{\varepsilon}\right)^{1/4} \tag{2.13}$$

  The conservation of the dissipation rate of energy allows to link the Kolmogorov scale to the integral length scale with:

$$\frac{\mathcal{L}}{\eta} \sim Re_{\mathcal{L}}^{3/4} \tag{2.14}$$

In the Kolmogorov theory, the inverse cascade or backscatter which corresponds to a transfer of energy from the smaller scales to the largest ones through the pairing interaction and amalgamation of vortices, is not taken into account. In order to solve a turbulent flow, several numerical resolution methods can be applied. In this PhD thesis, three are presented, but only two are detailed:

- the Direct Numerical Simulation (DNS) approach consists in resolving all the scales of the turbulent spectrum;
- the Large Eddy Simulation (LES) approach consists in resolving the largest scales (see Fig 2.1) where the main energy part is present and modeling the dissipation of smaller scales;
- the Reynolds-Averaged Navier-Stokes (RANS) consists in modeling all the spectrum in order to compute the average flow (in the statistical sense).

Direct Numerical Simulations (DNS) resolve numerically all the turbulent length scales of the Navier-Stokes equations. However, this approach needs a sufficiently refined mesh to capture the dissipative smallest scales down to the Kolmogorov scale η. The number of points needed to solve a three-dimensional flow using DNS is estimated around $Re_{\mathcal{L}}^{9/4}$ for a free flow [Pope 2000]. An additional difficulty arises, as the time step has to be small enough to reproduce the dynamic of smallest scales and is around the Kolmogorov temporal scale defined as:

$$\tau_\eta = \left(\frac{\nu}{\varepsilon}\right)^{1/2} \tag{2.15}$$

One way to grasp the meaning of this time scale is to associate it with the fictional time to dissipate an amount of energy k at the constant rate ε.

For high Reynolds wall-bounded flows, the length scales of turbulence rapidly decrease as the wall is approached and require an extremely fine mesh in the near-wall region [Pope 2000]. This means that most of the computational resources are spent in solving that region rather than the outer layer. The nozzle studied in this thesis has a Reynolds number above 10^6 and a DNS approach appears to be unfeasible due to high computational demand. DNS is indeed applicable to low Reynolds number and/or academic cases. With the improvement of computing power resources, DNS should be applied to higher Reynolds number flow in the medium and long term. Meanwhile, some alternative solutions have been developed to study turbulent flows with a certain degree of turbulence modeling: the Large Eddy Simulations (LES) and the Reynolds-Averaged Navier-Stokes (RANS) approaches described in the next paragraph as they are used during the PhD thesis.

2.3 Three-dimensional turbulent flows simulation

CEDRE is a multi-physics platform for both research and industrial applications dedicated to the fields of aerodynamics, heat transfer, combustion, icing, propulsion and aeroacoustic [Chevalier 2005, Refloch 2011]. The software is based on a multi-solver approach where the fluid solver can be run alone or coupled to additional solvers to perform multi-physics computations. In this thesis, only the fluid solver CHARME (Calcul Hybride d'Aérothermique et Réactif Multi-Espèce) solving the fluid mechanics equations is used. CEDRE uses unstructured generalized meshes and is used to perform numerical simulations of reactive or high-speed flows inside complex geometries, such as combustion chambers or nozzles for example. Flow physics in such configurations is often governed by the non-linear Navier-Stokes equations and is characterized by the Reynolds number. In a realistic combustion chamber, the flow is turbulent and has a high-Reynolds number. The two resolutions methods available in the solver CEDRE to model such turbulent flow, the Reynolds-Averaged Navier-Stokes (RANS) and the Large Eddy Simulations (LES), are detailed. Finally, the time and spatial schemes used for the numerical simulations are introduced.

2.3.1 Reynolds-Averaged Navier-Stokes equations (RANS)

2.3.1.1 Averaging operation of the Navier-Stokes equations

RANS computations are commonly used in the industry during the conception process due to the relatively short restitution time. The approach requires modeling the entire turbulence spectrum. The cost of this approach is relatively low and is well integrated in the design process of the aero-engines industry. Due to the strong hypotheses made on the model, this approach is not adapted for transient and unsteady flow. The RANS method consists in solving the statistically averaged Navier-Stokes equations. The instantaneous quantities are decomposed into averaged and fluctuating quantities as proposed by Reynolds [Reynolds 1895].

$$\varphi = \overline{\varphi} + \varphi' \tag{2.16}$$

However, for compressible flow, a filtering corresponding to a statistical ensemble average proposed by Favre [Favre 1965] is preferred to avoid cross-terms that are difficult to model in the mass equation. This filtering writes:

$$\varphi = \widetilde{\varphi} + \varphi'' \tag{2.17}$$

where $\widetilde{\varphi} = \dfrac{\overline{\rho\varphi}}{\overline{\rho}}$ and $\overline{\rho\varphi''} = 0$. By neglecting the viscosity fluctuations and the nonlinearity of the heat flux, Eqs. 2.4 become:

$$\begin{cases} \dfrac{\partial \overline{\rho}}{\partial t} + \dfrac{\partial \overline{\rho}\widetilde{u_k}}{\partial x_k} = 0 \\ \dfrac{\partial \overline{\rho}\widetilde{u_i}}{\partial t} + \dfrac{\partial(\overline{\rho}\widetilde{u_i}\widetilde{u_k} + \overline{P}\delta_{ik} - \widetilde{\tau_{ik}}^*)}{\partial x_k} = \dfrac{\partial \widetilde{\tau_{ik}^R}}{\partial x_k} \qquad (i = \{1,2,3\}) \\ \dfrac{\partial \overline{\rho}\widetilde{E}}{\partial t} + \dfrac{\partial(\overline{\rho}\widetilde{E}\widetilde{u_k} + \overline{P}\widetilde{u_k} - \widetilde{\tau_{kl}}^*\widetilde{u_l} + \widetilde{q_k}^*)}{\partial x_k} = -\dfrac{\partial \widetilde{q}_{t_k}}{\partial x_k} + \dfrac{\partial \widetilde{\tau_{kl}^R}\widetilde{u_l}}{\partial x_k} \end{cases} \tag{2.18}$$

where

$$\begin{aligned} \overline{\rho}\widetilde{E} &= \overline{\rho e} + \frac{1}{2}\overline{\rho}\widetilde{u_l}\widetilde{u_l} + \frac{1}{2}\overline{\rho}\widetilde{u_l'' u_l''} \\ \widetilde{\tau_{ij}}^* &= \mu(\widetilde{T})\left(\frac{\partial \widetilde{u_i}}{\partial x_j} + \frac{\partial \widetilde{u_j}}{\partial x_i} - \frac{2}{3}\frac{\partial \widetilde{u_k}}{\partial x_k}\delta_{ij}\right) \\ \widetilde{q_k}^* &= -\lambda(\widetilde{T})\frac{\partial \widetilde{T}}{\partial x_k} \\ \widetilde{\tau_{ik}^R} &= -\overline{\rho}\widetilde{u_i'' u_k''} \\ \widetilde{q}_{t_k} &= \overline{(\rho e'' + P)u_k''} \end{aligned}$$

$\widetilde{\tau_{ik}^R}$ and $\widetilde{q}_{t_k}$ are respectively the turbulent Reynolds stress and heat flux tensor. These nonlinear terms are related to the effect of turbulence on the average quantities in the flow. They need to be modeled and are replaced by simplified terms replicating the effect of turbulence (turbulence model).

2.3.1.2 RANS equation closure

In order to close the set of equation 2.18, the Reynolds stress tensor ($\widetilde{\tau_{ik}^R}$) and the turbulent heat flux ($\widetilde{q}_{t_k}$) need to be modeled by applying a turbulence model. Several models have been developed over the last forty years. Two main categories of models exist:

- First order models that are based on the Boussinesq assumption. They link the Reynolds stress tensor and the turbulent heat flux to a viscosity coefficient and the mean strain tensor. Those quantities are resolved using an algebraic relation [Prandtl 1925, Johnson 1985] or using transport equations to quantify turbulence properties using Spalart Allmaras model [Spalart 1994], $k-\varepsilon$ models [Jones 1972, Launder 1974] or $k-\omega$ models [Kolmogorov 1991, Wilcox 1988, Menter 1993] for instance.

- Second order models or Reynolds Stress Models (RSM). They use a different approach by resolving directly the transport equations of the Reynolds stress tensor ($\widetilde{\tau_{ik}^R}$) com-

ponents. However, higher order fluctuating terms appear using this approach and also need to be modeled.

In this work, a numerical study on a converging-diverging nozzle is carried out. Only the $k-\omega$ Shear-Stress Transport (SST) of Menter [Menter 1993] is described as it will be used during the RANS computation in chapter 3. The reader is invited to read the literature regarding the other approaches if interested. The diverging part of the nozzle is the critical part of the computation. Indeed, the presence of an adverse pressure gradient (APG) in the diverging zone may lead to the presence of a detached flow. As a consequence, the choice of a $k-\omega$ model is made for its capability to take into account a potential APG in the wall region. The $k-\omega$ model proposed by Wilcox [Wilcox 1988] could be sufficient, but even if this model is simple and robust, it suffers from its extreme sensitivity to the value of ω at the limit of the boundary layer. Menter [Menter 1992] showed in 1992 that this behavior is due to a lack of diffusivity in the shear region due to the formulation of the model. Consequently, the $k-\omega$ Shear-Stress Transport (SST) of Menter [Menter 1993] is chosen. It is, in fact, a hybrid approach combining the k–ω proposed by Wilcox [Wilcox 1988] and the $k-\varepsilon$ [Jones 1972, Launder 1974]. The $k-\omega$ model is applied in the boundary layer region while the $k-\varepsilon$ one is used for detached regions and the other parts of the flow. The transition between the two models [Menter 1994] is ensured by $\omega = \frac{\varepsilon}{\beta^* k}$ with $\beta^* = C_\mu = 0.09$, where β^* is the constant of the Wilcox's $k-\omega$ model and C_μ is the constant of the $k-\varepsilon$ one.

2.3.2 Large eddy simulation (LES)

The Large Eddy Simulation (LES) approach consists in resolving the largest scales where the main part of the turbulent kinetic energy is present and modeling the smallest scales where the dissipation takes place. The LES approach and the wall treatment are explained in the following sections.

2.3.2.1 Filtering operation of the Navier-Stokes equations

The small scales, which are excluded from the spatial filtering process as they are not resolved by the mesh, are called the sub-grid scale (SGS) and are modeled with a SGS turbulence model. The cutoff length of the filter is usually placed in the inertial range of the turbulent spectrum (where the energy spectrum has a constant slope equal to $\kappa^{\sim -5/3}$ (see Fig. 2.1). The procedure of decomposing the variables as a sum of a mean and a fluctuating part is the same as in the RANS method (Eq. 2.17). This filter can be seen as a convolution function (G) and can be applied to any field $\varphi(x)$. If G is the filter convolution kernel, the

filtering method can be seen as:

$$\overline{\rho}\widetilde{\varphi}(x) = \int_{+\infty}^{-\infty} \rho\varphi(x')G(x-x')dx' \tag{2.19}$$

The filter function satisfies the condition:

$$\int_{-\infty}^{+\infty} G(x)dx = 1 \tag{2.20}$$

G has an associated cutoff length scale Δ_{cut} but also a cutoff time scale τ_{cut}. This process is in fact a low-pass filtering in the spectral domain. Any field variable denoted as $\varphi(x)$ can be decomposed as a resolved part denoted $\overline{\varphi}$[1] and a filtered part or unresolved part φ'. Applying the filtering operation described previously results in the appearance of unknown SGS stresses. The Navier-Stokes equations 2.4 become after applying the filter:

$$\begin{cases} \dfrac{\partial\overline{\rho}}{\partial t} + \dfrac{\partial\overline{\rho}\widetilde{u_k}}{\partial x_k} = 0 \\ \dfrac{\partial\overline{\rho}\widetilde{u_i}}{\partial t} + \dfrac{\partial(\overline{\rho}\widetilde{u_i}\widetilde{u_k})}{\partial x_k} = -\dfrac{\partial(\overline{P}\delta_{ik} - \overline{\tau_{ik}}^* - \tau_{ik}^L)}{\partial x_k} \\ \dfrac{\partial\overline{\rho}\widetilde{E}}{\partial t} + \dfrac{(\partial(\overline{\rho}\widetilde{E}\widetilde{u_k})}{\partial x_k} = -\dfrac{\partial(\overline{P}\widetilde{u_k} - \overline{\tau_{kl}}^*\widetilde{u_l} + q_{t_k}^L + \overline{q_k}^*)}{\partial x_k} + \dot{\mathcal{Q}} \end{cases} \qquad (i = \{1,2,3\}) \tag{2.21}$$

where

$$\begin{aligned} \overline{\tau_{ij}}^* &= \mu(\widetilde{T})\left(\frac{\partial\widetilde{u_i}}{\partial x_j} + \frac{\partial\widetilde{u_j}}{\partial x_i} - \frac{2}{3}\frac{\partial\widetilde{u_k}}{\partial x_k}\delta_{ij}\right) \\ \overline{q_k}^* &= -\lambda(\widetilde{T})\frac{\partial\widetilde{T}}{\partial x_k} \\ \tau_{ik}^L &= \widetilde{u_i u_k} - \widetilde{u_i}\widetilde{u_k} \\ q_{t_k}^L &= \overline{\rho}(\widetilde{u_k E} - \widetilde{u_k}\widetilde{E}) \\ \dot{\mathcal{Q}} &\quad \text{is the heat source terms if present} \end{aligned}$$

τ_{ik}^L and $q_{t_k}^L$, where the superscript L refers to LES, are respectively the turbulent stress tensor and the turbulent heat flux tensor. Fig. 2.2 gives an illustration of different eddy sizes that are resolved (blue) and unresolved (red) by the grid mesh represented in the background. A good LES mesh is capable to fairly capture down to the inertial range and cut off the small part of the turbulent energy contained in the smaller scales.

This unsteady formulation makes LES a very attractive approach for simulating turbulent flows as it can capture accurately large scale unsteady features, provide access to the turbulence characteristics and finally reduce the modeling requirements. However, the

[1]Similar notations for $\widetilde{f}$ and $\overline{f}$ are used here in RANS and LES. These quantities denote ensemble averages in RANS whereas they correspond to filter quantities in LES.

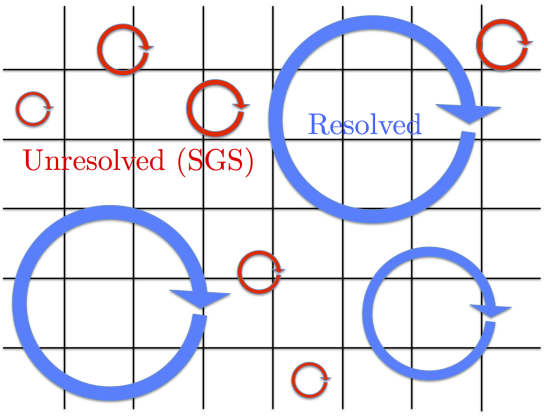

Figure 2.2: Schematic view of the resolved eddies in blue and the unresolved eddies (SGS) in red when the background grid corresponds to the mesh.

disadvantage of this method lies in its computational cost, much higher than for steady RANS computations. The increasing computational resources and the storage capabilities however make this approach more accessible even for relatively high Reynolds number flows. To apply this approach, the set of equations 2.21 needs to be closed, this procedure is described in the next section.

2.3.2.2 LES equations closure

In order to close the system and have a consistent set of equations, it is necessary to model the SGS terms. These SGS terms should hold only a small portion of the kinetic energy and are responsible for the dissipation of energy in the turbulent cascade. Neglecting this energy should result very quickly in an energy accumulation in the system and a divergence of the numerical computation. To avoid this problem, a modeling of the SGS terms is performed to mimic the real behavior of the finest turbulent scales onto the resolved field. To achieve this objective, as with several RANS turbulence models, the Boussinesq assumption is commonly used. It links the Reynolds Stress tensor τ_{ik}^L to the filtered strain rate tensor $\widetilde{S}_{ij}$ (Eq. 2.7) by introducing the kinematic turbulent viscosity μ_t. It reads for compressible flows:

$$\tau_{ik}^L = -2\mu_t \left(\widetilde{S}_{ij} - \frac{\delta_{ij}}{3} \widetilde{S}_{kk} \right) + \frac{\delta_{ij}}{3} \overline{\rho} \tau_{kk} \tag{2.22}$$

Several SGS models can be found in the literature. For example, one can cite the commonly used Smagorinsky SGS model [Smagorinsky 1963], the Wall Adapting Local Eddy-viscosity model (WALE) [Nicoud 1999] or the σ-model [Nicoud 2011]. In the absence of the σ-model and due to a lack of validation of the WALE model in the CEDRE solver, the SGS model of Smagorinsky is used during this thesis for the two LES computations described in chapter

4. This model is simple and robust. The turbulent viscosity is defined as:

$$\mu_t = \overline{\rho}(C_s\Delta_i)^2\sqrt{2\overline{S_{ij}S_{ij}}} \tag{2.23}$$

where C_s is the Smagorinsky coefficient usually fixed around 0.18 and obtained by assuming a statistically converged flow in the spectral domain [Sagaut 2006]. Δ_i is the mesh scale and is evaluated for an unstructured grid as:

$$\Delta_i = 6\frac{V_i}{\sum_k A_{i,k}} \tag{2.24}$$

where V_i is the volume of the i-cell delimited by n faces of area $A_{i,k=1..n}$. For a cubic cell mesh, Δ_i is simply the length of the side edge while for a tetrahedron, it corresponds to the diameter of the inscribed sphere. When one wants to apply LES to a bounded flow, the question arises whether or not the behavior of the model is correct down to the wall if the mesh is too coarse. With a simple model such as Smagorinsky, it is not the case. Because of that the user is left with a first option which is to refine the grid at the wall and capture a large part of the turbulent spectrum down to the wall or use an additional wall model compatible with the SGS model at hand. To this end the next section describes the near-law commonly adopted in LES.

2.3.2.3 Near-Wall law

The near-wall treatment as well as the boundary layer simulation are still challenging issues for numerical computations no matter the type of simulation. For LES computations, according to Chapman [Chapman 1979], 90% of the total turbulent kinetic energy needs to be resolved by the large scales. For high Reynolds wall-bounded flows, the length scales of turbulence rapidly decrease as the wall is approached and it requires an extremely fine mesh in the near-wall region [Pope 2000, Kawai 2012]. This means that most of the computational resources are spent in solving that region rather than the outer layer. As a consequence, two different approaches (illustrated in Fig. 2.3) are employed when simulating boundary layers with LES:

(1) Wall resolved LES

In this approach, an attempt to resolve all the scales of the boundary layer and most of the turbulence produced is carried out. This implies a very fine mesh resolution at the wall. It is characterized by the maximum non-dimensional wall normal distance (or wall unit) of the first node close to the wall of $y^+ < 5$ (viscous sub-layer, see Fig. 2.4). Von Kármán [von Kármán 1931] defined y^+ as the non-dimensional wall distance for a wall-bounded flow.

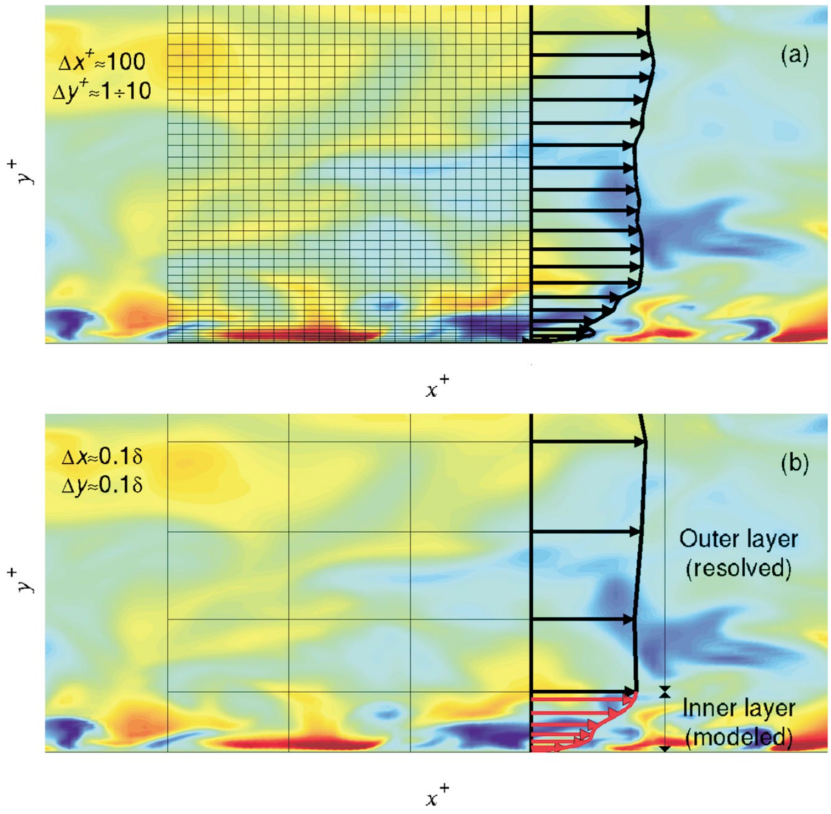

Figure 2.3: Wall layer modeling approaches from [Piomelli 2002]. (a) Resolved inner boundary layer. (b) Modeled inner boundary layer.

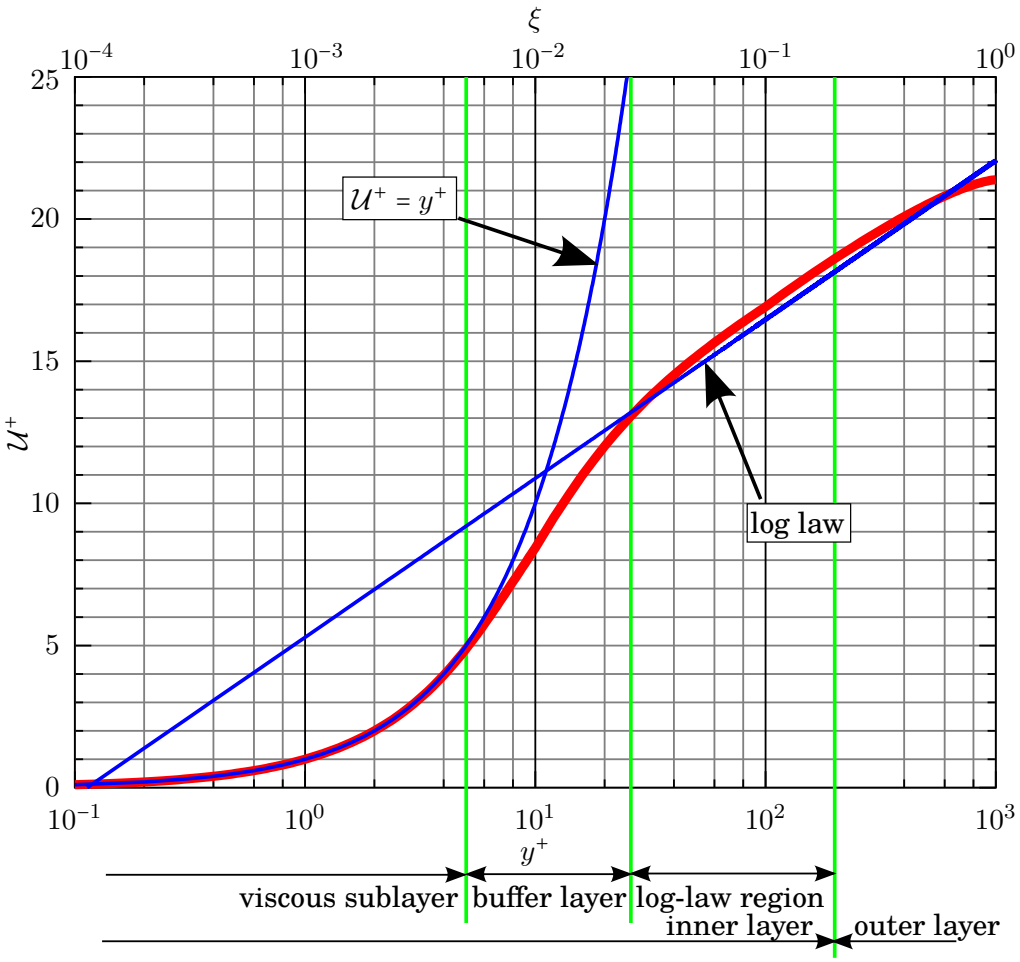

Figure 2.4: Law-of-the-wall with mixing length model. ξ is the height ratio of the flow.

In this layer,

$$\mathcal{U}^+ = y^+ \tag{2.25}$$

$$y^+ = \frac{yU_\tau}{\nu} \tag{2.26}$$

$$U_\tau = \sqrt{\frac{\tau_w}{\rho}} \tag{2.27}$$

$$\mathcal{U}^+ = \frac{U}{U_\tau} \tag{2.28}$$

where

- y^+ is the non-dimensional distance to the wall.
- y the distance to the wall.
- U_τ is the friction velocity.
- τ_w is the wall shear stress
- U^+ is the dimensionless velocity.
- U is the velocity tangent to the wall.

In the buffer layer ($5 \leq y^+ \leq 30$) neither the $\mathcal{U}^+ = y^+$ nor the logarithmic-law (defined in the next paragraph) can be applied. This very accurate approach which does not require any further modeling demands extreme computational resources. An estimation of this cost has been given by Choi & Moin [Choi 2012] showing to scale with $Re^{13/7}$ and reaching almost the requirements for a DNS computation $Re^{9/4}$.

(2) Wall modeled LES

In this approach the resolution of the small length scales in the inner boundary layer and the flow gradients at the viscous sublayer are not carried out and are considered in a Reynolds-averaged sense. Their contributions are modeled and the outer boundary layer, where the length scales are larger, is resolved instead. The first node, close to the wall, is placed in the logarithmic region of the turbulent boundary layer at a wall unit $30 \leq y^+ \leq 200$ (logarithmic-law region). Several wall modeling approaches of the inner layer have been analyzed by Piomelli & Balaras [Piomelli 2002]. The most common one is the computation of the wall shear stress by the wall model (using flow variables from the LES flow field and a law-of-the-wall, frequently analytical) and the transfer of the flow quantities to the LES solver. In general, one uses conventional wall laws based on the local equilibrium assumption, mimicking the behavior of a zero pressure gradient boundary layer following the log-law. The problem is locally reformulated into finding the wall friction velocity, which can be expressed this time

as:

$$U^+ = \frac{1}{\kappa_v} \ln(y^+) + B \tag{2.29}$$

where κ_v is the von Kármán constant and B is a constant whose value is generally set to 5.25. This approach reaches its limits when simulating boundary layers with non-zero pressure gradient. Yet, in the diverging part of the nozzle an APG is present and the application of conventional laws might give poor results. The cost of the wall modeled approach was calculated in [Choi 2012] to scale only with Re, highlighting the significant gains compared to the wall-resolved approach. Table 2.1 shows an estimation of the number of mesh points needed for wall resolved and wall modeled LES as a function of the Reynolds number.

Re_c	N_{wm} (wall-modeled LES)	N_{wr} (wall-resolved LES)
10^6	3.63×10^7	5.23×10^7
10^7	8.20×10^8	7.76×10^9
10^8	9.09×10^9	5.98×10^{11}
10^9	9.26×10^{10}	4.34×10^{13}

Table 2.1: Approximate number of grid points required for the simulation of flow over an airfoil without separation, using wall-modeled and wall-resolved LES. $Re_c = u_c c/\nu$ were c is the chord length. Results extracted from Choi & Moin [Choi 2012].

In this thesis, a wall modeled LES approach is retained for the LES computations described in chapter 4. The conventional wall law, that might give poor results due to the presence of an APG in the nozzle diverging part, is replaced by the Simple Integrated Boundary Layer Equations (SIBLE) wall law proposed by Chedevergne [Chedevergne 2010]. The resolution process consists in the resolution of a system of one-dimension boundary layer equations on each wall-cell. A recurrence procedure allows the numerical integration of the system. The closure of the system is ensured by choosing an eddy viscosity formulation based on a mixing length model. Each wall-cell is discretized in the direction normal to the wall into N nodes using a geometrical series with a constant ratio r. The reader is invited to read the article [Chedevergne 2010] for more details regarding the numerical resolution process of the wall model.

2.3.3 Parameters of the computations

The last part of this section describes the spatial and the temporal schemes and the thermodynamic properties of the flow used during the RANS and the LES computations. Regarding the spatial scheme, the same parameters are chosen for the RANS and the LES

computations. Indeed a second order spatial scheme is used as it was the most accurate available at the beginning of the thesis[2].

2.3.3.1 Spatial scheme

The resolution of the Navier-Stokes equations 2.4 requires a spatial discretization method which needs to be conservative. In the solver CEDRE, the Finite Volume Method (FVM) is used. The fluid domain is divided into small volumes whose sizes are defined by the smallest fluctuations of interest. One can distinguish between conservative quantities (momentum, energy by unit volume, etc.) and primitive variables (velocity, pressure, temperature). In the solver, the flux balance from all the faces of a cell is treated with conservative variables. A cell-centered formulation is retained (computed conservative variables are located at the center of the cells) rather than a vertex-centered formulation (computed conservative variables are located at the nodes of the cells). In order to obtain the velocity at the center of the cell, a Green method described in [Bertier 2006] is retained. After that, the computation of the hyperbolic flux (Euler flux containing the advection terms and the compressibility effects) at the cell faces is possible using a second order Monotonic Upstream Schemes for Conservation Laws (MUSCL) widely used in fluid mechanics. An ODFI flux scheme is retained for the computations. It corresponds to a Riemann solver or Flux Difference Splitting (FDS) based on the resolution of a linearized Riemann problem (see Eq. 2.30) where the intermediate state $\boldsymbol{U}(x,t)$ is evaluated as an arithmetic mean.

$$\begin{cases} \dfrac{\partial \boldsymbol{U}}{\partial t} + \boldsymbol{A}\dfrac{\partial \boldsymbol{U}}{\partial x} = 0 \\ \boldsymbol{U}(x,t) = \dfrac{\boldsymbol{U}_L + \boldsymbol{U}_R}{2} \end{cases} \tag{2.30}$$

where $\boldsymbol{A}$ is a linearized and diagonalizable matrix with real eigenvalues and the subscripts $()_L$ and $()_R$ refer respectively to the left and right value. $\boldsymbol{A}$ is in fact the Jacobian matrix associated to the normal projection of the Euler hyperbolic flux on a cell face. $\boldsymbol{U}$ is the velocity vector. Finally, the dissipative flux, which contains the viscous stresses and the heat transfer, is obtained by a simple centered scheme.

2.3.3.2 Temporal scheme

Regarding the temporal scheme, two different schemes are used for the RANS and the LES computations. Writing $\Delta t = t^{n+1} - t^n$, one can distinguish an explicit scheme for which the solution at the time step $n+1$ only depends on the solution at n, and an implicit scheme for which the solution at $n+1$ results from an iterative process.

[2] Recently, higher order spatial scheme (4^{th} order) have been implemented in the solver CEDRE.

- For the LES, an explicit temporal scheme is required for the application at the boundaries of the non-reflecting boundary conditions (NSCBC) [Poinsot 1992, Selle 2004, Yoo 2005, Lodato 2008] recently implemented in the 3D solver CEDRE (see Appendix A for additional details). It has been shown by Kaufmann *et al.* [Kaufmann 2002] that acoustic of entropy fluctuations can be injected through these boundaries conditions. In the solver, two approximations or three approximations Runge-Kutta schemes, denoted respectively as RK2 and RK3, are available [Butcher 1996]. It was observed that the gain in terms of accuracy using the RK3 rather than the RK2 is not worthwhile the time spent for one iteration. As a consequence, the RK2 scheme is chosen instead. An explicit scheme is stable only if the Courant-Friedrichs-Lewy (CFL) is smaller than a given limit depending on the scheme at hand. This condition can be expressed in 1D as:

$$\Delta t < CFL_{max} \frac{\Delta x}{|\boldsymbol{U}| + C} \tag{2.31}$$

  where Δx is the mesh size. In general, the CFL can not be larger than 1. However, for the RK2 scheme used during this work, this theoretical number is even reduced to 0.5.

- For the RANS, an implicit θ-scheme is preferred as the aim is to obtain a steady solution with a large time step. The value of θ is fixed at 1 which corresponds to a Euler scheme. This approach allows the possibility to override the CFL requirement for the time step with the condition to perform enough sub-iterations between each time step to ensure a satisfactory convergence of the fluxes. Finally, the iterative resolution of the linear system is achieved by the use of a Generalized Minimal Residual Method (GMRES) developed by Saad & Schultz [Saad 1986].

2.3.3.3 Thermodynamic properties of the considered flow

In this work, a small portion of the combustion chamber (1/3 of the total length) is considered. Is it assumed that this region is not in the reaction zone. Therefore, only air is considered for the numerical computations. It is assumed to be a perfect gas where the interactions between the molecules are ignored. The specific heat capacity at constant pressure for air is evaluated in a polynomial form depending on the temperature:

$$c_p(T) = \sum_{k=0}^{n} a_k \left(\frac{T}{T_0}\right)^k \tag{2.32}$$

where $T_0 = 1000$ K is a temperature scale. For the numerical computation, $n = 7$ and the coefficients a_k ($\mathrm{J.mol^{-1}.K^{-1}}$) are given in the Table 2.2. In addition, the specific enthalpy and entropy for a perfect modeled gas are directly deduced by integration from a reference

a_k	Value ($\mathrm{J.mol^{-1}.K^{-1}}$)
a_0	30.654884
a_1	−15.230388
a_2	43.949342
a_3	−42.747854
a_4	21.632853
a_5	−6.0749147
a_6	0.89733242
a_7	−0.054422652

Table 2.2: Values of the a_k coefficients.

state giving:

$$\begin{cases} h(T) = h_{ref} + \int_{T_{ref}}^{T} C_p(T)dT \\ s(T) = s_{ref} + \int_{T_{ref}}^{T} \dfrac{C_p(T)}{T}dT \end{cases} \tag{2.33}$$

and $0\ \mathrm{K} \leq T \leq 4000\ \mathrm{K}$. The entropy fluctuations are computed from the unsteady and mean quantities assuming a linearized expression:

$$\frac{s'}{C_p} = \frac{T'}{T_0} - \frac{\gamma_0 - 1}{\gamma_0}\frac{P'}{P_0} \tag{2.34}$$

Regarding the transport properties, the dynamic viscosity has already been defined in Eq. 2.6 using the Sutherland law. For the specific thermal conductivity (λ), the Eucken equation for heat conductivity is applied to provide:

$$\lambda = \mu\left[C_p(T) + \frac{5\mathcal{R}}{4\mathcal{M}}\right] \tag{2.35}$$

For $T = 300\mathrm{K}$, $\mu = 1.856 \times 10^{-5}\ \mathrm{kg.m^{-1}.s^{-1}}$, $\mathcal{M}$ is the molar mass of air fixed at 2.8965161×10^{-2} $\mathrm{kg.mol^{-1}}$ and $\mathcal{R} = 8.314472\ \mathrm{J.mol^{-1}.K^{-1}}$. The thermodynamic properties used during the numerical computations are summarized in Table 2.3.

Variable	Value	Unit
Reference enthalpy: h_{ref}	−125.53	$\mathrm{J.mol^{-1}}$
Reference entropy: s_{ref}	198.822	$\mathrm{J.K^{-1}.mol^{-1}}$

Table 2.3: Thermodynamic properties of air.

Chapter 3

Development of a two-dimensional axisymmetric semi-analytical model for estimating ICN in nozzle flows

If you can't explain it simply, you don't understand it well enough.

Albert Einstein

Contents

Now that the tools used during this PhD thesis have been presented, it is time to get straight to the heart of the matter of this thesis. In chapter 1, entropy wave distortion was briefly mentioned. Such a distortion can be observed in numerical simulations and originates from the variable acceleration profile in the nozzle as one goes from the centerline to the

outer wall. Even if this distortion is difficult to measure in experiments, it can reasonably be assumed as real. In order to take this phenomenon into account, the radial evolution of the convected entropy front through the nozzle must be incorporated. The model proposed here combines a 2D modeling of the entropy fluctuations, with longitudinal and radial dependencies, and a 1D acoustic propagation. This last assumption is justified by the fact that the transverse acoustic modes of the nozzle are associated with frequencies that are well beyond the spectral region of interest. This model needs mean flow profiles either analytical or extracted from a CFD computation. This model was presented during the 21st AIAA/CEAS Aeroacoustics Conference [Zheng 2015]. *The following chapter is divided into three sections. The hypotheses of validity of this model are first introduced. Then, the set of equations is detailed. Finally, its implementation is described and the methodology of the resolution process is given.*

3.1 Hypotheses of the semi-analytical model

Configurations showing a cylindrical symmetry are considered in the present section. In what follows, the axis of symmetry is the x-axis. Five major assumptions are used to develop this ICN model.

- The Euler equations are used, neglecting all the viscous terms.
- The turbulent fluctuations are neglected.
- The swirl is also neglected.
- All the flow variables are supposed to be axisymmetric with longitudinal and radial dependencies (the flow is axisymmetric along the x-direction).
- Acoustic fluctuations are considered one-dimensional along the nozzle. Indeed, radial modes are neglected as they are cut off at low frequencies.

Chu & Kovásznay's [Chu 1958] decomposition of the modes of fluctuations in the flow is used. Only first order coupling terms are considered in which the entropy mode is supposed to be isobaric (P'_e=0). For each flow variable, $()_0$ and $()'$ respectively refer to the mean value and the fluctuating part. In addition the density fluctuating part is also decomposed as an entropic and an acoustic parts denoted respectively as $()'_e$ and $()'_a$ giving $\rho' = \rho'_e + \rho'_a$. The linearized entropy relation writes:

$$\frac{s'}{C_p} = \frac{P'_a}{\gamma P_0} - \frac{\rho'}{\rho_0} \tag{3.1}$$

Thus,

$$\frac{\rho'_e}{\rho_0} = \frac{-s'}{C_p} \tag{3.2}$$

$$\frac{\rho'_a}{\rho_0} = \frac{P'_a}{\gamma P_0} \tag{3.3}$$

Since acoustic fluctuations are purely along the x-direction, it gives $u'_r = 0$ or $u_r = u_{0r}$. In addition, ${P_a}'$ and u'_x are also considered to be 1D giving $u_x = u_{0x} + u'_x$ and $P = P_0 + {P_a}'$.
One can remark that even if P'_a is uniform in a given section, this does not imply that ρ'_a is also uniform as the mean flow variables can evolve with the radial position. In addition, a sectional mean integration formula is used to reduce the radial dependent flow variables to 1D quantities. The integration is performed as follows:

$$\overline{f} = \frac{1}{A_x} \int_{A_x} f dA \tag{3.4}$$

where A_x stands for the cross section area at a given x-position. This yields for the axial mean velocity and the acoustic pressure fluctuation:

$$\overline{u'_x} = u'_x \text{ and } \overline{P'_a} = {P_a}' \tag{3.5}$$

since both variables are assumed to show no radial dependency.

3.2 2D set of equations

As presented in the state of the art, a distortion of the entropy wave can be observed in numerical simulations and originates from the variable acceleration profile in the nozzle as one goes from the centerline to the outer wall. The current one-dimensional models assume a mean flow uniform over the cross-section therefore the application to geometries representative of aero engine nozzles where important radial flow distortions may occur is very limited. In order to take this distortion phenomenon into account, a radial evolution of the convected entropy is introduced in the equations. This radial evolution of the entropy can be computed numerically from the mean flow velocities.

3.2.1 Presentation of the coordinate systems and of the Jacobian matrix

The objective of the present method being to take into account the deformation of the entropy perturbation due to the heterogeneous radial velocity profile, it is convenient to work with a local set of equations rather than a global coordinate system.

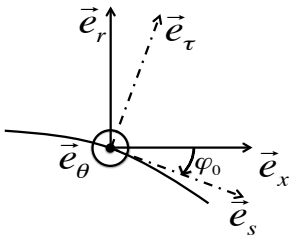

Figure 3.1: Local coordinate system $(\vec{e_x}, \vec{e_r}, \vec{e_\theta})$, particle coordinate system along a streamline $(\vec{e_s}, \vec{e_\tau}, \vec{e_\theta})$.

The coordinate system shown in Fig. 3.1 is used. $(\vec{e_s}, \vec{e_\tau}, \vec{e_\theta})$ is simply a rotation of an angle $\varphi_0(s,\tau)$ around the $\vec{e_\theta}$ axis of the original coordinate system $(\vec{e_x}, \vec{e_r}, \vec{e_\theta})$. $\vec{e_\theta}$ remains the same between the two coordinate systems. The idea is to take into account the curvature effect on the flow. For purposes of brevity $\varphi_0(s,\tau)$ is denoted as φ_0. In the $(\vec{e_s}, \vec{e_\tau}, \vec{e_\theta})$ coordinate system, the vectors $\vec{e_s}$ and $\vec{e_\tau}$ can be decomposed as:

$$\begin{cases} \vec{e_x} = \cos\varphi_0 \vec{e_s} + \sin\varphi_0 \vec{e_\tau} \\ \vec{e_r} = -\sin\varphi_0 \vec{e_s} + \cos\varphi_0 \vec{e_\tau} \end{cases} \tag{3.6}$$

so that

$$\begin{cases} x = \cos\varphi_0 s + \sin\varphi_0 \tau \\ r = -\sin\varphi_0 s + \cos\varphi_0 \tau \end{cases} \tag{3.7}$$

The chain rule derivation gives:

$$\begin{pmatrix} \dfrac{\partial}{\partial s} \\ \dfrac{\partial}{\partial \tau} \end{pmatrix} = \underbrace{\begin{bmatrix} \dfrac{\partial x}{\partial s} & \dfrac{\partial r}{\partial s} \\ \dfrac{\partial x}{\partial \tau} & \dfrac{\partial r}{\partial \tau} \end{bmatrix}}_{\boldsymbol{J}} \begin{pmatrix} \dfrac{\partial}{\partial x} \\ \dfrac{\partial}{\partial r} \end{pmatrix} \tag{3.8}$$

Keeping in mind that φ_0 is a function of s and τ, the Jacobian matrix J can be expressed as:

$$J = \begin{bmatrix} \cos\varphi_0 + r\dfrac{\partial\varphi_0}{\partial s} & -\sin\varphi_0 - x\dfrac{\partial\varphi_0}{\partial s} \\ \sin\varphi_0 + r\dfrac{\partial\varphi_0}{\partial \tau} & \cos\varphi_0 - x\dfrac{\partial\varphi_0}{\partial \tau} \end{bmatrix} = \begin{bmatrix} J_{11} & J_{12} \\ J_{21} & J_{22} \end{bmatrix} \tag{3.9}$$

Now that the Jacobian matrix and the coordinate systems have been introduced, the set of equations used for this two-dimensional model have to be expressed. The original approach presented here is to use equations commonly used in turbomachinery and to apply them for a nozzle flow. The streamlines curvature method of the Radial-Equilibrium proposed

by Smith [Smith 1966] and Novak [Novak 1967] is used to provide the momentum equations while the conservation of mass flux in the cylindrical coordinate system provides the continuity part of the system.

3.2.2 Continuity equation

Considering an infinitesimal volume $V = A_x dx$, the mass variation in V can be rewritten as the difference between the mass flux entering the domain and the one leaving it, giving:

$$\frac{\partial}{\partial t}\int_V \rho dV = \int_{A_x} [\rho u_x](x) dA \; - \int_{A_{x+dx}} [\rho u_x](x+dx) dA \tag{3.10}$$

The right-hand side terms can be rewritten using Eq. 3.4 as:

$$\int_{A_x} [\rho u_x](x) dA \; - \int_{A_{x+dx}} [\rho u_x](x+dx) dA = [A_x \overline{\rho u_x}](x) - [A_x \overline{\rho u_x}](x+dx) \tag{3.11}$$

Thus Eq. 3.10 can be rewritten in a surface integral form as:

$$\frac{\partial}{\partial t}\int_{A_x} \rho dA dx = -([A_x \overline{\rho u_x}](x+dx) - [A_x \overline{\rho u_x}](x)) \tag{3.12}$$

or

$$\frac{\partial}{\partial t}\int_{A_x} \rho dA = -\frac{\partial A_x \overline{\rho u_x}}{\partial x} \tag{3.13}$$

Applying Eq. 3.4 to the left-hand side of the previous equation, developing the right-hand side term and dividing all the terms by A_x finally yields:

$$\frac{\partial \overline{\rho}}{\partial t} + \frac{\partial \overline{\rho u_x}}{\partial x} \;\; = \;\; -\frac{1}{A_x}\overline{\rho u_x}\frac{dA_x}{dx} \tag{3.14}$$

The previous equation being now decomposed as a sum of a mean and a fluctuating part $\rho = \rho_0 + \rho'$ and $u_x = u_{0x} + u'_x$, the equation becomes to first order:

$$\frac{\partial \overline{\rho'}}{\partial t} + \frac{\partial \overline{\rho_0 u_{0x}}}{\partial x} + \frac{\partial \overline{\rho_0 u'_x}}{\partial x} + \frac{\partial \overline{\rho' u_{0x}}}{\partial x} = -\frac{1}{A_x}\overline{\rho_0 u_{0x}}\frac{dA}{dx} - \frac{1}{A_x}(\overline{\rho_0 u'_x} + \overline{\rho' u_{0x}})\frac{dA}{dx} \tag{3.15}$$

Using the mass conservation equation on the mean flow, the second term of the left-hand side cancels with the first term of the right-hand side, thus:

$$\frac{\partial \overline{\rho'}}{\partial t} + \frac{\partial \overline{\rho_0 u'_x}}{\partial x} + \frac{\partial \overline{\rho' u_{0x}}}{\partial x} = -\frac{1}{A_x}(\overline{\rho_0 u'_x} + \overline{\rho' u_{0x}})\frac{dA}{dx} \tag{3.16}$$

Using Eq. 3.5, the previous equation becomes:

$$\frac{\partial\overline{\rho'}}{\partial t}+\overline{\rho_0}\frac{\partial u_x'}{\partial x}+u_x'\frac{\partial\overline{\rho_0}}{\partial x}+\frac{\partial\overline{\rho' u_{0x}}}{\partial x}=-\frac{1}{A_x}(\overline{\rho_0}u_x'+\overline{\rho' u_{0x}})\frac{dA}{dx} \tag{3.17}$$

The terms $\frac{\partial\overline{\rho'}}{\partial t}$ and $\overline{\rho' u_{0x}}$ can be written using Eqs. 3.2 and 3.3 as:

$$\frac{\partial\overline{\rho'}}{\partial t}=-\frac{\partial}{\partial t}\overline{\left(\rho_0\frac{s'}{C_p}\right)}+\overline{\left(\frac{\rho_0}{\gamma P_0}\right)}\frac{\partial {P_a}'}{\partial t} \tag{3.18}$$

$$\overline{\rho' u_{0x}}=\overline{\rho_e' u_{0x}}+\overline{\rho_a' u_{0x}}=-\overline{\left(\rho_0 u_{0x}\frac{s'}{C_p}\right)}+\overline{\left(\frac{\rho_0 u_{0x}}{\gamma P_0}\right)}{P_a}' \tag{3.19}$$

Differentiating the previous equation over x gives:

$$\begin{aligned}\frac{\partial\overline{\rho' u_{0x}}}{\partial x} &= -\frac{\partial}{\partial x}\overline{\left(\rho_0 u_{0x}\frac{s'}{C_p}\right)}+\frac{\partial}{\partial x}\left[\overline{\left(\frac{\rho_0 u_{0x}}{\gamma P_0}\right)}{P_a}'\right] &(3.20)\\ &= -\frac{\partial}{\partial x}\overline{\left(\rho_0 u_{0x}\frac{s'}{C_p}\right)}+\overline{\left(\frac{\rho_0 u_{0x}}{\gamma P_0}\right)}\frac{\partial {P_a}'}{\partial x}+{P_a}'\frac{\partial}{\partial x}\overline{\left(\frac{\rho_0 u_{0x}}{\gamma P_0}\right)} &(3.21)\end{aligned}$$

Finally Eq. 3.17 becomes using Eqs. 3.18 and 3.21:

$$\begin{aligned}&-\overline{\rho_0\frac{\partial}{\partial t}\left(\frac{s'}{C_p}\right)}+\overline{\left(\frac{\rho_0}{\gamma P_0}\right)}\frac{\partial {P_a}'}{\partial t}+\overline{\rho_0}\frac{\partial u_x'}{\partial x}+u_x'\frac{\partial\overline{\rho_0}}{\partial x}-\frac{\partial}{\partial x}\overline{\left(\rho_0 u_{0x}\frac{s'}{C_p}\right)}+\overline{\left(\frac{\rho_0 u_{0x}}{\gamma P_0}\right)}\frac{\partial {P_a}'}{\partial x}\\ &+{P_a}'\frac{\partial}{\partial x}\overline{\left(\frac{\rho_0 u_{0x}}{\gamma P_0}\right)}=-\frac{1}{A_x}\overline{\rho_0}u_x'\frac{dA}{dx}+\frac{1}{A_x}\overline{\left(\rho_0 u_{0x}\frac{s'}{C_p}\right)}\frac{dA}{dx}-\frac{1}{A_x}{P_a}'\overline{\left(\frac{\rho_0 u_{0x}}{\gamma P_0}\right)}\frac{dA}{dx}\end{aligned} \tag{3.22}$$

This can be rewritten as:

$$\begin{aligned}&\left[\frac{\partial\overline{\rho_0}}{\partial x}+\frac{\overline{\rho_0}}{A_x}\frac{dA}{dx}\right]u_x'+\overline{\rho_0}\frac{\partial u_x'}{\partial x}+\left[\frac{1}{A_x}\overline{\left(\frac{\rho_0 u_{0x}}{\gamma P_0}\right)}\frac{dA}{dx}+\frac{\partial}{\partial x}\overline{\left(\frac{\rho_0 u_{0x}}{\gamma P_0}\right)}\right]{P_a}'\\ &+\left[\overline{\left(\frac{\rho_0}{\gamma P_0}\right)}\frac{\partial}{\partial t}+\overline{\left(\frac{\rho_0 u_{0x}}{\gamma P_0}\right)}\frac{\partial}{\partial x}\right]{P_a}'=\frac{1}{A_x}\overline{\left(\rho_0 u_{0x}\frac{s'}{C_p}\right)}\frac{dA}{dx}+\frac{\partial}{\partial x}\overline{\left(\rho_0 u_{0x}\frac{s'}{C_p}\right)}+\frac{\partial}{\partial t}\overline{\left(\rho_0\frac{s'}{C_p}\right)}\end{aligned} \tag{3.23}$$

or in a factorized form, by multiplying by the surface section A_x and using the relation $c_0^2=\frac{\gamma P_0}{\rho_0}$:

$$A_x\overline{\left(\frac{1}{c_0^2}\right)}\frac{\partial {P_a}'}{\partial t}+\frac{\partial}{\partial x}\left[A_x\overline{\left(\frac{u_{0x}}{c_0^2}\right)}{P_a}'\right]+\frac{\partial(A_x\overline{\rho_0}u_x')}{\partial x}=\frac{\partial}{\partial x}\left[A_x\overline{\left(\rho_0 u_{0x}\frac{s'}{C_p}\right)}\right]+A_x\frac{\partial}{\partial t}\overline{\left(\rho_0\frac{s'}{C_p}\right)} \tag{3.24}$$

3.2.3 Momentum equation

The momentum equation can be written using the local polar system $(\overrightarrow{e_s}, \overrightarrow{e_\tau}, \overrightarrow{e_\theta})$ from the streamlines curvature method of the Radial-Equilibrium [Smith 1966, Novak 1967]. The equation of motion can be expressed using the variables (s, τ, θ) represented in Fig. 3.2 as:

$$\begin{aligned}\frac{\partial \rho r u_s}{\partial t} + \frac{1}{r}\frac{\partial \rho r u_s u_\theta}{\partial \theta} + \frac{\partial \rho r u_s^2}{\partial s} + \frac{\partial \rho r u_s u_\tau}{\partial \tau} - \rho\left(u_\theta^2 + \omega^2 r^2 + 2\omega r u_\tau\right)\sin\varphi + 2\rho r u_\tau u_s K_s \\ -\rho r K_\tau\left(u_\tau^2 - u_s^2\right) = -r\frac{\partial P}{\partial s} + \frac{1}{r}\frac{\partial r\varepsilon_{s\theta}}{\partial \theta} + \frac{\partial r\varepsilon_{ss}}{\partial s} + \frac{\partial r\varepsilon_{s\tau}}{\partial \tau} - \varepsilon_{\theta\theta}\sin\varphi + rK_\tau\left(\varepsilon_{ss} - \varepsilon_{\tau\tau}\right) \\ + rK_s\left(\varepsilon_{s\tau} + \varepsilon_{\tau s}\right)\end{aligned} \tag{3.25}$$

$$\begin{aligned}\frac{\partial \rho r u_\tau}{\partial t} + \frac{1}{r}\frac{\partial \rho r u_\tau u_\theta}{\partial \theta} + \frac{\partial \rho r u_s u_\tau}{\partial s} + \frac{\partial \rho r u_\tau^2}{\partial \tau} - \rho\left(u_\theta^2 + \omega^2 r^2 + 2\omega r u_\tau\right)\cos\varphi + 2\rho r u_\tau u_s K_\tau \\ -\rho r K_s\left(u_s^2 - u_\tau^2\right) = -r\frac{\partial P}{\partial \tau} + \frac{1}{r}\frac{\partial r\varepsilon_{\tau\theta}}{\partial \theta} + \frac{\partial r\varepsilon_{\tau s}}{\partial s} + \frac{\partial r\varepsilon_{\tau\tau}}{\partial \tau} - \varepsilon_{\theta\theta}\cos\varphi + rK_s\left(\varepsilon_{\tau\tau} - \varepsilon_{ss}\right) \\ + rK_\tau\left(\varepsilon_{\tau s} + \varepsilon_{s\tau}\right)\end{aligned} \tag{3.26}$$

$$\begin{aligned}\frac{\partial \rho r u_\theta}{\partial t} + \frac{1}{r}\frac{\partial \rho r u_\theta^2}{\partial \theta} + \frac{\partial \rho r u_s u_\theta}{\partial s} + \frac{\partial \rho r u_\tau u_\theta}{\partial \tau} + \rho\left(u_\theta u_\tau + 2\omega r u_\tau\right)\cos\varphi + \rho\left(u_\theta u_s + 2\omega r u_s\right)\sin\varphi \\ +\rho r u_\theta\left(u_s K_\tau + u_\tau K_s\right) = -\frac{\partial P}{\partial \theta} + \frac{1}{r}\frac{\partial r\varepsilon_{\theta\theta}}{\partial \theta} + \frac{\partial r\varepsilon_{\theta s}}{\partial s} + \frac{\partial r\varepsilon_{\theta\tau}}{\partial \tau} + \varepsilon_{s\theta}\sin\varphi + \varepsilon_{\tau\theta}\cos\varphi \\ + r\left(\varepsilon_{\theta s}K_\tau + \varepsilon_{\theta\tau}K_s\right)\end{aligned} \tag{3.27}$$

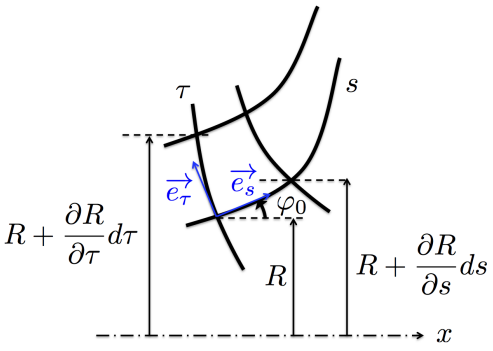

Figure 3.2: Schematic view of the streamlines curvature method.

K_s and K_τ are respectively the tangent and the normal curvatures defined as the fol-

lowing:

$$\begin{cases} K_s = \dfrac{1}{r_s} = \dfrac{\partial \varphi_0}{\partial s} \\ K_\tau = \dfrac{1}{r_\tau} = \dfrac{\partial \varphi_0}{\partial \tau} \end{cases} \tag{3.28}$$

where r_s and r_τ are respectively the radius curvatures over s and τ. ω is the angular velocity of the blade raw, in our case since no blades are present so that $\omega = 0$. $\varepsilon_{..}$ are the terms of the Cauchy stress tensor, since there is no deformation the Cauchy stress tensor is equal to zero. With the assumption of no tangential velocity ($u_\theta = 0$) the remaining quantities are independent of θ and Eq. 3.27 vanishes allowing to rewrite Eqs. 3.25 and 3.26 as:

$$\frac{\partial \rho r u_s}{\partial t} + \frac{\partial \rho r u_s^2}{\partial s} + \frac{\partial \rho r u_s u_\tau}{\partial \tau} + 2\rho r u_\tau u_s K_s - \rho r K_\tau \left(u_\tau^2 - u_s^2\right) = -r\frac{\partial P}{\partial s} \tag{3.29}$$

$$\frac{\partial \rho r u_\tau}{\partial t} + \frac{\partial \rho r u_s u_\tau}{\partial s} + \frac{\partial \rho r u_\tau^2}{\partial \tau} + 2\rho r u_\tau u_s K_\tau - \rho r K_s \left(u_s^2 - u_\tau^2\right) = -r\frac{\partial P}{\partial \tau} \tag{3.30}$$

3.2.3.1 s-direction equation

Let us start with Eq. 3.29 first. The term $\dfrac{\partial \rho r u_s}{\partial t}$ can be expressed also as:

$$\frac{\partial \rho r u_s}{\partial t} = \rho r \frac{\partial u_s}{\partial t} + r u_s \frac{\partial \rho}{\partial t} \tag{3.31}$$

The objective is to obtain the term $\rho r \dfrac{\partial u_s}{\partial t}$. The term $r u_s \dfrac{\partial \rho}{\partial t}$ is expressed using Eq. 3.32. This equation is the local continuity equation obtained from the streamlines curvature method of the Radial-Equilibrium.

$$\frac{\partial \rho}{\partial t} + \frac{1}{r}\left[\frac{1}{r}\frac{\partial \rho r u_\theta}{\partial \theta} + \frac{\partial \rho r u_s}{\partial s} + \frac{\partial \rho r u_\tau}{\partial \tau}\right] + \rho\left(u_s K_\tau + u_\tau K_s\right) = 0 \tag{3.32}$$

The last term of Eq. 3.31 then becomes:

$$r u_s \frac{\partial \rho}{\partial t} = r u_s \left(-\frac{1}{r}\left[\frac{\partial \rho r u_s}{\partial s} + \frac{\partial \rho r u_\tau}{\partial \tau}\right] - \rho\left(u_s K_\tau + u_\tau K_s\right)\right) \tag{3.33}$$

$$= -u_s \frac{\partial \rho r u_s}{\partial s} - u_s \frac{\partial \rho r u_\tau}{\partial \tau} - \rho r u_s^2 K_\tau - \rho r u_s u_\tau K_s \tag{3.34}$$

Using 3.29 and 3.34, $\rho r\frac{\partial u_s}{\partial t}$ is then

$$\begin{aligned}\rho r\frac{\partial u_s}{\partial t} &= \frac{\partial \rho r u_s}{\partial t} - r u_s\frac{\partial \rho}{\partial t}\\ &= -\frac{\partial \rho r u_s^2}{\partial s} - \frac{\partial \rho r u_s u_\tau}{\partial \tau} - 2\rho r u_\tau u_s K_s + \rho r K_\tau\left(u_\tau^2 - u_s^2\right) - r\frac{\partial P}{\partial s} + u_s\frac{\partial \rho r u_s}{\partial s}\\ &\quad + u_s\frac{\partial \rho r u_\tau}{\partial \tau} + \rho r u_s^2 K_\tau + \rho r u_s u_\tau K_s\end{aligned} \tag{3.35}$$

noticing that

$$\frac{\partial \rho r u_s^2}{\partial s} = u_s\frac{\partial \rho r u_s}{\partial s} + \rho r u_s\frac{\partial u_s}{\partial s} \tag{3.36}$$

$$\frac{\partial \rho r u_s u_\tau}{\partial \tau} = u_s\frac{\partial \rho r u_\tau}{\partial \tau} + \rho r u_\tau\frac{\partial u_s}{\partial \tau} \tag{3.37}$$

Eq. 3.35 becomes:

$$\rho r\frac{\partial u_s}{\partial t} = -\rho r u_s\frac{\partial u_s}{\partial s} - \rho r u_\tau\frac{\partial u_s}{\partial \tau} - \rho r u_\tau u_s K_s + \rho r u_\tau^2 K_\tau - r\frac{\partial P}{\partial s} \tag{3.38}$$

or

$$\frac{\partial u_s}{\partial t} + u_s\frac{\partial u_s}{\partial s} + u_\tau\frac{\partial u_s}{\partial \tau} + u_\tau u_s K_s - u_\tau^2 K_\tau = -\frac{1}{\rho}\frac{\partial P}{\partial s} \tag{3.39}$$

Eq. 3.39 becomes, in perturbed form:

$$\begin{aligned}\frac{\partial\left(u_{0s}+u_s'\right)}{\partial t} + \left(u_{0s}+u_s'\right)\frac{\partial\left(u_{0s}+u_s'\right)}{\partial s} + u_\tau'\frac{\partial\left(u_{0s}+u_s'\right)}{\partial \tau} + u_\tau'\left(u_{0s}+u_s'\right)K_s - u_\tau'^2 K_\tau\\ = -\frac{1}{\rho_0+\rho'}\frac{\partial\left(P_0+P_a{}'\right)}{\partial s}\end{aligned} \tag{3.40}$$

or

$$\begin{aligned}\frac{\partial u_s'}{\partial t} + \left(u_{0s}+u_s'\right)\frac{\partial\left(u_{0s}+u_s'\right)}{\partial s} + u_\tau'\frac{\partial\left(u_{0s}+u_s'\right)}{\partial \tau} + u_\tau'\left(u_{0s}+u_s'\right)K_s - u_\tau'^2 K_\tau\\ + \frac{1}{\rho_0}\left(1-\frac{\rho'}{\rho_0}\right)\frac{\partial\left(P_0+P_a{}'\right)}{\partial s} = 0\end{aligned} \tag{3.41}$$

Developing and linearizing the terms gives the following equation:

$$\frac{\partial u_s'}{\partial t} + u_\tau'\frac{\partial u_{0s}}{\partial \tau} + u_{0s}\frac{\partial u_{0s}}{\partial s} + u_{0s}\frac{\partial u_s'}{\partial s} + u_s'\frac{\partial u_{0s}}{\partial s} + u_\tau' u_{0s}K_s + \frac{1}{\rho_0}\frac{\partial P_0}{\partial s} + \frac{1}{\rho_0}\frac{\partial P_a{}'}{\partial s} - \frac{\rho'}{\rho_0^2}\frac{\partial P_0}{\partial s} = 0 \tag{3.42}$$

Since the mean flow satisfies Eq. 3.39

$$\frac{\partial u_s'}{\partial t} + u_\tau' \frac{\partial u_{0s}}{\partial \tau} + u_{0s} \frac{\partial u_s'}{\partial s} + u_s' \frac{\partial u_{0s}}{\partial s} + u_\tau' u_{0s} K_s + \frac{1}{\rho_0} \frac{\partial {P_a}'}{\partial s} - \frac{\rho'}{\rho_0^2} \frac{\partial P_0}{\partial s} = 0 \tag{3.43}$$

Injecting $\rho' = -\frac{\rho_0 s'}{C_p} + \frac{\rho_0}{\gamma P_0} P_a'$ and using $c_0^2 = \frac{\gamma P_0}{\rho_0}$, it comes

$$\frac{\partial u_s'}{\partial t} + u_\tau' \frac{\partial u_{0s}}{\partial \tau} + u_{0s} \frac{\partial u_s'}{\partial s} + u_s' \frac{\partial u_{0s}}{\partial s} + u_\tau' u_{0s} K_s + \frac{1}{\rho_0} \frac{\partial {P_a}'}{\partial s} + \frac{s'}{\rho_0 C_p} \frac{\partial P_0}{\partial s} - \frac{P_a'}{\rho_0^2 c_0^2} \frac{\partial P_0}{\partial s} = 0 \tag{3.44}$$

Keeping in mind that the objective is to solve the system in the $(\vec{e_x}, \vec{e_r}, \vec{e_\theta})$ coordinate system, the projection using Eq. 3.6 and assuming $u_r' = 0$ meaning that $u_s' = u_x' \cos\varphi_0$, $u_\tau' = u_x' \sin\varphi_0$ and $u_{0s} = u_{0x} \cos\varphi_0 - u_{0r} \sin\varphi_0$, with $\varphi_0 \in \left]-\frac{\pi}{2}; \frac{\pi}{2}\right[$, leads to:

$$\begin{aligned} &\frac{\partial u_x'}{\partial t} + \tan\varphi_0 u_x' \frac{\partial u_{0s}}{\partial \tau} + u_{0s} \frac{\partial u_x'}{\partial s} + \frac{u_{0s} u_x'}{\cos\varphi_0} \frac{\partial \cos\varphi_0}{\partial s} + u_x' \frac{\partial u_{0s}}{\partial s} + u_x' \tan\varphi_0 u_{0s} K_s \\ &\quad + \frac{1}{\rho_0 \cos\varphi_0} \frac{\partial {P_a}'}{\partial s} + \frac{s'}{\rho_0 C_p \cos\varphi_0} \frac{\partial P_0}{\partial s} - \frac{P_a'}{\rho_0^2 c_0^2 \cos\varphi_0} \frac{\partial P_0}{\partial s} = 0 \end{aligned} \tag{3.45}$$

The terms $\frac{\partial u_x'}{\partial s}$ and $\frac{\partial {P_a}'}{\partial s}$ are then projected in the $(\vec{e_x}, \vec{e_r}, \vec{e_\theta})$ coordinate system using the Jacobian matrix (Eq. 3.9).

$$\begin{aligned} \frac{\partial u_x'}{\partial s} &= \left(\frac{\partial u_x'}{\partial x} \times J_{11} + \frac{\partial u_x'}{\partial r} \times J_{12} \right) \\ &= \left(\frac{\partial u_x'}{\partial x} \times J_{11} \right) = \left(\cos\varphi_0 + r \frac{\partial \varphi_0}{\partial s} \right) \frac{\partial u_x'}{\partial x} \end{aligned} \tag{3.46}$$

and

$$\begin{aligned} \frac{\partial {P_a}'}{\partial s} &= \left(\frac{\partial {P_a}'}{\partial x} \times J_{11} + \frac{\partial {P_a}'}{\partial r} \times J_{12} \right) \\ &= \left(\frac{\partial {P_a}'}{\partial x} \times J_{11} \right) = \left(\cos\varphi_0 + r \frac{\partial \varphi_0}{\partial s} \right) \frac{\partial {P_a}'}{\partial x} \end{aligned} \tag{3.47}$$

$\frac{\partial {P_a}'}{\partial \tau}$ is also projected in the $(\vec{e_x}, \vec{e_r}, \vec{e_\theta})$ coordinate system (this term is used in τ-direction equation) giving

$$\begin{aligned} \frac{\partial {P_a}'}{\partial \tau} &= \left(\frac{\partial {P_a}'}{\partial x} \times J_{21} + \frac{\partial {P_a}'}{\partial r} \times J_{22} \right) \\ &= \left(\frac{\partial {P_a}'}{\partial x} \times J_{21} \right) = \left(\sin\varphi_0 + r \frac{\partial \varphi_0}{\partial \tau} \right) \frac{\partial {P_a}'}{\partial x} \end{aligned} \tag{3.48}$$

Eq. 3.45 therefore rewrites:

$$\begin{aligned}\frac{\partial u_x'}{\partial t}+\tan\varphi_0 u_x'\frac{\partial u_{0s}}{\partial \tau}+u_{0s}\left(\cos\varphi_0+r\frac{\partial\varphi_0}{\partial s}\right)\frac{\partial u_x'}{\partial x}-\frac{u_{0s}u_x'}{\cos\varphi_0}\sin\varphi_0\frac{\partial\varphi_0}{\partial s}+u_x'\frac{\partial u_{0s}}{\partial s}\\ +u_x'\tan\varphi_0 u_{0s}K_s+\frac{1}{\rho_0\cos\varphi_0}\left(\cos\varphi_0+r\frac{\partial\varphi_0}{\partial s}\right)\frac{\partial {P_a}'}{\partial x}-\frac{P_a'}{\rho_0^2c_0^2\cos\varphi_0}\frac{\partial P_0}{\partial s}=-\frac{s'}{\rho_0 C_p\cos\varphi_0}\frac{\partial P_0}{\partial s}\end{aligned} \tag{3.49}$$

or finally

$$\begin{aligned}\frac{\partial u_x'}{\partial t}+\left[\tan\varphi_0\frac{\partial u_{0s}}{\partial\tau}-u_{0s}\tan\varphi_0\frac{\partial\varphi_0}{\partial s}+\frac{\partial u_{0s}}{\partial s}+\tan\varphi_0 u_{0s}K_s\right]u_x'\\ +u_{0s}\left(\cos\varphi_0+r\frac{\partial\varphi_0}{\partial s}\right)\frac{\partial u_x'}{\partial x}+\frac{1}{\rho_0}\left(1+\frac{r}{\cos\varphi_0}\frac{\partial\varphi_0}{\partial s}\right)\frac{\partial {P_a}'}{\partial x}-\frac{P_a'}{\rho_0^2c_0^2\cos\varphi_0}\frac{\partial P_0}{\partial s}\\ =-\frac{s'}{\rho_0 C_p\cos\varphi_0}\frac{\partial P_0}{\partial s}\end{aligned} \tag{3.50}$$

Applying the spatial averaging (Eq. 3.4), the previous equation finally becomes

$$\begin{aligned}\frac{\partial u_x'}{\partial t}+\overline{\left[\tan\varphi_0\frac{\partial u_{0s}}{\partial\tau}+\frac{\partial u_{0s}}{\partial s}\right]}u_x'+\overline{u_{0s}\left(\cos\varphi_0+r\frac{\partial\varphi_0}{\partial s}\right)}\frac{\partial u_x'}{\partial x}+\overline{\frac{1}{\rho_0}\left(1+\frac{r}{\cos\varphi_0}\frac{\partial\varphi_0}{\partial s}\right)}\frac{\partial {P_a}'}{\partial x}\\ -\overline{\frac{1}{\rho_0^2c_0^2\cos\varphi_0}\frac{\partial P_0}{\partial s}}P_a'=-\overline{\frac{s'}{\rho_0 C_p\cos\varphi_0}\frac{\partial P_0}{\partial s}}\end{aligned} \tag{3.51}$$

At this stage it is possible to solve the system since there are two unknowns (u_x' and P_a') for two Eqs. (3.24 and 3.51). However it is also interesting to express Eq. 3.52 since this additional equation can be used to check the validity of the hypotheses made on the flow and so to obtain a consistent model.

3.2.3.2 τ-direction equation

Let us work with Eq. 3.30 now. The term $\frac{\partial\rho r u_\tau}{\partial t}$ can be also expressed as:

$$\frac{\partial\rho r u_\tau}{\partial t}=\rho r\frac{\partial u_\tau}{\partial t}+r u_\tau\frac{\partial\rho}{\partial t}$$

Once again the objective is to get an expression of the term $\rho r\frac{\partial u_\tau}{\partial t}$. The term $r u_\tau\frac{\partial\rho}{\partial t}$ is obtained using Eq. 3.32, a similar approach as in 3.2.3.2 is adopted to give:

$$\frac{\partial u_\tau}{\partial t}+u_s\frac{\partial u_\tau}{\partial s}+u_\tau\frac{\partial u_\tau}{\partial\tau}+u_\tau u_s K_\tau-u_s^2K_s=-\frac{1}{\rho}\frac{\partial P}{\partial\tau} \tag{3.52}$$

Developing the linearized terms and using the decomposition mentioned in the previous section, 3.52 becomes since the mean flow satisfies Eq. 3.52:

$$\frac{\partial u'_\tau}{\partial t} + u_{0s}\frac{\partial u'_\tau}{\partial s} + u'_\tau u_{0s}K_\tau - 2u_0 u'_s K_s + \frac{1}{\rho_0}\frac{\partial P'_a}{\partial \tau} - \frac{P'_a}{\rho_0^2 c_0^2}\frac{\partial P_0}{\partial \tau} = -\frac{s'}{\rho_0 C_p}\frac{\partial P_0}{\partial \tau} \tag{3.53}$$

Projecting the previous equation in the $(\overrightarrow{e_x}, \overrightarrow{e_r}, \overrightarrow{e_\theta})$ coordinate system as in 3.2.3.1 gives:

$$\begin{aligned}\sin\varphi_0\frac{\partial u'_x}{\partial t} + u_{0s}\sin\varphi_0\frac{\partial u'_x}{\partial s} + u_{0s}u'_x\frac{\partial \sin\varphi_0}{\partial s} + u'_x\sin\varphi_0 u_{0s}K_\tau \\ -2u_0u'_x\cos\varphi_0 K_s + \frac{1}{\rho_0}\frac{\partial P'_a}{\partial \tau} - \frac{P'_a}{\rho_0^2c_0^2}\frac{\partial P_0}{\partial \tau} = -\frac{s'}{\rho_0 C_p}\frac{\partial P_0}{\partial \tau}\end{aligned} \tag{3.54}$$

Using Eq. 3.48, Eq. 3.54 therefore rewrites

$$\begin{aligned}\sin\varphi_0\frac{\partial u'_x}{\partial t} + u_{0s}\sin\varphi_0\left(\cos\varphi_0 + r\frac{\partial\varphi_0}{\partial s}\right)\frac{\partial u'_x}{\partial x} + u_{0s}u'_x\cos\varphi_0\frac{\partial\varphi_0}{\partial s} + u'_x\sin\varphi_0 u_{0s}K_\tau \\ -2u_0u'_xK_s\cos\varphi_0 + \frac{1}{\rho_0}\left(\sin\varphi_0 + r\frac{\partial\varphi_0}{\partial\tau}\right)\frac{\partial {P_a}'}{\partial x} - \frac{P'_a}{\rho_0^2c_0^2}\frac{\partial P_0}{\partial\tau} = -\frac{s'}{\rho_0C_p}\frac{\partial P_0}{\partial\tau}\end{aligned} \tag{3.55}$$

or

$$\begin{aligned}\sin\varphi_0\frac{\partial u'_x}{\partial t} + \left(u_{0s}\cos\varphi_0\frac{\partial\varphi_0}{\partial s} + u_{0s}\sin\varphi_0K_\tau - 2u_0K_s\cos\varphi_0\right)u'_x \\ +u_{0s}\sin\varphi_0\left(\cos\varphi_0 + r\frac{\partial\varphi_0}{\partial s}\right)\frac{\partial u'_x}{\partial x} + \frac{1}{\rho_0}\left(\sin\varphi_0 + r\frac{\partial\varphi_0}{\partial\tau}\right)\frac{\partial {P_a}'}{\partial x} - \frac{P'_a}{\rho_0^2c_0^2}\frac{\partial P_0}{\partial\tau} = -\frac{s'}{\rho_0C_p}\frac{\partial P_0}{\partial\tau}\end{aligned} \tag{3.56}$$

Applying the mean section formula Eq. 3.4 on Eq. 3.56 gives

$$\begin{aligned}\overline{\sin\varphi_0}\frac{\partial u'_x}{\partial t} + \overline{\left(u_{0s}\cos\varphi_0\frac{\partial\varphi_0}{\partial s} + u_{0s}\sin\varphi_0K_\tau - 2u_0K_s\cos\varphi_0\right)}u'_x \\ \overline{+u_{0s}\sin\varphi_0\left(\cos\varphi_0 + r\frac{\partial\varphi_0}{\partial s}\right)}\frac{\partial u'_x}{\partial x} + \overline{\frac{1}{\rho_0}\left(\sin\varphi_0 + r\frac{\partial\varphi_0}{\partial\tau}\right)}\frac{\partial {P_a}'}{\partial x} - \overline{\frac{1}{\rho_0^2c_0^2}\frac{\partial P_0}{\partial\tau}}P'_a = -\overline{\frac{s'}{\rho_0C_p}\frac{\partial P_0}{\partial\tau}}\end{aligned} \tag{3.57}$$

3.3 Implementation

The system to solve is composed of two equations:

$$A_x\overline{\left(\frac{1}{c_0^2}\right)}\frac{\partial {P_a}'}{\partial t} + \frac{\partial}{\partial x}\left[A_x\overline{\left(\frac{u_{0x}}{c_0^2}\right)}{P_a}'\right] + \frac{\partial(A_x\overline{\rho_0}u'_x)}{\partial x} = \frac{\partial}{\partial x}\left[A_x\overline{\left(\rho_0u_{0x}\frac{s'}{C_p}\right)}\right] + A_x\frac{\partial}{\partial t}\overline{\left(\rho_0\frac{s'}{C_p}\right)} \tag{3.24}$$

and

$$\frac{\partial u_x'}{\partial t} + \overline{\left[\tan\varphi_0 \frac{\partial u_{0s}}{\partial \tau} + \frac{\partial u_{0s}}{\partial s}\right]} u_x' + \overline{u_{0s}\left(\cos\varphi_0 + r\frac{\partial \varphi_0}{\partial s}\right)} \frac{\partial u_x'}{\partial x} + \overline{\frac{1}{\rho_0}\left(1 + \frac{r}{\cos\varphi_0}\frac{\partial \varphi_0}{\partial s}\right)} \frac{\partial {P_a}'}{\partial x} - \overline{\frac{1}{\rho_0^2 c_0^2 \cos\varphi_0}\frac{\partial P_0}{\partial s}} P_a' = -\overline{\frac{s'}{\rho_0 C_p \cos\varphi_0}\frac{\partial P_0}{\partial s}} \tag{3.51}$$

3.3.1 Harmonic regime

To numerically solve the above system Eqs. 3.24 and 3.51, it is useful to express these two equations in the frequency domain. Assuming a harmonic regime of angular frequency ω, pressure, velocity and entropy fluctuations can be expressed as:

$$u_x' = \widehat{u}(x)e^{i\omega t} \tag{3.58}$$

$$P_a{}' = \widehat{P_a}(x)e^{i\omega t} \tag{3.59}$$

$$\frac{s'}{C_p} = \widehat{\sigma}(x,r)e^{i\omega t} \tag{3.60}$$

where

$$\widehat{\sigma}(x,r) = \mathcal{S}e^{\left(-i\omega \int_{s_1}^{s} \frac{d\zeta}{\sqrt{u_{0x}^2(\zeta) + u_{0r}^2(\zeta)}}\right)} \tag{3.61}$$

with $\mathcal{S} = s'_{peak}/C_p$ the amplitude of the entropy fluctuation. With this expression, the entropy is supposed to be planar at the position of injection for a purpose of simplification. $\widehat{\sigma}(x,r)$ can be computed analytically and corresponds to the Fourier transform of the entropy fluctuation in the nozzle at the position (x,r) knowing the initial position at (x_1,r_1). Using Eqs. 3.58-3.60, Eq. 3.24 can be rewritten as:

$$\left(A_x\overline{\left(\frac{1}{c_0^2}\right)}i\omega + \frac{\partial}{\partial x}\left[A_x\overline{\left(\frac{u_{0x}}{c_0^2}\right)}\right]\right)\widehat{P_a}(x) + A_x\overline{\left(\frac{u_{0x}}{c_0^2}\right)}\frac{\partial \widehat{P_a}(x)}{\partial x} + \frac{\partial\left(A_x\overline{\rho_0}\right)}{\partial x}\widehat{u}(x) + A_x\overline{\rho_0}\frac{\partial \widehat{u}(x)}{\partial x} = \frac{\partial}{\partial x}\left[A_x\overline{(\rho_0 u_{0x}\widehat{\sigma}(x,r))}\right] + A_x i\omega\overline{(\rho_0\widehat{\sigma}(x,r))} \tag{3.62}$$

and Eq. 3.51 becomes:

$$\left[i\omega + \overline{\left(\tan\varphi_0\frac{\partial u_{0s}}{\partial \tau} + \frac{\partial u_{0s}}{\partial s}\right)}\right]\widehat{u}(x) + \overline{u_{0s}\left(\cos\varphi_0 + r\frac{\partial\varphi_0}{\partial s}\right)}\frac{\partial \widehat{u}(x)}{\partial x} + \overline{\frac{1}{\rho_0}\left(1 + \frac{r}{\cos\varphi_0}\frac{\partial\varphi_0}{\partial s}\right)}\frac{\partial \widehat{P_a}(x)}{\partial x} - \overline{\frac{1}{\rho_0^2 c_0^2\cos\varphi_0}\frac{\partial P_0}{\partial s}}\widehat{P_a}(x) = -\overline{\frac{\widehat{\sigma}(x,r)}{\rho_0\cos\varphi_0}\frac{\partial P_0}{\partial s}} \tag{3.63}$$

3.3.2 Methodology of the resolution process

Before introducing the precise resolution process, it is useful to explain the general methodology used in the study, as described in Fig. 3.3. Five steps are needed to evaluate the nozzle transfer functions using the two-dimensional model (blue box in Fig. 3.3). Each box numbered from 1 to 5 is described in this section.

(1) **Mean flow**: As mentioned in the introduction, this model uses a steady nozzle flow as an input. This steady nozzle flow can be obtained by performing a numerical simulation or generated manually. It contains all the mean flow variables expressed in Eqs. 3.62 and 3.63. However, as the entropy fluctuations are not present in the inputs, they need to be computed. These additional steps (red box in Fig. 3.3) are numbered i and ii. A method based on the streamlines generation is adopted here for computing the entropy fluctuations.

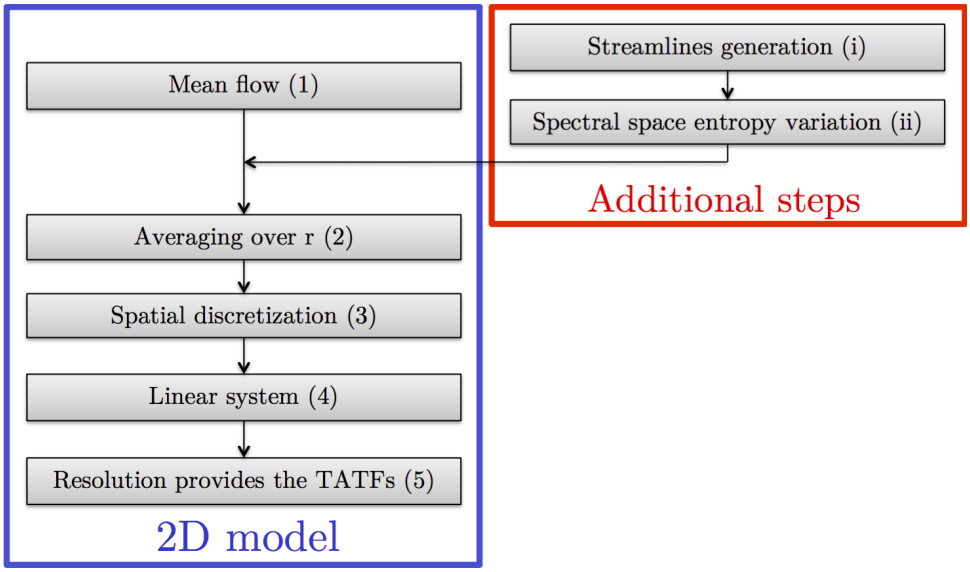

Figure 3.3: Methodology of the resolution process adopted in this PhD thesis.

(i) **Streamlines generation**: From the 2D mean flow velocity field, streamlines of the flow are generated using a temporal approach. This step is important to accurately compute the deformation of the entropy wave. A time marching method is adopted here to follow the trajectory of a particle and is used to generate a streamline. In this view, several particles are convected for different initial radial positions at the inlet of the configuration.

Those streamlines, illustrated in Fig. 3.4 (a), can be seen for each axial positions in 2D as delimiting different rings contributing differently to the ICN emitted by the nozzle.

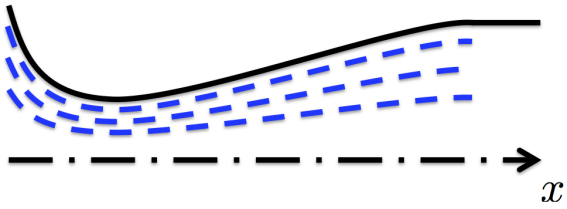

Figure 3.4: Example of three generated streamlines inside a nozzle represented in dotted blue lines. The full black line represents the external geometry of the nozzle.

(ii) **Spectral space entropy variation**: Since the velocity inside each tube is different, the convection time varies and increases as one goes from the centerline to the nozzle wall. Furthermore, by assuming a constant radial velocity between two streamlines for a given x position, the entropy fluctuations can be transported numerically using the 2D mean flow velocity. The accuracy of this approach is ensured by using enough streamlines (thus a sufficiently small radial distance Δ_r between two streamlines) to correctly predict the actual distortion occurring inside the geometry. The distortion of the entropy front is depicted by the term:

$$\int_{s_1}^{s} \frac{d\zeta}{\sqrt{u_{0x}^2(\zeta) + u_{0r}^2(\zeta)}}$$

(2) **Averaging over r**: Acoustic perturbations are supposed to be one-dimensional only, subsequently, the section averaging, Eq. 3.4, is applied at each axial position to obtain 1D flow variables depending only on the axial coordinate x. **One can notice that by doing so, the amplitude of the radially averaged entropy fluctuation differs from that obtained for one dimensional flows.**

(3) **Spatial discretization**: In order to solve the system, a spatial discretization along the axial direction of the nozzle is applied. The nozzle is divided into $n-1$ elements related to $n-1$ center points and n nodes numbered from 1 to n. As an illustration, an element is shown in Fig. 3.5. $\mathcal{F}$ represents any flow variable at the center of the element c_k and $c_1 \leq c_k \leq c_{n-1}$.

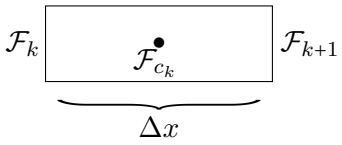

Figure 3.5: Schematic view of one element. $\mathcal{F}$ represents any flow variable at the center of the element c_k and $c_1 \leq c_k \leq c_{n-1}$.

One can assume that in a given element the term $\| u_{0s} \|$ is constant. This allows to write the expression of the phase shift of the entropy fluctuation at each element node k, where s is the curvilinear abscissa:

$$\int_{s_1}^{s_k} \frac{d\zeta}{\sqrt{u_{0x}^2(\zeta) + u_{0r}^2(\zeta)}} = \sum_{i=1}^{k-1} \frac{s_{i+1} - s_i}{\sqrt{u_{0x_{ci}}^2 + u_{0r_{ci}}^2}} \tag{3.64}$$

Assuming the element as shown in Fig. 3.5, a second order spatial discretization is used to express the values and the derivatives of the pressure and velocity perturbations at the center of the element from the values at the nodes[1]:

$$\mathcal{F}_{c_k} = \frac{\mathcal{F}_{k+1} + \mathcal{F}_k}{2} \tag{3.65}$$

$$\mathcal{F}'_{c_k} = \frac{\mathcal{F}_{k+1} - \mathcal{F}_k}{\Delta x} \tag{3.66}$$

By doing so, one can rewrite Eqs. 3.62 and 3.63 in a factorized form for the element c_k as:

$$\begin{aligned}
&\left[\frac{1}{2}\left(A_x\overline{\left(\frac{1}{c_0^2}\right)}i\omega + \frac{\partial}{\partial x}\left[A_x\overline{\left(\frac{u_{0x}}{c_0^2}\right)}\right]\right) + \frac{A_x}{\Delta x}\overline{\left(\frac{u_{0x}}{c_0^2}\right)}\right]\widehat{P_{k+1}} \\
&+\left[\frac{1}{2}\left(A_x\overline{\left(\frac{1}{c_0^2}\right)}i\omega + \frac{\partial}{\partial x}\left[A_x\overline{\left(\frac{u_{0x}}{c_0^2}\right)}\right]\right) - \frac{A_x}{\Delta x}\overline{\left(\frac{u_{0x}}{c_0^2}\right)}\right]\widehat{P_k} \\
&+\left(\frac{1}{2}\frac{\partial\left(A_x\overline{\rho_0}\right)}{\partial x} + \frac{A_x\overline{\rho_0}}{\Delta x}\right)\widehat{u_{k+1}} + \left(\frac{1}{2}\frac{\partial\left(A_x\overline{\rho_0}\right)}{\partial x} - \frac{A_x\overline{\rho_0}}{\Delta x}\right)\widehat{u_k} \\
&= \frac{\partial}{\partial x}\left[A_x\overline{(\rho_0 u_{0x}\widehat{\sigma}(x,r))}\right] + A_x i\omega\overline{(\rho_0\widehat{\sigma}(x,r))} = \widehat{S_{c_k}^C}
\end{aligned} \tag{3.67}$$

and:

$$\begin{aligned}
&\left[\frac{i\omega}{2} + \frac{1}{\Delta x}\overline{u_{0s}\left(\cos\varphi_0 + r\frac{\partial\varphi_0}{\partial s}\right)} + \frac{1}{2}\overline{\left(\tan\varphi_0\frac{\partial u_{0s}}{\partial\tau} + \frac{\partial u_{0s}}{\partial s}\right)}\right]\widehat{u_{k+1}} \\
&+\left[\frac{i\omega}{2} - \frac{1}{\Delta x}\overline{u_{0s}\left(\cos\varphi_0 + r\frac{\partial\varphi_0}{\partial s}\right)} + \frac{1}{2}\overline{\left(\tan\varphi_0\frac{\partial u_{0s}}{\partial\tau} + \frac{\partial u_{0s}}{\partial s}\right)}\right]\widehat{u_k} \\
&-\left[\overline{\frac{1}{2\rho_0^2c_0^2\cos\varphi_0}\frac{\partial P_0}{\partial s}} - \frac{1}{\Delta x}\overline{\frac{1}{\rho_0}\left(1 + \frac{r}{\cos\varphi_0}\frac{\partial\varphi_0}{\partial s}\right)}\right]\widehat{P_{k+1}} \\
&-\left[\overline{\frac{1}{2\rho_0^2c_0^2\cos\varphi_0}\frac{\partial P_0}{\partial s}} + \frac{1}{\Delta x}\overline{\frac{1}{\rho_0}\left(1 + \frac{r}{\cos\varphi_0}\frac{\partial\varphi_0}{\partial s}\right)}\right]\widehat{P_k} = -\overline{\frac{\widehat{\sigma}(x,r)}{\rho_0\cos\varphi_0}\frac{\partial P_0}{\partial s}} = \widehat{S_{c_k}^M}
\end{aligned} \tag{3.68}$$

For each element c_k, $\widehat{S_{c_k}^C}$ (resp. $\widehat{S_{c_k}^M}$) stands for the source term in the continuity (resp. momentum) equation.

[1]The size of the elements can be made arbitrarily small.

(4) **Linear system**: Rewriting the entire system for the nozzle, a linear system of $2(n-1)$ equations is obtained. The last two conditions required to close and then solve the system are given by the boundary conditions. Here, the impedance relations at the nozzle extremities are used to link the pressure and the velocity fluctuations:

$$\widehat{P} - Z\widehat{\overline{\rho_0 c_0}u} = 2\overline{\rho_0 {c_0}^2}\widehat{P_f} \tag{3.69}$$

where Z is the reduced impedance and is equal to $Z = -1$ at the nozzle inlet and $Z = +1$ at the outlet for perfectly non-reflective boundary conditions. $\widehat{P_f}$ is the nondimensional acoustic forcing. It can either be $\widehat{P^+_{1f}}$ at the nozzle entrance or $\widehat{P^-_{nf}}$ at the exit, so that:

$$\widehat{P^+_{1f}} = \frac{1}{2}\left(\frac{\widehat{P_1}}{\overline{\gamma P_0}} + \frac{\widehat{\overline{\rho_0 c_0}}}{\overline{\rho_0 {c_0}^2}}\widehat{U_1}\right) \tag{3.70}$$

$$\widehat{P^-_{nf}} = \frac{1}{2}\left(\frac{\widehat{P_n}}{\overline{\gamma P_0}} - \frac{\widehat{\overline{\rho_0 c_0}}}{\overline{\rho_0 {c_0}^2}}\widehat{U_n}\right) \tag{3.71}$$

In the case of an entropy forcing, the forcing contributes through the source terms $\widehat{S^C_{c_1}}$ and $\widehat{S^M_{c_1}}$. The final matrix of $2n$ lines can then be written as follows in the general case:

$$\left|\begin{array}{cccccccc}
1 & Z_1\overline{\rho_0 c_0} & 0 & .. & .. & .. & .. & .. \\
\lambda^1_{c_1} & \lambda^2_{c_1} & \lambda^3_{c_1} & \lambda^4_{c_1} & 0 & .. & .. & .. \\
\phi^1_{c_1} & \phi^2_{c_1} & \phi^3_{c_1} & \phi^4_{c_1} & 0 & .. & .. & .. \\
.. & .. & .. & .. & .. & .. & .. & .. \\
.. & 0 & \lambda^1_{c_k} & \lambda^2_{c_k} & \lambda^3_{c_k} & \lambda^4_{c_k} & 0 & .. \\
.. & 0 & \phi^1_{c_k} & \phi^2_{c_k} & \phi^3_{c_k} & \phi^4_{c_k} & 0 & .. \\
.. & .. & .. & .. & .. & .. & .. & .. \\
.. & .. & .. & 0 & \lambda^1_{c_{n-1}} & \lambda^2_{c_{n-1}} & \lambda^3_{c_{n-1}} & \lambda^4_{c_{n-1}} \\
.. & .. & .. & 0 & \phi^1_{c_{n-1}} & \phi^2_{c_{n-1}} & \phi^3_{c_{n-1}} & \phi^4_{c_{n-1}} \\
.. & .. & .. & .. & .. & 0 & 1 & Z_n\overline{\rho_0 c_0}
\end{array}\right|
\left|\begin{array}{c}
\widehat{P_1} \\ \widehat{U_1} \\ .. \\ .. \\ \widehat{P_k} \\ \widehat{U_k} \\ .. \\ .. \\ \widehat{P_n} \\ \widehat{U_n}
\end{array}\right|
=
\left|\begin{array}{c}
2\overline{\rho_0 {c_0}^2}\widehat{P^+_1} \\ \widehat{S^C_{c_1}} \\ \widehat{S^M_{c_1}} \\ .. \\ \widehat{S^C_{c_k}} \\ \widehat{S^M_{c_k}} \\ .. \\ \widehat{S^C_{c_{n-1}}} \\ \widehat{S^M_{c_{n-1}}} \\ 2\overline{\rho_0 {c_0}^2}\widehat{P^-_n}
\end{array}\right| \tag{3.72}$$

where the expressions of the coefficients for the element c_k are:

$$\lambda^1_{c_k} = \left[\frac{1}{2}\left(A_x\overline{\left(\frac{1}{c_0^2}\right)}i\omega + \frac{\partial}{\partial x}\left[A_x\overline{\left(\frac{u_{0x}}{c_0^2}\right)}\right]\right) - \frac{A_x}{\Delta x}\overline{\left(\frac{u_{0x}}{c_0^2}\right)}\right]_{c_k} \tag{3.73}$$

$$\lambda^2_{c_k} = \left[\frac{1}{2}\frac{\partial\left(A_x\overline{\rho_0}\right)}{\partial x} - \frac{A_x\overline{\rho_0}}{\Delta x}\right]_{c_k} \tag{3.74}$$

$$\lambda^3_{c_k} = \left[\frac{1}{2}\left(A_x\overline{\left(\frac{1}{c_0^2}\right)}i\omega + \frac{\partial}{\partial x}\left[A_x\overline{\left(\frac{u_{0x}}{c_0^2}\right)}\right]\right) + \frac{A_x}{\Delta x}\overline{\left(\frac{u_{0x}}{c_0^2}\right)}\right]_{c_k} \tag{3.75}$$

$$\lambda^4_{c_k} = \left[\frac{1}{2}\frac{\partial\left(A_x\overline{\rho_0}\right)}{\partial x} + \frac{A_x\overline{\rho_0}}{\Delta x}\right]_{c_k} \tag{3.76}$$

$$\phi^1_{c_k} = \left[-\overline{\frac{1}{2\rho_0^2c_0^2\cos\varphi_0}\frac{\partial P_0}{\partial s}} - \frac{1}{\Delta x}\overline{\frac{1}{\rho_0}\left(1+\frac{r}{\cos\varphi_0}\frac{\partial\varphi_0}{\partial s}\right)}\right]_{c_k} \tag{3.77}$$

$$\phi^2_{c_k} = \left[\frac{i\omega}{2} - \frac{1}{\Delta x}\overline{u_{0s}\left(\cos\varphi_0 + r\frac{\partial\varphi_0}{\partial s}\right)} + \frac{1}{2}\overline{\left(\tan\varphi_0\frac{\partial u_{0s}}{\partial\tau} + \frac{\partial u_{0s}}{\partial s}\right)}\right]_{c_k} \tag{3.78}$$

$$\phi^3_{c_k} = \left[-\overline{\frac{1}{2\rho_0^2c_0^2\cos\varphi_0}\frac{\partial P_0}{\partial s}} + \frac{1}{\Delta x}\overline{\frac{1}{\rho_0}\left(1+\frac{r}{\cos\varphi_0}\frac{\partial\varphi_0}{\partial s}\right)}\right]_{c_k} \tag{3.79}$$

$$\phi^4_{c_k} = \left[\frac{i\omega}{2} + \frac{1}{\Delta x}\overline{u_{0s}\left(\cos\varphi_0 + r\frac{\partial\varphi_0}{\partial s}\right)} + \frac{1}{2}\overline{\left(\tan\varphi_0\frac{\partial u_{0s}}{\partial\tau} + \frac{\partial u_{0s}}{\partial s}\right)}\right]_{c_k} \tag{3.80}$$

$$\widehat{S^C_{c_k}} = \left[\frac{\partial}{\partial x}\left[A_x\overline{(\rho_0u_{0x}\widehat{\sigma}(x,r))}\right] + A_xi\omega\overline{(\rho_0\widehat{\sigma}(x,r))}\right]_{c_k} \tag{3.81}$$

$$\widehat{S^M_{c_k}} = \left[-\overline{\frac{\widehat{\sigma}(x,r)}{\rho_0\cos\varphi_0}\frac{\partial P_0}{\partial s}}\right]_{c_k} \tag{3.82}$$

(5) **Resolution**: Now that the system has been expressed in a matrix form, it is possible to inverse the relation and to obtain $\widehat{P_k}$ and $\widehat{U_k}$ for each element. In particular, $\widehat{P_1}$, $\widehat{U_1}$, $\widehat{P_n}$ and $\widehat{U_n}$ provide the acoustic invariants $\widehat{P_1^-} = \frac{1}{2}\left(\frac{\widehat{P_1}}{\overline{\gamma P_0}} - \frac{\overline{\rho_0c_0}}{\overline{\rho_0{c_0}^2}}\widehat{U_1}\right)$ and $\widehat{P_n^+} = \frac{1}{2}\left(\frac{\widehat{P_n}}{\overline{\gamma P_0}} + \frac{\overline{\rho_0c_0}}{\overline{\rho_0{c_0}^2}}\widehat{U_n}\right)$ leaving the nozzle and used to evaluate the TATFs.

Chapter 4

3D numerical simulations of the DISCERN nozzle

A computer lets you make more mistakes faster than any invention in human history - with the possible exceptions of handguns and tequila.

Mitch Ratliffe

Contents

In this chapter a description of the different numerical simulations performed during this PhD thesis is done. First, the studied configuration is introduced. Then, a RANS computation is carried out giving the different flow characteristics and also a mean flow field used as

an input for the application of the two-dimensional axisymmetric model in chapter 5. The validity of this mean field is ensured by the comparison to the mean flow obtained from a Large Eddy Simulation of the nozzle without any excitation (thereafter denoted "background noise LES"). In addition to this background noise LES computation, two LES computations forced with inlet entropy fluctuations are also performed. The first LES is forced with an incoming 900 Hz *entropy fluctuation in order to collect the background noise mainly related to the turbulent boundary layers. It also enables us to study the amount of dissipation experienced by temperature disturbances as they travel in the nozzle. The second LES forced with a multi-harmonic entropy fluctuation (411 to 905* Hz*) provides the TATFs that are compared in chapter 5 to the prediction of the new semi-analytical 2D model developed in this thesis.*

4.1 Introduction of the studied configuration

The nozzle studied here is one of the shapes designed in the framework of the project ANR/ FRAE DISCERN [Ducruix 2011] and studied experimentally in the acoustic part of the project EU/FP7 RECORD studying the mechanisms of generation and transmission of CN. The DISCERN nozzle has been optimized in order to generate maximum ICN using the in-house software Marcan Evolution [Giauque 2013]. A sketch of the experimental setup is visible on the left of Fig. 4.1. In the experimental setup the combustion chamber is fed by two stages of injectors, which are not considered in the computations. A view of the DISCERN nozzle with some flow characteristics is represented on the right of Fig 4.1. This nozzle is studied in the subsonic regime with an accelerated flow inside the nozzle up to a Mach number of 0.8 at the throat. However, in the supersonic case, this nozzle is capable to ensure the presence of a normal shock in the diverging part for an inlet pressure P_{in} bellow 180000 Pa for an atmospheric pressure outlet (101325 Pa). The nozzle length is 18.5 cm long. Additional characteristics regarding the nozzle are given in Table 4.1.

In addition to this nozzle, a small portion of the combustion chamber (1/3 of the total real length) is added at the nozzle inlet. It is in this zone that the injection of entropy fluctuations takes place. It has been verified numerically with reactive simulations of the combustion chamber, performed at ONERA during the project RECORD, that the retained inlet position of the present numerical domain is located downstream of the flame location. This portion of the square combustion chamber has a cross-sectional area of 7 cm $\times$ 7 cm and a length of 5 cm. This length was decided during a pre-study carried out before the beginning of the thesis. Indeed, it cannot be further reduced if one wants to impose one-dimensional fluctuations at the inlet and permit the natural stretching of the waves (see Fig. 4.10) as they travel towards the throat of the nozzle. At the end of the nozzle, an

additional constant radius cylinder of 5 cm in length is also added. In this area an axial stretching of the mesh is applied in order (i) to remove the turbulent structures and prevent the generation of spurious acoustics at the outlet and (ii) to maintain the Mach number constant in the zone where acoustic measurements are undertaken. This gives a total length of 28.5 cm for the computational domain. The three-dimensional computational domain is visible in Fig. 4.2, where three zones represented in blue, red and gray are respectively the combustion chamber, the nozzle and the constant radius cylinder. For the numerical computations, the Mach number at the inlet of the domain is set at $M_{inlet} = 0.01$ in order to achieve $M_{throat} = 0.8$. The temperature inside the combustion chamber is set to 1300 K.

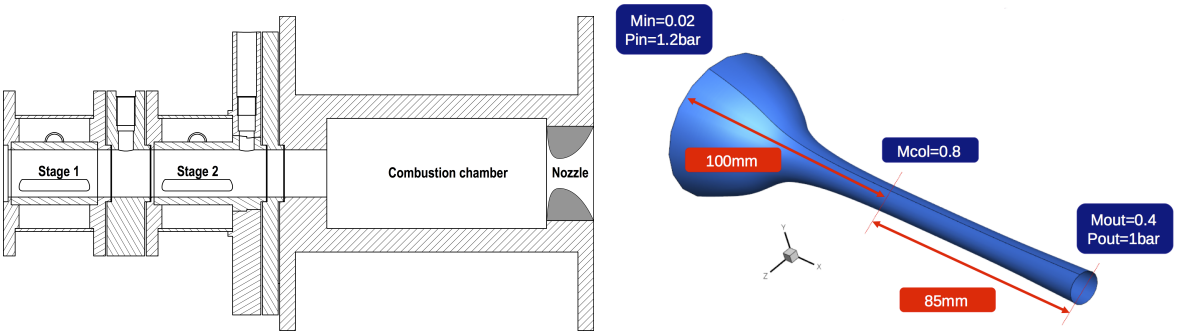

Figure 4.1: Schematic view of the experimental test bench at EM2C (*left*) and the DISCERN nozzle with some flow properties (*right*).

Characteristics	Inlet	Outlet
Mass flow ($g.s^{-1}$)	11.5	
Temperature (K)	1300	1270
Diameter (mm)	59	13.9

Table 4.1: Additional characteristics of the DISCERN nozzle.

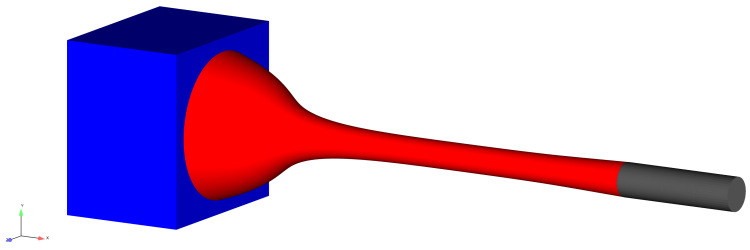

Figure 4.2: Schematic view of the 3D compuational domain of the study.

4.2 RANS computation

The goal of this RANS computation is to obtain the mean flow that is used as an input for the two-dimensional axisymmetric semi-analytical model in chapter 5.

4.2.1 Mesh and global parameters of the RANS computation

The RANS mesh has 4.8 million cells and is composed of tetrahedral, hexahedral and prismatic elements (see Fig. 4.3). Two hexahedral zones are present at the inlet and the outlet of the domain (see Fig. 4.5). These zones are needed during the LES computations to improve the stability of the Navier-Stokes characteristic boundary conditions (NSCBC) [Poinsot 1992, Selle 2004, Yoo 2005, Lodato 2008] recently implemented in the 3D solver CEDRE. The tetrahedral mesh size inside the nozzle as well as the hexahedral mesh size inside the combustion chamber are set to 0.6 mm. Close to the nozzle walls, two prismatic layers are added. Those two layers grow progressively from the nozzle inlet to the nozzle throat. At the nozzle throat position the y^+ of the first prismatic layers is 62 ($y^+ = 1$ corresponding to 15 $\mu\mathrm{m}$). One can question why the prismatic layers are increased while in a converging area the boundary layers tend to be very small, this choice is only justify by a simplified meshing procedure.

Fig. 4.4 shows a cut of the mesh at the throat. After the throat, the thickness of the layers is kept constant till the end of the computational domain. In addition, inside the cylindrical part, an axial stretching of 2% of the mesh size is applied to limit the total number of elements. Table 4.2 gives a summary of the mesh properties inside the domain.

Combustion chamber		**Nozzle**	**Constant cylinder part**		
Hexa	Tetra	Prisms + Tetra	Prisms and Tetra	2% axial stretching: Prisms and Tetra	Hexa + Prisms
x = -5 cm to -1.7 cm	x = -1.7 cm to 0 cm	x = 0 cm to 18.5 cm	x = 18.5 cm to 21.1 cm	x = 21.1 cm to 22.2 cm	x = 22.2 cm to 23.5 cm

Table 4.2: Mesh types inside the computational domain.

The turbulent quantities imposed at the inlet boundary for the RANS computations using the $k-\omega$ SST Menter turbulent model are obtained using the isotropic homogeneous turbulence assumption and considering the velocity fluctuation being 5% of the mean velocity. This gives k = 0.288 and ω = 136.8 which is evaluated using the turbulence length scale of a fully developed pipe flow ($0.038d$, where d is the diameter of a circular pipe equals

to the diameter of the nozzle throat). This corresponds to the most favorable case where the turbulence is the largest. The inlet boundary condition is based on the total temperature and mass flow set respectively to T_i = 1300.15 K and 11.4856 $\mathrm{g.s^{-1}}$, which corresponds to an axial velocity of 6.974 $\mathrm{m.s^{-1}}$. The outlet boundary condition is a regular subsonic outflow controlled by the pressure set at 101325 Pa. All the walls are set to be adiabatic and the computational time step is 3×10^{-5} s with a one step implicit scheme. The convergence of the computation with such a large time step is made possible by using 100 sub-iterations for each implicit time step.

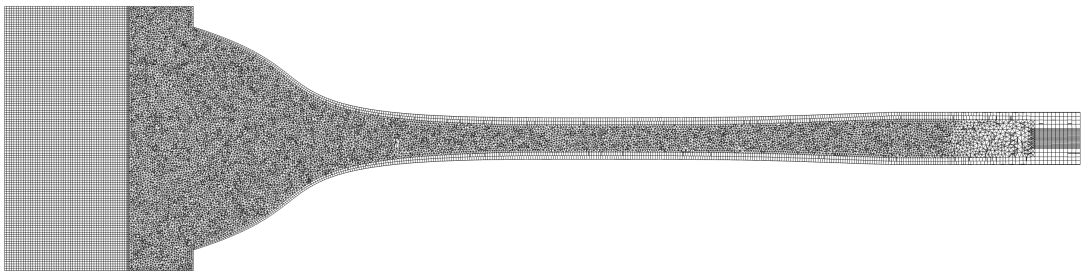

Figure 4.3: Longitudinal cross section view of mesh.

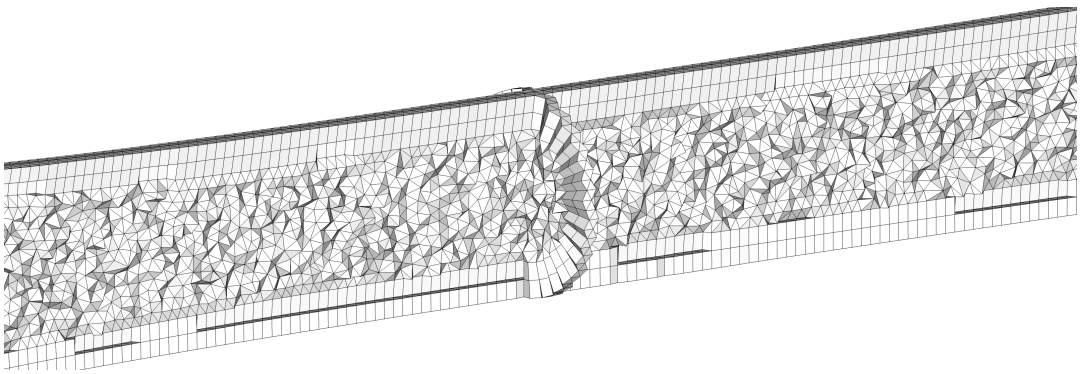

Figure 4.4: Longitudinal cross section close view of mesh at the theoretical throat.

4.2.2 Flow fields characteristics

The convergence of the RANS computation is first ensured by looking at the mass conservation between the inlet and the outlet. The left-hand side of Fig. 4.6 shows the absolute difference between the inlet and the outlet mass flux using a log scale. The total mass flow imbalance is around 5.10^{-5} $\mathrm{kg.s^{-1}}$. This represents less than 0.44% of the inlet injection. In

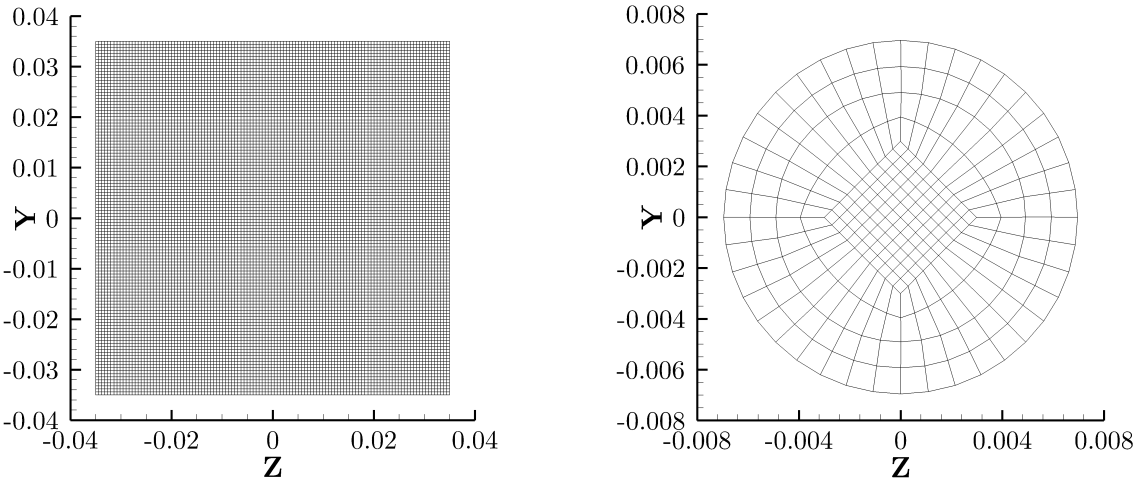

Figure 4.5: Cross sectional view of hexahedral mesh at the inlet and the outlet of the computational domain.

addition, the right-hand side of Fig. 4.6 shows the convergence of the resolved variables and it can be seen that the computation is indeed converged. Note that the initial values of the maximum residuals (t = 0) was not recorded during the computation. Due to the presence of the boundary layers, the location of maximum velocity is displaced by approximately 2.5 cm when compared to the geometrical throat. Both sections (theoretical and numerical throats) are represented in Fig. 4.7. The Mach number at the effective throat for this RANS computation is 0.785. The pressure in the combustion chamber is 124600 Pa (see Fig. 4.8). A longitudinal cut colored by temperature is shown in Fig. 4.9. A comparison of the RANS results to the LES or 1D results is performed in the next section.

In addition, due to the presence of the square combustion chamber, four recirculation zones appear. They are represented in Fig. 4.10 where the axial velocity is voluntarily saturated at 12 $\mathrm{m.s^{-1}}$. Inside the diverging part of the nozzle, no separation of the boundary layers is present. The same behavior has been observed while using another RANS mesh with 15 prismatic layers at the boundary and with y^+=1 but without hexahedral regions inside the combustion chamber or the constant cylinder. This mesh contains 7.7 million cells and the flow fields are very close to the one presented here. These results are not included in this manuscript as the idea was to have similar mesh types between the RANS and the LES computations described in the next section.

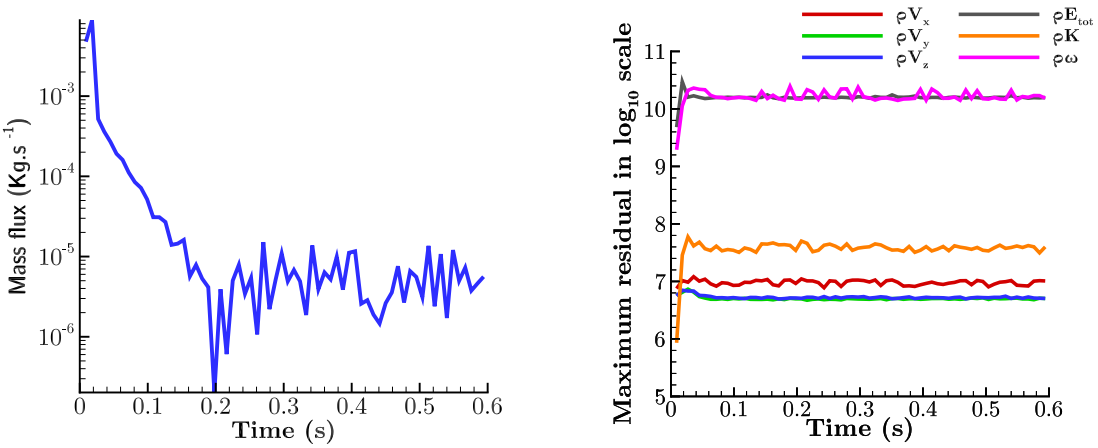

Figure 4.6: Total mass flux absolute difference between the inlet and the outlet of the computational domain in the RANS computation (*left*). Maximum residuals of the resolved variables in $\log_{10}$ scale (*right*).

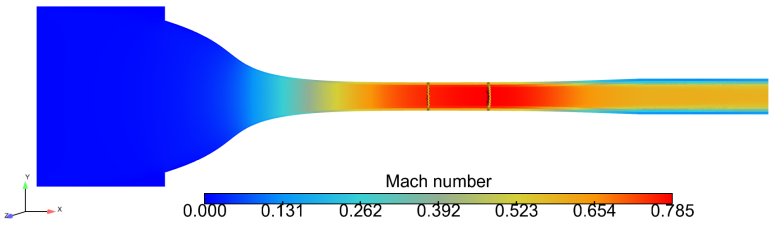

Figure 4.7: Overall longitudinal cross sectional view of the Mach number inside the computational domain for the RANS computation. The theoretical and effective throat positions are also represented.

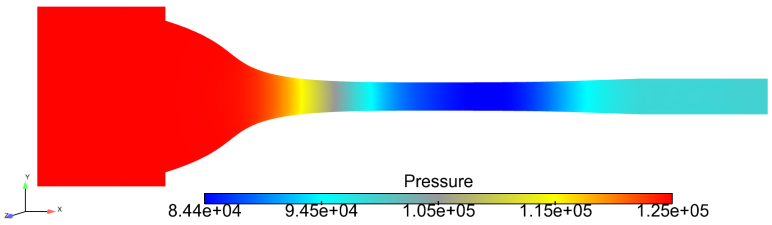

Figure 4.8: Longitudinal cross sectional view of the pressure for the RANS computation.

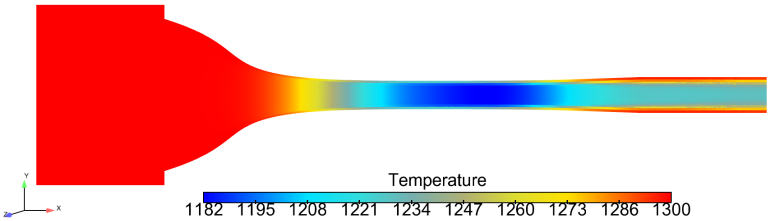

Figure 4.9: Longitudinal cross sectional view of the temperature for the RANS computation.

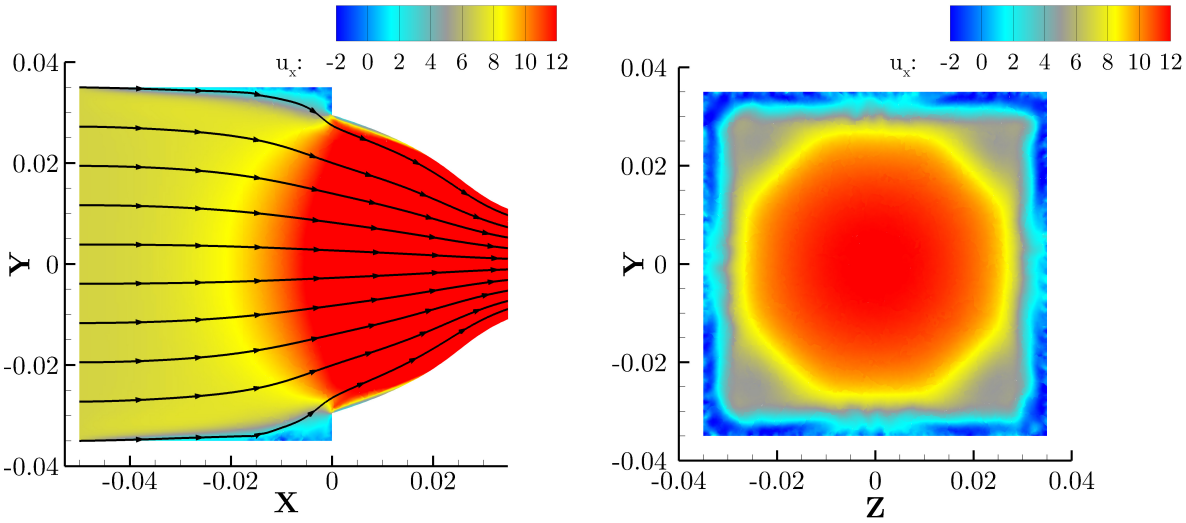

Figure 4.10: Cross sectional zoomed view of the combustion chamber colored by the axial velocity ($\mathrm{m.s^{-1}}$) with streamlines (*left*). Spanwise view of the combustion chamber at the location $x = -0.005$ m (*right*). The axial velocity is voluntarily saturated in order to see recirculation areas due to the square combustion chamber.

4.3 LES computations

The choice of a LES approach to study ICN is justified by the fact that in addition to obtain the TATFs of the DISCERN nozzle, it is also interesting to explore the possible effects of the turbulent boundary layers upon the generation of this kind of combustion noise. Indeed, LES has a good capability to simulate the interaction between the turbulent boundary layers, the entropy and the acoustic disturbances.

4.3.1 Mesh and global parameters of the LES computations

In the domain, the velocity at the inlet is set to approximately $7\ \mathrm{m.s^{-1}}$. Depending on the type of wave one wants to simulate (entropy or acoustic), the Number of Points per Wavelength (here $NPW = 30$) one can afford, and the characteristic frequency of the wave (here $f_{max} = 900$ Hz), one obtains three limiting scales that represent the smallest sizes one should enforce in the mesh in order to propagate those waves without too much dissipation. They are respectively defined according to their critical zone. For P^+ and the entropy waves, the critical zone is the combustion chamber while for P^- it is the throat of the nozzle. The three limiting scales are defined as:

$$\Delta_{entro} = \frac{u_{min}}{NPW \times f_{max}} = \frac{7}{30 \times 900} = 0.259\ \mathrm{mm} \tag{4.1}$$

and

$$\Delta_{acou} = \frac{u_{min} + c}{NPW \times f_{max}} = \frac{707}{30 \times 900} = 26.2\ \mathrm{mm} \tag{4.2}$$

as well as

$$\Delta_{upward_{acou}} = \frac{c_{throat} - u_{max-throat}}{NPW \times f_{max}} = \frac{680 \times (1 - 0.8)}{30 \times 900} = \frac{136}{30 \times 900} = 5.03\ \mathrm{mm} \tag{4.3}$$

where NPW is the number of grid points per wavelength and f_{max} is 900 Hz, the maximum considered frequency for the entropy forcing. Looking at the three previous values, the $\Delta_{entro} = 0.259\ \mathrm{mm}$ is the critical size inside the combustion chamber. The mesh size can be increased up to 5.03 mm at the throat. However, one should keep in mind that the diameter of the nozzle at the throat is 10 mm and increasing the mesh size up 5.03 mm is not a appropriate idea. For aerodynamic purposes, the mesh size inside the nozzle is chosen at Δ_{entro} also.

The mesh used in this section is a hybrid mesh composed of the same zones as previously described in the RANS section 4.2. The size for the hexahedra and tetrahedra are set to $0.259\ \mathrm{mm}$ inside the combustion chamber and the nozzle. This mesh allows the propagation

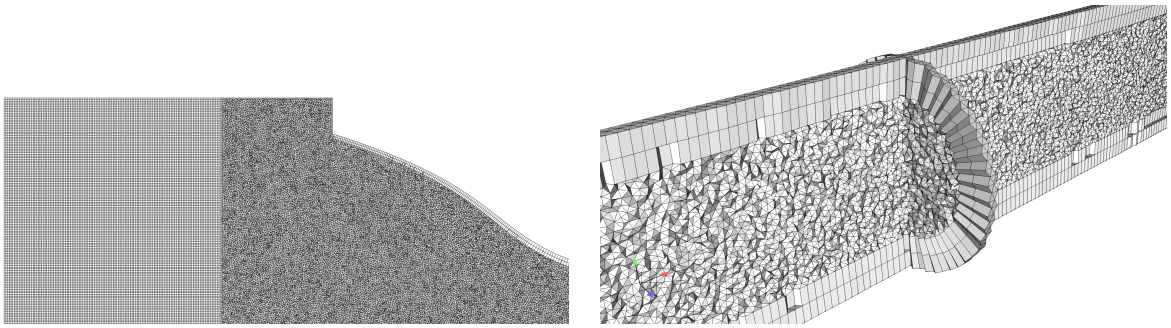

a b

Figure 4.11: (a) Longitudinal cross sectional view of the end of the combustion chamber and the nozzle inlet. (b) Longitudinal cross sectional view of the two prismatic layers used near the nozzle wall as well as the nozzle throat.

of entropy waves inside the nozzle and acoustic waves and with minimum numerical dispersion and dissipation. Inside the nozzle, a prismatic layer composed of two layers ($y^+ = 57$ for each layer). The large value of the y^+ for the first cell allows to consider the latter to be in the logarithmic region of the turbulent boundary layer. This makes possible the application of the wall model SIBLE [Chedevergne 2010] for the computation of the wall friction. In the downstream cylinder, once again an axial stretching of 2% is applied starting at 21.1 cm. The maximum mesh size at the outlet of the domain is 0.70 mm. The stretched zone and the downstream hexahedral zone help to dissipate the turbulent structures. This gives a total of 56 millions cells. Fig. 4.11 shows some details of the LES mesh used for the computations.

A second order explicit Runge-Kutta (RK2) scheme is used for the computation with a time step of $\Delta t = 2.7 \times 10^{-8}$ s. This corresponds to a maximum CFL number of 0.14. The spatial scheme is the second order MUSCL scheme. A Smagorinsky subgrid scale model is applied with the default parameters in the solver CEDRE. The recently implemented NSCBC are used both at the inlet and the outlet of the computational domain. Following Selle *et al.* [Selle 2004] and Lodato [Lodato 2008], the inlet relaxation coefficients are set at 0.2 while at the outlet the value is 0.5 (higher acoustic reflection) with a characteristic length of 0.285 m. The slightly larger value at the outlet is due to stability reason: it ensures that the pressure does not drift during the simulations. At the inlet, the target velocity is fixed at 6.974 $\mathrm{ms}^{-1}$and the target temperature at 1300 K. At the outlet, the pressure is relaxed toward 101325 Pa.

Finally, cross sectional plane surfaces are used inside the combustion chamber and the cylindrical part for the LES acoustic post-treatment presented in chapter 5. The positions of the planar surfaces are shown in Fig. 4.12 where the colors refer to those used in Fig. 4.2.

Tables 4.3 and 4.4 give the exact positions of each planar surface.

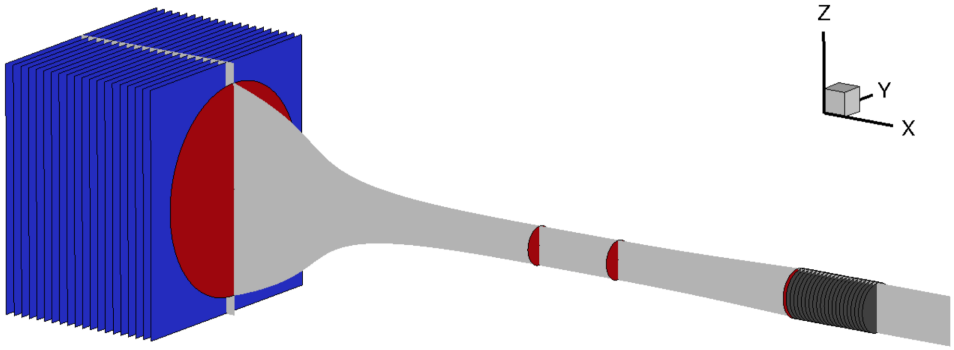

Figure 4.12: Schematic view of the plane surfaces of sensors used for the acoustic treatment.

Combustion chamber	**Constant cylinder part**
20 plane surfaces	21 plane surfaces
x = -5 cm to -2.5 mm step size: 2.5 mm	x = 18.6 cm to 21.1 cm step size: 1.25 mm

Table 4.3: Number and positions of the plane surfaces used for the acoustic treatment.

Nozzle			
Inlet	Theoretical throat	Effective throat	Outlet
x = 0	x = 0.1024 m	x = 0.126 m	x = 0.185 m

Table 4.4: Additional plane surfaces used inside the DISCERN nozzle

The initialization and the convergence to a steady state (in terms of mass flux) of this configuration are achieved after 43.5 ms of simulated time and all the following LES computations are started at this point. This time corresponds to 5.8 Flow Through Time of the computational domain.

4.3.2 Unperturbed Large Eddy Simulation of the configuration ("Background Noise" case)

In order to study the background noise in the configuration, a first non-forced LES computation is performed. This "background noise" LES is computed during 17.4 ms and provides a mean flow that can be compared to the RANS results. A good agreement in the results

allows to use the mean flow from the RANS computation rather than the one LES as an input for the two-dimensional axisymmetric semi-analytical.

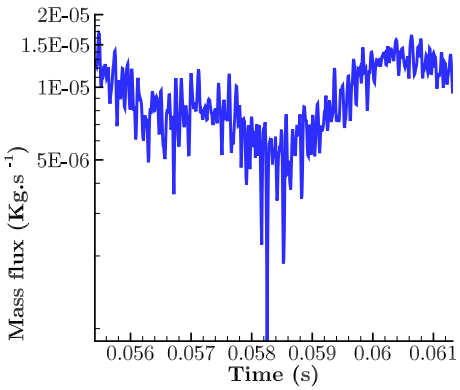

Figure 4.13: Total mass flux absolute difference between the inlet and the outlet of the computational domain in the LES computation.

First, the convergence of this LES is assessed on zero order quantities such as the total mass flux imbalance in the domain. Fig. 4.13 shows the variation of the absolute total mass variation between the inlet and the outlet over time. It can be seen, as in the RANS case (see Fig. 4.6), that the absolute total mass flux variation is fluctuating around 10^{-5} $\mathrm{kg.s^{-1}}$ and represents less than 0.1% of the entering mass flow. These additional 17.4 ms corresponds to 2.3 Flow Through Time of the total geometry. The next paragraphs compare the characteristics of the mean flows obtained either by LES or RANS. First, a comparison between the axial profile of the pressure, temperature and Mach number is performed. In addition to the LES and RANS results, the one-dimensional isentropic perfect gas flow in a variable section duct solution is also added to the plots. The axial profiles are represented in Fig. 4.14.

Regarding the pressure signals, some discrepancies appear between the LES and the RANS computations especially inside the combustion chamber. The reason is due to a different estimation of the pressure losses. The one-dimensional isentropic perfect gas flow assumption does not take into account the pressure losses occurring inside the nozzle, giving a pressure in the combustion chamber lower than for the 3D computations. The temperature profiles are also different between RANS and LES but the general shape is quite similar. This discrepancy comes from a different maximum throat Mach number. Indeed, the Mach number in LES is around 0.81 while for RANS it is at 0.785. Even with these different Mach numbers, RANS and LES computations predict the same position for the effective throat (difference of 0.1 mm) while the one-dimensional solution, which does not take into account the development of the boundary layer, assumes the maximum Mach

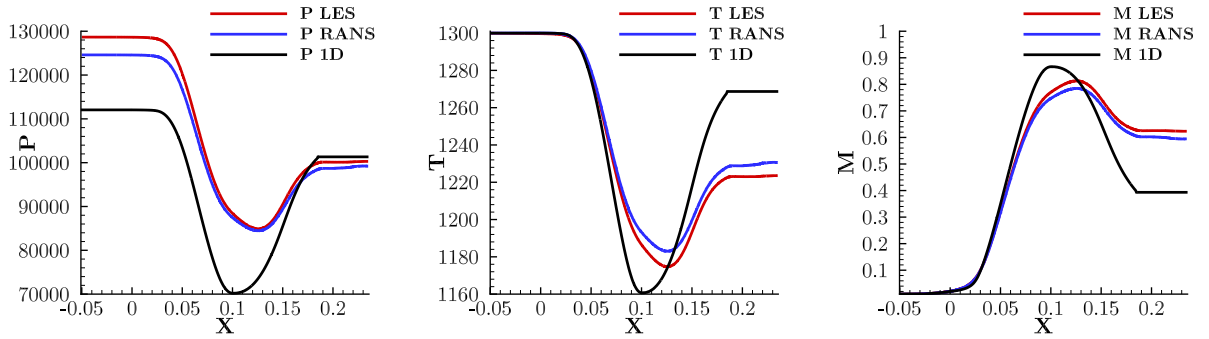

Figure 4.14: Plots of the axial pressure, temperature and Mach number profiles at the centerline of the nozzle from the LES (red), RANS (blue) and the one-dimensional isentropic perfect gas flow in a variable section duct solution (black).

number at the theoretical throat. The one-dimensional Mach number is overestimated and reaches 0.86, this is imputed to the design process based on a heat capacity ratio of 1.4 instead of 1.32 for the computations.

The same type of comparison is performed in the radial direction at different axial locations, between RANS and LES computations. First, this comparison is carried out at nozzle **inlet**. Due to different pressure loss estimations between RANS and LES computations, the radial pressure profile cannot be directly compared. In order to compare the radial profiles of pressure, the averaged value obtained for both simulations is subtracted beforehand. Fig. 4.15 shows a really good agreement between the two different approaches. Note also that the velocity at the walls does not go to zero as the value is taken at the center of the first cell and not directly at the wall.

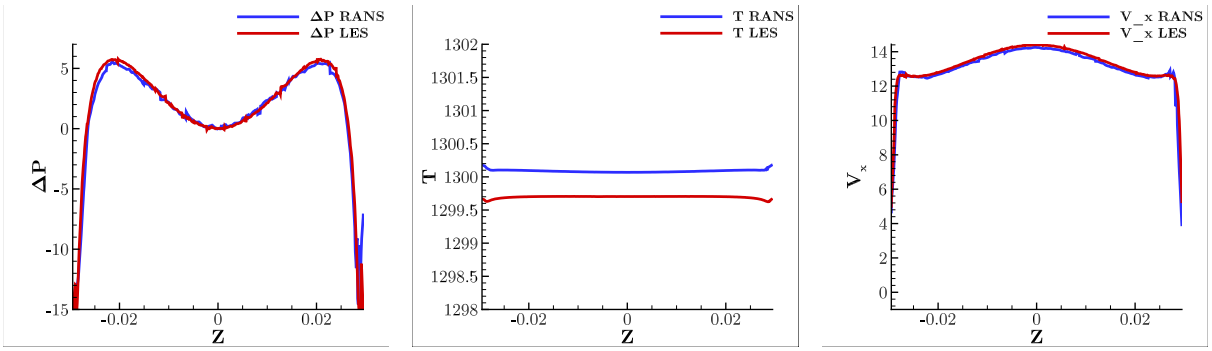

Figure 4.15: Plots of the radial evolution of the pressure, the temperature and velocity profiles at the inlet of the nozzle.

The same comparison is made at the **effective throat** position ($x = 0.126$ m). The pressure correction is applied also for the temperature and the axial velocity. In general, the shapes of the different profiles are quite similar (see Fig. 4.16).

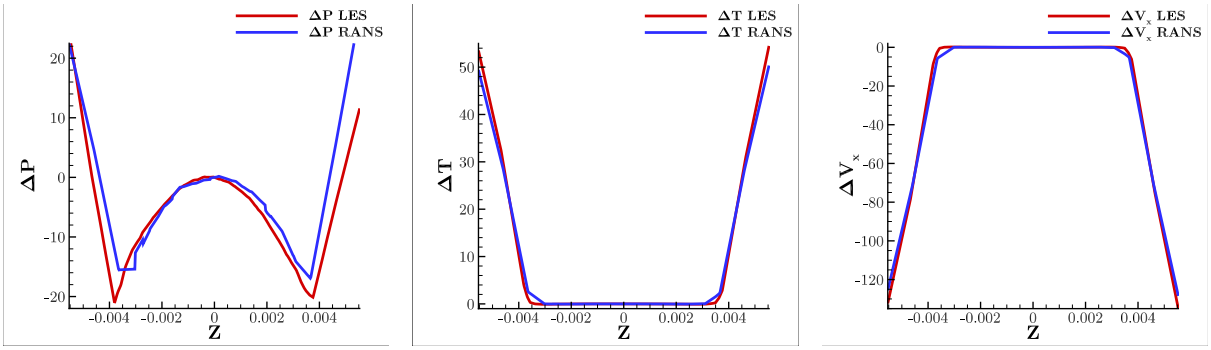

Figure 4.16: Plots of the radial pressure, temperature and velocity profiles at the effective throat.

Similar observations are made at the nozzle **outlet**, see Fig. 4.17.

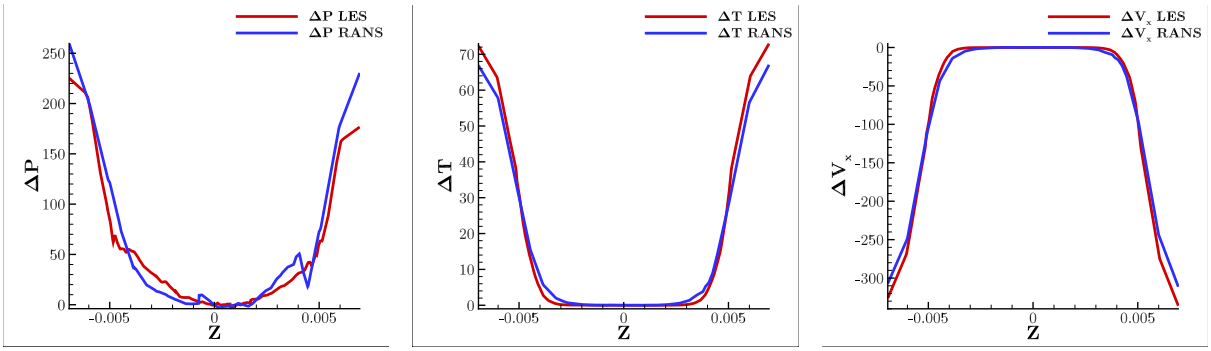

Figure 4.17: Plots of the radial pressure, temperature and velocity profiles at the outlet of the nozzle.

4.3.3 900 Hz harmonic entropy forcing LES

A first computation with a 900 Hz entropy forcing at the inlet is achieved. This value corresponds to the highest possible frequency to achieve a simulation without noticeable numerical dissipation, and therefore to the lowest required simulated time. This computation was performed at ONERA on the supercomputer Stelvio [ONERA 2009] on 900 CPUs. There are multiple reasons for undertaking this first step using a single harmonic frequency for the forcing. The main reason is that the development of post-processing tools is easier in this context. Also, it enables us to precisely study the dissipation of the entropy waves due to numerical effects. Finally, the TATFs obtained at 900 Hz from this LES computation is performed in chapter 5 and compared to the TATFs obtained using a multi-harmonic forcing. This comparison is an assessment of the multi-harmonic approach and the capability to treat a large frequency band with only one computation.

The amplitude of the forcing is set to 40 K, representing 3% of the mean temperature in the chamber which is 1300 K. The precise entropy fluctuations are obtained by subtracting

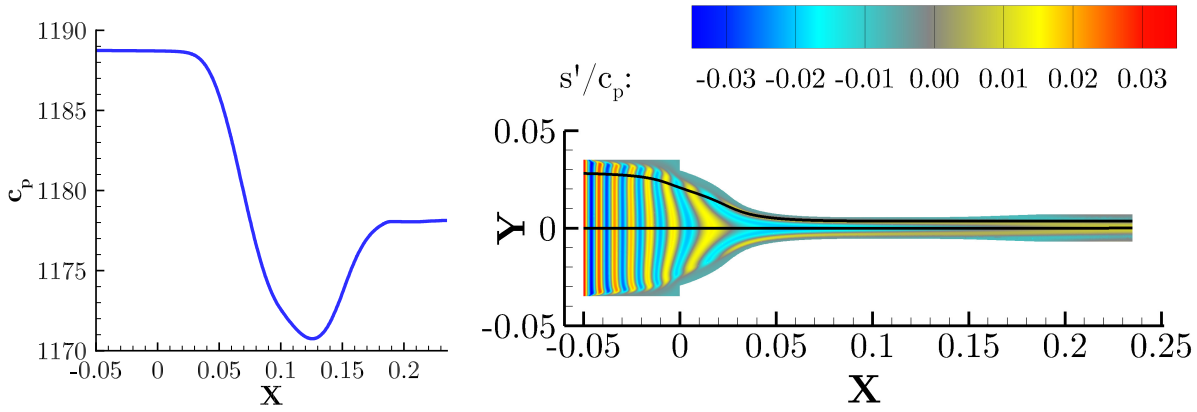

Figure 4.18: Axial specific heat at constant pressure in $\mathrm{J.kg^{-1}.K^{-1}}$ from the "Background noise" LES (*left*). Longitudinal cross section view of the dimensionless entropy fluctuations for a 900Hz entropy forcing LES at the inlet with two streamlines represented in black line (*right*).

the mean flow values from the "Background noise" LES to the instantaneous field of the 900 Hz harmonically forced LES and then normalizing by C_p taken at the inlet, as the C_p varies inside the nozzle (see *left* in Fig. 4.18). The right of Fig. 4.18 shows the dimensionless entropy fluctuations inside the computational domain. The non-axisymmetric behavior of the flow inside the combustion chamber has already been mentioned in the previous section (see Fig. 4.10). This phenomenon is present in the "Background noise" LES but it is more visible in the 900 Hz harmonic entropy forcing LES see *left* of Fig. 4.19. However, at the effective throat as well as at nozzle outlet, the flow can be considered as quasi axisymmetric (see *center* and *right* of Fig. 4.19). This axisymmetric condition is important as the new semi-analytical 2D model is based on an axisymmetric flow condition.

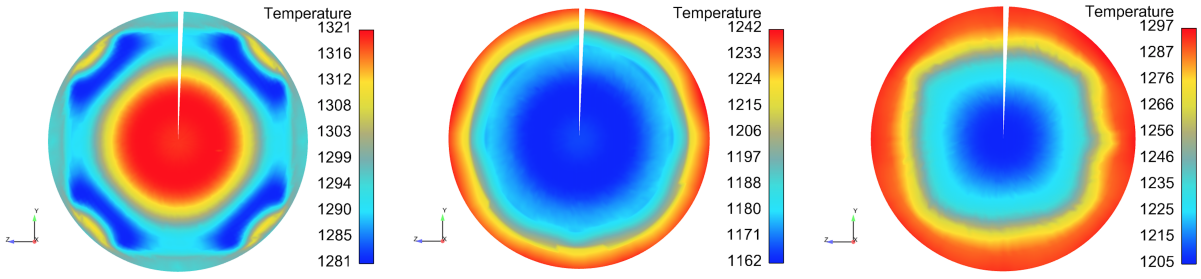

Figure 4.19: Cross sectional view colored by the temperature at the nozzle inlet (*left*), the effective throat (*center*) and the nozzle outlet (*right*).

The entropy fluctuation is computed using Eq. 2.34 and is represented in Fig. 4.18. One can notice that the amplitude of the fluctuating entropy wave fronts decreases as they

approach the nozzle inlet meaning that some dissipation/diffusion occurs inside the computational domain. Two streamlines are also added in the figure, they correspond to the location where two studies on the dissipation/diffusion phenomena are carried out. The dissipation phenomenon is the numerical reduction of the amplitude of the entropy signal. The dispersion phenomenon is the numerical change in phase of the entropy signal. Finally, the diffusion phenomenon is the thermal diffusion or also called the shear dispersion.

4.3.3.1 Axial dissipation/diffusion

Fig. 4.20 represents the non-dimensional entropy fluctuations at the centerline of the combustion chamber over the axial nozzle distance (blue) but also along the streamline close to the wall (red) previously introduced in Fig. 4.18. Table 4.5 summarizes the axial dissipation/diffusion of the injected entropy fluctuations inside the combustion chamber. The reference axial position is set to 0 at the nozzle inlet.

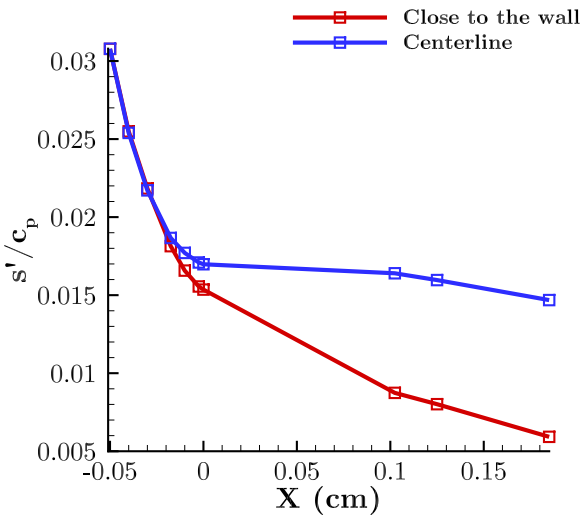

Figure 4.20: Plots of the axial dimensionless entropy fluctuation s'/C_p for a streamline along the nozzle axis (blue) and for a streamline close the nozzle wall (red).

One can notice that even if the mesh has been optimized for 30 points per wavelength. Around 45% of the dissipation/diffusion is located in the upstream hexahedral zone due to the low inlet velocity ($M = 0.01$). Appendix C gives a study on the thermal and viscous diffusion as well as the mesh dissipation in a computational domain comparable to the combustion chamber. It can be concluded that the thermal diffusion is the main responsible of the amplitude decrease occurring in this region. In the test cases, it is expected to be 100 times larger than the viscous diffusion while the mesh dissipation is estimated to be around 5.78%. The position $x = -1.75$ cm is interesting as this is the location at which the

mesh elements transition from hexahedra (-5 cm $\leq x \leq -1.7$ cm) to tetrahedra (occuring at $x = -1.7$ cm). In the tetrahedral zone of the combustion chamber, the amplitude decrease is reduced due to an increase of the velocity ($M = 0.02$). Even if the thermal diffusion in the combustion chamber is not negligible, this is not an issue for the prediction of ICN as long as the real entropy fluctuations profile entering the nozzle is known and no or sufficiently small dissipation occurs inside the nozzle. Inside the nozzle, the flow is strongly accelerated

Position (m)	**Average maximum peak amplitude**	**Dissipation/diffusion (%)**
-0.05	0.030741416	0 (reference value)
-0.04	0.024882328	-19.06
-0.03	0.021406792	-30.37
-0.0175	0.018417221	-40.09
-0.01	0.017599159	-42.75
-0.0025	0.017022382	-44.63
0	0.016906554	-45.00

Table 4.5: Axial dissipation/diffusion inside the combustion chamber for a streamline along the nozzle axis.

thus the axial numerical dissipation is supposed to be negligible. Table 4.6 gives a summary of the axial diffusion where the reference state is taken this time at the nozzle inlet. It should be retained that diffusion occurs inside the nozzle (13% between inlet and outlet).

Position (m)	**Average maximum peak amplitude**	**Diffusion (%)**
0	0.016906554	0 (reference value)
0.1024	0.016406430	-2.96
0.126	0.015974835	-5.51
0.185	0.014726004	-12.90

Table 4.6: Axial diffusion inside the nozzle.

4.3.3.2 Dissipation/diffusion along a streamline close to the nozzle wall

The axial streamline is the location where the velocity is maximum, consequently the dissipation/diffusion have been evaluated for the most favorable case. A look on the second streamline represented in Fig. 4.18 is carried out. The same type of analysis as done previously is applied for this streamline. Fig. 4.20 also shows the non-dimensional entropy fluctuations along the streamline close to the nozzle wall over axial distance (red). Table 4.7 summarizes the axial dissipation/diffusion of the injected entropy fluctuations inside

the combustion chamber. The values in red represent significant variation compared to Table 4.5. The reference position is set to 0 at the nozzle inlet.

Position (m)	**Average maximum peak amplitude**	**Dissipation/diffusion (%)**
-0.05	0.030740188	0 (reference value)
-0.04	0.024904242	-18.98
-0.03	0.021516735	-30.04
-0.0175	0.017830772	-42.00
-0.01	0.016487801	-46.36
-0.0025	0.015523422	-49.50
0	0.015335994	-50.11

Table 4.7: Dissipation/diffusion inside the combustion chamber observed for the streamline close the nozzle wall.

It can be noticed that the dimensionless entropy fluctuation signals are not perfectly steady, this phenomenon is understandable as the velocity is quite small close to the wall. However, it can be seen that the average peak amplitude remains the same. In addition, this time as the velocity is not as large as for the axial value, some dissipation might still occurs inside the nozzle. Table 4.8 gives a summary of the axial dissipation/dispersion where the reference state is taken this time at the nozzle inlet. One can notice that the dissipation/diffusion phenomena are very important especially inside the converging region (42.25%) while in the diverging region it is 18.31%. Compared to the evaluation performed on the axis, the wave attenuation is increased by 47.66 points. Thus, the LES TATFs predicted in the chapter 5 are likely to present slight discrepancies, all the more important as the forcing frequency is important.

Position (m)	**Average maximum peak amplitude**	**Dissipation/diffusion (%)**
0	0.015335993	0 (reference value)
0.1024	0.008856476	-42.25
0.126	0.008158938	-46.80
0.185	0.006047780	-60.56

Table 4.8: Dissipation/diffusion at the streamline close the nozzle wall.

4.3.4 Multi-harmonic entropy forcing LES

Several types of forcing have been studied by Polifke [Polifke 2014] or Jaensch *et al.* [Jaensch 2014]. In this section, a frequency comb forcing of 7 frequencies going from 411.52 to 905.35 Hz (with a frequency step $\Delta f = 82.30$ Hz) is used for the determination of the TATFs of the nozzle. The main reason for the low frequency limit is defined by the necessity to have a long enough temporal signal compatible with to the computational cost. The frequency step is limiting the total signal length needed to be able to distinguish properly the injected frequencies. One point between each forced frequency in the computed spectra is the least to be achieved and it can be done at a reasonable cost.

4.3.4.1 Phases optimization

In order to stay in the linear domain, a maximum entropy fluctuation of 5% (65 K) of the combustion chamber mean temperature is required at the inlet. For 7 frequencies in the comb, the natural way to choose the amplitude is to divide the total temperature fluctuation by the number of frequencies, thus giving an amplitude of 9.29 K. Using 7 random phases with an amplitude (see Table 4.9) of 1 K for each frequency gives a temperature signal represented in Fig. 4.21. It can be seen in this figure that the maximum amplitude reached is 5.8 K. With these phases, it is possible to increase the amplitude for each frequency up to 11.20 K rather than the theoretical 9.29 K.

Frequency (Hz)	**Initial phase value** (rad)	**Optimized phase value** (rad)
411.52	0.0001412331	1.736084
493.83	0.5342746	0.6656057
576.13	3.77841	6.003267
658.44	5.602159	1.792779
740.74	6.081845	0.7952823
823.05	1.191856	2.746402
905.35	3.235689	5.077471

Table 4.9: Values of the original and the optimized phases using the Crest-Factor minimization. The number of digits is due to the capability of the solver CEDRE to handle double precision floats.

In order to maximize the signal to noise ratio, a different approach is used here. A phase optimization based on the Crest-Factor minimization proposed by Guillaume *et al.* [Guillaume 1991] is applied. An optimization algorithm is developed allowing to maximize the signal to noise ratio by optimizing the phases for the different frequencies of interest[1]. This method can be directly applied as the injection of the temperature fluctuations at the inlet

[1]The reader is referred to the paper of [Guillaume 1991] for details regarding the optimization algorithm.

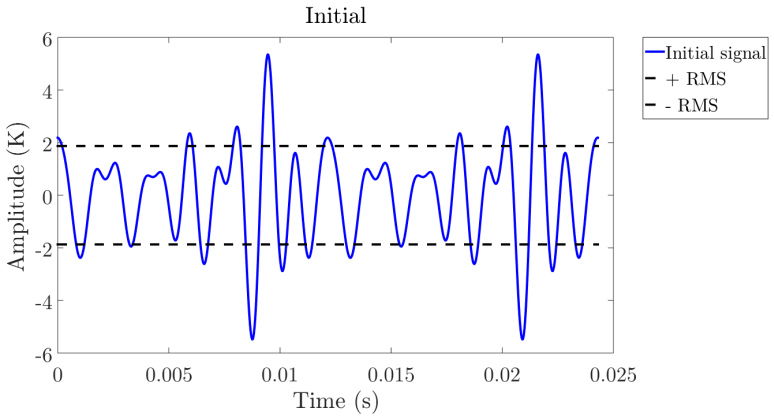

Figure 4.21: Initial signal with 7 random phases for an amplitude of 1K for each frequency.

of the domain through the NSCBC is a multisine periodic signal. Indeed, the injected temperature signal is a sum, in this case, of 7 cosine functions with an amplitude of 1 K. The l_p-norm of the function $x(t)$ taken over the interval [0, T] is denoted by $l_p(x)$ and is defined as:

$$l_p(x) = \left[\frac{1}{T} \int_0^T | x(t) |^p \, dt \right]^{\frac{1}{p}}, p \geq 1 \tag{4.4}$$

During the optimization process, the l_p-norm is computed up to $p = 256$. The optimization is started using the initial phases of Table 4.9 and the optimized phases are shown in the last column. No gain in the crest-factor reduction was seen for p number larger than 256. Fig. 4.22 gives a view of the optimized temperature signal after the crest-factor minimization. It can be seen that the maximum amplitude is this time around 3 K meaning that only 3 frequencies can be in-phase over time. This method allows to increase the amplitude of the forcing up to 21.5 K for each frequency rather than 11.20 K and to double the noise to signal ratio.

4.3.4.2 Results

The numerical computation was started at GENCI on the supercomputer OCCIGEN [CINES 2014] and completed at ONERA on the supercomputer Stelvio. Fig. 4.23 shows the injected temperature at the inlet of the domain over time. The maximum injected temperature fluctuation is 63.76 K. The amplitude represented in Fig. 4.22 needs to be multiplied by a factor of 21.5 and a comparison of the theoretical signal and the measured one is plotted in Fig. 4.23. One can notice a good agreement in terms of the shape of the temperature signal and that the phase optimization has been successfully applied.

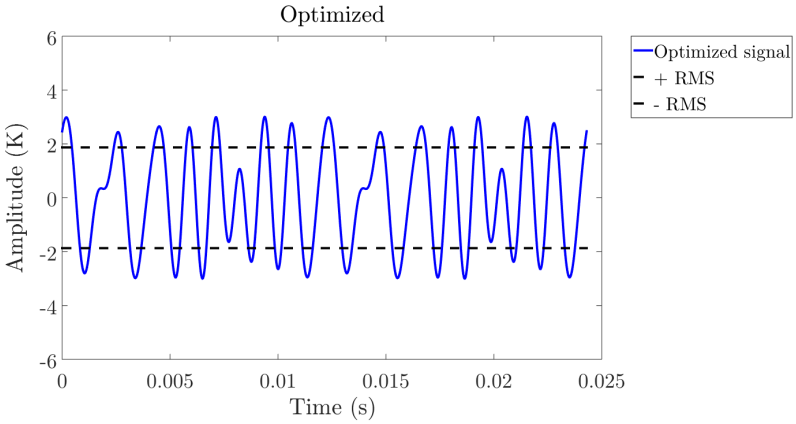

Figure 4.22: Optimized signal using the new phases. The maximum total amplitude is 3 K.

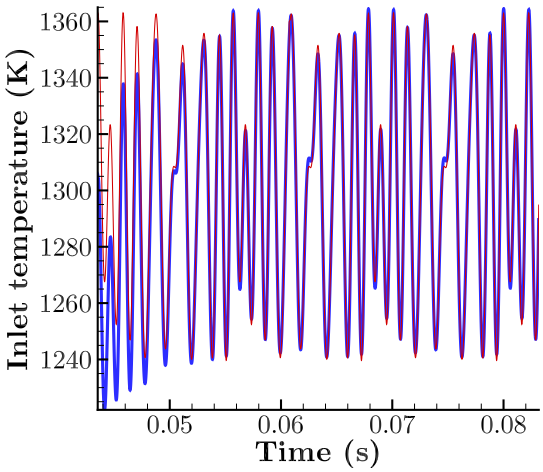

Figure 4.23: Superposition of the temporal evolution of the temperature at the inlet boundary for the LES computation (*blue*) and the theoretical temperature signal (*red*).

The entropy fluctuations are obtained by the same approach as in the 900 Hz harmonic entropy forcing. It is represented in Fig. 4.24.

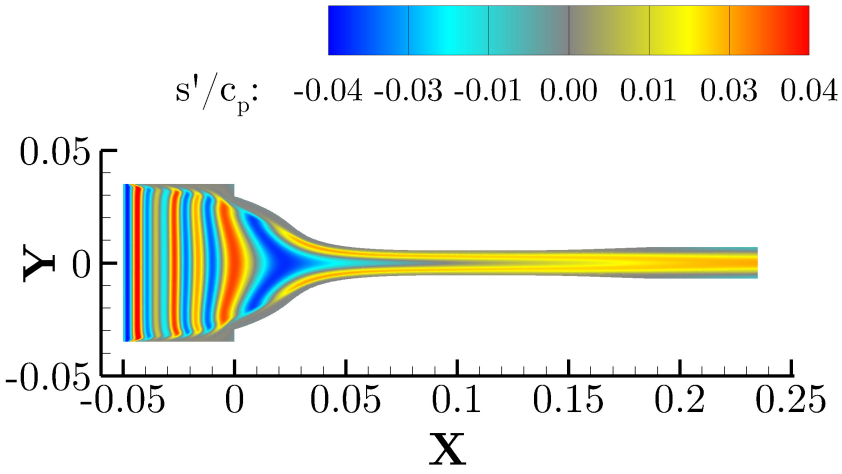

Figure 4.24: Longitudinal cross section view of the dimensionless entropy fluctuations for a 411 to 905 Hz entropy forcing at the inlet at a random time.

Finally, Fig. 4.25 shows the Q-criterion (second invariant of the velocity gradient tensor) [Cantwell 1993] colored by the axial velocity. One can notice that strong turbulent structures are present downstream of the nozzle throat showing the interest of a LES approach for the study of ICN even in the framework of a simple nozzle case. Indeed, the effect of these structures and their interactions with the entropy fluctuations are captured by the plane surfaces of sensors inside the cylindrical part as well as in the combustion chamber. The acoustic analysis performed in chapter 5 therefore includes these effects but also a variable specific heat ratio (γ). They are likely to be partly responsible for the discrepancies that might arise between LES and the results from the model.

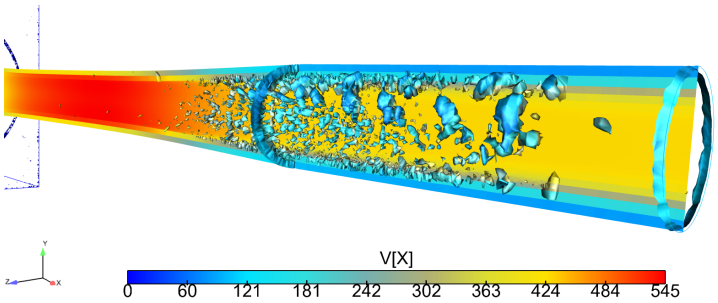

Figure 4.25: Longitudinal cross section view close to the nozzle outlet of the Q-criterion colored by the axial velocity.

Chapter 5

Comparison of the results from the different methods and validation of the 2D model

Success is a science; if you have the conditions, you get the result.

Oscar Wilde

Contents

This chapter presents the comparisons between the two-dimensional model, the one-dimensional model MarCan and LES computations. Since the 2D model proposed in this work relies on streamlines in the flow, the capability of the model to reconstruct the convected entropy waves using the streamlines is first validated by comparison with the effective entropy wave computed from the 900 Hz entropy forced LES. In a second step, two comparisons of the models are presented assuming perfectly non-reflective boundary conditions: (1) a strictly one-dimensional mean flow is used for the 2D model to assess its capability to retrieve the one-dimensional analytical results provided by Onera's 1D tool MarCan, (2) the RANS mean flow is used as an input for the two-dimensional model. Finally, the impedances present in the LES are taken into account in the 2D model and results are compared with the transfer functions obtained from LES.

5.1 Validation of the convection of the entropy waves by the 2D model

This section aims to validate the convection of the entropy waves implemented in the 2D model using the streamlines. This validation is achieved by comparison with the results of the 900 Hz harmonic entropy forcing LES, for identical amplitudes of the inlet entropy wave. On one hand, a harmonic entropy wave is forced into a 3D LES at 900 Hz. The transport of these waves (i.e convection, dispersion and dissipation) are thereby directly determined by the solver CEDRE. On the other hand, streamlines are first extracted from the mean flow obtained from LES. Then, unsteady entropy fluctuations are imposed as boundary conditions at the left end of streamlines and are transported along the lines thanks to a dedicated 1D solver. This validation step is crucial because the 2D model relies on these streamlines to determine the acoustic and entropy transfer functions of the nozzle. A comparison of the two methods is made in Fig. 5.1 where modeled and simulated entropy fluctuations flow fields are combined in one figure. The *top-half* of this figure shows the entropy waves artificially transported along the streamlines whereas the *bottom-half* displays the entropy fluctuations directly obtained with CEDRE. As the model only considers axisymmetrical geometries, it is not possible to reproduce the squared-shape combustion chamber and an approximated geometry is used. The real geometry is indicated with dotted lines in the figure, highlighting the difference of geometry between the two cases. The use of this configuration is justified in the section 5.2.2.

The shape of the waves is well predicted by the model, however one can notice several discrepancies. First, it can be seen in LES an important amplitude decrease of the entropy wave in the overall domain. This effect is important especially inside the combustion

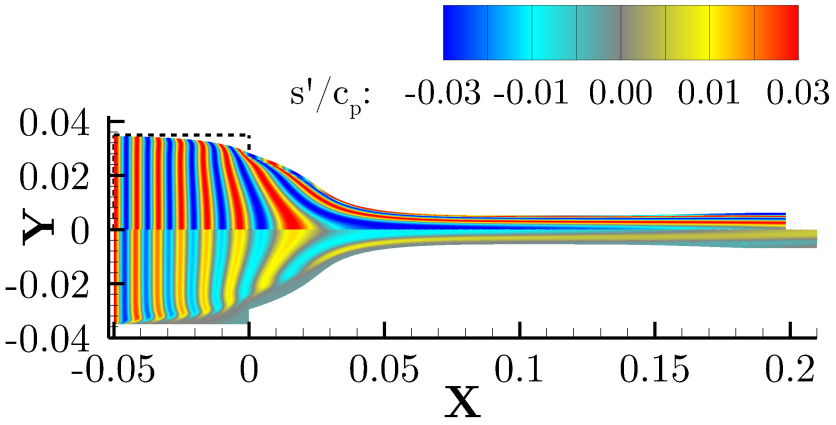

Figure 5.1: Comparison between the convected entropy waves using the streamlines generation method computed by the two-dimensional model at 900 Hz (*top*) and the 900 Hz harmonic entropy forcing LES (*bottom*). The dashed lines represent the combustion chamber.

chamber and close to the walls as already explained in chapter 4. Outside the boundary layer, the thermal diffusion is expected to be less important inside the nozzle and the downstream additional constant radius cylinder where the axial velocity is greatly larger than upstream. Secondly inside the nozzle and close to the wall contrary to the LES observation, the modeled entropy waves are still present and convected far downstream. This is because in the LES the thermal diffusion tends to smooth the entropy waves (temperature gradient) while this thermal diffusion is not considered in the model. By neglecting this physical phenomenon in the model, an overestimation of the source terms close to the wall inside the nozzle is expected. The thermal diffusion and the mesh dissipation occurring inside the combustion chamber is not a crippling issue. Indeed, it is possible to rescale the inlet entropy fluctuation amplitude in the model by the effective value entering the nozzle in the LES to overcome this problem. Doing so, Fig. 5.2 is obtained.

In this figure, the LES field is voluntary saturated to the values entering the nozzle. As a conclusion, the streamlines generation method works pretty well regarding the prediction of the shape of the entropy waves except in the region close to the wall of the nozzle, and as long as the thermal dissipation arising inside the combustion chamber is compensated for. This last point is not satisfactory and represents one of the main improvements that should be brought to the 2D model before it can be used efficiently as a stand-alone tool.

The convergence of the solution of the downstream transfer function (P_2^+/σ) regarding the number of streamlines used for computing the entropy source terms is represented in Fig. 5.3. The amplitude is more affected by the number of streamlines than the phase. It can be seen that convergence of the solution is reached with 50 streamlines, in this case.

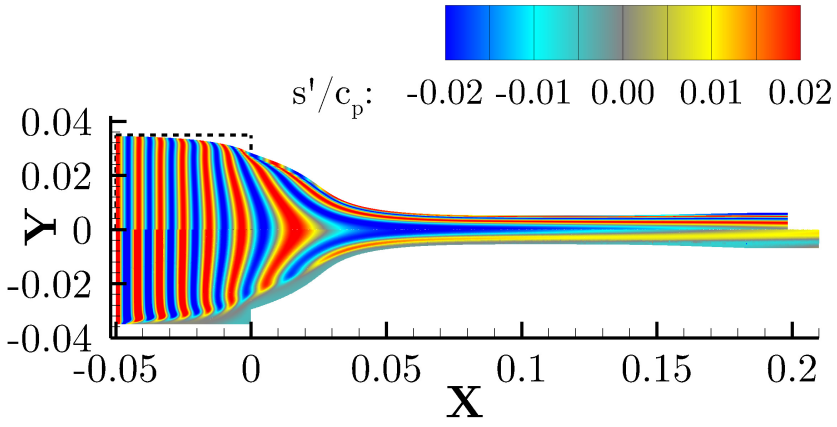

Figure 5.2: Comparison between the convected entropy waves using the streamlines generation method computed by the two-dimensional model at 900 Hz (*top*) and the 900 Hz harmonic entropy forcing LES (*bottom*). The levels are scaled by the axial amplitude of the entropy fluctuation in the LES at the entrance of the nozzle (x=0).

Of course, such an investigation should be performed for any other geometry.

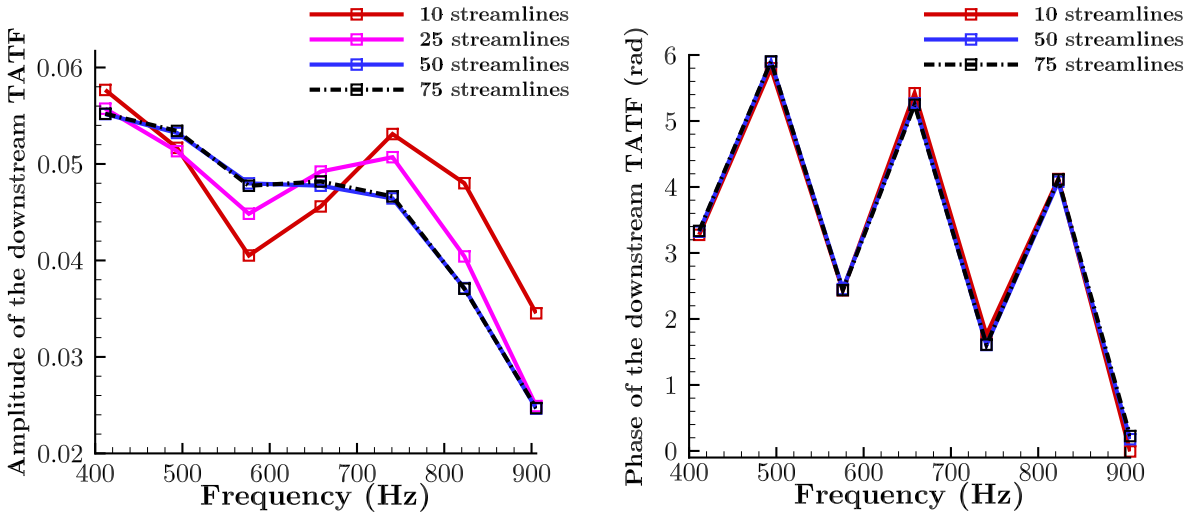

Figure 5.3: Amplitude (*left*) and phase (*right*) of the downstream transfer function (P_2^+/σ) as a function of the number of streamlines used.

5.2 Comparison of the 1D and 2D models in the context of perfectly non-reflective boundary conditions

5.2.1 One-dimensional mean flow

Before introducing more complexity, it is interesting to validate the implementation of the new 2D model by comparing the results it provides with the ones obtained from usual 1D analytical models. This one-dimensional mean flow is extruded in the radial direction to provide a 2D mean flow for the model. The model is applied with this mean flow and the equations to resolve remain unchanged. Indeed, degenerating the two-dimensional axisymmetric model (Eqs. 3.24 and 3.51) for one-dimensional flows gives the same equations as the ones of Marble & Candel [Marble 1977] (see Appendix D for additional details). Therefore, one should retrieve the usual one-dimensional solutions when using the 2D model with one-dimensional flows. A test case is proposed here as a first validation of the model for one-dimensional flows. The case considered corresponds to the DISCERN nozzle with the flow regime described in the previous chapter.

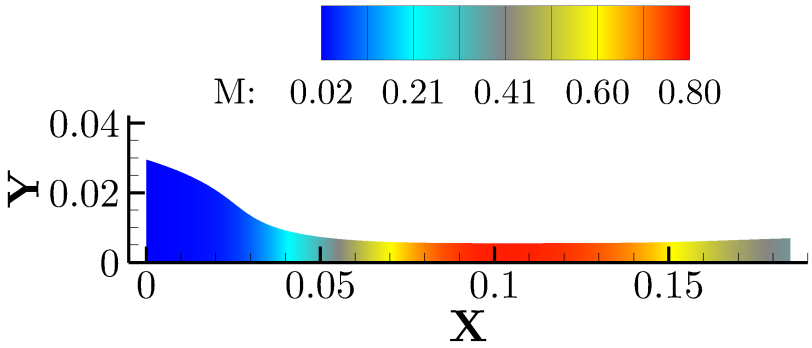

Figure 5.4: View of the Mach number profile inside the DISCERN nozzle in the one-dimensional case.

The 2D mean flow is obtained by solving the isentropic quasi one-dimensional perfect gas flow equations in a variable section duct and extruded in the radial direction. The evolution of the Mach number through the nozzle is reproduced in Fig. 5.4. Figures 5.5 and 5.6 compare the transfer functions obtained using the present two-dimensional model and using the one-dimensional analytical tool MarCan [Giauque 2012] developed at ONERA. The amplitude of the transfer functions P_1^-/σ and P_2^+/σ which correspond to the generated acoustic waves traveling respectively upstream and downstream are shown in Fig. 5.5. It can be observed that for this nozzle operating condition $|P_1^-/\sigma|$ is around 10 times smaller than $|P_2^+/\sigma|$. The phase of the transfer functions is visible in Fig. 5.6. One can see a perfect agreement between the analytical one-dimensional method and the semi-analytical two-

dimensional model both in amplitude and phase. From these results, one can consider that the implementation of the model is correct.

For the comparisons performed in the rest of this chapter, the solutions provided by MarCan are obtained using this isentropic quasi one-dimensional perfect gas flow.

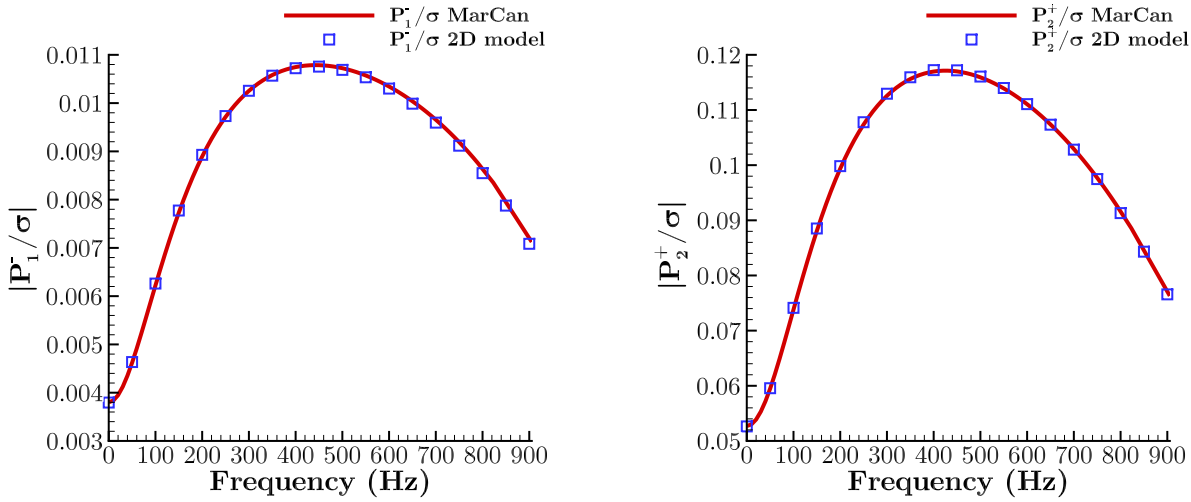

Figure 5.5: Amplitude of the transfer functions with a one-dimensional mean flow. (*left*) $|P_1^-/\sigma|$ and (*right*) $|P_2^+/\sigma|$.

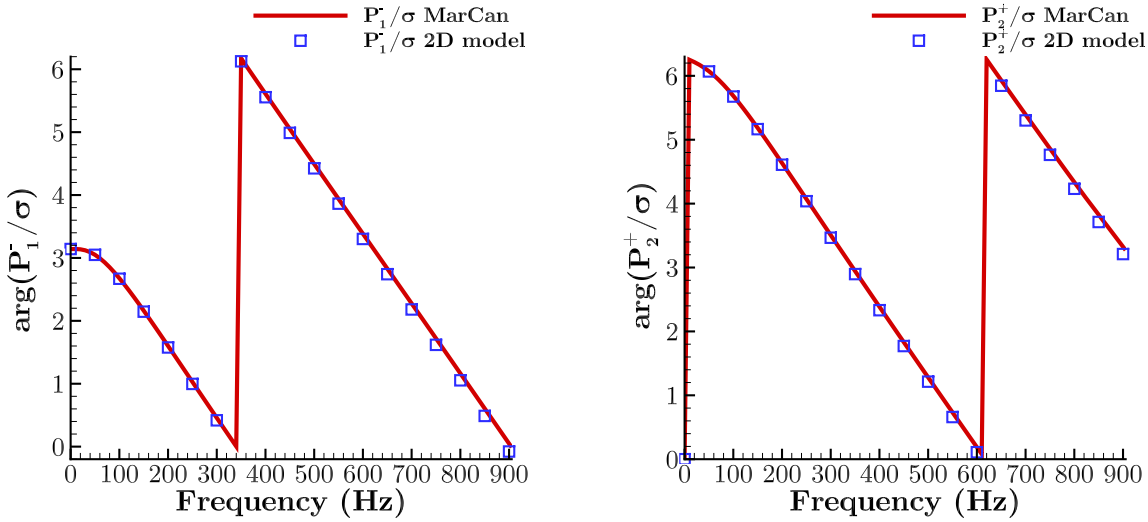

Figure 5.6: Phase of the transfer functions with a one-dimensional mean flow. (*left*) $\arg(P_1^-/\sigma)$ and (*right*) $\arg(P_2^+/\sigma)$.

5.2.2 Two-dimensional mean flow

From the observation of the flow field of the RANS computation or LES, one can see that the entropy waves are already distorted when they enter the nozzle. For the sake of simplicity,

the injected waves at the inlet of the model are supposed to be planar[1], it is then logical to consider the presence of the combustion chamber in the model as it is present in the LES. Unfortunately, the combustion chamber has a square shape and the model can only handle axisymmetric geometries. In addition, the flow presents recirculation zones in which it difficult to clearly define streamlines. In order to consider this region in the 2D model, its shape has to be modified. This is done by extending the nozzle lines inside the combustion chamber using a fourth order polynomial equation constrained by smooth junctions at both extremities. The added part is similar to the curvature of the most external (radially) streamlines presented in Fig. 4.10. The extended geometry is represented in Fig. 5.7 on the left with the black lines delimiting the edges of the real combustion chamber. Fig. 5.7 on the right shows a longitudinal view of the extended nozzle colored in blue and the initial combustion chamber colored in red. The mean flow obtained from the RANS computation is interpolated on this new three-dimensional mesh and is azimuthally averaged to obtain a two-dimensional flow field. With these modifications, it is now possible to apply the two-dimensional model with either acoustic or entropy forcing. The last case represents the main interest of this study.

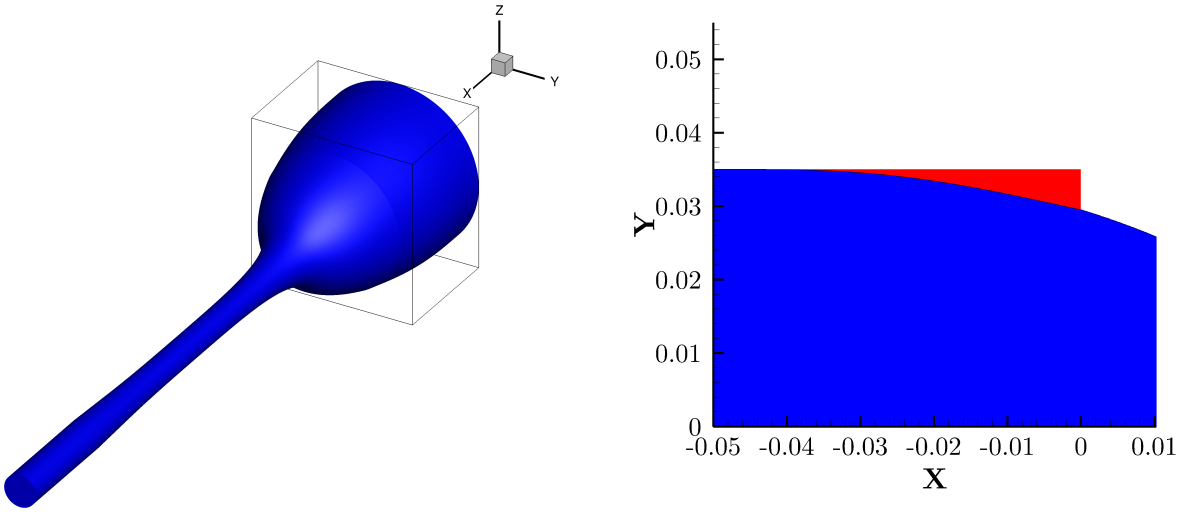

Figure 5.7: Geometry of the considered nozzle. (*left*) Three-dimensional view of the nozzle (*blue*) with the edges of the initial combustion chamber (*black square*). (*right*) Close axial cut view of the combustion chamber where the zone in red represents the combustion chamber and in blue the extended nozzle.

[1]This hypothesis is not restrictive and any axisymmetric entropy wave pattern can be injected through a modulation of the phase term of the entropy fluctuation in Eq. 3.64 (not tested during this thesis).

5.2.2.1 Acoustic forcing at the inlet

An acoustic wave is imposed at the inlet of the configuration. The results obtained with the two-dimensional model and MarCan are illustrated in Fig. 5.8. Looking at the amplitude, discrepancies are quite small for P_1^-/P_1^+ between MarCan and the 2D model. The trend of the phase is well retrieved for P_1^-/P_1^+. Although remaining acceptable, discrepancies are greater between MarCan and the 2D model for P_2^+/P_1^+ both in amplitude and phase. Despite the 1D assumption made in the 2D model for the acoustic perturbations, contributions of the radial gradients of the mean flow remain in the model and explain the differences observed between the 2 models. It is also worth mentioning that due to the hypotheses made, the 2D model does not verify the conservation of acoustic energy through the nozzle. The 2D model only uses the transport information along the streamlines (Eq. 3.57 is not used). Because of that the strict conservation of the energy along the nozzle is not enforced which might explain the discrepancies with the 1D model in which such conservation principle is directly used. However the discrepancies are quite small and still remain acceptable.

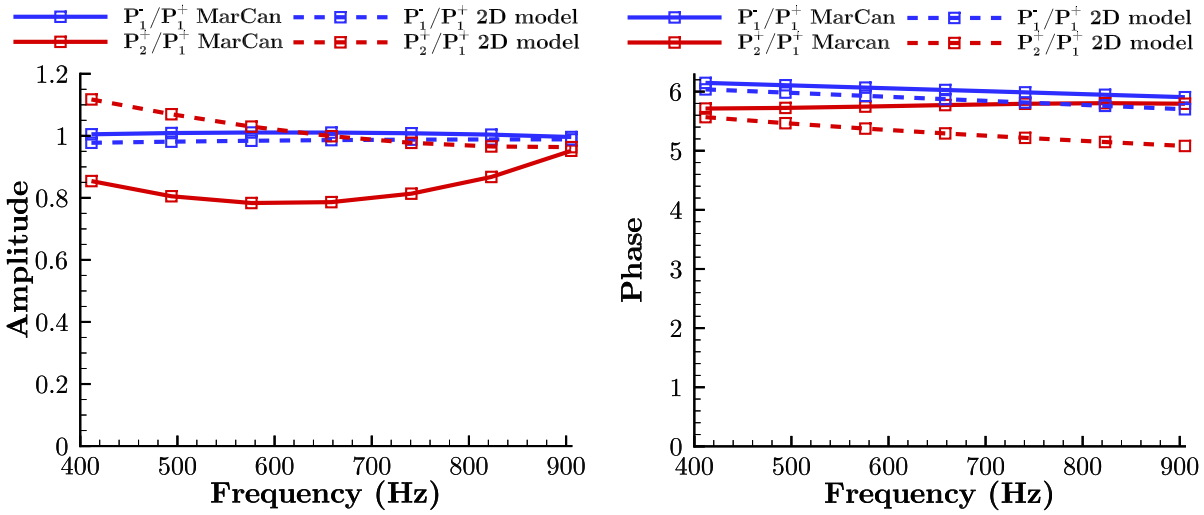

Figure 5.8: Illustration of the amplitude (*left*) and phase (*right*) of the ATFs obtained using the two-dimensional model and MarCan for an acoustic forcing at the inlet.

5.2.2.2 Acoustic forcing at the outlet

An acoustic forcing is now applied at the outlet boundary. The solutions are compared to the ones provided by MarCan in Fig. 5.9. For the phases, the trend for both outgoing waves is well retrieved. For the amplitude, $|P_1^-/P_2^-|$ obtained with the 2D model is similar to the value provided by MarCan. The amplitude $|P_2^+/P_2^-|$ is slightly different between MarCan and the 2D model especially at low frequency. Once again, although the assumptions

made in the 2D model explain the discrepancies observed with the 1D solution and these differences remain acceptable.

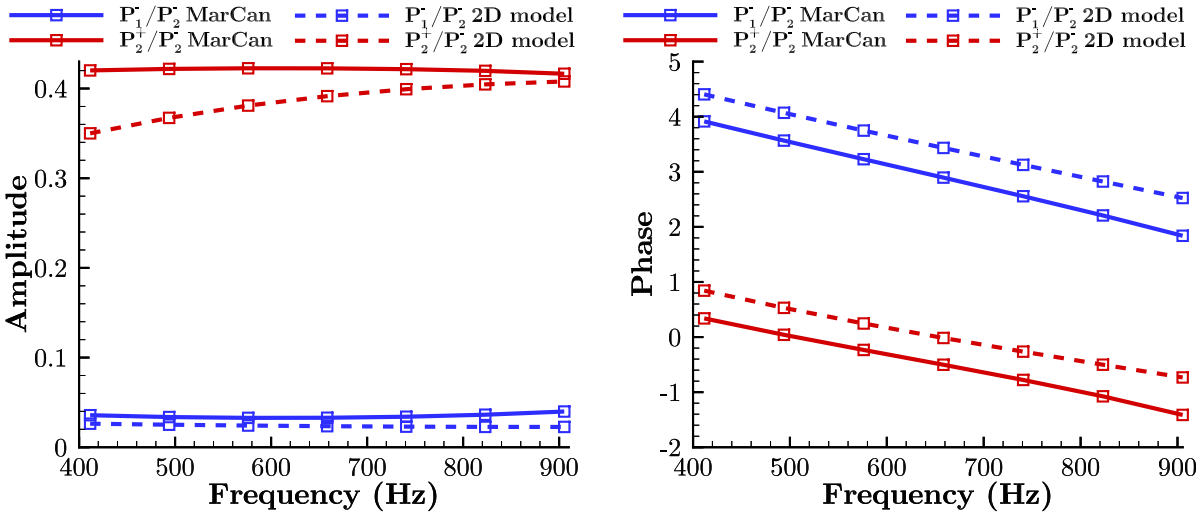

Figure 5.9: Illustration of the amplitude (*left*) and phase (*right*) of the ATFs obtained using the two-dimensional model and MarCan for an acoustic forcing at the outlet.

Globally, in the case of an acoustic forcing scattering predicted by the 2D model is very close to the 1D results. This result is quite logical since even though the model uses 2D average fields, they mostly concern convected quantities. Acoustic in this model is still assumed to be 1D (i.e. having no radial dependence).

5.2.2.3 Entropy forcing

The 2D model proposed in this study has been developed by the author because of the suspicion that the radial evolution of the convection velocity might have an influence on the indirect acoustic transfer function. The following comparison is therefore the most interesting one as far as the 2D model is concerned. The amplitude and phase of the TATFs obtained with MarCan and the 2D model are represented in Fig. 5.10. It was already observed in the previous subsection 5.2.1 that for this nozzle operating condition, the amplitude of downstream TATF $|P_2^+/\sigma|$ is ten times larger than the upstream TATF $|P_1^-/\sigma|$ for MarCan. The same behavior is found by the 2D model. One should realize that this result by itself should not be generalized since it is strongly influenced by the shape of the nozzle, the maximum flow velocity

The first impression is that the distortion of the entropy waves by the convection field does have an influence upon the generated noise. Looking at the amplitude, the generated noise is divided by a ratio of 2 (-6 dB) with the 2D model in the upstream region, compared to

MarCan. This reduction reaches a maximum ratio of 2.4 (-7.6 dB) downstream of the nozzle. In order to help the reader and provide order of magnitude, it is recalled that, for example, that a value of 0.055 corresponds to 111 dB for a temperature fluctuation amplitude of only 1 K in the combustion chamber. This order of magnitude shows the efficiency of the generation process of indirect noise and explains by itself the renewed interest it undergoes. The phases of both outgoing waves are also quite different than in MarCan but the tendency is however in agreement with MarCan.

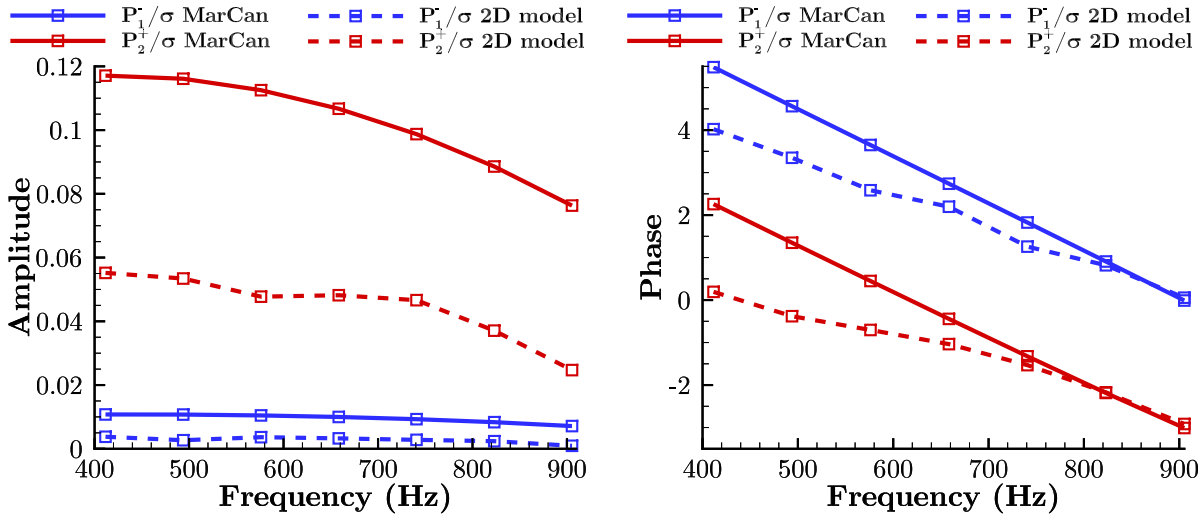

Figure 5.10: Illustration of the amplitude (*left*) and phase (*right*) of TATFs obtained using the two dimensional model and MarCan.

5.3 Analysis of the results with partially reflective boundary conditions

It has already been said that the LES reflection coefficient at the inlet and at the outlet cannot be set to 0. Otherwise, a potential drift of the mean quantities can occur leading to computational instabilities. This section aims at characterizing the effective reflection coefficients present in the Large Eddy Simulations in order to take them into account in MarCan and the two-dimensional model.

5.3.1 1D characteristics filtering

All over the study, acoustic waves are considered to be 1D. In order to separate P^+ over P^-, a 1D characteristics filtering is applied in the combustion chamber and in the cylinder downstream of the nozzle. To apply the 1D characteristics filtering method, one needs to know the 1D fluctuating and the mean part of the pressure and velocity. From the LES

computations, they are obtained using the plane sensors described in chapter 4 where a spatial averaging of the variables is applied. Due to the small velocities of the flow in the combustion chamber, thin boundary layers and small radial gradient; the averaging procedure is quite immediate and the quantities are filtered using the characteristic method to obtain P_1^-, P_1^+ and consequently, the inlet reflecting coefficient R_{in}.

One should pay more attention in the region downstream of the nozzle where a flow with thick boundary layers is observed. The averaging procedure is not that easy in this region. Fig. 5.11 shows the fluctuating values of the pressure (*left*) and axial velocity (*right*) using different number of points in the radial direction in the averaging process. In this figure, it is expressed in terms of percentage of the downstream total surface area. It can be seen that on the left-hand side of Fig. 5.11, the three curves are superimposed showing that hypothesis of one-dimensional waves is ensured for the pressure fluctuations.

On the other hand, the axial velocity fluctuations are strongly dependent on the surface area used for the averaging procedure (see right of Fig. 5.11). Indeed, the axial velocity is the largest at the centerline and decreases as one goes to the wall.

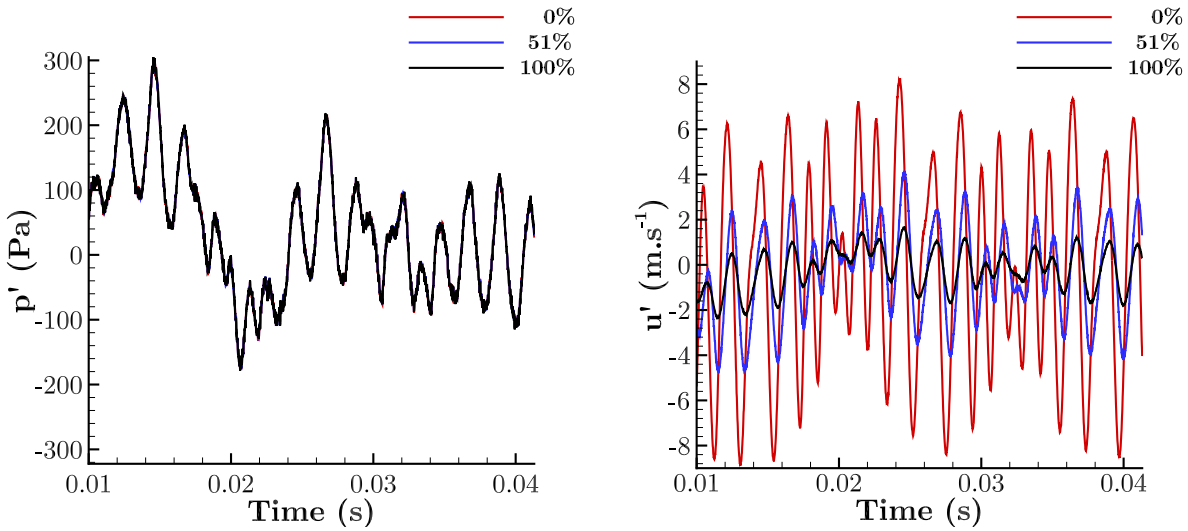

Figure 5.11: Illustration of the downstream one-dimensional azimuthally averaged value of the pressure (*left*) and axial velocity (*right*) fluctuations at plane of sensors 3 (see 4.3) for the multi-harmonic entropy forced LES computation. The numbers are expressed in terms of the surface area percentage used in the averaging process, where 0% represents the axial value and 100% is the complete surface.

Another possible way to illustrate this is to look at the two-dimensional spatial root mean square (rms) value of the pressure and the axial velocity. As an illustration, rms values of the pressure and axial velocity are plotted for the plane of sensors 3 in Fig. 5.12. The range of variation of the velocity rms is much larger than for the pressure rms. One can

also remark the remaining pattern of the square combustion chamber in the illustrations. A strong spot for u' located at $(y, z) = (0, -0.005)$ (inside the boundary layer) is also visible, this might be due to an insufficient converged flow in this region.

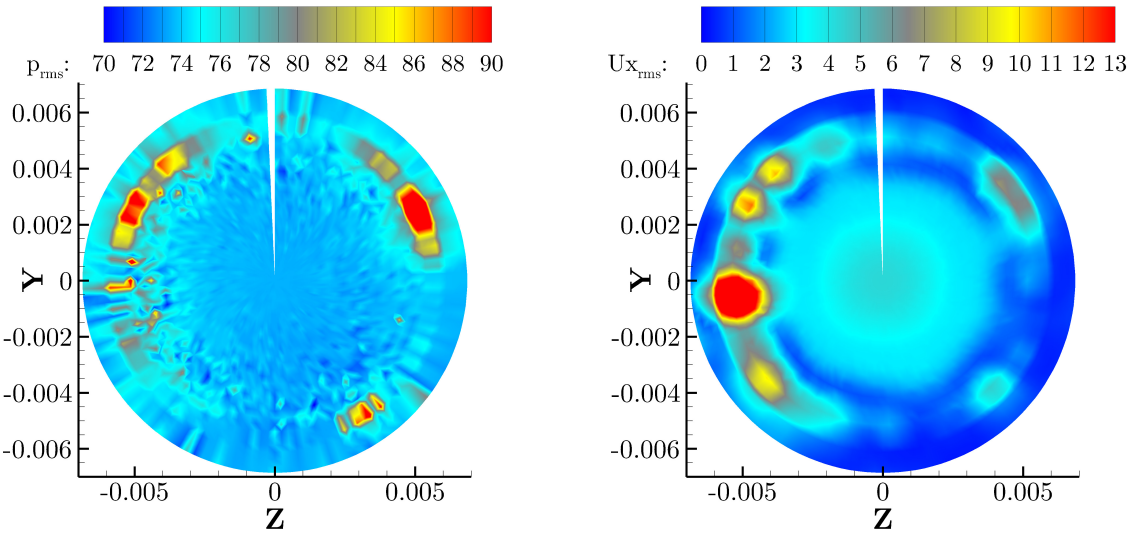

Figure 5.12: Rms value of the pressure (*left*) and the axial velocity (*right*) at plane sensor 3. Both illustrations are voluntarily saturated.

It was seen that the spatially averaged values of the velocity could not be used for the 1D characteristics filtering. It is then necessary to adopt an another approach to reconstruct the acoustic waves using only the pressure fluctuating signals.

5.3.2 Acoustic waves reconstruction and downstream reflecting coefficient

In this section, the method of the acoustic wave reconstruction in the downstream duct is described. In this duct, the velocity fluctuations are not 1D because of the thick boundary layer, the characteristics filtering therefore cannot be performed. Another solution is to perform the waves separation using the pressure fluctuations solely, which is essentially 1D. Assuming a harmonic regime, the system to be solved writes:

$$\begin{cases} p' & = p^+ + p^- \\ \dfrac{\partial p'}{\partial x} & = -iK_x^+ p^+ - iK_x^- p^- \end{cases} \tag{5.1}$$

where the wavenumbers are expressed as:

$$K_x^+ = \frac{\omega}{u_0 + c_0} \tag{5.2}$$

$$K_x^- = \frac{\omega}{u_0 - c_0} \tag{5.3}$$

K_x^+ and K_x^- are given by the mean flow, p' is the pressure fluctuations signal presented previously and $\frac{\partial p'}{\partial x}$ is obtained by finite difference method. This gives a closed system with two unknowns p^+ and p^- for two equations.

Figure 5.13: Illustration of the five-point stencil in one-dimension.

For the resolution process, 21 plane surfaces are available in the region downstream of the nozzle. However the first two surfaces are not considered because the flow is not perfectly stabilized in this region. The system is solved by setting $x = 0$ at each position to simplify the resolution. This has only an effect on the phase of the solutions which is considered later during the phase-shifting procedure of all the waves to the same reference position. The resolution is made in the spectral domain. A five-point stencil illustrated in Fig. 5.13 is used for the evaluation of the pressure derivative. The formula is easily retrieved using the Taylor expansion of $f(x + \Delta x)$, $f(x + 2\Delta x)$, $f(x - \Delta x)$ and $f(x - 2\Delta x)$ giving:

$$f'(x) = \frac{-f(x + 2\Delta x) + 8f(x + \Delta x) - 8f(x - \Delta x) + f(x - 2\Delta x)}{12\Delta x} \tag{5.4}$$

u_0 and c_0 correspond respectively to one-dimensional averaged value of the axial velocity and speed of sound[2]. Fig. 5.14 illustrates the Fast Fourier Transform (FFT) of the one-dimensional value of the pressure signals recorded at position 3, 11 and 19.

The resolution process allows to obtain p_2^+ and p_2^- at 15 different positions. As an example, Fig. 5.15 shows the results for positions 11 and 19. It is important to notice that in the figure, the amplitude has **not** been non-dimensionalized by γP_0. The evolution of the 2 acoustic waves is very similar the 2 positions, in both amplitude and phase.

The averaged amplitude of p_2^+ and p_2^- is directly obtained by averaging the 15 solutions. The phase of each wave for each position is phase-shifted to a common reference position and then averaged. From these data, it is possible to compute the outlet reflection coefficient $R_{out} = \frac{p_2^-}{p_2^+}$ which is illustrated in Fig. 5.16. Since the resolution process is not perfect, error bars are included in the plots. A discussion on the reflection coefficients is proposed

[2]During the thesis, other values of u_0 have been tested without having a strong impact on the results.

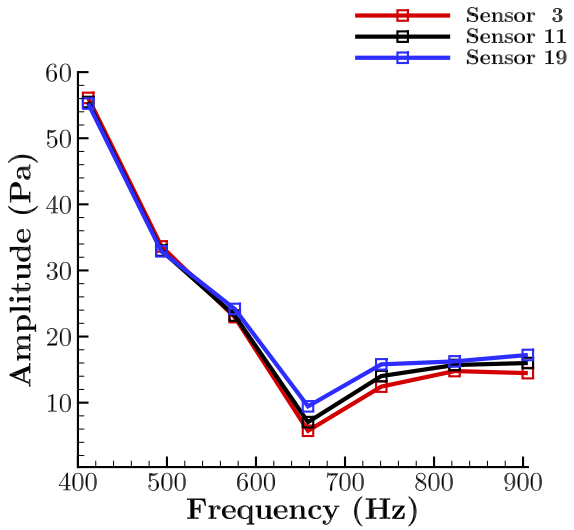

Figure 5.14: FFT of the one-dimensional value of the pressure signals recorded at position 3, 11 and 19.

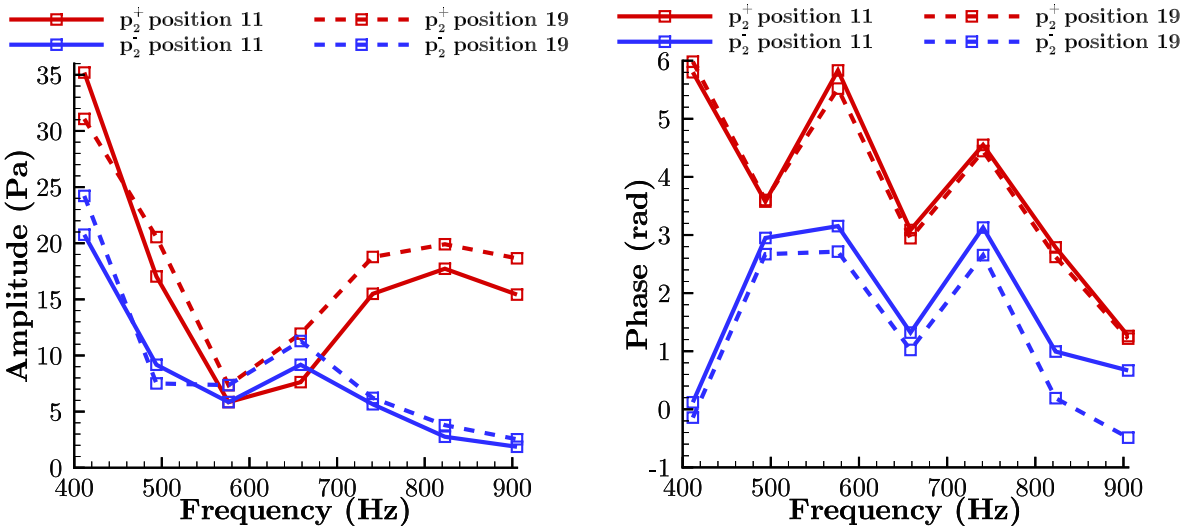

Figure 5.15: Illustration of the amplitude (*left*) and phase (*right*) of the solutions p_2^+ and p_2^- at two different positions.

in the next paragraph.

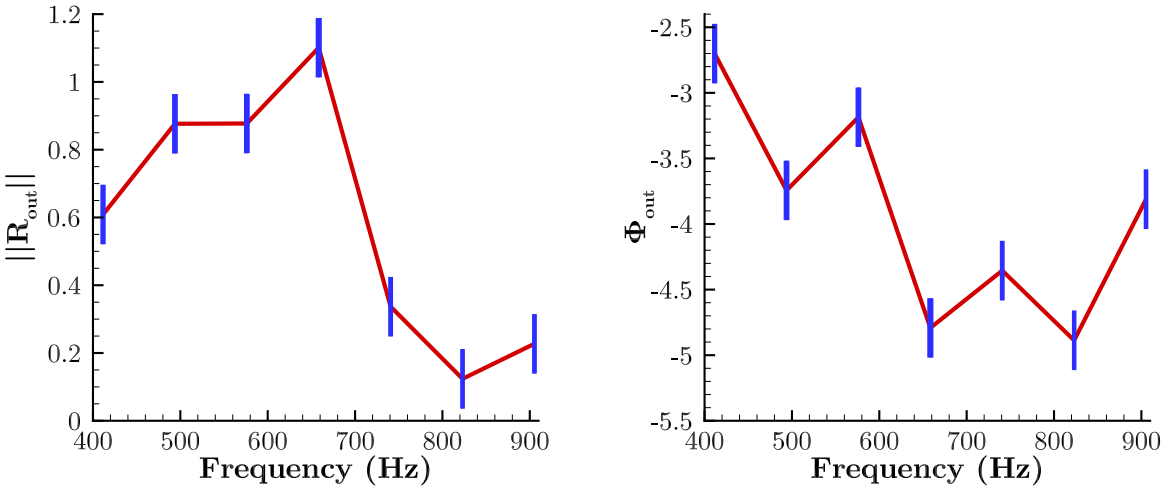

Figure 5.16: Amplitude (*left*) and phase (*right*) of the outlet reflecting coefficient. The blue lines represent the error bars.

5.3.3 Effective reflection coefficients

Now that the reflection coefficients have been obtained from the multi-harmonic entropy forcing 3D LES, it is relevant to compare the amplitudes and phases of R_{in} and R_{out} to the analytical expressions given by [Selle 2004]. The expressions of the terms are presented in Appendix B where the validation of the NSCBC implementation is performed in the one-dimensional case.

The first analysis is made for the inlet reflection coefficient, visible in Fig. 5.17. One can note that the point for $f = 905$ Hz is not displayed in the graphs. Indeed, at this frequency, the small pressure amplitudes involved inside the combustion chamber, P_1^+ are masked by the background noise (of numerical nature and of the order of 1 Pa in amplitude) and the $\| R_{in} \|$ is likely not to be physical. In contrary to Appendix B where the NSCBC performs well in the one-dimensional case the agreement is not that good in the 3D LES computations. For the amplitude (*left*), the first two points are close to the theoretical values in terms of amplitude and phase. After that, the values in amplitude and phase are strongly different than the theoretical value of Selle *et al.* meaning that the background noise strongly pollute the pressure signal. It is the author belief that this is due to the background numerical noise which has a constant amplitude with frequency whereas the "physical" pressure fluctuation decreases with the frequency. This combined dependence on frequency makes the reflection coefficient more sensitive to the numerical background noise as the frequency increases.

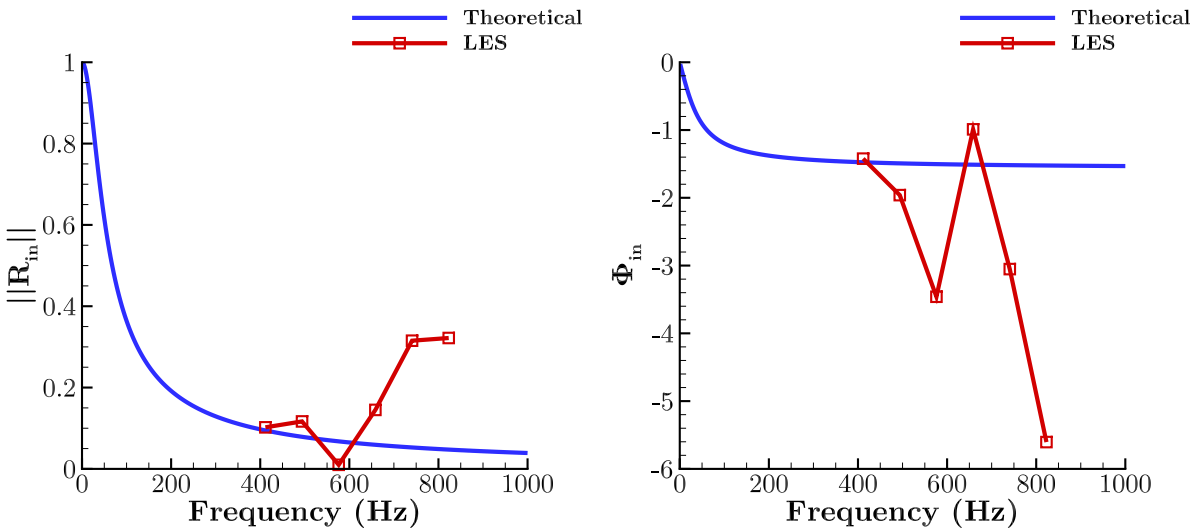

Figure 5.17: Inlet reflection coefficient of the LES and analytical expressions given by Selle *et al.* [Selle 2004]: Amplitude (*left*) and phase (*right*).

Considering now R_{out}, the amplitude and phase are represented in Fig. 5.18. For the phase, although not perfect, the comparison holds for frequency higher than 600 Hz. At lower frequency, the comparison is quite arguable. For the amplitude, the comparison reveals strong discrepancies both in term of amplitude and trend for all the frequencies. One possible explanation is related to the fact that in the cylindrical region where the acoustic analysis is made, turbulent boundary layers are present that generated additional noise in the upstream direction which might be mistaken with reflected noise from the outlet boundary. One should also remind that a "simple" determination of the reflection coefficient at the outlet is not possible because of the acoustic identification method used.

It can also be seen that for $f = 658$ Hz, the reflection coefficient is slightly greater than unity. It might seem to be not physical, but if one performs an acoustic energy balance [Cantrell 1964, Goldstein 1976, Minotti 2004] at the outlet it proves to be possible see Appendix F. In our case at the outlet boundary condition the maximum value reached is 1.1 so 21% of the acoustic energy is indeed reflected.

5.3.4 Comparison of the different approaches using the LES impedances

The TATFs obtained using the different approaches (two-dimensional model, MarCan and LES) and the acoustic impedances obtained by LES are plotted in this section. The results of the 900 Hz harmonic forcing LES are also added in the figures. Except for the 900 Hz harmonic forcing LES, the results for the outgoing waves are represented in blue and for the ingoing waves in red. A good match is found between the 900 Hz harmonic and the

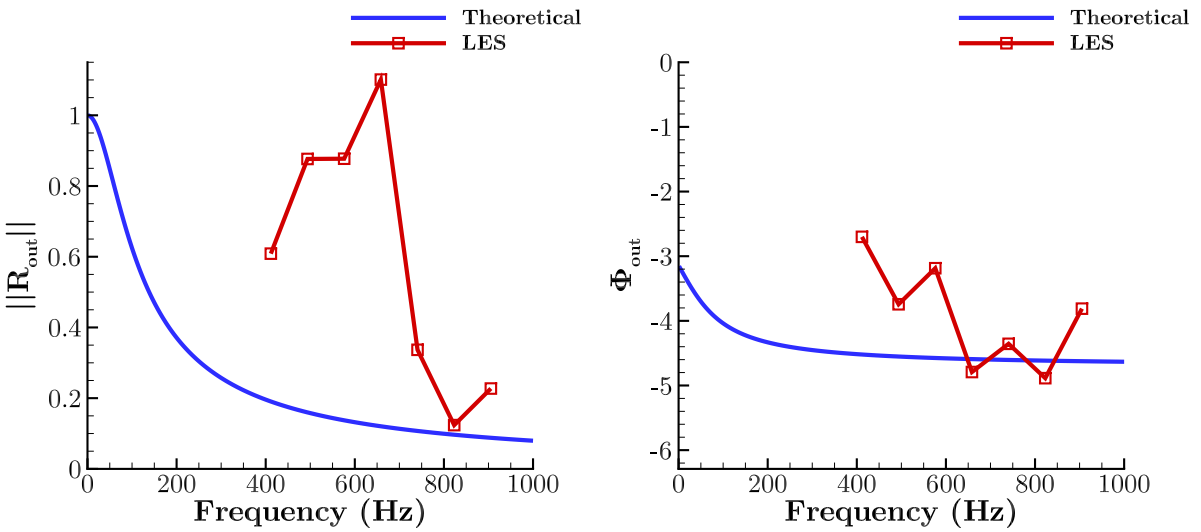

Figure 5.18: Outlet reflecting coefficient of the LES and the analytical expressions given by Selle *et al.* [Selle 2004]: Amplitude (*left*) and phase (*right*).

multi-harmonic entropy forcing LES both in amplitude and phase. This shows the interest and the potential of the multi-harmonic approach [Giauque 2005]. Besides, the proof of acoustic generation due to entropy forcing in the 2D model is given in Appendix G.

5.3.4.1 Upstream zone

The first comparison concerns the upstream zone. The amplitude and phase of the upstream outgoing TATF P_1^-/σ are plotted in Fig. 5.19. As for the purely non-reflecting case, the amplitude predicted by the two-dimensional model is 2 to 3 times smaller than 1D results. The LES results in this thesis show that the TATFs are twice smaller than the one predicted by the two-dimensional model. Still, the model gives a good improvement of the results compared to MarCan. Moreover, the shape and the tendency of the phase are well retrieved between the different approaches.

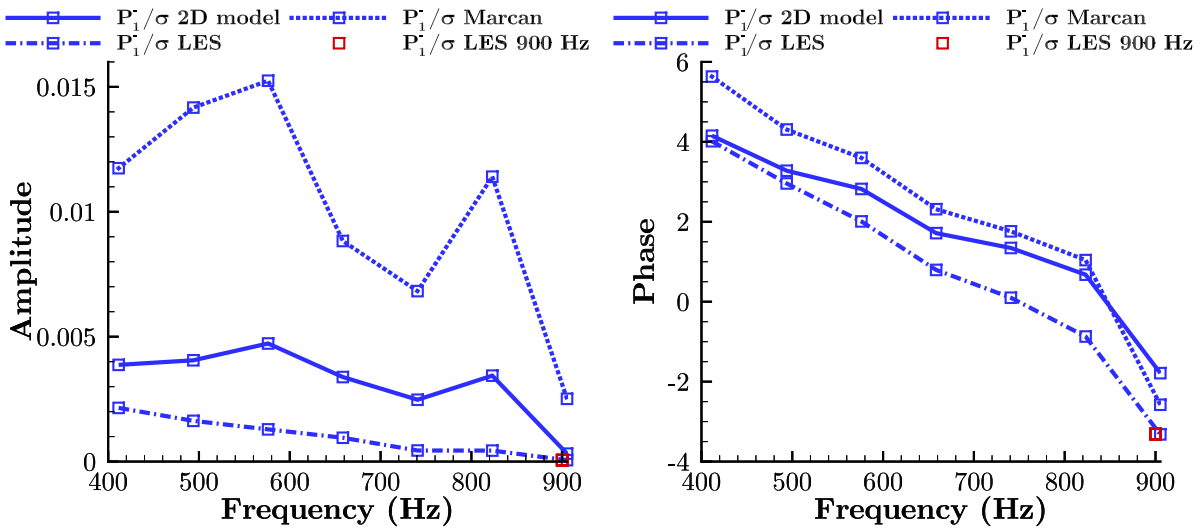

Figure 5.19: Amplitude (*left*) and phase (*right*) of the TATF of the upstream outgoing wave P_1^-.

5.3.4.2 Downstream zone

A focus is carried out now in the downstream region. The amplitude and phase of the downstream outgoing TATF P_2^+/σ are represented in Fig. 5.20. Once again, the amplitude of P_2^+/σ predicted by MarCan is largely overestimated compared to the LES and the 2D model reduces the discrepancy by at least a factor of two. The computed amplitude provided by the model is higher than in the LES until 905 Hz where a match is found. Regarding the phase obtained by the three approaches, it decreases in the three cases, but the phase variation occurs more rapidly in the LES than for MarCan and the 2D model.

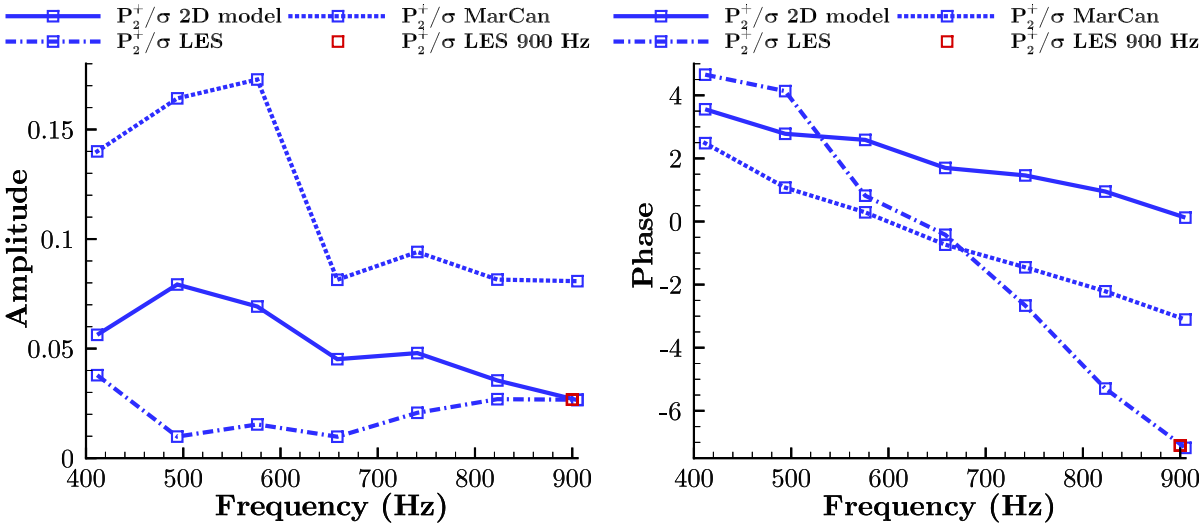

Figure 5.20: Amplitude (*left*) and phase (*right*) of the TATF of the downstream outgoing wave P_2^+.

5.4 Conclusions

The validation of the entropy wave distortion has been carried out and a good comparison has been found between the modeled convection using the streamlines and the 900 Hz harmonic entropy forced LES. Aside from the thermal diffusion in the combustion chamber due to the very low convection velocity, the main discrepancy is visible at the nozzle boundaries where the model predicts distorted entropy waves while in LES, the thermal diffusion tends to damp the temperature fluctuations. It could be really interesting to incorporate in the future the thermal diffusion phenomenon in the convection model. In addition, this method has been applied to a nozzle but it is no difficulty to extend it to turbine stages in the future.

A comparison of the two-dimensional and one-dimensional (MarCan) models on a 1D flow showed a perfect agreement proving that the degeneration of the equations of the 2D model is working well. The developed model is then used with a 2D RANS flow and non-reflecting boundaries. Acoustic and entropy forcing computations are carried out and compared to MarCan. For the acoustic forcing small discrepancies are observed, they come from the contributions of the radial gradients of the mean flow despite the 1D acoustics propagation and remain small. Regarding the entropy forcing, an important decrease of at least a factor of two in the TATFs is found with the new model.

In a next step, the effective reflection coefficients from LES have been imposed in the two- and one-dimensional models and new comparisons have been made. It is seen that the transfer functions of the LES are largely lower than their estimation with the 1D model. The 2D model drastically improves the agreement of the transfer functions with the LES, even if some differences remain. It should however be reminded that several assumptions are made in the model that make the comparison to LES difficult: the LES are performed with a variable specific heat ratio, thermal diffusion, numerical dissipation, turbulence features and a three dimensional geometry which was unfortunately not axisymmetric. It should be interesting to perform in the future a numerical simulation with all the assumption made in the model to complete the validation of this model. In addition, at the current stage, no experimental data on the configuration are available to validate the LES findings.

It can be finally concluded that this model improves the results compared to a purely one-dimensional approach by at least a factor of two. The use of a RANS flow field improves significantly the ICN estimation and as this type of computation is less time consuming than LES it allows a rapid estimation of the generated ICN in an industrial context for aero-engines.

General conclusions and outlook

Conclusions

This PhD thesis deals with the subject of indirect combustion noise (ICN) estimation in nozzle flows using numerical and analytical tools in the purpose of developing a two-dimensional axisymmetric model.

In a first step, a brief overview of the literature on ICN over the last four decades is carried out both analytically, experimentally and numerically. Analytically, even if Crocco & Sirignano [Crocco 1967] and Bohn [Bohn 1976] developed approaches to study 3D and 2D effects, their models suffer from restrictions that make them unsuitable for configurations of interest. Crocco & Sirignano assume for instance a purely uniform flow over a sectional surface and Bohn a small deformation of the flow due to the contraction (nozzle). As a consequence, analytically only one-dimensional models are of practical interest. Numerically and experimentally, the general conclusions are that 3D effects are really important for estimating ICN. Especially, the temperature gradient (between the entropy wave fluctuations and the mean flow) but also the entropy waves distortion need to be taken into account for the prediction of ICN analytically [Knobloch 2015b]. The literature review highlighted the need to develop a two-dimensional axisymmetric model for estimating ICN in nozzle flows.

For the comparison and the validation of the 2D model, several tools are needed. ONERA's 1D solvers Sunday and MarCan are first described. They are used to demonstrate the limitation of 1D solvers for the prediction of ICN. After a brief introduction of the equations of Fluid mechanics and the theory of Turbulence, ONERA's 3D Navier-Stokes solver CEDRE is then presented in details both for RANS and LES computations. These 3D numerical computations are later exploited for the validation of the 2D model.

After that, the 2D model is described. The hypotheses of the model are first presented. In order to take into account the entropy waves distortion, the radial evolution of the convected entropy fronts through the nozzle must be incorporated in the model. This is done by adding a modeled convection using the streamlines method. The Euler equations are rewritten in 2D form for the entropic part while acoustic perturbations are considered to be 1D: those equations are deeply explained and derived successively. The equations are finally expressed in a Matrix form allowing their resolution and to obtain the Thermo-Acoustic Transfer Functions (TATFs).

Numerical simulations of the flow through a nozzle are carried out in chapter 4. A RANS and a LES computations are first run to provide the mean flow requested by the 2D model and to ensure that this mean flow does not depend on the modeling used in the numeri-

cal simulation. LES simulations are then pursued with a harmonic or a multi-harmonic entropy forcing, in particular to quantify numerical dissipation as well as thermal and viscous diffusions. In the configuration considered, it is shown that thermal diffusion is important and this phenomenon, not taken into account in the 2D model, is most likely to occur in realistic aero engines. Limitations of the present LES computations have been highlighted and improvements may be achieved by using better suited sub-grid scale and wall-law models as well as more efficient non reflective boundary conditions. A grid convergence study would also help to enforce the reliability of the numerical results. Despite these limitations, it is the writer's belief that the results obtained are globally representative of the flow physics of the nozzle configuration and are sufficient for a first validation of the developed model.

Finally in the last chapter, the 2D model is validated by comparison with the numerical results of the LES. The modeled entropy convection is first compared with the entropy fronts distortion observed in the LES with harmonic entropy forcing. Despite the discrepancies close to the wall where the 2D model predicts the presence of entropy waves that are damped by thermal diffusion in the LES, the convected entropy waves method developed during this study is found to be accurate. The TATFs are then estimated with the 2D model using the RANS mean flow as input. First evaluations are performed considering non-reflecting boundaries and results are compared with the 1D model MarCan. For the acoustic forcing small discrepancies are observed; they come from the contributions of the radial gradients of the mean flow despite the 1D acoustic propagation and remain small. Regarding the entropy forcing, an important decrease of at least a factor of two in the TATFs is found with the new model, which evidences the strong influence of the distortion of the entropy fronts in ICN generation. In the final step of the validation, the 2D model is confronted to the ICN computed with the LES. To this end, the effective reflection coefficients from LES are imposed in the two- and one-dimensional models. It is seen that the transfer functions of the LES are largely lower than their estimation with the 1D model. The 2D model drastically improves the agreement of the transfer functions with the LES, even if some differences remain. It should however be reminded that several assumptions are made in the model that make the comparison to LES difficult. The "reference" LES computations are performed with a variable specific heat ratio, include thermal diffusion, numerical dissipation, turbulence features and a three-dimensional geometry that cannot be taken perfectly into account by the 2D model.

Within this work the proof of the importance of entropy waves distortion to the ICN generation[3] was assessed. The study revealed a great improvement in the estimation of ICN by taking into account these distortions. A decrease in the amplitude by a factor of

[3] Previously observed on the engine representative MT1 transonic high-pressure turbine.

2 (6 dB) is found by the 2D model compared to 1D models. The estimation of ICN in an industrial context remains possible with this new model, as it requires solely the 2D mean flow inside the nozzle that can be quickly provided by a RANS simulation.

Outlook

It has been evidenced that the main discrepancy of the model occurs at the nozzle boundaries where it predicts distorted entropy waves while physically the thermal diffusion tends to damp the temperature fluctuations as observed in LES. In the future, the model could be improved by incorporating the thermal diffusion phenomenon in the convection step.

In this thesis, in the absence of data regarding the shape and amplitude of the entropy fluctuations in the combustion chamber just downstream of the flame, planar entropy waves are used. Other wave structures, such as entropy spots as done by Mishra & Bodony [Mishra 2013], can however be imposed at domain inlet in the model with no difficulty.

In addition, future work could focus on the contribution of the various effects not taken into account in the 2D model for entropy noise generation, such as varying specific heat ratio, entropy-turbulence and acoustic-turbulence interactions, thermal diffusion, etc. Such an investigation could be achieved by comparison with LES results, which include the above-mentioned effects, with other numerical approaches such as RANS+CAA for instance. At the current stage, no experimental data on the configuration are available to validate the LES findings. Additional numerical computations and experimental campaigns are required to really understand the contribution of ICN to the total noise of an aero engine and in the future to be able to reduce it.

Concerning the 2D model, due to a lack of time the normal momentum equation, Eq. 3.57, was not studied during this PhD. The evaluation of this equation should give a strong indication of the accuracy of the developed model. A strong limitation of the model is the absence of vorticity waves and their inclusion in a new version of the model would be highly beneficial. To end, the model was shown not to conserve the acoustic energy. Considering the remarks above a deeper analysis of the energy conservation, including energy budgets, seems to be of interest.

Finally, this method has been applied to a nozzle but its extension to a stator stage does not seem to present any difficulty. The extension to the rotor, however, seems more complicated due to the rotating geometry and base flow.

Appendices

Appendix A

Injection of entropy perturbations in CEDRE with the NSCBC formulation

---

For purpose of brevity and simplicity, the NSCBC in 1D are described in this appendix even if the formulation of Lodato *et al.* [Lodato 2008] is implemented in CEDRE. NSCBC are based on the decomposition of the flow into characteristic waves leaving or entering the domain. This decomposition was first proposed by Thompson for inviscid flows [Thompson 1987, Thompson 1990] and adapted to viscous flows by Poinsot & Lele [Poinsot 1992]. Poinsot & Lele demonstrated that for a one-dimensional flow, only three characteristic waves are present, see Figure A.1. The concerned wave equations are:

$$L_1 = (u-c)\left(\frac{\partial p}{\partial x} - \rho c \frac{\partial u}{\partial x}\right), \quad \text{backward acoustic wave} \tag{A.1}$$

$$L_2 = u\left(c^2\frac{\partial \rho}{\partial x} - \frac{\partial p}{\partial x}\right), \quad \text{entropy wave} \tag{A.2}$$

$$L_5 = (u+c)\left(\frac{\partial p}{\partial x} + \rho c \frac{\partial u}{\partial x}\right), \quad \text{forward acoustic wave} \tag{A.3}$$

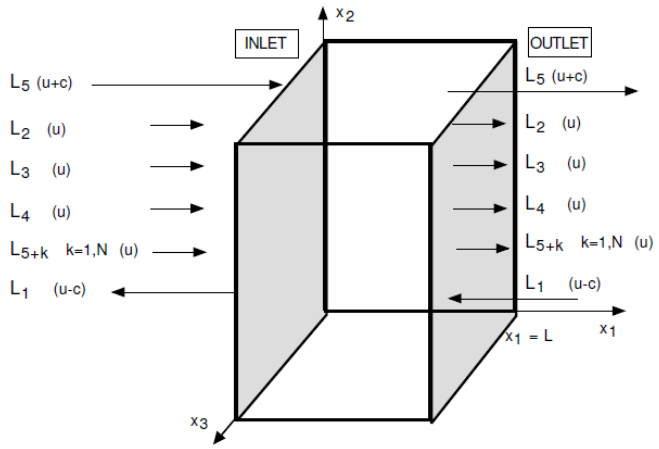

Figure A.1: Boundary conditions located on the x_1 axis extracted from [Poinsot 2012].

where L_1 and L_5 define the sound waves moving in the negative and positive x_1 directions respectively and L_2 is the entropy wave. L_3 and L_4 are the amplitudes of characteristic waves associated with vorticity and L_{5+k} are the amplitudes of the characteristic waves of the reacting species. Hence it is possible to inject perturbations through a proper definition of the ingoing L_i's. In our case, at the inlet for a subsonic flow, only the entropy injection is explained. To prevent any drift of the mean quantities, a partially reflecting boundary condition is preferred and the L_i's are expressed as a sum of a theoretical and a relaxation terms:

$$L_i = L_{i_{theo}} + L_{i_{relax}} \tag{A.4}$$

If one injects only entropy fluctuations at the inlet of the the computation domain, $L_{3_{theo}} = L_{4_{theo}} = L_{5+k_{theo}} = L_{5_{theo}} = 0$ and L_1 is directly imposed by CEDRE. In the formalism of Selle *et al.* [Selle 2004], the expression of L_5 is then

$$L_5 = L_{5_{relax}} = K_5(u - u_\infty) = \Sigma_5 \frac{\rho c^2}{L} \tag{A.5}$$

where u_∞ (the velocity at infinity) is introduced to prevent any drift of the mean static velocity at the inlet, K_5 is a constant, Σ_5 is the inlet relaxation coefficient and L is a characteristic size of the domain. The entropy equation is then defined as:

$$L_2 = \frac{1}{2}(\gamma - 1)(L_1 + L_5) + \frac{\rho c^2}{T}\frac{\partial T'}{\partial t} \tag{A.6}$$

where T' represents only the imposed entropy fluctuations due to the temperature fluctuations. This relation links directly the target entropy fluctuation and the characteristic wave L_2.

At the outlet for a subsonic flow, L_2, L_3, L_4, L_5, L_{5+k} are leaving the domain, they are imposed by the solver CEDRE. Only L_1 is entering the domain ($L_{1_{theo}} = 0$) and is defined as

$$L_1 = L_{1_{relax}} = K_1(p - p_\infty) = \Sigma_1(1 - M^2)\frac{c}{L}(p - p_\infty) \tag{A.7}$$

where p_∞ (the pressure at infinity) is introduced to prevent any drift of the mean static pressure at the outlet, K_1 is a constant, Σ_1 is the outlet relaxation coefficient and M is the maximum Mach number in the flow.

Appendix B

Validation of the NSCBC on a one-dimensional domain

As the NSCBC have been recently implemented in the solver CEDRE, it is necessary to validate them. To this end, two test cases are presented here. These cases are conducted on a one-dimensional duct of 259 $\mathrm{mm} \times 0.259$ mm composed of structured quadrihedral elements. It has one cell along the radial direction ($\Delta_y = 0.259$ mm) and 1000 cells ($\Delta_x = 0.259$ mm) in the axial direction. The flow properties correspond to those in the combustion chamber, as detailed in chapter 4. The other numerical parameters are identical to those of chapter 4 except for the type of forcing. A multi-harmonic acoustic forcing composed of 7 frequencies going from 411 to 905 Hz (with a frequency step around $\Delta f = 82$ Hz) is injected at the inlet for the first case and at the outlet for the second one. The amplitude of the 7 frequencies in the comb is imposed at 1.4 Pa for each frequency.

B.1 Acoustic forcing at the inlet

The aim of this test case is to compute the outlet reflection coefficient under the injection of a multi-harmonic acoustic forcing at the inlet (P_1^+). Using the same subscript as in Fig. 1.3, the outlet reflection coefficient is defined as:

$$R_{out} = \frac{P_2^-}{P_2^+} \tag{B.1}$$

where all the three terms are complex numbers. The numerical amplitude and phase are compared to the analytical expressions given by Selle *et al.* [Selle 2004] defined respectively as:

$$\| R_{out} \| = \frac{1}{\sqrt{1 + \left(\frac{2\omega}{K_1}\right)^2}} \tag{B.2}$$

and

$$\Phi_{out} = -\pi - \arctan\left(\frac{2\omega}{K_1}\right) \tag{B.3}$$

where

$$K_1 = \Sigma_1(1 - M^2)\frac{c}{L} \tag{B.4}$$

In the LES computation, the outlet relaxation coefficient (Σ_1) is set at 0.5 in accordance to the value of chapter 4. ρ and c are directly obtained from the computation. Fig. B.1 shows both the amplitude and phase of the outlet reflection coefficient from numerical computation in blue and also using the analytical expression in red. A perfect match is found for the results showing a good behavior of the recently implemented NSCBC for the outlet reflection coefficient for an ingoing multi-harmonic acoustic wave.

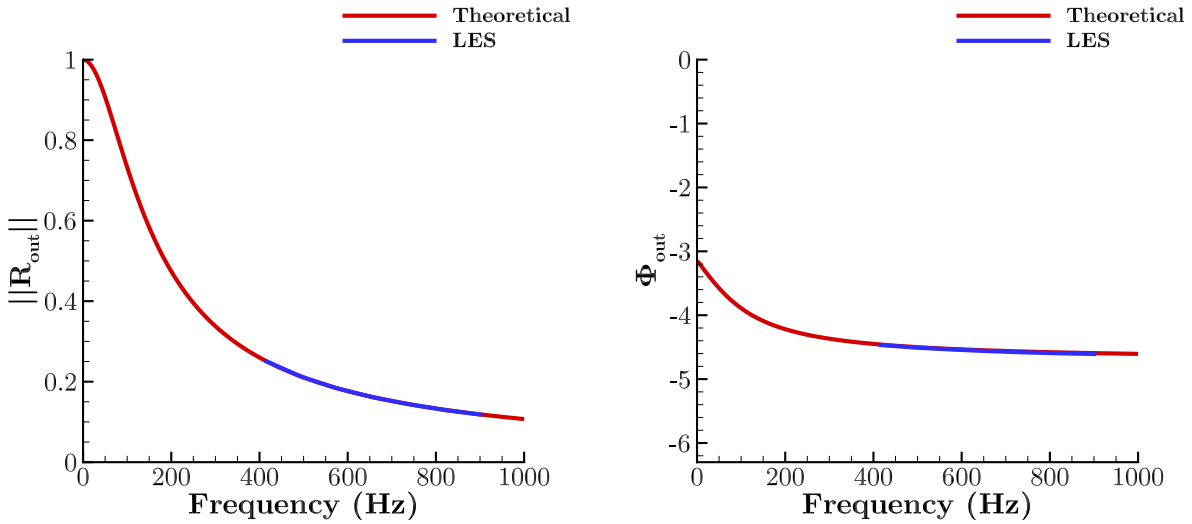

Figure B.1: Illustration of the amplitude (*left*) and phase (*right*) of the outlet reflecting coefficient. Blue: One-dimensional LES results and red: Analytical solution.

B.2 Acoustic forcing at the outlet

In a similar way as in the previous section, a computation with a multi-harmonic acoustic forcing at the outlet (P_2^-) is carried out aimed at computing the inlet reflecting coefficient expressed as:

$$R_{in} = \frac{P_1^+}{P_1^-} \tag{B.5}$$

A similar approach as the one adopted by Selle *et al.* for the outlet reflecting coefficient is applied to the inlet to obtain the analytical amplitude and phase of the inlet reflecting coefficient. This time, they are defined as:

$$\| R_{in} \| = \frac{1}{\sqrt{1 + \left(\frac{2\rho c\omega}{K_5}\right)^2}} \tag{B.6}$$

and

$$\Phi_{in} = -\arctan\left(\frac{2\rho c\omega}{K_5}\right) \tag{B.7}$$

where

$$K_5 = \Sigma_5 \frac{\rho c^2}{L} \tag{B.8}$$

In the LES computation, the inlet relaxation coefficient (Σ_5) is set to 0.2 in accordance with the value of chapter 4.

The analytical and numerical amplitudes (*left*) and phases (*right*) of the inlet reflection coefficient are illustrated in Fig. B.2. A very good agreement is found for the amplitude. Minor discrepancies arise for the phase with increasing frequency. However, they remain quite small. It can be concluded that the recently implemented NSCBC are acting as a first order low-pass filter as expected. Moreover, due to the lower value of the relaxation coefficient Σ_5 at the upstream boundary compared to Σ_1, the acoustic reflection is less important at the upstream boudary than at the downstream boundary.

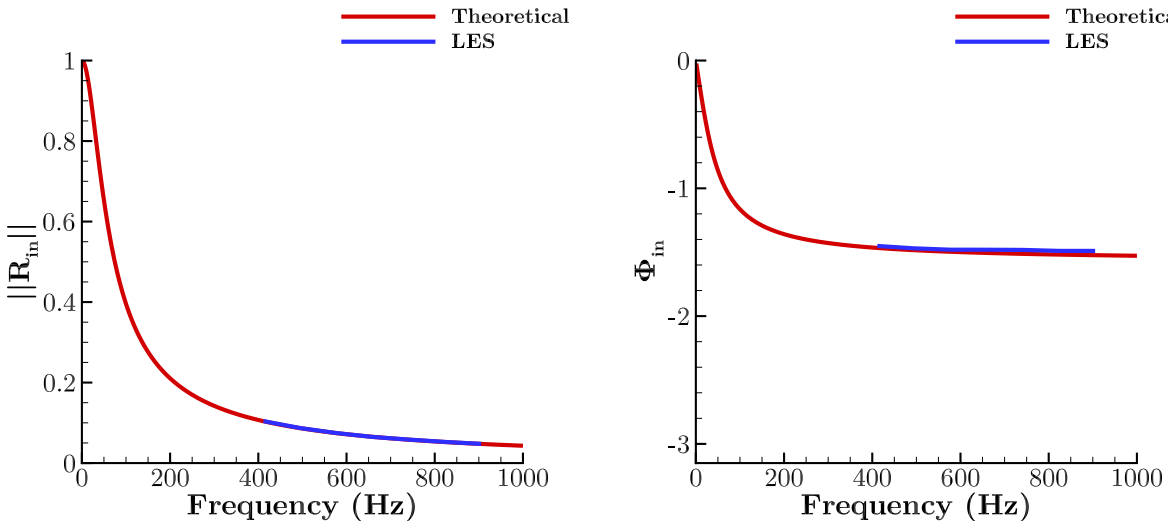

Figure B.2: Illustration of the amplitude (*left*) and phase (*right*) of the inlet reflecting coefficient. Blue: One-dimensional LES results and red: Analytical solution.

Appendix C

Test case on the diffusion and the numerical dissipation in a one-dimensional domain

In order to study the convective and viscous diffusion phenomena as well as the numerical dissipation (either due to the temporal or spatial scheme) occurring inside the nozzle, several test cases are presented here.

These cases are conducted on a one-dimensional computational domain of 259 $\mathrm{mm} \times 0.259$ mm). It is made long enough to ensure no potential reflection at the outlet. Two structured quadrihedral meshes are generated. They both have one cell along the radial direction ($\Delta_y = 0.259$ mm) but differ in the number of cells in the axial direction. *Mesh 1* has 1000 cells ($\Delta_x = 0.259$ mm) and *Mesh 2* 2000 cells ($\Delta_x = 0.1295$ mm). The mesh size of *Mesh 1* is chosen in accordance to the nozzle LES computations presented in this thesis which is supposed to withstand 30 NPW at 900 Hz, whereas Mesh 2 contains twice as much elements (60 NPW) for the same frequency

The different test cases are summed up in Table C.1. Case 1 corresponds to the reference

Case	Mesh	Equations	Time step	Specificity/Goal
Case 1	Mesh 1	Navier-Stokes	2.7×10^{-8}	Comparison to the LES results
Case 2	Mesh 1	Navier-Stokes	2.7×10^{-7}	Influence of the time step
Case 3	Mesh 2	Navier-Stokes	2.7×10^{-8}	Numerical dissipation
Case 4	Mesh 1	Navier-Stokes	2.7×10^{-8}	High Prandtl number (144500)
Case 5	Mesh 1	Euler	2.7×10^{-8}	No diffusive terms

Table C.1: Summary of the different numerical test cases.

simulation, with numerical parameters identical to the 900 Hz harmonic forcing LES. Only one parameter is changed for cases 2-5 to evaluate its contribution on the diffusion and dissipation of the entropy wave. The velocity, temperature at the inlet and the pressure at the outlet of the 900 Hz harmonic forcing LES are used to initialize the following computations. After reaching a steady state, the computations are forced at 900 Hz at the inlet.

The amplitude of the forcing is set to 40 K but due to the inlet relaxation factor set at 0.2, it slightly varies between the different test cases.
One sensor is placed at the inlet and another one 5 cm downstream as it corresponds to the length of the combustion chamber in the LES configuration. They are respectively denoted Sen_1 and Sen_2.

C.1 Case 1

In this test case, only the mesh differs from the 900 Hz harmonic forcing LES of Chapter 4. It is the reference case for the following computations. The two-dimensional views of the flow inside the computation domain are plotted between 0 and 5 cm. In addition, as the radial dimension is really small compared to the length, the XY aspect ratio is set to be independent. One can see in Fig.C.1 the two dimensional evolution of the non-dimensional entropy disturbance amplitude. The diffusion and dissipation mechanisms found in the 900 Hz LES computation (see Fig. 4.18) are also present in this reference test case. This means that the accelerating flow present in the 900 Hz harmonic forcing LES is not responsible of the diffusion and the dissipation phenomena. In order to characterize precisely the decrease in amplitude of the forcing, the dimensionless entropy disturbance signals recorded at Sen_1 and Sen_2 are plotted in Fig. C.2. Their respective amplitudes are 0.029 and 0.01152, which corresponds to an attenuation of the wave of 60.27 %.

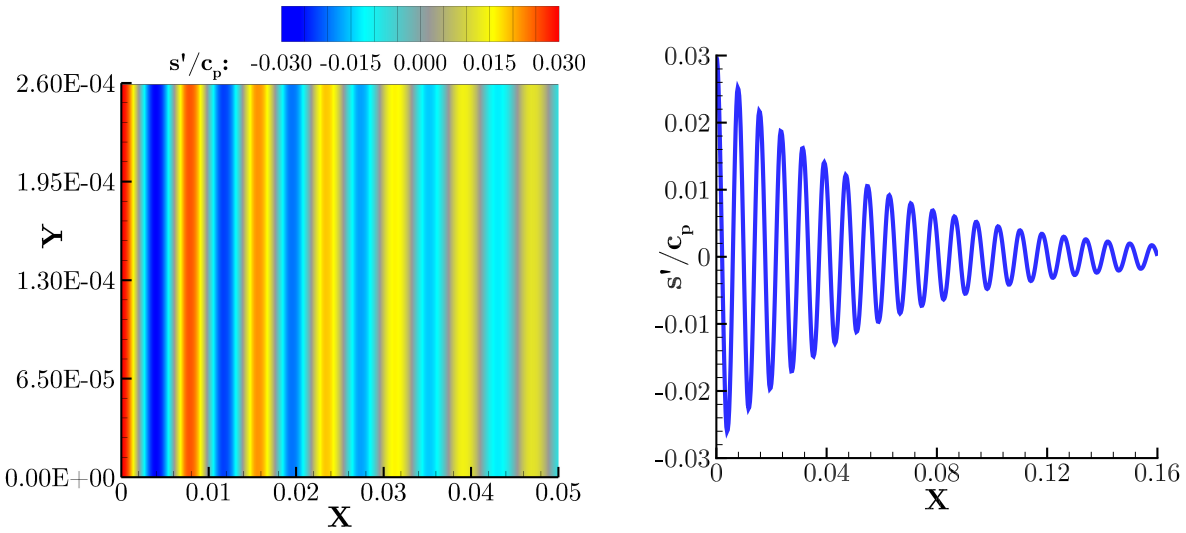

Figure C.1: (*left*) Colored view of the computational domain and (*right*) axial evolution of the dimensionless amplitude of the entropy disturbances for Case 1.

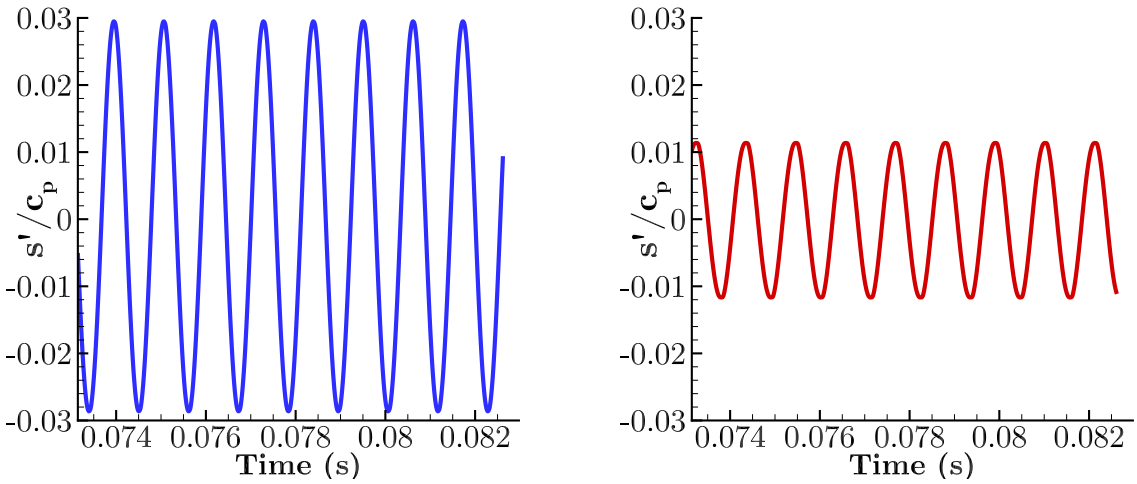

Figure C.2: Dimensionless entropy fluctuations signals recorded for Case 1 at Sen_1 (*left*) and Sen_2 (*right*).

C.2 Case 2

For this computation, the time step of the temporal scheme is increased by a factor of ten which is possible due to the absence of the nozzle. The aim of this computation is to characterize the effect of the temporal scheme on the convection of the entropy wave. Once again, a part of the computational domain colored by the temperature is visible in Fig. C.3 and Sen_1 and Sen_2 are again plotted in Fig. C.4. This time, Sen_1 recorded an amplitude of 0.02905 and Sen_2 of 0.01152. It corresponds to an amplitude decrease of 60.34 % which is identical to the reference case. This shows that the number of temporal iterations does not influence the results on the diffusion/dissipation and also that the numerical dissipation in the LES computations is only due to the mesh size.

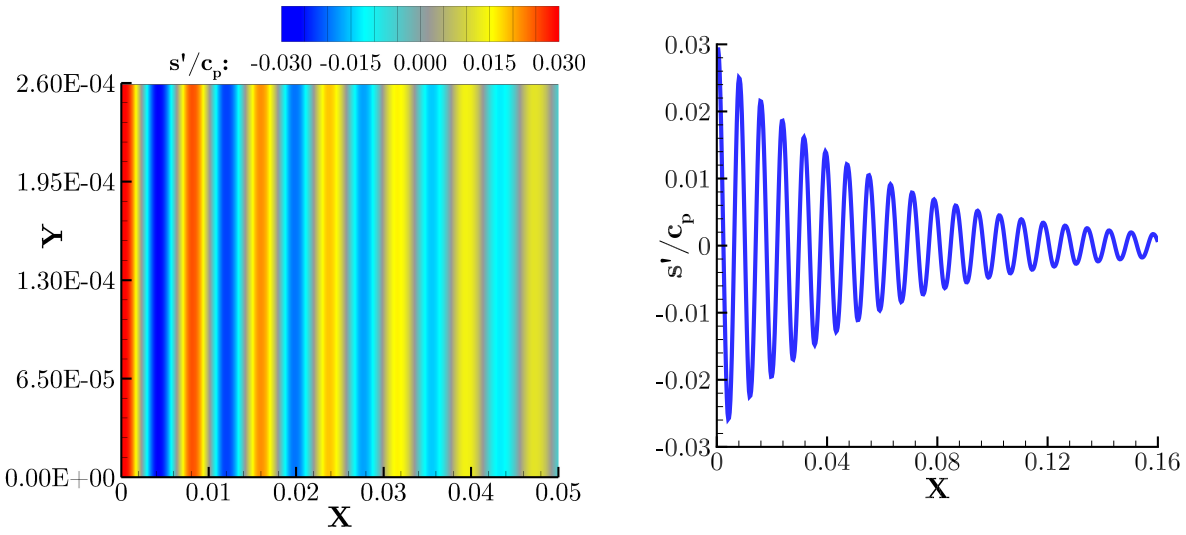

Figure C.3: (*left*) Colored view of the computational domain and (*right*) axial evolution of the dimensionless amplitude of the entropy disturbances for Case 2.

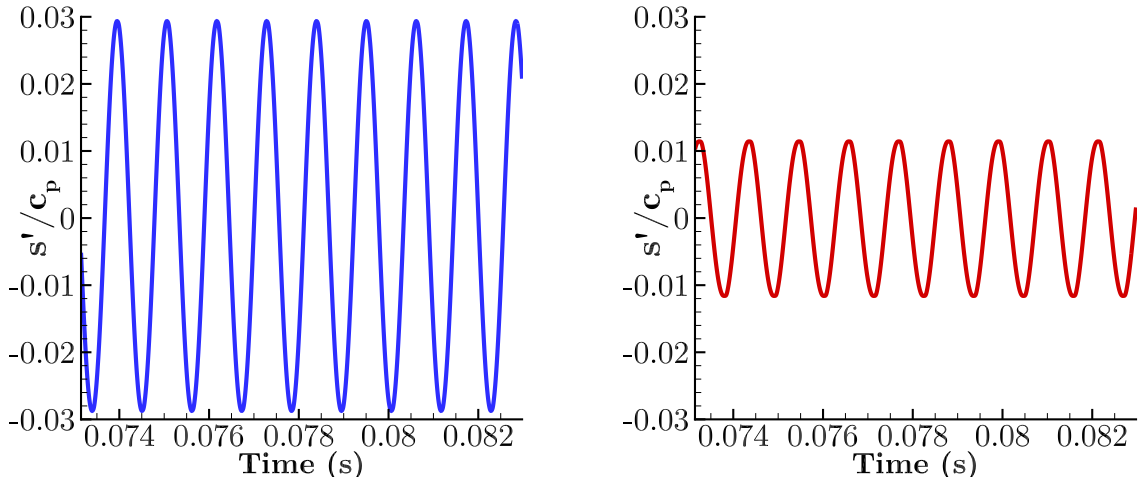

Figure C.4: Dimensionless entropy fluctuations signals recorded for Case 2 at Sen_1 (*left*) and Sen_2 (*right*).

C.3 Case 3

Case 3 differs from Case 1 by the use of *Mesh 2*. The NPW is increased to 60 for the frequency of 900 Hz. This computation is carried out in order to study the influence of a finer mesh grid on the amplitude decrease. A close view of the upstream computational domain colored by s'/C_p is represented in Fig. C.5. One can see that the results are not strongly different than Fig. C.1. Indeed, in this case the amplitude captured at Sen_1 is

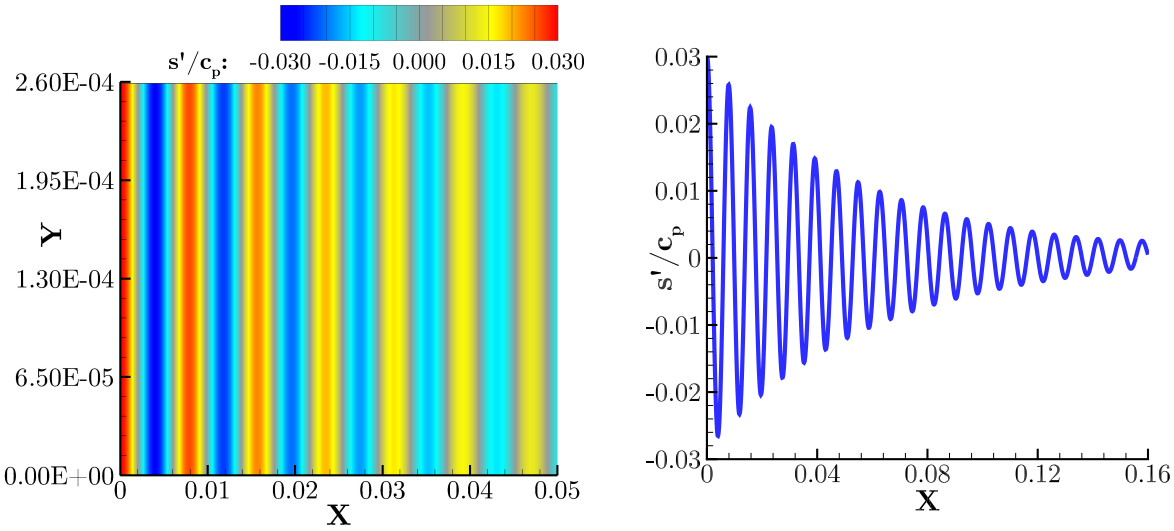

Figure C.5: (*left*) Colored view of the computational domain and (*right*) axial evolution of the dimensionless amplitude of the entropy disturbances for Case 3.

0.02918 and 0.01223 for Sen_2. Both signals recorded by the two sensors are plotted in Fig. C.6. The amplitude decreases by about 58.08 %. Comparing to the reference case (Case 1), it represents a reduction of 2.26 points only. Doubling the axial number of cells has not a significant improvement on the diffusion and the numerical dissipation of the entropy wave.

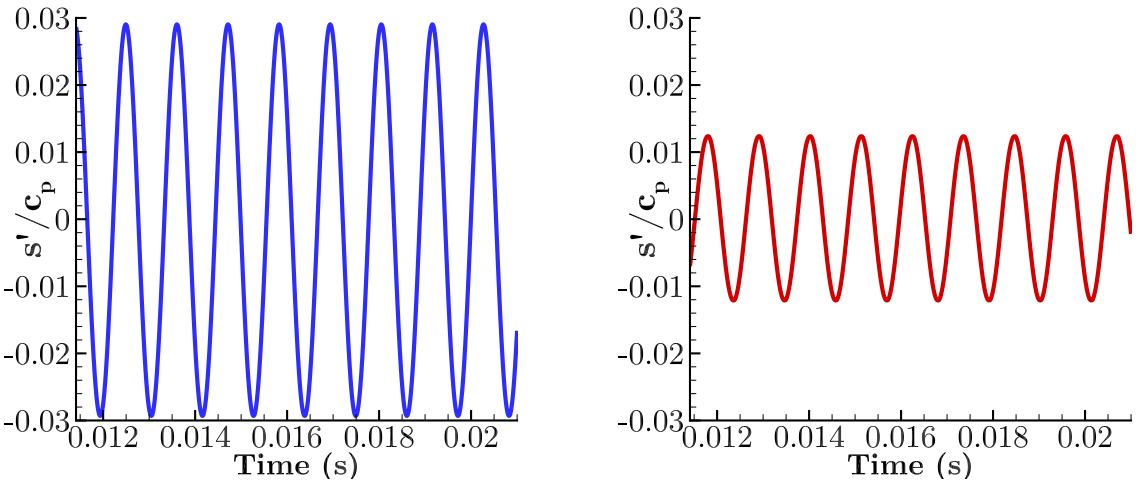

Figure C.6: Dimensionless entropy fluctuations signals recorded for Case 3 at Sen_1 (*left*) and Sen_2 (*right*).

C.4 Case 4

The aim of this computation is to characterize the influence of the thermal diffusion on the attenuation of injected entropy disturbances. This is done by changing artificially the heat conduction coefficient. The heat conduction coefficient initially computed using Eucken's law defined in Eq. 2.10 is substituted by Eq. C.1 and corresponds to the Prandtl law equation.

$$\Lambda = \frac{\mu C_p}{Prt} \tag{C.1}$$

where Prt is the Prandtl number. This number represents the ratio between the viscous diffusion rate and the thermal diffusion rate. A high Prt means that the thermal diffusion is negligible. A stable computation is found with a Prt smaller than 144500 and Λ is then deduced using Eq. C.2 to give $\Lambda = 4.27 \times 10^{-7}$ W.m^{-1}.K^{-1} (for case 1, $Prt = 0.7648$ or $\Lambda = 8.0347 \times 10^{-2}$ W.m^{-1}.K^{-1}).

$$Prt = \frac{\mu C_p}{\Lambda} = \frac{5.19 \times 10^{-5} 1184}{\Lambda} = 144500 \tag{C.2}$$

The computation is carried out and a part of the computational domain colored by the temperature is represented in Fig. C.7. It can be seen that the amplitude decrease is considerably reduced. More precisely, Fig. C.8 shows the signal of s'/C_p at the two sensors. On average, the amplitude of the entropy fluctuation is 0.0289 at Sen_1 and 0.0271 at Sen_2. In terms of percentage, it corresponds to an attenuation of 6.23 %. Assuming that the thermal dissipation is close to zero in this case (even if the Prt cannot be set to infinity for stability reason), one can compare the results to the reference case and quantify the

thermal dissipation to be 54 points.

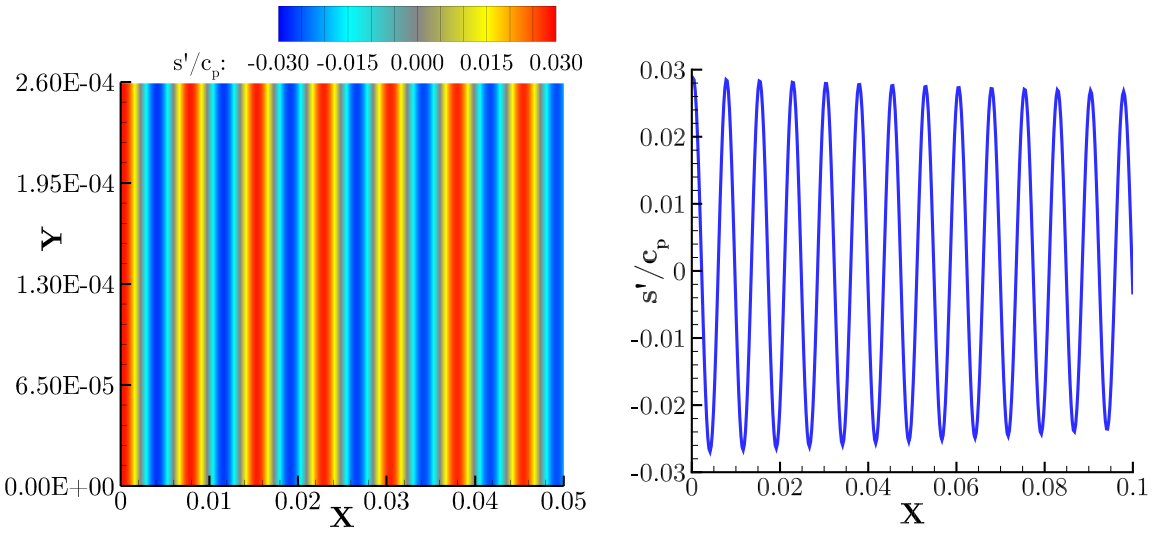

Figure C.7: (*left*) Colored view of the computational domain and (*right*) axial evolution of the dimensionless amplitude of the entropy disturbances for Case 4.

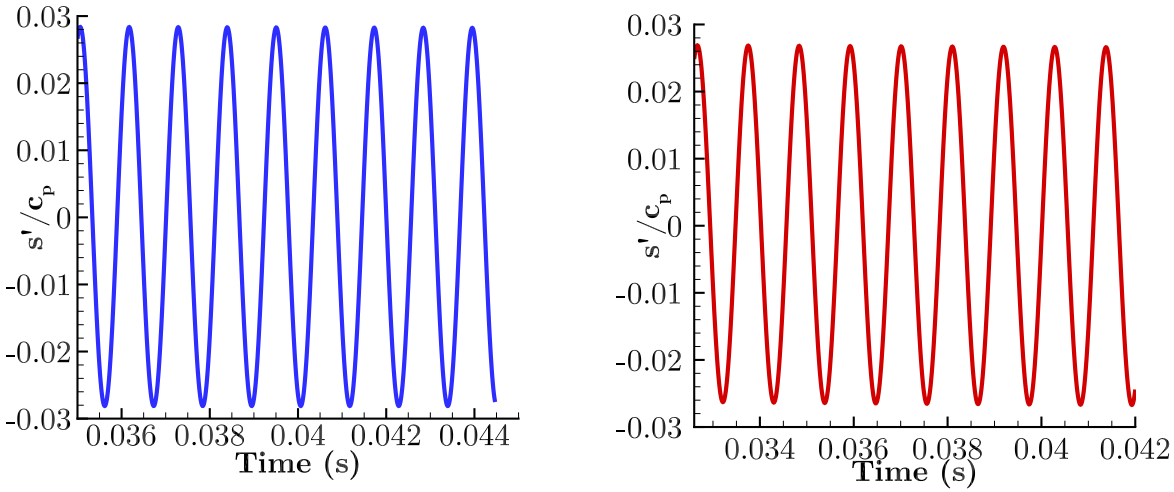

Figure C.8: Dimensionless entropy fluctuations signals recorded for Case 4 at Sen_1 (*left*) and Sen_2 (*right*).

C.5 Case 5

In the last case, the Euler equations are resolved rather than the Navier-Stokes equations. The diffusive terms are not taken into account in this computation and the numerical dissipation due to the mesh is characterized. One can see in Fig. C.9 the decrease of the

amplitude of the forcing. Looking at the recorded dimensionless signals in Fig. C.10, the mean maximum amplitude at Sen_1 is 0.03092 and 0.02913 at Sen_2. This gives a 5.78% decrease, which corresponds quasi-exclusively to the numerical dissipation due to the mesh. Comparing Case 5 and Case 4 gives an idea about the viscous dissipation inside the geometry. Assuming that the thermal diffusion is close to zero for Case 4, it gives an estimation of 0.45 point for the viscous dissipation.

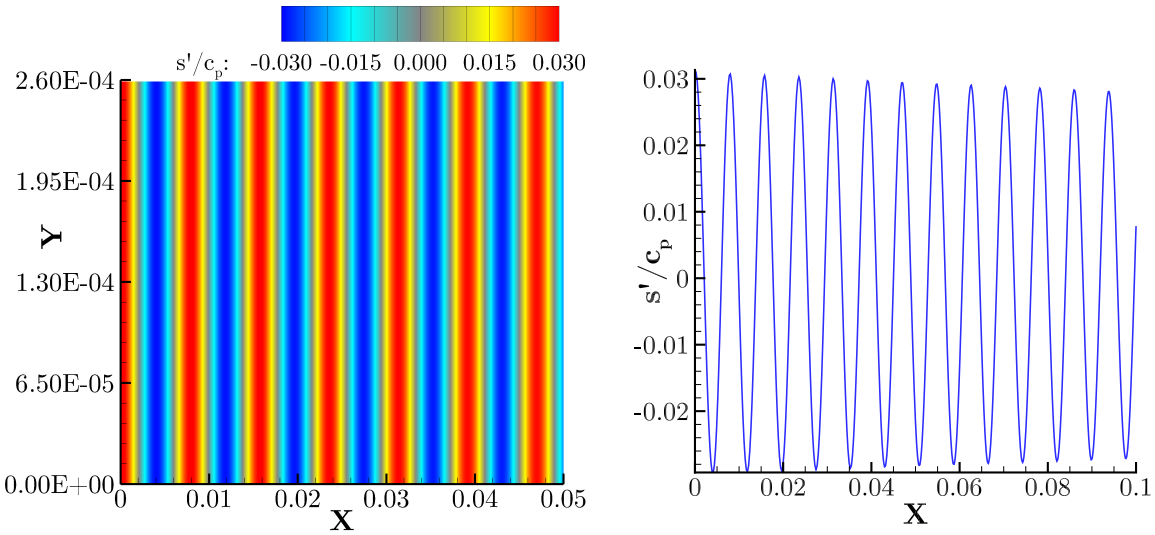

Figure C.9: (*left*) Colored view of the computational domain and (*right*) axial evolution of the dimensionless amplitude of the entropy disturbances for Case 5.

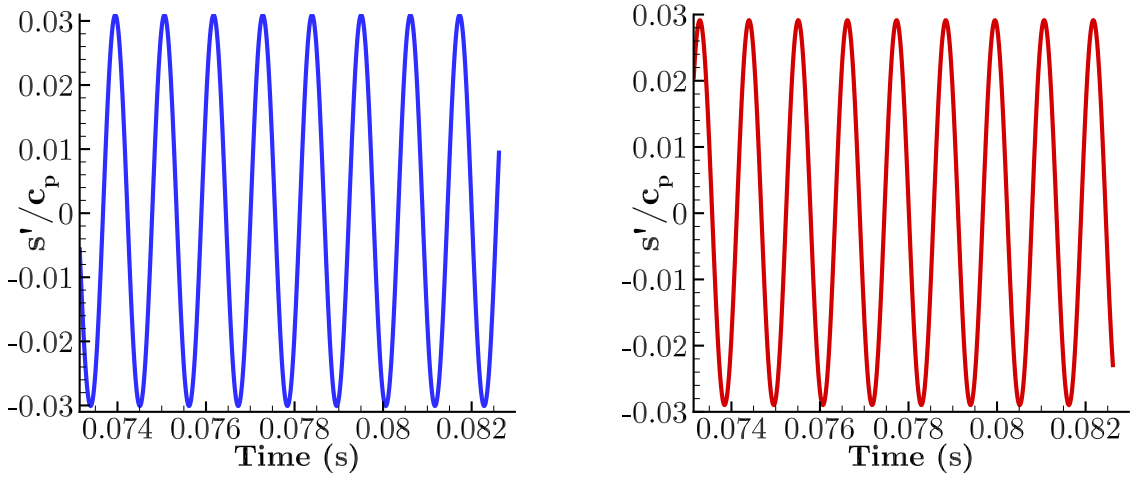

Figure C.10: Dimensionless entropy fluctuations signals recorded for Case 5 at Sen_1 (*left*) and Sen_2 (*right*).

C.6 Dispersion of the different cases

The attenuation of the entropy wave for the 5 cases has been studied previously, the dispersion is now addressed in this section. The phases are plotted in Fig. C.11 both at the inlet (Sen_1) and at 5 cm (Sen_2). For the cases 1-4, the dispersion is similarly the same at around $\frac{\pi}{100}$ rad. Only Case 5 has a phase shift close to zero ($\frac{\pi}{1600}$ rad). It seems that a better coding of the numerical scheme inside the solver has been reached for the Euler equations than the Navier-Stokes equations. However, the phase shift of cases 1-4 remains small and acceptable for our study allowing to conclude that the numerical scheme used in this study is enough to ensure a small dispersion of the injected entropy waves even while solving the Navier-Stokes equations.

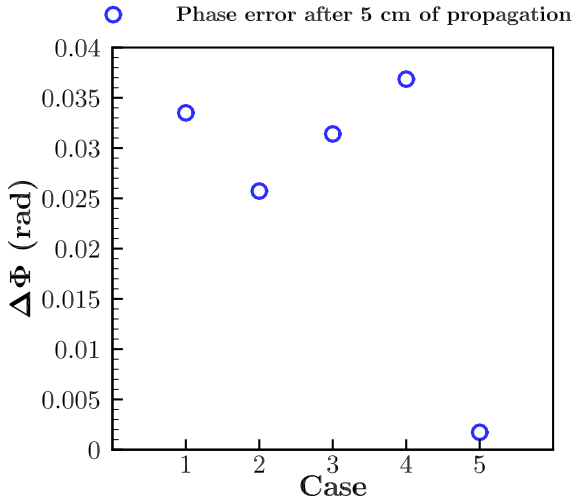

Figure C.11: Phase error after 5 cm of propagation.

C.7 Conclusions

The comparison between Case 1 and Case 2 shows that the temporal numerical scheme has no influence on the temperature amplitude decrease inside the domain. Case 5 shows that the mesh size of 0.259 mm gives a numerical dissipation of 5.78% and the same phenomenon is likely to occur in the 900 Hz harmonic and multi-harmonic LES computations. However, one needs to remember that this numerical dissipation is less important for frequencies lower than 900 Hz. In addition, inside the combustion chamber the flow is accelerated, going from 7 $\mathrm{m.s^{-1}}$ up to 14 $\mathrm{m.s^{-1}}$ at the nozzle inlet, and this dissipation is likely to be overestimated. Furthermore, the comparison of Case 3 and Case 1 shows only a small reduction of the amplitude decrease, meaning that a mesh size of 0.259 mm is a good compromise in terms of accuracy and number of cells. It should also be reminded that the

numerical dissipation due to the mesh occurring inside the combustion chamber is not a real issue for computing the TATFs, as long as the dissipation is negligible between the inlet and the outlet of the nozzle. Looking at the dispersion of injected entropy waves, it can be concluded that the numerical scheme used in this PhD thesis is enough to ensure a small dispersion.

Finally, the diffusion phenomenon occurring inside the combustion chamber is a physical phenomenon that should be present in real engines. The diffusion occurring in the nozzle is mainly due to the thermal diffusion, it is around 100 times larger than the viscous diffusion. It has a major impact on ICN. From the combustion chamber to the nozzle inlet, it tends to smooth in our case the entropy waves and in real engines the entropy spots.

Appendix D

Retrieving Marble & Candel equations for the 2D-model

D.1 Continuity equation

In 1D, Eq. 3.62 can be rewritten as:

$$\left(A\left(\frac{1}{c_0^2}\right)i\omega + \frac{\partial}{\partial x}\left[A\left(\frac{u_{0x}}{c_0^2}\right)\right]\right)\widehat{P_a}(x) + A\left(\frac{u_{0x}}{c_0^2}\right)\frac{\partial\widehat{P_a}(x)}{\partial x} + \frac{\partial\left(A\rho_0\right)}{\partial x}\widehat{u}(x) + A\rho_0\frac{\partial\widehat{u}(x)}{\partial x} = \frac{\partial}{\partial x}\left[A\rho_0 u_{0x}\widehat{\sigma}(x)\right] + Ai\omega\rho_0\widehat{\sigma}(x) \tag{D.1}$$

In 1D, one can also write ${c_0}^2 = \frac{\rho_0}{\gamma P_0}$. Doing the variable change as mentioned in the paper of Marble & Candel, which is $\xi = \left(\frac{x}{x_*}\right)^2$, allows to write ${c_0}^2 = \left(\frac{\gamma+1}{2}\right){c_*}^2 - \left(\frac{\gamma-1}{2}\right){u_{0x}}^2$. Assuming that the velocity $u_{0x}(x)$ increases linearly with distance along the nozzle give the relation $\frac{u_{0x}(x)}{c_*} = \frac{x}{x_*} = \sqrt{\xi}$. Other substitutions are also used according to their paper: $\tau = \frac{c_* t}{x_*}$, $\Omega = \frac{x_*\omega}{c_*}$, $d\xi = \frac{2x}{{x_*}^2}dx$ and $\frac{\partial u_{0x}}{\partial x} = \frac{c_*}{x_*}$. The terms denoted as $(.)_*$ refer to the values taken at the throat. Since the mean flow satisfies the momentum equation D.2 in 1D:

$$\frac{\partial u_x}{\partial t} + u_x\frac{\partial u_x}{\partial x} = -\frac{1}{\rho}\frac{\partial P}{\partial x} \tag{D.2}$$

The relation $\frac{1}{\rho_0}\frac{\partial P_0}{\partial x} = -u_{0x}\frac{\partial u_{0x}}{\partial x}$ is also valid.

$$\begin{aligned}\frac{\partial}{\partial x}\left(\frac{\widehat{u}(x)}{u_{0x}}\right) &= \frac{1}{u_{0x}}\frac{\partial\widehat{u}(x)}{\partial x} - \frac{\widehat{u}(x)}{{u_{0x}}^2}\frac{\partial u_{0x}}{\partial x}\\ \frac{\partial}{\partial x}\left(\frac{\widehat{P_a}(x)}{\gamma P_0}\right) &= \frac{1}{\gamma P_0}\frac{\partial\widehat{P_a}(x)}{\partial x} - \frac{\widehat{P_a}(x)}{\gamma {P_0}^2}\frac{\partial P_0}{\partial x}\end{aligned} \tag{D.3}$$

By doing so, one can simplify the Eq. D.1 and obtain:

$$\left(A\left[\frac{\rho_0}{\gamma P_0}\right]i\omega+\frac{\partial}{\partial x}\left[A\left(\frac{u_{0x}\rho_0}{\gamma P_0}\right)\right]\right)\widehat{P_a}(x)+A\left(\frac{u_{0x}\rho_0}{\gamma P_0}\right)\frac{\partial\widehat{P_a}(x)}{\partial x}+\frac{dA}{dx}\rho_0\widehat{u}(x)+\frac{\partial\rho_0}{\partial x}A\widehat{u}(x) \\ +A\rho_0\frac{\partial\widehat{u}(x)}{\partial x}=\frac{\partial}{\partial x}\left[A\rho_0u_{0x}\widehat{\sigma}(x)\right]+Ai\omega\rho_0\widehat{\sigma}(x) \tag{D.4}$$

For the left-hand side terms:

$$\begin{aligned}LHS=&\left(A\left[\frac{\rho_0}{\gamma P_0}\right]i\omega+\frac{\partial}{\partial x}\left[A\left(\frac{u_{0x}\rho_0}{\gamma P_0}\right)\right]\right)\widehat{P_a}(x)+A\left(\frac{u_{0x}\rho_0}{\gamma P_0}\right)\frac{\partial\widehat{P_a}(x)}{\partial x}+\frac{dA}{dx}\rho_0\widehat{u}(x)\\&+\frac{\partial\rho_0}{\partial x}A\widehat{u}(x)+A\rho_0\frac{\partial\widehat{u}(x)}{\partial x}\\=&A\rho_0i\omega\left(\frac{\widehat{P_a}(x)}{\gamma P_0}\right)+u_{0x}\rho_0\frac{dA}{dx}\left(\frac{\widehat{P_a}(x)}{\gamma P_0}\right)+A\frac{\partial u_{0x}\rho_0}{\partial x}\left(\frac{\widehat{P_a}(x)}{\gamma P_0}\right)+Au_{0x}\rho_0\widehat{P_a}(x)\frac{\partial}{\partial x}\left(\frac{1}{\gamma P_0}\right)\\&+A\left(\frac{u_{0x}\rho_0}{\gamma P_0}\right)\frac{\partial\widehat{P_a}(x)}{\partial x}+\frac{dA}{dx}\rho_0u_{0x}\frac{\widehat{u}(x)}{u_{0x}}+\frac{\partial\rho_0}{\partial x}Au_{0x}\frac{\widehat{u}(x)}{u_{0x}}+A\rho_0\frac{\partial\widehat{u}(x)}{\partial x}\end{aligned}$$

Using the relations Eq. D.3 leads to:

$$\begin{aligned}LHS=&A\rho_0i\omega\left(\frac{\widehat{P_a}(x)}{\gamma P_0}\right)+u_{0x}\rho_0\frac{dA}{dx}\left(\frac{\widehat{P_a}(x)}{\gamma P_0}\right)+A\frac{\partial u_{0x}\rho_0}{\partial x}\left(\frac{\widehat{P_a}(x)}{\gamma P_0}\right)\\&+Au_{0x}\rho_0\widehat{P_a}(x)\frac{\partial}{\partial x}\left(\frac{1}{\gamma P_0}\right)+Au_{0x}\rho_0\left[\frac{\partial}{\partial x}\left(\frac{\widehat{P_a}(x)}{\gamma P_0}\right)+\frac{\widehat{P_a}(x)}{{\gamma P_0}^2}\frac{\partial P_0}{\partial x}\right]\\&+\frac{dA}{dx}\rho_0u_{0x}\frac{\widehat{u}(x)}{u_{0x}}+\frac{\partial\rho_0}{\partial x}Au_{0x}\frac{\widehat{u}(x)}{u_{0x}}+A\rho_0\left[u_{0x}\frac{\partial}{\partial x}\left(\frac{\widehat{u}(x)}{u_{0x}}\right)+\frac{\widehat{u}(x)}{u_{0x}}\frac{\partial u_{0x}}{\partial x}\right]\end{aligned}$$

But $\frac{\partial}{\partial x}\left(\frac{1}{\gamma P_0}\right)=-\frac{1}{{\gamma P_0}^2}\frac{\partial P_0}{\partial x}$, then:

$$\begin{aligned}LHS=&\left(\frac{\partial\rho_0}{\partial x}Au_{0x}+\frac{dA}{dx}\rho_0u_{0x}+A\rho_0\frac{\partial u_{0x}}{\partial x}\right)\frac{\widehat{u}(x)}{u_{0x}}+A\rho_0i\omega\left(\frac{\widehat{P_a}(x)}{\gamma P_0}\right)\\&+\left(u_{0x}\rho_0\frac{dA}{dx}+A\frac{\partial u_{0x}\rho_0}{\partial x}\right)\left(\frac{\widehat{P_a}(x)}{\gamma P_0}\right)+Au_{0x}\rho_0\frac{\partial}{\partial x}\left(\frac{\widehat{P_a}(x)}{\gamma P_0}\right)+A\rho_0u_{0x}\frac{\partial}{\partial x}\left(\frac{\widehat{u}(x)}{u_{0x}}\right)\end{aligned} \tag{D.5}$$

The first and the third terms are equal to zero using the continuity equation, the previous equation can be simplified to give finally:

$$LHS=A\rho_0i\omega\left(\frac{\widehat{P_a}(x)}{\gamma P_0}\right)+Au_{0x}\rho_0\frac{\partial}{\partial x}\left(\frac{\widehat{P_a}(x)}{\gamma P_0}\right)+A\rho_0u_{0x}\frac{\partial}{\partial x}\left(\frac{\widehat{u}(x)}{u_{0x}}\right) \tag{D.6}$$

$$\frac{LHS}{A\rho_0}=i\omega\left(\frac{\widehat{P_a}(x)}{\gamma P_0}\right)+u_{0x}\frac{\partial}{\partial x}\left(\frac{\widehat{P_a}(x)}{\gamma P_0}\right)+u_{0x}\frac{\partial}{\partial x}\left(\frac{\widehat{u}(x)}{u_{0x}}\right) \tag{D.7}$$

The variable change from x to ξ proposed by Marble & Candel leads to:

$$\frac{\partial}{\partial x}\left(\frac{\widehat{u}(x)}{u_{0x}}\right) = \frac{\partial}{\partial \xi}\left(\frac{\widehat{u}(\xi)}{u_{0x}}\right)\frac{\partial \xi}{\partial x} = \frac{\partial}{\partial \xi}\left(\frac{\widehat{u}(\xi)}{u_{0x}}\right)\frac{2\sqrt{\xi}}{x_*} \tag{D.8}$$

$$\frac{\partial}{\partial x}\left(\frac{\widehat{P_a}(x)}{\gamma P_0}\right) = \frac{\partial}{\partial \xi}\left(\frac{\widehat{P_a}(\xi)}{\gamma P_0}\right)\frac{\partial \xi}{\partial x} = \frac{\partial}{\partial \xi}\left(\frac{\widehat{P_a}(\xi)}{\gamma P_0}\right)\frac{2\sqrt{\xi}}{x_*} \tag{D.9}$$

The phase shift can (assuming that $\xi_1 = \left(\frac{x_1}{x_*}\right)^2$) also be rewritten as when injecting the relations D.8 and D.9 in the Eq. D.7 to give:

$$\frac{LHS}{A\rho_0} = i\omega\left(\frac{\widehat{P_a}(\xi)}{\gamma P_0}\right) + u_{0x}\frac{\partial}{\partial \xi}\left(\frac{\widehat{P_a}(\xi)}{\gamma P_0}\right)\frac{2\sqrt{\xi}}{x_*} + u_{0x}\frac{\partial}{\partial \xi}\left(\frac{\widehat{u}(\xi)}{u_{0x}}\right)\frac{2\sqrt{\xi}}{x_*} \tag{D.10}$$

$$\frac{LHS}{A\rho_0} = i\omega\left(\frac{\widehat{P_a}(\xi)}{\gamma P_0}\right) + \frac{\partial}{\partial \xi}\left(\frac{\widehat{P_a}(\xi)}{\gamma P_0} + \frac{\widehat{u}(\xi)}{u_{0x}}\right)u_{0x}\frac{2\sqrt{\xi}}{x_*} \tag{D.11}$$

$$\frac{LHS}{A\rho_0} = i\omega\left(\frac{\widehat{P_a}(\xi)}{\gamma P_0}\right) + \frac{\partial}{\partial \xi}\left(\frac{\widehat{P_a}(\xi)}{\gamma P_0} + \frac{\widehat{u}(\xi)}{u_{0x}}\right)\sqrt{\xi}c_*\frac{2\sqrt{\xi}}{x_*} \tag{D.12}$$

$$\frac{LHS}{A\rho_0}\frac{x_*}{c_*} = i\omega\frac{x_*}{c_*}\left(\frac{\widehat{P_a}(\xi)}{\gamma P_0}\right) + 2\xi\frac{\partial}{\partial \xi}\left(\frac{\widehat{P_a}(\xi)}{\gamma P_0} + \frac{\widehat{u}(\xi)}{u_{0x}}\right) \tag{D.13}$$

Then,

$$\frac{LHS}{A\rho_0}\frac{x_*}{c_*} = i\Omega\left(\frac{\widehat{P_a}(\xi)}{\gamma P_0}\right) + 2\xi\frac{\partial}{\partial \xi}\left(\frac{\widehat{P_a}(\xi)}{\gamma P_0} + \frac{\widehat{u}(\xi)}{u_{0x}}\right) \tag{D.14}$$

For the right-hand side:

$$RHS = \frac{\partial}{\partial x}\left[A\rho_0 u_{0x}\widehat{\sigma}(x)\right] + Ai\omega\rho_0\widehat{\sigma}(x) \tag{D.15}$$

where $\widehat{\sigma}(x) = Se^{-i\omega\int_{x_1}^{x}\frac{d\zeta}{u_{0x}(\zeta)}}$ and can be simplified using:

$$\begin{aligned} e^{-i\omega\int_{x_1}^{x}\frac{d\zeta}{u(\zeta)}} &= e^{-i\omega\int_{\xi_1}^{\xi}\frac{x_*}{2c_*\alpha}d\alpha} = e^{-i\omega\frac{x_*}{2c_*}\left[ln\alpha\right]_{\xi_1}^{\xi}} \\ &= e^{-i\omega\frac{x_*}{2c_*}ln\frac{\xi}{\xi_1}} = e^{\frac{-i\Omega}{2}ln\frac{\xi}{\xi_1}} = \left(\frac{\xi}{\xi_1}\right)^{\frac{-i\Omega}{2}} \end{aligned} \tag{D.16}$$

Thus,

$$\begin{aligned} RHS = &\left(\rho_0 u_{0x} S\frac{dA}{d\xi} + A u_{0x} S\frac{\partial \rho_0}{\partial \xi} + A\rho_0 S\frac{\partial u_{0x}}{\partial \xi}\right)\frac{\partial \xi}{\partial x}\left(\frac{\xi}{\xi_1}\right)^{-\frac{i\Omega}{2}} \\ &+ A\rho_0 u_{0x} S\frac{\partial}{\partial x}\left(\frac{\xi}{\xi_1}\right)^{-\frac{i\Omega}{2}} + Ai\omega\rho_0 S\left(\frac{\xi}{\xi_1}\right)^{-\frac{i\Omega}{2}} \end{aligned} \tag{D.17}$$

$$\begin{aligned} RHS = &S\frac{\partial \xi}{\partial x}\left(\rho_0 u_{0x}\frac{dA}{d\xi} + A\frac{\partial \rho_0 u_{0x}}{\partial \xi}\right)\left(\frac{\xi}{\xi_1}\right)^{-\frac{i\Omega}{2}} \\ &+ A\rho_0 u_{0x} S\frac{\partial \xi}{\partial x}\frac{\partial}{\partial \xi}\left(\frac{\xi}{\xi_1}\right)^{-\frac{i\Omega}{2}} + Ai\omega\rho_0 S\left(\frac{\xi}{\xi_1}\right)^{-\frac{i\Omega}{2}} \end{aligned} \tag{D.18}$$

The first line of the equation is equal to zero using the continuity equation.

$$RHS = A\rho_0 u_{0x} S\frac{\partial \xi}{\partial x}\frac{\partial}{\partial \xi}\left(\frac{\xi}{\xi_1}\right)^{-\frac{i\Omega}{2}} + Ai\omega\rho_0 S\left(\frac{\xi}{\xi_1}\right)^{-\frac{i\Omega}{2}} \tag{D.19}$$

$$RHS = A\rho_0 u_{0x} S\frac{2\sqrt{\xi}}{x_*}\frac{\partial}{\partial \xi}\left(\frac{\xi}{\xi_1}\right)^{-\frac{i\Omega}{2}} + Ai\omega\rho_0 S\left(\frac{\xi}{\xi_1}\right)^{-\frac{i\Omega}{2}} \tag{D.20}$$

$$RHS = A\rho_0 u_{0x} S\frac{-i\Omega}{2}\frac{1}{\xi_1}\frac{2\sqrt{x}}{x_*}\left(\frac{\xi}{\xi_1}\right)^{-\frac{i\Omega}{2}-1} + Ai\omega\rho_0 S\left(\frac{\xi}{\xi_1}\right)^{-\frac{i\Omega}{2}} \tag{D.21}$$

$$RHS = A\rho_0\sqrt{\xi}c_* S\frac{-i\omega x_*}{2c_*}\frac{1}{\xi_1}\frac{2\sqrt{\xi}}{x_*}\left(\frac{\xi}{\xi_1}\right)^{-\frac{i\Omega}{2}-1} + Ai\omega\rho_0 S\left(\frac{\xi}{\xi_1}\right)^{-\frac{i\Omega}{2}} \tag{D.22}$$

One can notice that those two terms canceled. So the final simplified equation is then $i\Omega\left(\frac{\widehat{P_a}(\xi)}{\gamma P_0}\right) + 2\xi\frac{\partial}{\partial \xi}\left(\frac{\widehat{P_a}(\xi)}{\gamma P_0} + \frac{\widehat{u}(\xi)}{u_{0x}}\right) = 0$ which corresponds in the spectral domain to the Equation 41 of the Marble & Candel article.

D.2 Momentum equation

In 1D, Eq. 3.63 becomes using $\varphi_0 = 0$, $x = s$ and $u_{0s} = u_{0x}$:

$$\left(i\omega + \frac{\partial u_{0x}}{\partial x}\right)\widehat{u}(x) + u_{0x}\frac{\partial \widehat{u}(x)}{\partial x} + \frac{1}{\rho_0}\frac{\partial \widehat{P_a}(x)}{\partial x} - \left(\frac{1}{c_0^2\rho_0^2}\frac{\partial P_0}{\partial x}\right)\widehat{P_a}(x) = -\frac{1}{\rho_0}\widehat{\sigma}(x)\frac{\partial P_0}{\partial x} \tag{D.23}$$

Relations in the section D.1 are also used giving:

$$\left(i\omega + \frac{\partial u_{0x}}{\partial x}\right)\widehat{u}(x) + u_{0x}\frac{\partial \widehat{u}(x)}{\partial x} + \frac{1}{\rho_0}\frac{\partial \widehat{P_a}(x)}{\partial x} - \left(\frac{1}{c_0^2\rho_0^2}\frac{\partial P_0}{\partial x}\right)\widehat{P_a}(x) = -\frac{1}{\rho_0}\widehat{\sigma}(x)\frac{\partial P_0}{\partial x} \tag{D.24}$$

Since the mean flow satisfies the momentum equation D.2, the relation $\frac{1}{\rho_0}\frac{\partial P_0}{\partial x} = -u_{0x}\frac{\partial u_{0x}}{\partial x}$ is also valid then $\left(-\frac{1}{c_0^2\rho_0^2}\frac{\partial P_0}{\partial x}\right)\widehat{P_a}(x) = u_{0x}\frac{\partial u_{0x}}{\partial x}\frac{\widehat{P_a}(x)}{\gamma P_0}$. Injecting this relation in the previous equation gives:

$$\begin{aligned} u_{0x}\left(i\omega + \frac{\partial u_{0x}}{\partial x}\right)\frac{\widehat{u}(x)}{u_{0x}} + u_{0x}\left[u_{0x}\frac{\partial}{\partial x}\left(\frac{\widehat{u}(x)}{u_{0x}}\right) + \frac{\widehat{u}(x)}{u_{0x}}\frac{\partial u_{0x}}{\partial x}\right] \\ +{c_0}^2\left[\frac{\partial}{\partial x}\left(\frac{\widehat{P_a}(x)}{\gamma P_0}\right) + \frac{\widehat{P_a}(x)}{\gamma {P_0}^2}\frac{\partial P_0}{\partial x}\right] + u_{0x}\frac{\partial u_{0x}}{\partial x}\frac{\widehat{P_a}(x)}{\gamma P_0} = \widehat{\sigma}(x)u_{0x}\frac{\partial u_{0x}}{\partial x} \end{aligned} \tag{D.25}$$

Keeping in mind that ${c_0}^2 = \left(\frac{\gamma+1}{2}\right){c_*}^2 - \left(\frac{\gamma-1}{2}\right){u_{0x}}^2$ hence

$$\begin{aligned} {c_0}^2\frac{\partial}{\partial x}\left(\frac{\widehat{P_a}(x)}{\gamma P_0}\right) &= \left[(\frac{\gamma+1}{2}){c_*}^2 - (\frac{\gamma-1}{2}){u_{0x}}^2\right]\frac{\partial}{\partial x}\left(\frac{\widehat{P_a}(x)}{\gamma P_0}\right) \\ &= \left[(\frac{\gamma+1}{2}){c_*}^2 - (\frac{\gamma-1}{2}){u_{0x}}^2\right]\frac{\partial}{\partial \xi}\left(\frac{\widehat{P_a}(\xi)}{\gamma P_0}\right)\frac{\partial \xi}{\partial x} \\ &= \left[(\frac{\gamma+1}{2}){c_*}^2 - (\frac{\gamma-1}{2}){u_{0x}}^2\right]\frac{\partial}{\partial \xi}\left(\frac{\widehat{P_a}(\xi)}{\gamma P_0}\right)\frac{2\sqrt{\xi}}{x_*} \\ &= \frac{\sqrt{\xi}}{x_*}\left[(\gamma+1){c_*}^2 - (\gamma-1)(\sqrt{\xi}c_*)^2\right]\frac{\partial}{\partial \xi}\left(\frac{\widehat{P_a}(\xi)}{\gamma P_0}\right) \\ &= \frac{\sqrt{\xi}{c_*}^2}{x_*}\left[(\gamma+1) - (\gamma-1)\xi\right]\frac{\partial}{\partial \xi}\left(\frac{\widehat{P_a}(\xi)}{\gamma P_0}\right) \\ &= u_{0x}\frac{c_*}{x_*}\left[(\gamma+1) - (\gamma-1)\xi\right]\frac{\partial}{\partial \xi}\left(\frac{\widehat{P_a}(\xi)}{\gamma P_0}\right) \end{aligned} \tag{D.26}$$

And

$$\begin{aligned} {c_0}^2\frac{\widehat{P_a}(x)}{\gamma {P_0}^2}\frac{\partial P_0}{\partial x} &= \frac{\widehat{P_a}(x)}{\gamma P_0}\frac{\gamma}{\rho_0}\frac{\partial P_0}{\partial x} \\ &= -\gamma u_{0x}\frac{\partial u_{0x}}{\partial x}\frac{\widehat{P_a}(x)}{\gamma P_0} \\ &= -\gamma u_{0x}\frac{c_*}{x_*}\frac{\widehat{P_a}(\xi)}{\gamma P_0} \end{aligned} \tag{D.27}$$

Eq. D.25 finally becomes:

$$u_{0x}\left(i\omega + 2\frac{c_*}{x_*}\right)\frac{\widehat{u}(\xi)}{u_{0x}} + {u_{0x}}^2\frac{\partial}{\partial\xi}\left(\frac{\widehat{u}(\xi)}{u_{0x}}\right)\frac{\partial\xi}{\partial x} + u_{0x}\frac{c_*}{x_*}\left[(\gamma+1)-(\gamma-1)\xi\right]\frac{\partial}{\partial\xi}\left(\frac{\widehat{P_a}(\xi)}{\gamma P_0}\right) \\ -\gamma u_{0x}\frac{c_*}{x_*}\frac{\widehat{P_a}(\xi)}{\gamma P_0} + u_{0x}\frac{c_*}{x_*}\frac{\widehat{P_a}(\xi)}{\gamma P_0} = S\left(\frac{\xi}{\xi_1}\right)^{-\frac{i\Omega}{2}} u_{0x}\frac{c_*}{x_*} \tag{D.28}$$

Hence,

$$u_{0x}\left(i\omega + 2\frac{c_*}{x_*}\right)\frac{\widehat{u}(\xi)}{u_{0x}} + {u_{0x}}^2\frac{2\sqrt{\xi}}{x_*}\frac{\partial}{\partial\xi}\left(\frac{\widehat{u}(\xi)}{u_{0x}}\right) + u_{0x}\frac{c_*}{x_*}\left[(\gamma+1)-(\gamma-1)\xi\right]\frac{\partial}{\partial\xi}\left(\frac{\widehat{P_a}(\xi)}{\gamma P_0}\right) \\ -\gamma u_{0x}\frac{c_*}{x_*}\frac{\widehat{P_a}(\xi)}{\gamma P_0} + u_{0x}\frac{c_*}{x_*}\frac{\widehat{P_a}(\xi)}{\gamma P_0} = S\left(\frac{\xi}{\xi_1}\right)^{-\frac{i\Omega}{2}} u_{0x}\frac{c_*}{x_*} \tag{D.29}$$

The previous equation can be simplified by $u_{0x}\dfrac{c_*}{x_*}$ knowing that $u_{0x} = \sqrt{\xi}c_*$:

$$i\omega\frac{x_*}{c_*}\frac{\widehat{u}(\xi)}{u_{0x}} + 2\frac{\widehat{u}(\xi)}{u_{0x}} + \sqrt{\xi}c_*\frac{2\sqrt{\xi}}{x_*}\frac{x_*}{c_*}\frac{\partial}{\partial\xi}\left(\frac{\widehat{u}(\xi)}{u_{0x}}\right) + \left[(\gamma+1)-(\gamma-1)\xi\right]\frac{\partial}{\partial\xi}\left(\frac{\widehat{P_a}(\xi)}{\gamma P_0}\right) \\ -(\gamma-1)\frac{\widehat{P_a}(\xi)}{\gamma P_0} = S\left(\frac{\xi}{\xi_1}\right)^{-\frac{i\Omega}{2}} \tag{D.30}$$

Finally,

$$\left(i\Omega + 2\xi\frac{\partial}{\partial\xi}\right)\frac{\widehat{u}(\xi)}{u_{0x}} + \left[(\gamma+1)\frac{1}{\xi}-(\gamma-1)\right]\xi\frac{\partial}{\partial\xi}\left(\frac{\widehat{P_a}(\xi)}{\gamma P_0}\right) + 2\frac{\widehat{u}(\xi)}{u_{0x}} \\ -(\gamma-1)\frac{\widehat{P_a}(\xi)}{\gamma P_0} = S\left(\frac{\xi}{\xi_1}\right)^{-\frac{i\Omega}{2}} \tag{D.31}$$

Which corresponds to Eq. 42 in the article of Marble & Candel in the spectral domain.

Appendix E

1D characteristics filtering

All over the study, acoustic waves are considered to be 1D. In order to separate P^+ over P^-, a 1D characteristics filtering is applied in the combustion chamber and in the cylinder downstream of the nozzle. To apply the 1D characteristics filtering method, one needs to know the 1D fluctuating and the mean part of the pressure and velocity. From the LES computations, they are obtained using the plane sensors described in chapter 4 where a spatial averaging along the section of the variables is applied. The Riemann invariants are used at each positions (i) to give P_i^+ and P_i^-. P_i^+ and P_i^- are expressed as a sum of an acoustic and a non acoustic part.

$$P_i^+(t) = P_{i_{ac}}^+(t) + P_{i_{nac}}^+(t)$$
$$P_i^-(t) = P_{i_{ac}}^-(t) + P_{i_{nac}}^-(t)$$

The non acoustic part needs to be filtered. The procedure is detailed for the acoustic wave propagating in the positive x-direction (the same method is applied in the negative x-direction).

As an example, if the reference position is chosen for $i = 1$, in order to find $P_{1_{ac}}^+(t)$, let us consider the acoustic propagation of a one-dimensional wave. If $\Delta t_{12_{ac}}^+$ is the time needed for the wave from 1 to reach the point called 2. Two equations can be written:

$$P_1^+(t) = P_{1_{ac}}^+(t) + P_{1_{nac}}^+(t)$$
$$P_2^+(t + \Delta t_{12ac}^+) = P_{1_{ac}}^+(t) + P_{2_{nac}}^+(t + \Delta t_{12ac}^+)$$

Those two equations show that without any dissipation, after the time $\Delta t_{12_{ac}}^+$, the acoustic wave at position 2 is the same as in 1. This is not valid for the turbulent or the entropy waves which are not necessarily correlated. Based on Kopitz [Kopitz 2005] studies, the acoustic filtering method uses the propagating characteristic of the acoustic information at a specific speed to filter the non acoustic one (defined as $P_{1_{nac}}^+(t)$, $P_{2_{nac}}^+(t + \Delta t_{12_{ac}}^+)$ and so

on). Regarding this, one can write for n points:

$$
\begin{aligned}
P_1^+(t) &= P_{1_{ac}}^+(t) + \langle P_{1_{nac}}(t) \\
P_2^+(t + \Delta t_{12_{ac}}^+) &= P_{1_{ac}}^+(t) + P_{2_{nac}}^+(t + \Delta t_{12_{ac}}^+) \\
P_3^+(t + \Delta t_{12_{ac}}^+ + \Delta t_{23_{ac}}) &= P_{1_{ac}}^+(t) + P_{3_{nac}}^+(t + \Delta t_{12_{ac}}^+ + \Delta t_{23_{ac}}^+) \\
\vdots &= \vdots \\
P_n^+(t + \Delta t_{12_{ac}}^+ + \cdots + \Delta t_{(n-1)n_{ac}}^+) &= P_{1_{ac}}^+(t) + P_{n_{nac}}^+(t + \Delta t_{12_{ac}}^+ + \cdots + \Delta t_{(n-1)n_{ac}}^+)
\end{aligned}
$$

Summing all the terms on the left-hand side and in the right-hand side gives:

$$
\sum_{i=1}^{n} P_i^+(t + \sum_{j=1}^{i} \Delta t_{(j-1)j_{ac}}^+) = nP_{1_{ac}}^+(t) + \sum_{i=1}^{n} P_{i_{nac}}(t + \sum_{j=1}^{i} \Delta t_{(j-1)j_{ac}}^+)
$$

assuming $\Delta t_{01_{ac}} = 0$.

The last term in the right hand side goes to zero when n is becoming large. The reason is that this term is a sum uncorrelated terms. Thus with $\frac{1}{n}\sum_{i=1}^{n} P_{i_{ac}}^+(t + \sum_{j=1}^{i} \Delta t_{(j-1)j_{ac}}^+) \sim 0$, one can write:

$$
P_{1_{ac}}^+(t) \approx \frac{\sum_{i=1}^{n} P_i^+(t + \sum_{j=1}^{i} \Delta t_{(j-1)j_{ac}}^+)}{n}
$$

The acoustic propagation speed is defined as $u + c$, where u is the local fluid speed and c is the local speed of sound.The times Δt^+ is defined as:

$$
\Delta t_{(j-1)j_{ac}}^+ = \frac{D_{(j-1)j}}{V_{(j-1)j}} = \frac{D_{(j-1)j}}{\frac{u_{(j-1)} + u_j}{2} + \frac{c_{(j-1)} + c_j}{2}} \tag{E.1}
$$

Where $D_{(j-1)j}$ is the distance between the point $j-1$ and j and using the assumption that the acoustic propagation speed is the average of the propagating speed at $j-1$ and j.

The same procedure can be applied for the acoustic wave going in the negative x-direction, this time the acoustic propagation speed is defined as $c - u$.

$$
\Delta t_{(j-1)j}^- = \frac{D_{(j-1)j}}{V_{(j-1)j}} = \frac{D_{(j-1)j}}{-\frac{u_{(j-1)} + u_j}{2} + \frac{c_{(j-1)} + c_j}{2}} \tag{E.2}
$$

Appendix F

Acoustic energy balance at the outlet of the domain

The acoustic intensity (or acoustic energy flux) [Cantrell 1964, Goldstein 1976, Minotti 2004] can be written as:

$$\overrightarrow{I^+} = \frac{1}{\rho_0 c_0}(1+M_0)^2 p_2^{+2}\overrightarrow{e_x} \tag{F.1}$$

and

$$\overrightarrow{I^-} = -\frac{1}{\rho_0 c_0}(1-M_0)^2 p_2^{-2}\overrightarrow{e_x} \tag{F.2}$$

The objective is to quantify the ratio $\left|\frac{I^-}{I^+}\right|$ and to check if this term is smaller than unity. It writes:

$$\left|\frac{I^-}{I^+}\right| = \frac{(1-M_0)^2}{(1+M_0)^2}\frac{p_2^{-2}}{p_2^{+2}} \tag{F.3}$$

$$= \frac{(1-M_0)^2}{(1+M_0)^2}R_{out}^2 \tag{F.4}$$

At the outlet, $M_0 = 0.413$ so the ratio becomes:

$$\left|\frac{I^-}{I^+}\right| = 0.175 R_{out}^2 \tag{F.5}$$

This means that for a total reflection of the wave $\| R_{out} \| = 2.4$, in our case at the outlet boundary condition the maximum value reached is 1.1 so 21% of the acoustic energy is indeed reflected.

Appendix G

Proof of acoustic generation due to entropy forcing in the 2D model

---

The objective here is to ensure that the outgoing acoustic waves found by the 2D model in the configuration are primarily due to the entropy forcing and not to the acoustic forcing issuing from the reflection of the acoustic waves on the domain boundaries. The outgoing waves P_1^- and P_2^+ can be expressed respectively as the sum of three different contributions:

$$P_1^- = \left[\frac{P_1^-}{\sigma}\right]\sigma + \left[\frac{P_1^-}{P_1^+}\right]P_1^+ + \left[\frac{P_1^-}{P_2^-}\right]P_2^- \tag{G.1}$$

and

$$P_2^+ = \left[\frac{P_2^+}{\sigma}\right]\sigma + \left[\frac{P_2^+}{P_1^+}\right]P_1^+ + \left[\frac{P_2^+}{P_2^-}\right]P_2^- \tag{G.2}$$

In Eq. G.1, the terms $[P_1^-/\sigma]$, $[P_1^-/P_1^+]$, $[P_1^-/P_2^-]$ (respectively $[P_2^+/\sigma]$, $[P_2^+/P_2^-]$ and $[P_2^+/P_1^+]$ for Eq. G.2) are the (T)ATFs obtained using perfectly non-reflective boundary conditions (see section 5.2.2) while P_1^+ and P_2^- correspond to the amplitude of the acoustic waves entering the nozzle with the partially reflective boundaries. If one assume $\sigma = 1$, it is possible to respectively plot the first and the sum of the last two terms of Eqs. G.1 and G.2 to verify that the first term in both equations is the main contributor. They are plotted in Fig. G.1 for Eq. G.1 (*left*) and Eq. G.2 (*right*).

Looking at the *left* of Fig. G.1, one can see that the term $[P_1^-/\sigma] * \sigma$ has a greater contribution compared to the sum of the two other terms. Except for the point at 493 Hz between where the first term is 1.22 times larger than the sum of the two others, a factor above 2 is found for the other frequency. In addition, once again the frequency at 905 Hz is removed from the figure where it was seen that in the upstream region of the nozzle that P_1^+ is strongly polluted by the background noise. Despite a not negligible contribution of the second and third terms in the RHS of Eq. G.1, it can be concluded than the outgoing waves P_1^- is for the most part generated by the entropy forcing.

Looking at the *right* of Fig. G.1, the same conclusion can be stated namely that the term $[P_2^+/\sigma] * \sigma$ represented in blue is at least 2 times larger than the sum of the two last terms. Once again, it can be concluded than the outgoing waves P_2^+ is for the most part

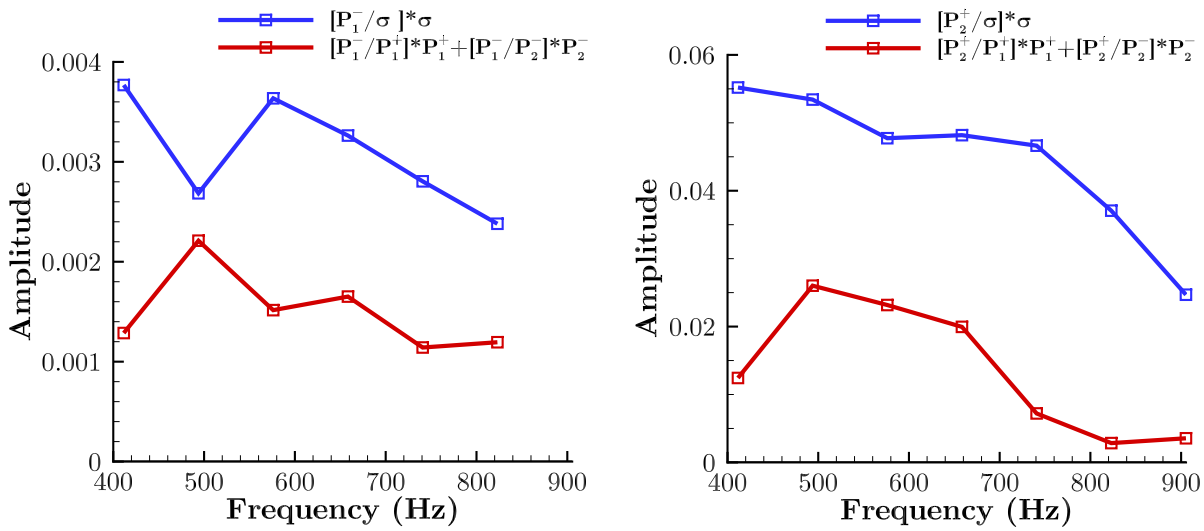

Figure G.1: Illustrations of P_1^- terms (*left*) and P_2^+ terms(*right*).

generated by the entropy forcing even though the sum of the last terms represented in red has also a non negligible contribution.

List of Figures

List of Tables

Bibliography

[Bake 2007] F. Bake, U. Michel and I. Röhle. *Investigation of entropy noise in aero-Engine combustors*. Journal of Engineering for Gas Turbines and Power, vol. 129, pp. 370–376, 2007.

[Bake 2008] F. Bake, N. Kings and I. Röhle. *Fundamental mechanism of entropy noise in aero-engines: experimental investigation*. Journal of Engineering for Gas Turbines and Power, vol. 130, pp. 1–6, 2008.

[Bake 2009a] F. Bake, N. Kings, A. Fischer and I. Röhle. *Experimental investigation of the entropy noise mechanism in aero-engines*. International Journal of Aeroacoustics, vol. 8, pp. 125–142, 2009.

[Bake 2009b] F. Bake, N. Kings, A. Fischer and I. Röhle. *Indirect combustion noise: investigations of noise generated by the acceleration of flow inhomogeneities*. Workshop BRUCO, Ecole Centrale Paris, 2009.

[Bake 2009c] F. Bake, C. Richter, B. Mühlbauer, N. Kings, I. Röhle, F. Thiele and B. Noll. *The entropy wave generator (EWG): a reference case on entropy noise*. Journal of Sound and Vibration, vol. 326, pp. 574–598, 2009.

[Bauerheim 2016] M. Bauerheim, I. Duran, T. Livebardon, F. Wang, S. Moreau and T. Poinsot. *Transmission and reflection of acoustic and entropy waves through a statir-rotor stage.* Journal of Sound and Vibration, vol. 374, pp. 260–278, 2016.

[Baum 1994] M. Baum, T. Poinsot and D. Thevenin. *Accurate boundary conditions for multicomponent reactive flows*. Journal of Computational Physics, vol. 116, pp. 247–261, 1994.

[Berland 2007] J. Berland, C. Bogey, O. Mardsen and C. Bailly. *High-order, low dispersive and low dissipative explicit schemes for multiple-scaleand boundary problems.* Journal of Computational Physics, vol. 224, pp. 637–662, 2007.

[Bertier 2006] N. Bertier. *Simulation des grandes échelles en aérothermique sur des maillages non-structurés généraux.* PhD thesis, Université Pierre et Marie Curie, Paris, France, 2006.

[Blacodon 2009] D. Blacodon. *Combustion-noise characterization of a turbofan engine with spectral estimation method*. Journal of Propulsion and Power, vol. 25, n°. 2, pp. 374–379, 2009.

[Bloy 1979] A. W. Bloy. *The pressure waves produced by the convection of temperature disturbances in high subsonic nozzle flows*. Journal of Fluid Mechanics, vol. 94, n°. 3, pp. 465–475, 1979.

[Bogey 2004] C. Bogey and C. Bailly. *A family of low dispersive and low dissipative explicit schemes for flow and noise computations*. Journal of Computational Physics, vol. 194, pp. 194–214, 2004.

[Bohn 1976] M. S. Bohn. *Noise produced by the interaction of acoustic waves and entropy waves with high-speed nozzle flows.* PhD thesis, California Institute of Technology Pasedana, 1976.

[Bohn 1977] M. S. Bohn. *Response of a subsonic nozzle to acoustic and entropy disturbances*. Journal of Sound and Vibration, vol. 52, pp. 283–297, 1977.

[Bragg 1963] S. L. Bragg. *Combustion noise*. Journal of Institute of Fuel, vol. 36, pp. 12–16, 1963.

[Butcher 1996] J. C Butcher. *A history of Runge-Kutta methods*. Applied Numerical Mathematics, vol. 20, pp. 247–260, 1996.

[Cacqueray 2010] N. D. Cacqueray. *Méthodes numériques pour les écoulements supersoniques avec application au calcul du bruit rayonné par un jet sur-détendu*. PhD thesis, École Centrale de Lyon, Lyon, France, 2010.

[Candel 1972] S. M. Candel. *Analytical studies of some acoustic problems of jet engines*. PhD thesis, California Institute of Technology, CA, USA, 1972.

[Candel 2009] S. M. Candel, D. Durox, S. Ducruix, A. L. Birbaud, N. Noiray and T. Schuller. *Flame dynamics and combustion noise: progress and challenges.* International Journal of Aeroacoustics, vol. 8, pp. 1–56, 2009.

[Cantrell 1964] R.-H. Cantrell and R.-W. Hart. *Interaction between sound and flow in acoustic cavities : mass, momentum and energy considerations.* Journal of the Acoustical Society of America, vol. 36, 1964.

[Cantwell 1993] B. J. Cantwell. *On the behavior of velocity gradient tensor invariants in direct numerical simulations of turbulence.* Physics of Fluid A: Fluid Dynamics (1989-1993), vol. 5, 1993.

[Chapman 1979] D. R. Chapman. *Computational aerodynamics development and outlook*. AIAA Journal, vol. 17, n°. 12, pp. 1293–1313, 1979.

[Chedevergne 2010] F. Chedevergne. *Advanced wall model for aerothermodynamics*. International Journal of Heat and Fluid Flow, vol. 31, pp. 916–924, 2010.

[Chevalier 2005] P. Chevalier, B. Courbet, D. Dutoya, P. Klotz, E. Ruiz, J. Troyes and P. Villedieu. *CEDRE: development and validation of a multiphysic computational software*. 1^{st} EUCASS, Moscow, 2005.

[Choi 2012] H. Choi and P. Moin. *Grid-point requirements for large eddy simulation: Chapman's estimates revisited*. Physics of Fluids, vol. 24, pp. 011702–011702–5, 2012.

[Chu 1958] B. Chu and L. S. G. Kovàsznay. *Non-linear interactions in a viscous heat-conducting compressible gas*. Journal of Fluid Mechanics, vol. 3, pp. 494–514, 1958.

[CINES 2014] CINES. *OCCIGEN: the new supercomputer*. 2014.

[Crocco 1953] L. Crocco. *Supercritical gaseous discharge with high frequency oscillations.* Aerotechnica, vol. 33, pp. 46–53, 1953.

[Crocco 1967] L. Crocco and W. A. Sirignano. *Behavior of supercritical nozzles under three dimensional oscillatory conditions.* AGARD - Advisory Group for Aerospace Research and Development (North Atlantic Treaty Organisation), vol. 117, 1967.

[Culick 1983] F. Culick and T. Rogers. *The response of normal shocks in diffusers.* AIAA Journal, vol. 21, pp. 1382–1390, 1983.

[Cumpsty 1977] N. A. Cumpsty and F. E. Marble. *The interaction of entropy fluctuations with turbine blade rows; a mechanism of turbojet engine noise*. Proceedings of the Royal Society of London, Series A, vol. 357, pp. 323–344, 1977.

[Dowling 2014] A.P. Dowling and Y. Mahmoudi. *Combustion noise*. Proceedings of the Combustion Institute, vol. 35, p. 65–100, 2014.

[Ducruix 2003] S. Ducruix, T. Schuller, D. Durox and S. Candel. *Combustion dynamics and instabilities: elementary coupling and driving mechanisms.* Journal of Propulsion and Power, vol. 19, n°. 5, pp. 722–734, 2003.

[Ducruix 2011] S. Ducruix. *Programme blanc, projet DISCERN*. ANR document scientifique, 2011.

[Duran 2011] I. Duran and S. Moreau. *Analytical and numerical study of the Entropy Wave Generator experiment on indirect combustion noise*. In 17^{th} AIAA/CEAS Aeroacoustics Conference, AIAA Paper, AIAA 2011-2829, Portland, OR, USA, 2011.

[Duran 2013a] I. Duran and S. Moreau. *Solution of the quasi-one-dimensional linearized Euler equations using flow invariants and the Magnus expansion*. Journal of Fluid Mechanics, vol. 723, pp. 190–231, 2013.

[Duran 2013b] I. Duran, S. Moreau and T. Poinsot. *Analytical and numerical study of combustion noise through a subsonic nozzle*. AIAA Journal, vol. 51, pp. 42–52, 2013.

[Duran 2015] I. Duran and A. S. Morgans. *On the reflection and transmission of circumferential waves though nozzles.* Journal of Fluid Mechanics, vol. 773, pp. 137–153, 2015.

[Eckstein 2006] J. Eckstein, E. Freitag, C. Hirsch and T. Sattelmayer. *Experimental study on the role of entropy waves in low-frequency oscillations in a RQL combustor*. Journal of Engineering for Gas Turbines and Power, vol. 128, pp. 264–270, 2006.

[Favre 1965] A. Favre. *Équations des gaz turbulens compressibles. I. Formes générales*. Journal de Mécanique, vol. 4, pp. 361–390, 1965.

[Giammar 1970] R. D. Giammar and A. A. Putnam. *Combustion roar of turbulent diffusion flames.* Journal of Engineering for Power, vol. 92, n°. 2, pp. 157–165, 1970.

[Giauque 2005] A. Giauque, L. Selle, L. Gicquel, T. Poinsot, H. Buechner, P. Kauffman and W. Krebs. *System identification of large-scale swirled partially premixed combustor using LES and measurements*. Journal of Turbulence, vol. 6, p. N21, 2005.

[Giauque 2012] A. Giauque, M. Huet and F. Cléro. *Analytical analysis of indirect combustion noise in subcritical nozzles*. Journal of Engineering for Gas Turbines and Power, vol. 134, n°. 11, p. 111202, 2012.

[Giauque 2013] A. Giauque, M. Huet, F. Cléro, S. Ducruix and F. Richecoeur. *Thermoacoustic shape optimization of a subsonic nozzle*. Journal of Engineering for Gas Turbines and Power, vol. 135, n°. 10, p. 102601, 2013.

[Giusti 2016] A. Giusti, N. A. Worth, E. Mastorakos and A. P. Dowing. *Experimental and numerical investigation into the propagation of entropy waves in a small-scale rig*. In 54^{th} AIAA Aerospace Sciences Meeting, AIAA Paper, AIAA 2016-1942, San Diego, CA, USA, 2016.

[Goh 2011] C. S. Goh and A. S. Morgans. *Phase prediction of the response of choked nozzles to entropy and acoustic disturbances*. Journal of Sound and Vibration, vol. 330, n°. 21, pp. 5184–5198, 2011.

[Goldstein 1976] M. E. Goldstein. Aeroacoustics. McGraw-Hill Inc., 1976.

[Guillaume 1991] P. Guillaume, J. Schoukens, R. Pintelon and I. Kollár. *Crest-Factor minimization using nonlinear Chebyshev approximation methods*. IEEE Transactions on Instrumentation and Measurements, vol. 40, n°. 6, pp. 982–989, 1991.

[Hassan 1974] H. A. Hassan. *Scaling on combustion-generated noise*. Journal of Fluid Mechanics, vol. 66, n°. 3, pp. 445–453, 1974.

[Hosseinalipour 2017] S. M. Hosseinalipour, A. Fattahi, H. Afshari and N. Karimi. *On the effects of convecting entropy waves on the combustor.* Applied Thermal Engineering, vol. 110, p. 901–909, 2017.

[Howe 2010] M. S. Howe. *Indirect combustion noise*. Journal of Fluid Mechanics, vol. 659, pp. 267–288, 2010.

[Hu 1996] F. Q. Hu, M. Y. Hussaini and J. L. Manthey. *Low-dissipation and low-dispersion Runge-Kutta schemes for computational acoustics.* Journal of Computational Physics, vol. 124, pp. 177–191, 1996.

[Huber 2008] A. Huber, P. Romann and W. Polifke. *Filter-based time-domain impedance boundary conditions for CFD applications.* Proceedings of ASME Turbo Expo, GT2008-51195, Berlin, Germany, 2008.

[Huet 2013] M. Huet and A. Giauque. *A nonlinear model for indirect combustion noise throught a compact nozzle.* Journal of Fluid Mechanics, vol. 733, pp. 268–301, 2013.

[Jaensch 2014] S. Jaensch, T. Emmert, C. F. Silva and W. Polifke. *A Grey-Box identification approach for thermoacoustic network models*. Proceedings of ASME Turbo Expo, GT2014-27034, Düsseldorf, Germany, 2014.

[Johnson 1985] D. A. Johnson and L. S. King. *A mathematically simple turbulence closure model for attached and separated turbulent boundary layers*. AIAA Journal, vol. 23, pp. 1684–1692, 1985.

[Jones 1972] W. P. Jones and B. E. Launder. *The prediction of laminarization with two-equation model of turbulence.* Journal of Heat and Mass Transfer, vol. 15, pp. 301–314, 1972.

[Kaji 1970a] S. Kaji and T. Okazaki. *Propagation of sound waves through a blade row I, analysis based on the semi-actuator disk theory*. Journal of Sound and Vibration, vol. 11, pp. 339–353, 1970.

[Kaji 1970b] S. Kaji and T. Okazaki. *Propagation of sound waves through a blade row II, analysis based on the semi-actuator disk theory*. Journal of Sound and Vibration, vol. 11, pp. 355–375, 1970.

[Kaufmann 2002] A. Kaufmann, F. Nicoud and T. Poinsot. *Flow forcing techniques for numerical simulation of combustion instabilities*. Combustion & Flame, vol. 131, n°. 4, pp. 371–385, 2002.

[Kawai 2012] S. Kawai and J. Larsson. *Wall-modeling in large eddy simulation: Length scales, grid resolution and accuracy*. Physics of Fluids, vol. 24, n°. 1, 2012.

[Knobloch 2015a] K. Knobloch, T. Werner and F. Bake. *Entropy noise generation and reduction in a heated nozzle flow*. In 21^{st} AIAA/CEAS Aeroacoustics Conference, AIAA Paper, AIAA 2015-2818, Dallas, TX, USA, 2015.

[Knobloch 2015b] K. Knobloch, T. Werner and F. Bake. *Noise generation in hot nozzle flow*. In Proceedings of ASME Turbo Expo 2015, GT2015-43702, Montréal, Canada, 2015.

[Kolmogorov 1991] A. N. Kolmogorov. *The local structure of turbulence in incompressible viscous fluid for very large reynolds numbers*. Proceeding of the Royal Society of London, Series A, vol. 434, n°. 15, pp. 9–13, 1991.

[Kopitz 2005] J. Kopitz. *Characteristics-based filter identification of planar acoustic waves in numerical simulation of turbulent compressible flow.* 12th international congress on sound and vibration, 2005.

[Kuo 1996] C. Y. Kuo and A. Dowling. *Oscillations of a moderately underexpanded choked jet impinging upon a flat plate.* Journal of Fluid Mechanics, vol. 315, pp. 267—291, 1996.

[Launder 1974] B. E. Launder and B. Sharma. *Application of the energy dissipation model of turbulence to the calculation of flow near spinning disc.* Letter in Heat and Mass Transfer, vol. 1, pp. 131–137, 1974.

[Leyko 2008] M. Leyko, F. Nicoud, S. Moreau and T. Poinsot. *Numerical and analytical investigation of the indirect noise in a nozzle*. In Proceedings of the Summer Programm, Center of Turbulence Research, 2008.

[Leyko 2009] M. Leyko, F. Nicoud and T. Pionsot. *Comparison of direct and indirect combustion noise mechanisms in a model combustor.* AIAA Journal, vol. 47, pp. 2709–2716, 2009.

[Leyko 2010] M. Leyko. *Mise en oeuvre et analyse de calculs aéroacoustiques de type SGE pour la prévision du bruit de chambres de combustion aéronautiques*. PhD thesis, Université de Toulouse, 2010.

[Leyko 2011] M. Leyko, S. Moreau, F. Nicoud and T. Poinsot. *Numerical and analytical modelling of entropy noise in a supersonic nozzle with a shock.* Journal of Sound and Vibration, vol. 330, n°. 16, pp. 3944–3958, 2011.

[Leyko 2014] M. Leyko, I. Duran, S. Moreau, F. Nicoud and T. Poinsot. *Simulation and modelling of the waves transmission and generation in a stator blade row in a combustion-noise framework.* Journal of Sound and Vibration, vol. 333, pp. 6090–6106, 2014.

[Li 2005] X. Li, C. Schemel, U. Michel and F. Thiele. *Azimuthal sound mode propagation in axisymmetric flow ducts*. AIAA Journal, vol. 42, n°. 10, p. 2019–2027, 2005.

[Livebardon 2016] T. Livebardon, S. Moreau, L. Gicquel, T. Poinsot and E. Bouty. *Combining LES of combustion chamber and an actuator disk theory to predict combustion noise in a helicopter engine.* Combustion and Flame, vol. 165, pp. 272–287, 2016.

[Lodato 2008] G. Lodato, P. Domingo and L. Vervisch. *Three-dimensional boundary conditions for direct and large-eddy simulation of compressible viscous flows*. Journal of Computational Physics, vol. 227, n°. 10, pp. 5105–5143, may 2008.

[Lourier 2014] J-M. Lourier, A. Huber, B. Noll and M. Aigner. *Numerical analysis of indirect combustion noise generation within a subsonic nozzle*. AIAA journal, vol. 52, n°. 10, pp. 2114–2126, 2014.

[Magnus 1954] W. Magnus. *On the exponential solution of differential equations for linear operator.* Communication Pure Applied Mathematics, vol. 7, n°. 4, pp. 649–673, 1954.

[Marble 1973] F. E. Marble. *Acoustic disturbance from gas non-uniformities convecting through a nozzle.* In Symposium on Transportation Noise, 1973.

[Marble 1977] F. E. Marble and S. M. Candel. *Acoustic disturbance from gas non-uniformities convected through a nozzle*. Journal of Sound and Vibration, vol. 55, pp. 225–243, 1977.

[Menter 1992] F. R. Menter. *Influence of freestream values on k-ω turbulence prediction*. AIAA Journal, vol. 30, n°. 8, pp. 1651–1659, 1992.

[Menter 1993] F. R. Menter. *Zonal two-equation k-omega turbulence models for aerodynamic flows*. 23^{rd} Fluids Dynamics, Plasmadynamics and Lasers Conderence, AIAA Paper, AIAA 93-2906, Orlando, FL, USA, 1993.

[Menter 1994] F. R. Menter. *Two-equation eddy-viscosity transport turbulence model for engineering applications.* AIAA Journal, vol. 32, n°. 8, pp. 1598–1605, 1994.

[Minotti 2004] A. Minotti. *Contribution à la mesure aéroacoutique par vélocimétrie laser Doppler*. PhD thesis, Ecole Nationale supérieure de l'aéronautique et de l'espace, 2004.

[Mishra 2013] A. Mishra and D.J. Bodony. *Evaluation of actuator disk theory for predicting indirect combustion noise*. Journal of Sound and Vibration, vol. 332, n°. 4, pp. 821–838, 2013.

[Moase 2007] W. Moase, M. J. Brear and C. Manzie. *The forced response of choked nozzles and supersonic diffusers*. Journal of Fluid Mechanics, vol. 585, pp. 281–304, 2007.

[Morfey 1973] C. L. Morfey. *Amplification of aerodynamic noise by convected flow inhomogeneities*. Journal of Sound and Vibration, vol. 31, pp. 391–397, 1973.

[Morgans 2013] A. S. Morgans, C. S. Goh and J. A. Dahan. *The dissipation and shear dispersion of entropy waves in combustor thermoacoustics.* Journal of Fluid Mechanics, vol. 733, n°. R2, 2013.

[Morgans 2015] A. S. Morgans and J. Li. *Analytical and numerical study of the Entropy Wave Generator experiment on indirect combustion noise*. In 22^{nd} International Congress on Sound and Vibration, Florence, Italy, 2015.

[Mühlbauer 2007] B. Mühlbauer, A. Widenhorn, M. Liu, B. Noll and M. Aigner. *Fundamental mechanism of entropy noise in aero-engines: Numerical simulation*. Proceeding of ASME Turbo Expo, GT2007-27173, Montréal, Canada, pp. 115–124, 2007.

[Mühlbauer 2008] B. Mühlbauer, B. Noll and M. Aigner. *Numerical investigation of entropy noise and its acoustic sources in aero-engines,*. pp. 209–220, 2008.

[Mühlbauer 2009] B. Mühlbauer, B. Noll and M. Aigner. *Numerical investigation of the fundamental mechanism of entropy noise generation in aero-engines*. Acta Acustica united with Acustica, vol. 95, n°. 3, pp. 470–478, 2009.

[Muir 1977a] R. S. Muir. *The application of a semi-actuator disk model to sound transmission calculations in turbomachinery part I: the single blade row*. Journal of Sound and Vibration, vol. 54, pp. 393–408, 1977.

[Muir 1977b] R. S. Muir. *The application of a semi-actuator disk model to sound transmission calculations in turbomachinery part II: multiple blade rows*. Journal of Sound and Vibration, vol. 55, pp. 355–349, 1977.

[Muthukrishnan 1977] M. Muthukrishnan. *An experimental study of the separation of combustion entropy noise.* PhD thesis, Gorgia Institute of Technology, 1977.

[Nicoud 1999] F. Nicoud and F. Ducros. *Subgrid-scale modelling based on the square of the velocity gradient tensor*. Flow Turbulence and Combustion, vol. 62, n°. 3, pp. 183–200, 1999.

[Nicoud 2011] F. Nicoud, H. Baya-Toda, O. Cabrit, S. Bose and J. Lee. *Using singular values to build a subgrid-scale model for large eddy simulations*. Physics of Fluids, vol. 23, n°. 8, 2011.

[Novak 1967] R. Novak. *Streamline curvature computing procedures for fluid-flow problems*. Journal of Engineering for Power, vol. 89, n°. 4, pp. 478–490, 1967.

[ONERA 2009] ONERA. *Les moyens de calcul intensifs*. 2009.

[Pickett 1975] G. F. Pickett. *Core engine noise due to temperature fluctuations convecting through turbine blade rows*. 2^{nd} Aeroacoustics Conference, AIAA Paper, AIAA 75-528, Hampton, VA, USA, 1975.

[Piomelli 2002] U. Piomelli and E. Balaras. *Wall-layer models for large eddy simulations*. Annual review of Fluid Mechanics, vol. 34, pp. 349–374, 2002.

[Piscoya 2004] R. Piscoya, M. Ochmann, H. Brick and P. Költzsch. *Modelling of combustion noise with boundary element method and equivalent source method*. 33^{rd} International COngress ans Exposition on Noise Control Engineering, Internoise., 2004.

[Poinsot 1992] T. J. Poinsot and S. K. Lele. *Boundary conditions for direct simulations of compressible viscous flows*. Journal of Computational Physics, vol. 101, n°. 1, pp. 104–129, 1992.

[Poinsot 2012] T. Poinsot and D. Veynante. Theoretical and numerical combustion, 3rd edition. R. T. Edwards, Flourtown, PA, USA, 2012.

[Polifke 2014] W. Polifke. *Black-box system identification for reduced order model construction*. Annals of Nuclear Energy, vol. 67, pp. 109–128, 2014.

[Pope 2000] S. B. Pope. Turbulent flows. Cambridge University Press, 2000.

[Prandtl 1925] L. Prandtl. *Bericht über Untersuchungen zur ausgebildeten Turbulenz*. Zeitschrift für Angewandte Mathematik und Mechanik, vol. 5, pp. 136–139, 1925.

[Refloch 2011] A. Refloch *et al. CEDRE Software*. Aerospace Lab Journal, vol. 2, 2011.

[Reynolds 1895] O. Reynolds. *On the dynamical theory of incompressible viscous fluids and the determination of the criterion.* Philisophical Transactions of the Royal Society of London, vol. 186, pp. 123–164, 1895.

[Richter 2005] C. Richter, L. Panek and F. Thiele. *On the application of CAA - Methods for the simulation of indirect combustion noise*. 11^{th} AIAA/CEAS Aeroacoustics Conference, AIAA Paper, AIAA 2005-2919, Monterey, CA, USA, 2005.

[Richter 2007] C. Richter and F. Thiele. *Zonal approaches for the simulation of indirect combustion noise*. 19^{th} International Congress and Acoustics, 2007.

[Saad 1986] Y. Saad and M. H. Schultz. *GMRES: A generalized minimal residual algorithm for solving nonsymmetric linear systems*. Journal on Scientific and Statistical Computing, vol. 7, n°. 3, pp. 856–869, 1986.

[Sagaut 2006] P. Sagaut. *Large-Eddy Simulation for incompressible flows*. Scientific Computation series. Springer-Verlag, Berlin, Germany, 3^{rd} edition, 2006.

[Sattelmayer 2003] T. Sattelmayer. *Influence of the combustor aerodynamics on combustion instabilities from equivalence ratio fluctuations.* Journal of Engineering for Gas Turbines and Power, vol. 125, pp. 11–19, 2003.

[Selle 2004] L. Selle, F. Nicoud and T. Poinsot. *The actual impedance of non-reflecting boundary conditions: implications for the computation of resonators*. AIAA journal, vol. 42, n°. 5, pp. 958–964, 2004.

[Smagorinsky 1963] J. Smagorinsky. *General circulation experimetns with the primitive equations.* Montly Weather Review, vol. 91, n°. 3, pp. 99–164, 1963.

[Smith 1966] L. H. Smith. *The Radial-Equilibrium Equation of Turbomachinery.* Journal of Engineering for Power, vol. 88, n°. 1, pp. 1–12, 1966.

[Snow 1952] C. Snow. *Hypergeometric and Legendre functions with applications to integral equations of potential theory.* National Bureau of Standards: Applied Mathematics Series, vol. 19, pp. 87–101, 1952.

[Spalart 1994] P. Spalart and S. Allmaras. *A one-equation turbulence model for aerodynamic flows*. La Recherche Aérospatiale, vol. 1, pp. 5–21, 1994.

[Stow 2002] S. R. Stow, A.P. Dowling and T. P. Hynes. *Reflection of circumferential modes in a choked nozzle*. Journal of Fluid Mechanics, vol. 467, pp. 215–239, 2002.

[Strahle 1971] W. C. Strahle. *On combustion generated noise*. 7^{th} AIAA/SAE Propulsion Joint Specialist Conference, AIAA Paper, AIAA 1971-735, Salt Lake City, UT, USA, pp. 71–735, 1971.

[Strahle 1973] W. C. Strahle. *A review of combustion generated noise*. AIAA Aeroacoustics Conference, AIAA paper, AIAA 1973-1023, Seattle, WA, USA, 1973.

[Strahle 1978] W. C. Strahle. *Combustion noise*. Progress in Energy and Combustion Science, vol. 4, n°. 3, pp. 157–176, 1978.

[Tam 1993] C. K. W. Tam and C. Webb. *Dispersion-relation-preserving finite difference schemes in computational aeroacoustics*. Journal of Computational Physics, vol. 107, n°. 2, pp. 262–281, 1993.

[Thompson 1987] K. W. Thompson. *Time dependent boundary conditions for hyperbolic systems*. Journal of Computational Physics, vol. 68, pp. 1–24, 1987.

[Thompson 1990] K. W. Thompson. *Time dependent boundary conditions for hyperbolic systems. Part 2.* Journal of Computational Physics, vol. 89, pp. 439–461, 1990.

[Tsien 1952] H. S. Tsien. *The transfer function of rocket nozzles.* Journal of the American Rocket Society, vol. 22, pp. 139–143, 1952.

[von Kármán 1931] T. von Kármán. *Mechanical Similitude and Turbulence*. Technical Memorandums National Advisory Commitee For Aeronautics, n°. 611, 1931.

[Widenhorn 2008] A. Widenhorn, B. Noll and M. Aigner. *Impedance boundary conditions for the numerical simulation of gas turbine combustion systems.* GT2008-50445, Proceedings of ASME Turbo Expo, Berlin, Germany, 2008.

[Wilcox 1988] D. C. Wilcox. *Reassessment of the scale-determining equation for advanced turbulence models.* AIAA Journal, vol. 26, pp. 1299–1310, 1988.

[Williams 1969] J. E. Ffowcs Williams and D. L. Hawkings. *Sound generated by turbulence and surfaces in arbitrary motion.* Philosophical Transactions of the Royal Society of London, vol. A269, pp. 321–342, 1969.

[X-Noise 1998] X-Noise. *X-noise, Aviation Noise Research Network and Coordination.* 1998.

[Xia 2016] Y. Xia, I. Duran, A. S. Morgans and X. Han. *Dispersion of entropy waves advecting through combustor chambers.* In 23^{nd} International Congress on Sound and Vibration, Athens, Greece, 2016.

[Yoo 2005] C. S. Yoo, Y. Wang, A. Trouvé and H. G. Im. *Characteristic boundary conditions for direct simulations of turbulent counterflow flames*. Combustion Theory and Modelling, vol. 9, n°. 4, pp. 617–646, Novembre 2005.

[Zheng 2015] J. Zheng, M. Huet, F. Cléro, A. Giauque and S. Ducruix. *A 2D-axisymmetric analytical model for the estimation of indirect combustion noise in nozzle flows.* 21^{st} AIAA/CEAS Aeroacoustics Conference, AIAA Paper, AIAA 2015-2974, Dallas, USA, 2015.

université PARIS-SACLAY
ÉCOLE DOCTORALE
Sciences mécaniques et énergétiques, matériaux et géosciences (SMEMAG)

Title: Analytical and numerical study of the indirect combustion noise generated by entropy disturbances in nozzle flows

Keywords: Combustion noise, entropy wave, indirect combustion noise, nozzle transfer functions, large eddy simulation

Abstract: Due to the reduction of jet mixing noise and fan noise in modern aero engines, the relative contribution of combustion noise (CN) has significantly increased over the last few decades. Two mechanisms have been identified as CN in the 70's: direct combustion noise (DCN) and indirect combustion noise (ICN). A focus is made on the ICN in this thesis with the development of a two-dimensional axisymmetric semi-analytical model taking into account the distortion of the entropy waves in order to predict the ICN for nozzle flows. The state of the art performed in the first chapter highlights the necessity to improve the prediction of ICN of 1D models by introducing the radial distortion of the entropy waves inside the nozzle. The second chapter of the manuscript details the ONERA's tools for studying ICN. The 2D model is developed in the third chapter where the Euler equations are rewritten in 2D form for the entropic part while acoustic perturbations are considered to be 1D. The fourth chapter describes the numerical computations performed during the thesis on the retained configuration (the DISCERN nozzle): a RANS and two large eddy simulations (LES) are carried out respectively for the use and the validation of the 2D model. In the last chapter, the application of the new model using the RANS mean flow field is performed, the results are compared to the 1D model and validated by confrontation with the LES predictions.

Titre : Étude analytique et numérique du bruit de combustion indirect généré par l'injection d'ondes entropiques dans une tuyère

Mots clefs : Bruit de combustion, onde d'entropie, bruit de combustion indirect, fonction de transfert d'une tuyère, simulation des grandes échelles

Résumé : Avec la réduction du bruit de jet et de soufflante dans les moteurs aéronautiques modernes, la contribution relative du bruit de combustion (BC) a augmenté de manière significative au cours des dernières décennies. Deux mécanismes ont été identifiés comme étant du BC dans les années 70 : le bruit de combustion direct (BCD) et le bruit de combustion indirect (BCI). Le cœur de la thèse est axé sur le BCI avec le développement d'un modèle semi-analytique 2D axisymétrique prenant en compte la distorsion des ondes entropiques afin de prédire le BCI dans des écoulements de tuyère. L'état de l'art réalisé dans le premier chapitre met en évidence la nécessité d'améliorer la prédiction du BCI des modèles 1D en introduisant la distorsion radiale des ondes entropiques dans la tuyère. Le second chapitre du manuscrit détaille les outils disponibles à l'ONERA pour l'étude du BCI. Le modèle 2D est développé dans le troisième chapitre où les équations d'Euler sont réécrites en 2D pour la partie entropique et en 1D pour les perturbations acoustiques. Le quatrième chapitre décrit les simulations numériques réalisées pendant la thèse sur la configuration retenue (la tuyère DISCERN) : un calcul RANS et deux simulations des grandes échelles (SGE) sont effectués respectivement pour l'utilisation et la validation du modèle 2D. Dans le dernier chapitre, l'application du nouveau modèle utilisant le champ moyen RANS est accompli, les résultats sont comparés au modèle 1D et validés par confrontation avec les prédictions SGE.

Université Paris-Saclay
Espace Technologique / Immeuble Discovery
Route de l'Orme aux Merisiers RD 128 / 91190 Saint-Aubin, France